



HAL
open science

Dynamic architectures of in vitro neuronal networks

Floriane Cohen

► **To cite this version:**

Floriane Cohen. Dynamic architectures of in vitro neuronal networks. *Neurons and Cognition* [q-bio.NC]. Université Paris sciences et lettres, 2018. English. NNT : 2018PSLET036 . tel-02512337

HAL Id: tel-02512337

<https://theses.hal.science/tel-02512337>

Submitted on 19 Mar 2020

HAL is a multi-disciplinary open access archive for the deposit and dissemination of scientific research documents, whether they are published or not. The documents may come from teaching and research institutions in France or abroad, or from public or private research centers.

L'archive ouverte pluridisciplinaire **HAL**, est destinée au dépôt et à la diffusion de documents scientifiques de niveau recherche, publiés ou non, émanant des établissements d'enseignement et de recherche français ou étrangers, des laboratoires publics ou privés.

THÈSE DE DOCTORAT

de l'Université de recherche Paris Sciences et Lettres
PSL Research University

Préparée à Institut Curie

Architectures dynamiques de réseaux neuronaux in vitro

Ecole doctorale n°564

Ecole doctorale Physique en Ile de France

Spécialité Physique

Soutenue par Floriane COHEN
le 12 décembre 2018

Dirigée par **Catherine VILLARD**

COMPOSITION DU JURY :

M. STUDER Vincent
CNRS (INSB), Président du jury

M. MARCAGGI Païkan
INSERM (UNIS), Rapporteur

M. CHARLOT Benoît
Université Montpellier (IES), Rapporteur

Mme VILLARD Catherine
Institut Curie, Directrice de thèse

|

Dynamic architectures of neuronal networks in vitro

Abstract

The function of the nervous system relies on the establishment of complex neuronal circuitry. During development, axon branching allows each neuron to establish synaptic contacts with multiple targets and is essential to the assembly of highly interconnected networks. Therefore, understanding the mechanisms underlying the control of neuronal branching is crucial in the study of neuronal circuit development.

In this thesis, we investigated this phenomenon by imposing morphological constraints to neurons through the use of different chemical micropatterning techniques. Using static micropatterns, we explored branching behavior in a wide range of geometries with a focus on the influence of branching angle. In parallel, we have also worked on the development of a dynamic patterning technique based on spontaneous adsorption of comb-like derivatives of poly-L-lysine to form switchable patterns on highly cell-repellent surfaces, with the aim of creating a platform allowing for spatio-temporally controlled generation of neurite branches.

Contents

Abstract.....	i
Chapter I. Introduction	2
I.A. The nervous system.....	5
I.A.1. Structure and evolution of the nervous system.....	5
I.A.2. Cells in the nervous systems.....	6
I.A.3. The neuronal cytoskeleton.....	10
I.B. Axon branching in the developing vertebrate CNS	18
I.B.1. Collateral branching.....	20
I.B.2. Branching through growth cone splitting	29
I.C. Axon turning through growth cone steering	31
I.C.1. The cytoskeletal dynamics of turning.....	31
I.C.2. Signaling mechanisms underlying turning	36
I.C.3. Conclusion	37
I.D. Studying neuronal branching <i>in vitro</i> : a review of different systems	37
I.D.1. Studying neuronal cell development <i>in vitro</i>	37
I.D.2. Microengineering tools to study neuronal growth <i>in vitro</i>	38
I.D.3. Application of microengineering tools to the study of neuronal branching <i>in vitro</i>	44
Chapter II. Materials and Methods	58
II.A. Introduction	60
II.B. Primary cell cultures.....	60
II.B.1. Neuronal cell cultures.....	60
II.B.2. Fixation.....	62
II.B.3. Immunofluorescence	63

II.C.	Patterned substrates	66
II.C.1.	Static patterns	66
II.C.2.	Dynamic patterns.....	71
II.D.	Microscopy observations.....	81
II.D.1.	Time-lapse experiments	81
II.D.2.	Fixed cells	81
II.E.	Analysis methods	81
II.E.1.	Growth cone analysis.....	81
II.E.2.	Branching probability and measure of branch length.....	84
II.E.3.	Time-lapse analysis	84
II.E.4.	Statistical tests	87
Chapter III.	Results	92
III.A.	Static micropatterning to study neuronal branching.....	94
III.A.1.	Introduction.....	94
III.A.2.	Methodology	95
III.A.3.	Analysis of growth cone morphology.....	101
III.A.4.	Static analysis of branching	110
III.A.5.	Dynamic analysis of neuronal branching on static patterns.....	131
III.A.6.	Conclusion	135
III.B.	Dynamic patterning to study neuronal branching.....	136
III.B.1.	Context and objective of the project	136
III.B.2.	Methodology and results	138
III.B.3.	Conclusion	147
Chapter IV.	Discussion	150
IV.A.	Actin based exploration of the GC microenvironment.....	152
IV.B.	Selection of direction by microtubules.....	153
IV.C.	Axons prefer going straight	154

IV.D. Conclusion.....	155
Bibliography.....	158
Chapter V. Appendix.....	177
V.A. List of all the branching configurations possible on the micropatterns	177
V.B. List of all the branching configurations possible on the micropatterns	
with $\alpha_1 = 0$	180

Introduction

The function of the nervous system relies on the establishment of complex neuronal circuitry. During development, axon branching allows each neuron to establish synaptic contacts with multiple targets. For example, single cortical axons from the thalamus can ramify in the motor, somatosensory, and higher order sensory cortices. The generation of these intricate connections is essential to the formation of highly interconnected networks of neurons. Therefore, understanding the mechanisms underlying the control of **neuronal branching** is crucial in the study of neuronal circuit development.

Studying neuronal cell culture *in vitro* allows for easier imaging as well as a greater degree of control of the cells microenvironment. One of the ways to achieve this control is through the use of microfabrication tools originally developed for microelectronics. The technology of **micropatterning** has been developed two decades ago with the aim of controlling neuronal cells shape and position. This technology makes it possible to reconstitute the neuronal cell physiological microenvironment *in vitro* in a highly controllable way. For this reason, micropatterning has often been used to study the complex biological mechanisms underlying neuronal growth such as polarization, axon guidance and branching.

During this PhD project, we investigated branching by imposing morphological constraints to neurons through the use of different chemical micropatterning techniques. (i) Using static micropatterns, we explored branching behavior in a wide range of geometries with a focus on the influence of branching angle (ii) In parallel, we also worked on the development of a dynamic patterning technique based on spontaneous adsorption of comb-like derivatives of poly-L-lysine to form switchable patterns on highly cell-repellent surfaces, with the aim of creating a platform allowing for spatio-temporally controlled generation of neurite branches.

In **Chapter I**, we will introduce the general context of this PhD including the structure of neuronal cells, the main steps of neuronal development *in vitro*, and neuronal branching. We will conclude this chapter with an overview of the principal examples in literature of microfabrication-based investigation of neuronal branching. The subject of **Chapter II** will be the methods employed during this work. In **Chapter III**, we will present our experimental

results. First, we will study the behavior of neurons on substrates patterned with narrow adhesive lines intersecting at varying angles. The distributions of branching probability and branches length as a function of branching angle will be analyzed. Then, we will describe our work on the development of a dynamic patterning technique to study neuronal branching. Finally, in **Chapter IV**, we will discuss the results obtained during this PhD.

Chapter I. Introduction

Contents

Chapter I. Introduction	2
I.A. The nervous system.....	5
I.A.1. Structure and evolution of the nervous system.....	5
I.A.2. Cells in the nervous systems.....	6
I.A.3. The neuronal cytoskeleton.....	10
I.B. Axon branching in the developing vertebrate CNS	18
I.B.1. Collateral branching.....	20
I.B.2. Branching through growth cone splitting	29
I.C. Axon turning through growth cone steering	31
I.C.1. The cytoskeletal dynamics of turning.....	31
I.C.2. Signaling mechanisms underlying turning	36
I.C.3. Conclusion	37
I.D. Studying neuronal branching <i>in vitro</i> : a review of different systems	37
I.D.1. Studying neuronal cell development <i>in vitro</i>	37
I.D.2. Microengineering tools to study neuronal growth <i>in vitro</i>	38
I.D.3. Application of microengineering tools to the study of neuronal branching <i>in vitro</i>	44

List of abbreviations and nomenclatures:

CNS	Central nervous system
PNS	Peripheral nervous system
AP	Action potential
ECM	Extracellular matrix
GTP	Guanosine triphosphate
ATP	Adenosine triphosphate
MT	Microtubule
+TIP	Plus end tracking protein
EB	End binding protein
MAP	Microtubule associated protein
GFP	Giant fluorescent protein
Arp2/3	Actin-related protein 2/3
NGF	Nerve Growth Factor
WAVE1	WASP-family verprolin homologous protein 1
Ena/VASP	Enabled/Vasodilator-stimulated phosphoprotein
ADF	Actin depolymerizing factor
DCX	Doublecortin

APC	Adenomatous polyposis coli
KIF2A	Kinesin-like protein 2A
PI3K	Phosphatidylinositol-4,5-bisphosphate 3-kinase
PTEN	Phosphatidylinositol-3,4,5-trisphosphate 3-phosphatase
TrkA	Tropomyosin receptor kinase A
GSK3β	Glycogen synthase kinase 3 beta
Rac1	Ras-related C3 botulinum toxin substrate 1
Wnt	Wingless-related integration site
ROCK	RhoA- Kinase
GEF	Guanine nucleotide exchange factor
GAP	GTPase activating protein
FAK	Focal adhesion kinase
MAG	Myelin-associated glycoprotein
PLL	Poly-L-lysine
PDL	Poly-D-lysine
PEG	Polyethylene Glycol
μCP	Microcontact Printing
PDMS	Polydimethylsiloxane

I.A. The nervous system

I.A.1. Structure and evolution of the nervous system

The nervous system is the part of an animal that coordinates its actions by transmitting electrochemical signals to and from different parts of its body. All living organisms can detect changes within themselves and within their environments. Once these changes have been detected, they must be analyzed so that the organisms can take the decisions necessary for their survival. As life on Earth evolved, the survival of organisms depended upon their ability to respond rapidly to variations in their surroundings. Speed of reaction was one of the key factors. Since communication from one cell to another through chemical signals was too slow, a new system enabling faster response appeared: the nervous system. This new system was based on transmission of electrical impulses from one region of the body to another. These almost instantaneous transmissions happened between specialized nerve cells, the neurons. Nervous systems are found in most multicellular animals from the level of cnidarians (corals, jellyfish) upward, but with a great diversity in terms of morphology and complexity. There are separated between two types: diffuse and centralized. Lower invertebrates such as the jellyfish or comb jellies do not possess a brain but instead a diffuse network of cells called a nerve net. In the case of higher invertebrates and vertebrates, a portion of the nervous system has reached a dominant role in integrating environmental stimuli and coordinating responses [1].

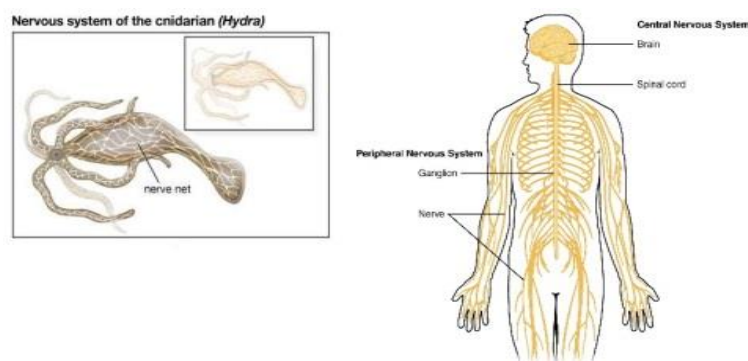


Figure I-1 : Nervous system of Hydra vs. Human nervous system . Primitive animals such as Hydra possess a nervous system consisting in a diffuse net of neurons. From Encyclopedia Britannica 2014, Inc and OpenStax Anatomy and Physiology, 2016

In vertebrates this centralization has given birth to a nervous system composed of two main parts: the Centralized Nervous System (CNS) and the Peripheral Nervous System (PNS).

The CNS is composed of the brain and the spinal cord. Impulses are transmitted to and from the CNS to the peripheral organs by nerve fibres, which make up most of the Peripheral Nervous System along with peripheral ganglia (a group of nerve cells providing intermediary connections with the CNS). Nerve fibres, commonly called nerves, are enclosed, cable-like bundles of axons (long projections of neurons), emanating from the brain and spinal cord and branching repeatedly to innervate every part of the body [2]. The neurons giving rise to these projections do not lie entirely within the nerves, their cell bodies are situated within the CNS or peripheral ganglia (**Figure I-1**). The nervous system is constituted of two main types of cells: neurons and glial cells, which will be described in the following paragraph.

I.A.2. Cells in the nervous systems

I.A.2.a) *Glial cells*

Glial cells or neuroglia are non-neuronal cells in the nervous system. The primary function of glia is to give neurons throughout the nervous system structural and metabolic support. This support includes the formation of myelin and the maintenance of homeostasis. In the CNS, glial cells are divided between 4 main types: astrocytes, microglia, oligodendrocytes and ependymal cells. Astrocytes are the most common type of macroglia found in the CNS. They have several projections that supply neurons with glucose by linking them to blood flow. Astrocytes also contribute to the formation of the blood brain barrier. Finally they regulate the external chemical environment of neurons by removing excess potassium ions and recycling neurotransmitters. Ependymal cells are involved in the secretion of the cerebrospinal fluid and the formation of the blood brain barrier. Oligodendrocytes form the myelin sheath by covering the CNS axons with their membrane. The myelin sheath provides insulation for the axons which increase the signal propagation speed. Microglia are the main players in the CNS active immune system; they are specialized macrophages capable of phagocytose. Many diseases are associated with deficient microglia such as Parkinson or Alzheimer disease.

I.A.2.b) *Neurons : a general introduction*

Neurons are highly specialized cells capable of communicating via synapses, which are membrane-to-membrane junctions containing molecular machinery that allows rapid transmission of signals, either electrical or chemical [2]. Because of their excitability, neurons

are considered the basic units of the nervous system. Neurons are present in both the CNS and the PNS, though in this work we will focus on neurons from the CNS.

I.A.2.b.1 Structure of neurons

All neurons share a common structure composed of a cell body, the soma, containing a nucleus and a number of organelles, from which extend thin processes called neurites which can either be the axon or a dendrite. Dendrites receive information from other cells, and the axon which carries information away from the soma. The soma has a typical size varying from 4 μ m for a granule cell to 100 μ m for a spinal cord motor neuron [3]. As it contains the nucleus, it is the place where most protein synthesis takes place. Neurites are about one micrometer thick in the CNS but can be much thicker in the PNS.

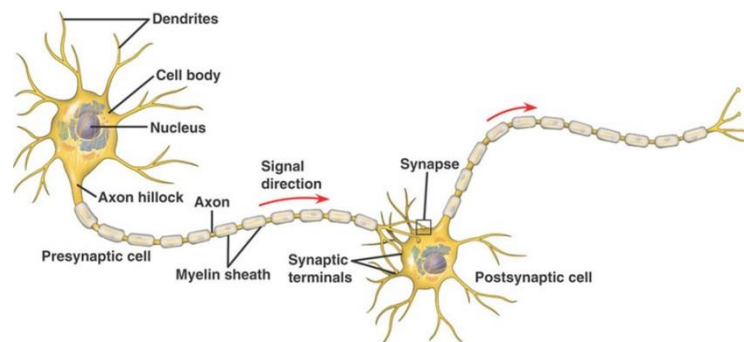


Figure I-2 : Neuronal structure. Adapted from <https://mikerbio.weebly.com>

Dendrites can extend up to hundreds of micrometers and branch multiple times, giving rise to a dense and intricate “dendritic tree”. Axons may grow over several meters before branching, up to a hundred times, to contact other cells (**Figure I-3**). The longest axons in the human body can reach a length up to 1.5m in adults, and 4 meters in the giraffe [4]. The end of the axon has branching terminals that release chemical substances known as neurotransmitters into a gap called the synaptic cleft between the terminals and the dendrites of the next neuron.

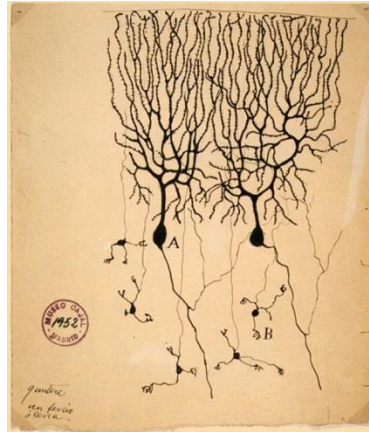


Figure I-3 : Drawing of neurons in the pigeon cerebellum, by Spanish neuroscientist Santiago Ramón y Cajal in 1899. (A) denotes Purkinje cells and (B) granule cells

These shared structural features reflect the way neurons function *in vivo*. The dendritic tree offers a large surface that is ideally suited to integrate multiple signals from other cells. The soma analyzes these signals and processes them into outputs. The axon enables the transmission of these outputs over long distances.

I.A.2.b.2 Diversity in neuronal form and function

There are over 200 different varieties of neuronal cells. Depending on the function of the neuron, the geometry of its different components (axon, dendrites and synaptic localization) can change dramatically.

Afferent or sensory neurons transmit signals from organs and tissues to the CNS. Efferent or motor neurons convey information from the CNS to the effector cells. Interneurons allow for direct communication between motor and sensory neurons.

Neurons can also be classified according to their morphology. The anatomist Camillo Golgi grouped neurons in two types: type I with long axons used to convey signals over long distances, and type II with shorter axons. One can also distinguish neurons according to their processes. For example, unipolar neurons possess only one process, bipolar neurons 1 axon and 1 dendrite and finally multipolar neurons are defined as having 1 axon and 2 or more dendrites (**Figure I-4**).

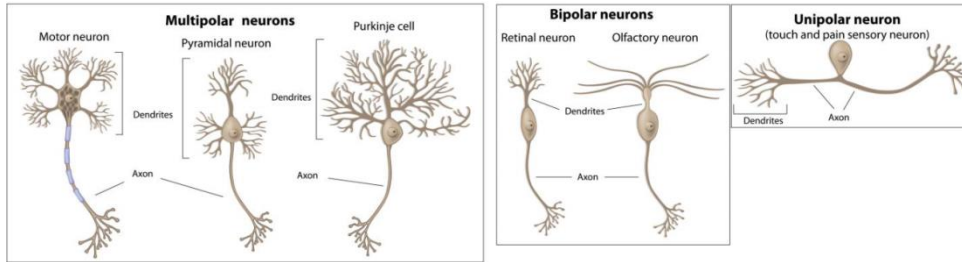


Figure I-4 : Different types of neurons, classified by morphology. Adapted from wisegeek.com

To finish with, some unique types of neurons can also be identified by their location in the nervous system and distinct shape: for example pyramidal cells with a triangular soma, or Purkinje cells which are huge neurons in the cerebellum.

I.A.2.b.3 Transmission of signals between neurons

In neurons, information travels via a short-lasting electrical event called the action potential (AP). The action potential is generated at the axon initial segment, a 30-40um long structure densely packed in ion channels located close to the soma. Like all cells, neurons possess a membrane that separates the intracellular medium from the outside. Because cells maintain a differential repartition of ions between the intracellular medium and the outside, there is an electrical difference of potential across the membrane. At rest (i.e. when the neuron is not generating a nerve impulse), this difference amounts to about -65mV.

Once generated in the axon initial segment, the axon potential then propagates down the axon, increasing the positive ion concentration, and therefore the potential of the membrane. When the membrane potential reaches a threshold of about -50mV, closed voltage-gated sodium channels open and sodium rushes into the cell (**Figure I-5 2.**). This increases the positive ion concentration and thus the membrane potential around these channels, which leads to the opening of nearby sodium channels further along the axon. (**Figure I-5 3.**) The depolarization quickly spreads along the axons (up to 120m/s in some nerve fibers) and stops when sodium channels enter transiently into a third state called the inactivated state.

As Na^+ ions flow into the axon, eventually they reach a concentration that is high enough to cause the opening of voltage-gated potassium (K^+) channels. This opening begins a phase of repolarization. Indeed it allows for the diffusion of K^+ potassium ions out of the axon which will in turn lead to the lowering of the potential across the membrane. Sodium channels also

close when the Na^+ concentration is high enough, entering an inactivated state. ((**Figure I-5** 4.).

The decrease of the membrane voltage caused by the outward flow of K^+ ions eventually leads to the closing of K^+ potassium channels. Then, ATP-powered potassium/sodium ion pump push the ions back to their original sides, thus resetting the axon membrane potential to its resting value.

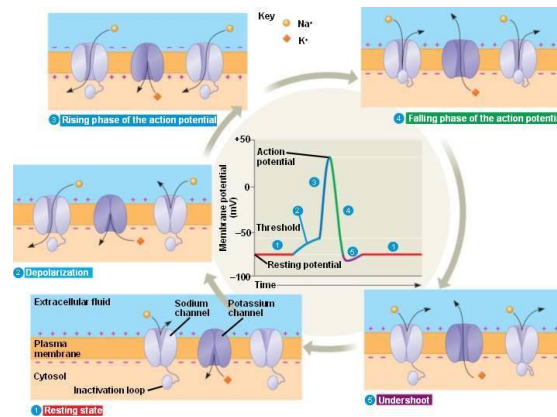


Figure I-5: Different stages of Action Potential propagation along the axon. From http://bio1152.nicerweb.com/Locked/media/ch48/action_potential.html

Finally, when the AP reaches the axon’s terminal arbor, the depolarization results in an opening of Ca^{2+} channels, which in turn lead to a release of neurotransmitters at the synapse.

The neurons’ ability to generate APs allows fast propagation of signals over long distances with relatively little dissipation.

I.A.3. The neuronal cytoskeleton

Neurons, as all eukaryotic cells, have a common envelope named the plasma membrane. This membrane is a bilayer of lipid molecules with many types of transmembrane proteins embedded in it, and constitutes the interface between the cell internal cytoplasm and the extracellular matrix (ECM). The cytoplasm is composed of a medium called the cytosol containing: the nucleus (inside which resides the cell’s genetic material), organelles (such as ribosomes or the mitochondria) and a complex network of interlinking filaments called the cytoskeleton.

The cytoskeleton gives the neuronal cell its shape and mechanical properties. It also plays a major role in the establishment of polarization, cellular compartmentalization, as well as in axon outgrowth, guidance and branching. Therefore, in the following section we will describe

the structural organization and dynamic remodeling of the cytoskeleton in various stages of neuronal development.

Actin and microtubules dominates the faster timescale dynamics of the neuronal cytoskeleton, particularly in highly motile regions such as the axonal growth cone (see **I.A.3.c**), where both types of filament can have half-lives as short as 1-2 minutes [5]. For this reason, we will mainly focus on these two components here. For information about neurofilaments we direct the reader to the following review [6].

After describing actin and microtubules organization, we will discuss the organization and dynamics of these elements in the two structures that play major roles in neuronal development: the growth cone and actin waves.

I.A.3.a) Microtubules

Microtubules are extended, dynamic polymers assembled from GTP-bound α - β -tubulin dimers (formed from six α - and seven β -isotypes)[7]. These heterodimers bind in a head-to-tail fashion to form polarized filaments and associate laterally to form a hollow tube with an diameter of about 25nm and a length between fractions to tens of microns [8]. The intrinsically unsymmetrical nature of microtubules is expressed by a (+) and a (-) end. At the (+)-end, β -subunits are exposed whereas at the (-)-end, α -subunits are exposed . Polymerization can happen at both ends but occurs most rapidly at the (+)-end through the addition or removal of α - β -tubulin dimers [9]. *De novo* MT formation in cells is typically supported by the γ -tubulin ring complex or by microtubules fragments[10].

Microtubules switch between phases of growth, pausing and disassembly in a process named dynamic instability (see **Figure I-6**). This process allows individual MTs to explore cellular regions and retract in case they do not find the proper environment [11].

A number of microtubule-binding proteins can act to variously stabilize, destabilize, cap, sever, bundle and localize filaments [12]. For example, plus-end tracking proteins (+TIPs) regulate MT dynamics by accumulating at the ends of growing MTs. Among these +TIPs, fluorescently tagged end binding proteins (EBs) are widely used to track growing MTs and provide an efficient tool to probe the MT organization in neuronal cells in vitro and in vivo [13].

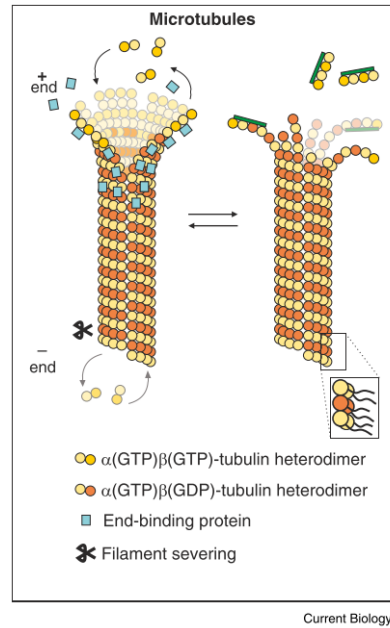


Figure I-6: Microtubule polymerization dynamics. Cartoon representing microtubule polymerization and depolymerization. For a growing microtubule (left), polymerization occurs primarily at the (+) end through the addition of α - β -tubulin heterodimers. After incorporation in the filament, hydrolysis of the β -tubulin-bound GTP takes place. A reduction in the concentration of free α - β -tubulin dimers leads to microtubule shrinkage (right). Adapted from [9]

Neuronal MTs guide intracellular transport and induce morphological changes during the various phases of neuronal development, as reviewed in [9]. In the following paragraph we will describe the architecture of the neuronal microtubule cytoskeleton.

Neurons have a very dense MT network. Typically, axonal cross sections contain between 10 and 100 MTs [14]. However, the organization of MTs in different parts of the neurons is very heterogeneous. More specifically, the stability, orientation, modification and associated proteins of MTs differ strongly in the axon and in dendrites. While MTs in axons of various types of cultured neurons were observed to be oriented uniformly (with their (+) distal to the cell body), dendrites were found to contain non-uniformly oriented MTs that were about half (+)end out and half (-) end out [15].

Amongst other key differences we should also mention the repartition of MAPs, microtubule-associated proteins who bind to the tubulin subunits to promote microtubule stabilization. MAP2 and Tau are the main MAPs that can be found in neurons. Of note, MAP2 is primarily present in dendrites (up to the Axon Initial Segment) and Tau only in axons. Consequently, the Tau protein and more specifically the gradient of Tau phosphorylation is used as an axonal

marker. The monoclonal Tau1-antibody which recognizes desphosphorylated serines sites is commonly used to identify the axon [16].

1.A.3.b) Actin filaments

Actin filaments, or F-actin, are extended, dynamic polymers, assembled from ATP-bound G-actin monomers. Two γ -actin and one β -actin isoforms dominate in brain tissues. Actin filaments are intrinsically polarized and have two ends named the barbed end and the pointed end [17]. They possess a diameter of 6 nm (versus 25nm for microtubules) and a length up to several micrometers. As can be seen in **Figure I-7**, G-actin monomers are added to the barbed end upon and later removed at the pointed end in a process called actin treadmilling. Actin nucleation and polymerization is regulated by several actin nucleators such as formins or the ARP2/3 complex[18].

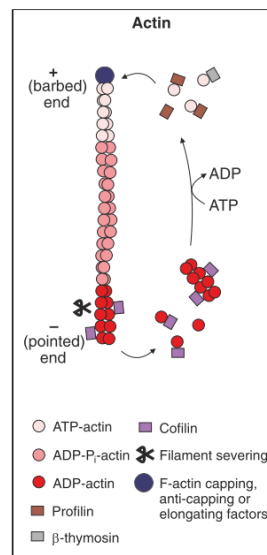


Figure I-7: Actin polymerization dynamics. Cartoon depicting actin treadmilling. The addition of ATP-actin monomers is regulated by profilin and elongating factors like formins. When ATP-actin monomers are incorporated in the filament, the ATP is hydrolysed. Depolymerization occurs at the pointed end upon detachment of ADP-bound actin monomers.

Actin filaments self-assemble in structures such as the lamellipodium and the filopodium. Lamellipodia are large actin projections of the cell. They are constituted of a quasi two-dimensional actin mesh. On the other hand, filopodia are finger-like structures composed of oriented, bundled actin filaments. Filopodia can usually be found at the front of the lamellipodium with the actin filaments (+) end oriented towards the protrusion direction.

Despite the fact that fine actin architectures have prolonged challenging to study due to F-actin small diameter (about 6nm), the emergence of non-diffraction-limited light microscopy techniques(such as super-resolution light microscopy) have provided major insight in actin architecture in neurons. For example, Stochastic Optical Reconstruction Microscopy (STORM) imaging of cultured hippocampal neurons has revealed the existence of actin rings periodically appearing along the neurites shaft [19].

I.A.3.c) Growth cone

The growth cone is a hand-like structure that can be found at the tip of a developing or regenerating neurite. It can translate environment signals (such as chemical guidance cues) into directional movement.

The structure of the growth cone is understandable in light of those functions it supports *in vivo*: guiding and driving neurite outgrowth.

The growth cone can be separated into three domains. First, the peripheral (P) domain at the leading edge of the growth cone contains dynamic, finger-like filopodia that explore the environment, separated by thin, lamellipodia-like veils (see **Figure I-8**). Individual dynamic microtubules explore this region, usually along filopodia [20]. The central (C) domain contains stable, bundled microtubules coming from the neurite shaft, as well as several organelles. To finish with, the transition (T) zone lies at the interface between the P and the C domains, and encloses actin arcs, which are actomyosin contractile structures, as was first reported in [21] . The shape and movement of the growth cone are determined by these cytoskeletal components on its journey during development.

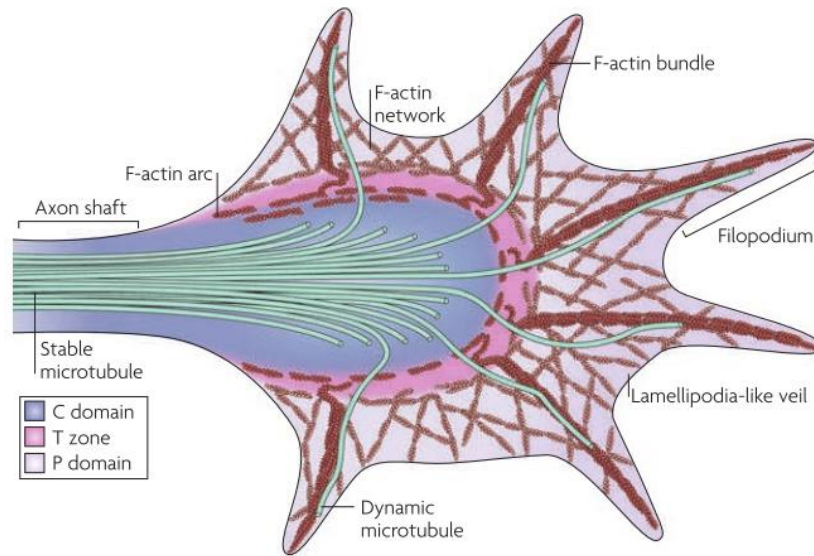


Figure I-8: The structure of the growth cone. From [20]

I.A.3.d) Actin waves

In 1998, Ruthel and Banker first reported having observed wave-like, F-actin filled membrane protrusions traveling along the axons and immature neurites of cultured rat hippocampal neurons[22]. These propagating structures were later coined “actin waves”.

Although these actin waves did not attract much attention at first, several recent studies have shed light on the molecular machinery behind the generation, mobility and functions of actin waves [23], [24]. Of note, actin waves have also been reported in organotypic hippocampal slices[25].

Actin waves usually emerge at the base of the neurites close to the cell body and slowly migrate to their tips with a speed of $\sim 2\text{--}3 \mu\text{m}/\text{min}$, flaring the plasma membrane during transit [23], [25]. As can be seen in **Figure I-9**, actin waves can easily be identified along the neurite shaft thanks to their characteristic fin-like lamellar shape on both sides of the shaft, forming lamellipodia and filopodia similarly to the growth cone.

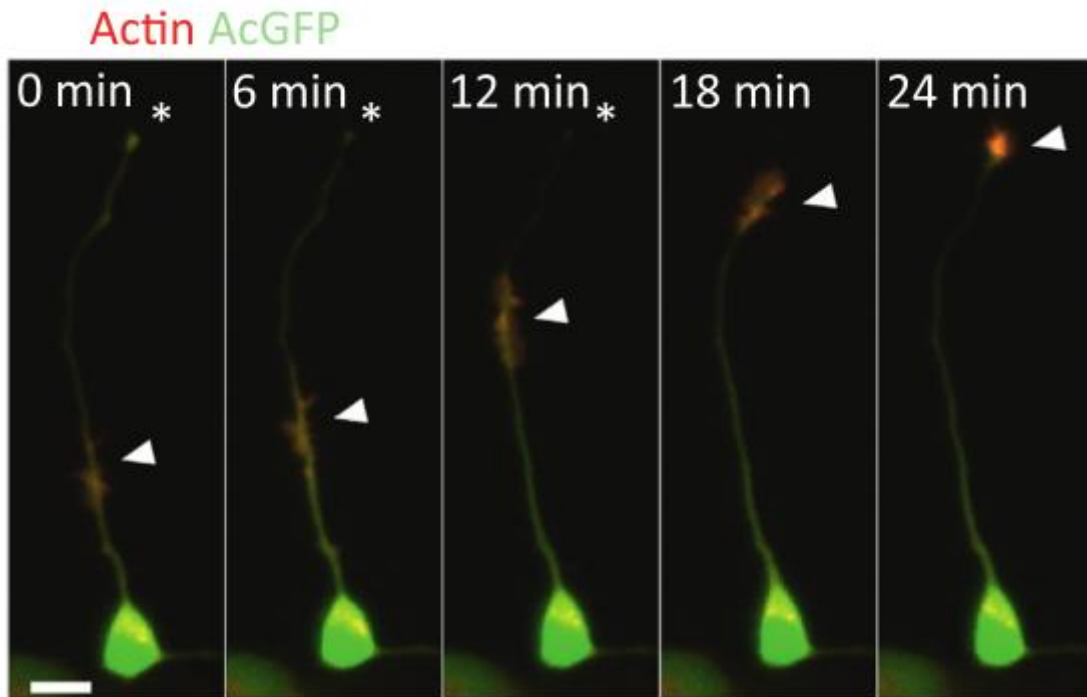


Figure I-9 : F-actin anterograde migration along an axon as waves. Fluorescence time-lapse images at 6-min intervals, and a corresponding phase-contrast image (leftmost frame), of a cultured hippocampal neuron expressing mRFP-actin and the volume marker AcGFP. From [23]

It has been suggested that actin waves are linked with outbursts of neurite growth and constitute, along with microtubules, a transport mechanism that brings actin and actin associated proteins toward the growth cone [23], [25]. Indeed, actin in waves maintains much of its cohesiveness during transport whereas actin in nonwave regions of the neurite rapidly diffuses as measured by live cell imaging of photoactivated GFP-actin [25]. Interestingly, the theory asserting that actin waves boost neurites outgrowth has been recently contested in [26], which proposes an alternative role for actin waves centering on maintaining the growth cone active during environmental exploration.

Actin waves also play a major part in neuronal branching, and have been shown to induce *de novo* neurite branching through their engorgement of filopodia along the neurite shaft, as can be seen in **Figure I-16** [25].

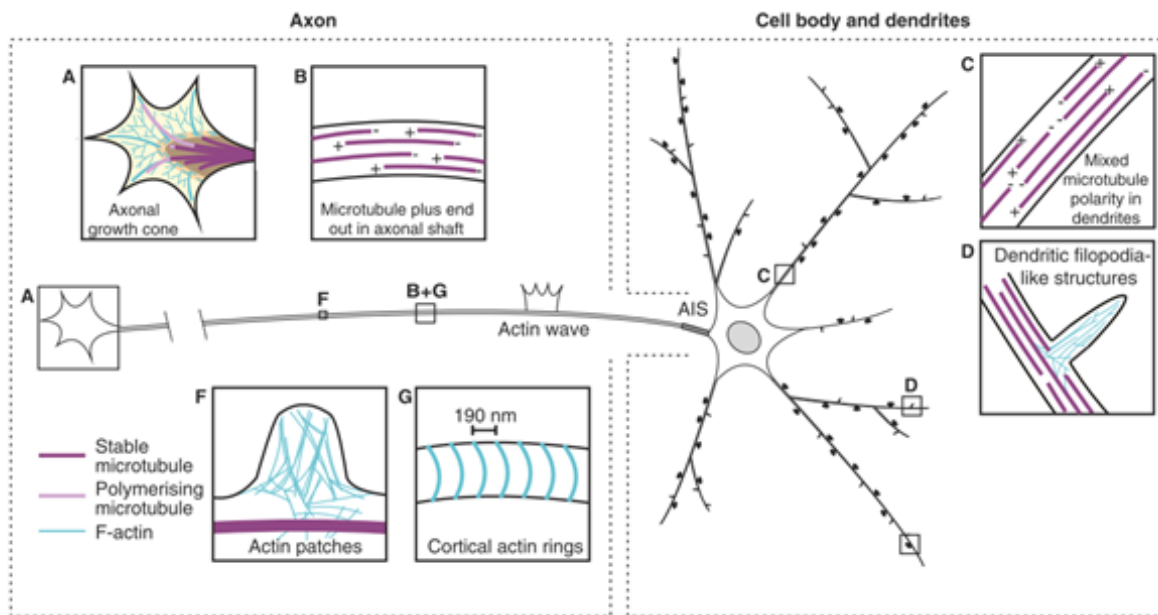


Figure I-10: Actin and microtubule architectures observed in cultured neurons. Cartoon representation of a mammalian hippocampal neuron *in vitro* A) the growth cone, at the tip of the axon, regulates axon outgrowth and guidance) and C) denotes the orientation of MTs in axon versus in dendrites respectively. D) filopodia-like structures on dendrites F) Local zone of actin accumulation “actin patches” have been suggested to be precursors of filopodia and branching points G) Actin rings have been observed along the neurite shaft. Adapted from [9]

I.B. Axon branching in the developing vertebrate CNS

The function of the nervous system relies on the establishment of complex neuronal circuitry. During development, each neuron must connect with multiple synaptic targets, sometimes in widely divergent regions of the nervous system. For example, single cortical axons from the thalamus can ramify in the motor, somatosensory, and higher order sensory cortices [27]. The generation of these intricate connections is crucial to the formation of highly interconnected networks of neurons. With organisms of larger size and increased complexity, this “problem of connectivity” becomes all the more challenging [28]. One of the goals of neurosciences is to understand the strategies used to build these neuronal networks. In the case of neuronal connectivity, natural selection has adopted the strategy of axon branching: each neuron makes contacts with its multiple targets through branching of its axon (see **Figure I-11**). Therefore, understanding the mechanisms behind the control of axon branching is a critical step in the study of neuronal circuit development. Furthermore, in the adult nervous system, the formation of axon branches also plays a key role in the system response to injury and neurodegeneration, and might contribute to plasticity [29].

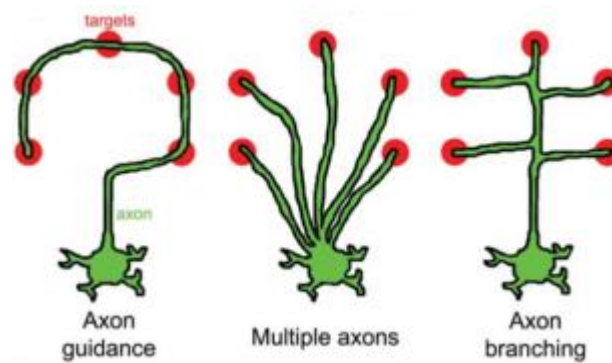


Figure I-11 : The problem of neuronal connectivity and the modes of axon branching. A neuron could reach out to multiple targets by (i) having a single axon guided to each target (ii) having several axons with each axon being guided to one or many targets; or (iii) having a single axon which separates into several branches and each branch contact one or more targets. Natural selection has selected the strategy of axon branching to solve the problem of neuronal connectivity. From [30]

Branching is triggered by local extracellular cues in the target regions, which signal through receptors on the axonal membrane. These receptors can activate intracellular signaling pathways that regulate the cytoskeleton dynamics.

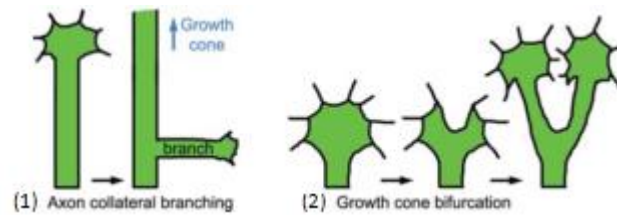


Figure I-12 : The two different modes of branching. (1) Axon collateral branching and (2) Growth cone bifurcation. From [30]

Axon branches can form through two distinct modes (see **Figure I-12**):

(1) In the mammalian CNS, branches typically extend interstitially from the axon shaft behind the terminal growth cone. This mode of branching is called collateral branching. This interstitial branching can occur days after axons have moved away from their target.

Corticospinal axons in rodents bypass spinal targets and later generate collateral branches that arborize once they have reached their target sites[31] (see **Figure I-13**).

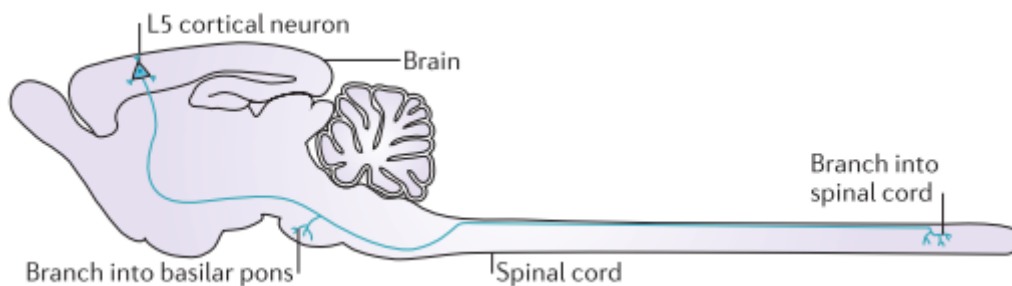


Figure I-13 : An example of interstitial branching in a developing CNS pathway : corticopontine and corticospinal branching: Cortical axons first bypass their target in the basilar pons but after a delay form branches that arborize in the pons [32]. Corticospinal axons in rodents bypass spinal targets and later generate collateral branches that arborize once they have reached their target sites. From [33]

(2) In certain circumstances, branches can be formed by splitting of the terminal growth cone, which can give rise to two Y or T shaped axon branches. For example in the mouse dorsal root entry zone, the growth cones of the dorsal root ganglion axons bifurcate to form two daughter branches that descend or ascend and arborize in the spinal cord [34] (see **Figure I-14**).

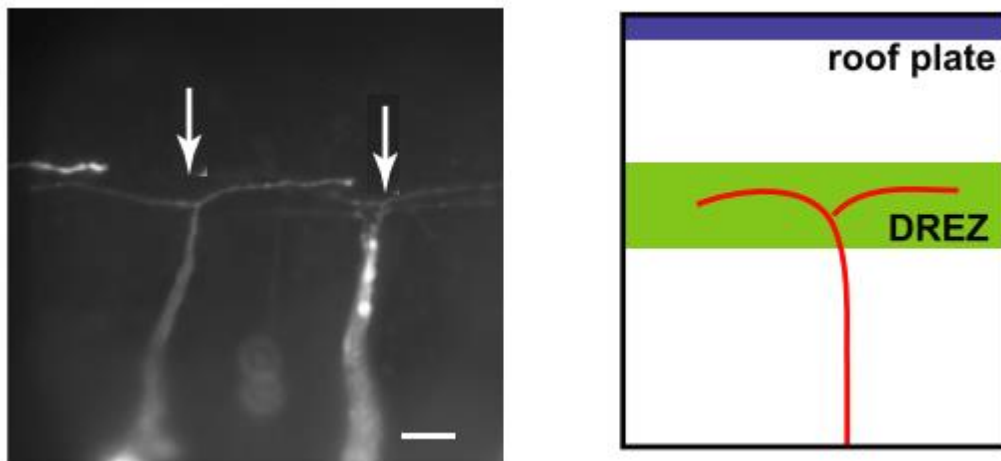


Figure I-14 : Branching through growth cone bifurcation: Sensory axons bifurcate at the Dorsal Root Entry Zone (DREZ). The daughter branches grow at a 90° angle from the initial direction, straight along the rostrocaudal axis. Neurons are visualized at the single cell level by Dil labeling using iontophoresis. Images were taken from the lateral side of the spinal cord in an open book preparation of E13.5 rat embryos. Arrows indicate the branching points, Scale bar 100µm. Adapted from [34]

These two modes of branching generate different geometries of branching and contribute in different ways to the establishment of neuronal circuitry. In the following section we will present both modes of branching, and give a brief overview of the current knowledge of the mechanisms underlying them, focusing on the cytoskeletal dynamics at branch points as well as the way intracellular signaling pathways regulate cytoskeletal reorganization.

I.B.1. Collateral branching

I.B.1.a) *Initiation of a branch*

Axon collateral branches are initiated by protrusive lamellipodia and filopodia emerging locally on the axon shaft. Dynamic studies of collateral branching have suggested three modes of axon collateral branching initiation, based on the observed phenomenology of branch formation: (a) through the emergence of filopodia or (b) lamellipodia, or through (c) growth cone pausing. (see **Figure I-15**).

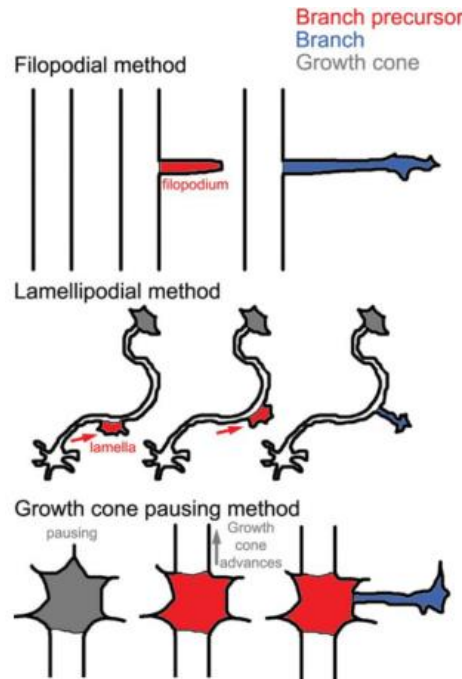


Figure I-15 : Methods of axon collateral branches initiation. This cartoon show the basic sequences of events for the initiation of branches through the filopodial, lamellar and growth cone pausing events. From [30]

In the filopodial branching mode, branches originate from axonal filopodial protrusions. Timelapse imaging of fluorescently labeled corticospinal axons showed that segments of corticospinal axons that are close to the pons initiate multiple filopodia, some of which undergo stabilization and mature into axon collateral branches[32]. *In vitro* sensory axons have been observed to give rise to branches through the protrusion of filopodia [35].

In the lamellipodia branching mode, some types of neurons generate branches from lamellipodia that actively migrate along the axon shaft, otherwise known as actin waves (see Actin waves). As seen in **Figure I-16**, timelapse imaging of hippocampus slices has revealed that waves can serve as precursors for collateral branching *in vivo* [25]. Lamellipodia can also arise from the axon shaft in the absence of waves. The same phenomenon has been observed *in vitro* [25].

Finally, in the growth cone pausing mechanism, the collateral branch is formed from sites along the axon shaft where the growth cone stalled during axon extension, leaving behind domains of persistent protrusions, after which it resumed its advance.

In each of these modes, axonal protrusive activity, whether it consists of filopodia or lamellipodia, is a crucial condition for the initiation of a collateral branch at a given site along the axon shaft [36].

I.B.1.b) The cytoskeletal dynamics of axon collateral branching

The basic of the cytoskeletal reorganization leading to axon collateral branch formation has been established by multiple studies [35], [37], [38]. Branches are first initiated by actin-filament-based filopodial or lamellipodial protrusions on the axon shaft. These protrusions are then invaded by microtubules which are subsequently stabilized as the branch continues to mature and extend. Each of these steps will be detailed in the sections below.

I.B.1.b.1 Actin dynamics

I.A.1.a)1.i Filopodia initiation

As detailed in I.A.3.d), filopodia are finger-like protrusions that contain bundled actin filaments. The rapidly polymerizing barbed ends of the actin filaments are oriented towards the tip of the filopodium, generating forces that push the membrane forward.

Unlike the growth cone, the consolidated axon shaft contains a relatively low level of actin filaments and exhibits very little protrusive activity. Filopodia can emerge from sites of transient accumulations of actin filaments called “actin patches”[39]. Actin patches have been observed to serve as precursors to the formation of axonal filopodia *in vivo*, for example in timelapse imaging of fluorescently labeled cortical pyramidal neurons in mice brain slices [40]. Although filopodia emerge from actin patches, only a small fraction of actin patches give rise to filopodia [41].

The formation of filopodia can generally be described in three basic steps: actin filament nucleation driving the generation of new actin filaments, elongation of nucleated actin filaments through polymerization at the barbed end, and the bundling of these elongating actin filaments. For each of these steps actin filaments are regulated by actin associated proteins (see **Figure I-18 a)**).

An important regulator in the nucleation step of the filopodial initiated branch formation is the Arp2/3 complex. The Arp 2/3 complex nucleates new actin filaments from the sides of existing filaments, and is required for NGF-induced actin formation, filopodia formation and branching of sensory axons[42]. Activation of Arp2/3 complex is driven by WAVE1 and Cortactin, as well as stabilization of the newly created filaments[43]. Additional actin filaments nucleators may be needed to create the mother filaments bound by the Arp2/3 complex, such as the actin nucleation factor cordon-bleu[44].

The initiation of a filopodium also requires the rapid elongation of actin filaments as well as the bundling of actin filaments. These mechanisms include several different actin associated proteins. ENA/VASP proteins bind to the barbed ends of actin filaments and promote actin filaments elongation. The actin-severing protein actin-depolymerizing factor (ADF)/cofilin enhances actin depolymerization, thus enhancing filament assembly by increasing the available pool of actin monomers and free barbed end [45].

1.A.1.a)1.ii Lamellipodia initiation

The understanding of the formation of axonal lamellipodia is still limited. Actin monomers in axonal waves undergo anterograde transport and turnover. Actin waves seem to propagate using directional actin treadmilling as the driving mechanical force [23]. Actin polymerization/depolymerization is correlated with the presence of several actin binding proteins, such as Arp3, desphosphorylated cofilin (driving actin filament turnover during protrusive activity) or shootin within the actin waves [23], [25], [46]. In cultured hippocampal neurons, doublecortin (DCX) accumulates both at the growth cones and within actin waves, and depletion of DCX prevents the formation of waves and axon branching[47]. DCX can interact with microtubules and also with actin filaments[48]. However neurons branching, which occurs through growth cone splitting, was not impaired by DCX depletion[47]. To finish with, inhibition of myosin II, a motor driving actomyosin contractility along antiparallel filaments, has been shown to promote axon branching and the presence of actin waves [25].

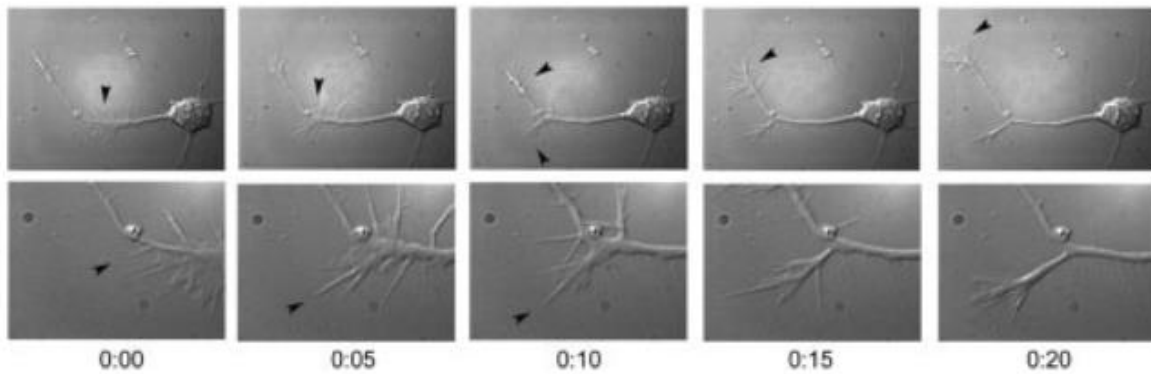


Figure I-16 : Neurite branch formation: Phase images of waves in stage 2-3 mice embryo hippocampal neurons. Time shown in min. A small filopodia protruding from the shaft before wave arrival (arrowhead, bottom row) undergoes engorgement upon wave arrival (0:05 min) inducing the subsequent elongation of a new branch. From [25]

I.B.1.b.2 Microtubule dynamics

Actin filament polymerization is the pushing force that drives membrane protrusion, but further development and stabilization of axon collateral branches necessitates the entry of dynamic microtubules in the membrane protrusions [33]. The targeting of microtubules into filopodia provides structural support for the nascent branch and also allows the delivery of axonal transport cargoes into the branch.

As seen in I.A.3.a), microtubules in axons are organized in stable parallel bundles. This was observed in chick sensory axons as well as in rodent hippocampal and cortical neurons [35],[38],[37] ; one of the first important early steps in axon branch formation is the splaying of bundled microtubules. This is followed by local fragmentation of microtubules at branch points which enables the entry of short microtubule fragments in the membrane protrusions see **Figure I-18 b)**). Only the filopodia containing microtubules can develop into stabilized mature branches, although even those branches that contain microtubules may eventually retract [49]. Several microtubules associated proteins (MAPs) are involved in this reorganization of the axonal microtubules.

First, microtubule severing proteins such as spastin and katanin can be involved in axon branching. Overexpression of these proteins in cultured hippocampal neurons leads to increased axon branching [50]. Of note, the stabilizing MAP tau has a protecting effect for microtubules against the severing effects of katanin [51]. This supports the hypothesis that a

detachment of tau from microtubules might be a regulating mechanism for branch formation. The microtubules plus end proteins (+TIPS) regulate MT dynamics and growth directionality by accumulating at the ends of growing MTs. For example the adenomatous polyposis coli protein (APC) binds to the plus end of microtubules and stabilize their growing ends. Knockout of APC in early developing mouse cortical neurons leads to excessive branching and a disrupted microtubules organization at branch points [52]. The exact nature of APC contribution to axonal branching is not yet fully understood.

Among other proteins that regulate branching, we can mention microtubules destabilizing proteins such as the kinesin KIF2A which has been shown in knockout mice to suppress collateral branch extension [53], and the microtubule binding proteins doublecortin (DCX), whose knockdown triggers excessive branching of cortical and granule neurons [54].

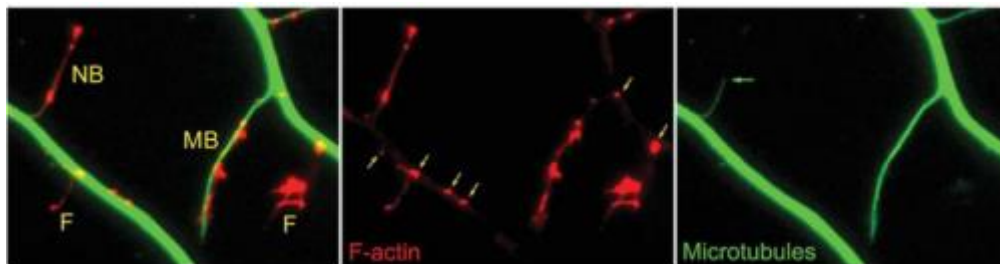


Figure I-17 : Example of the steps in the sequence of collateral branch formation captured in a fixed sample of cultured chicken embryonic sensory neurons. Examples of axonal filopodia (F), a nascent branch (NB) and a mature branch (MB) are shown. The rightmost filopodium also exhibits a lamellipodial protrusion at its tip. The yellow arrows in the F-actin panel denote axonal F-actin patches. A single microtubule is present in the nascent branch (green arrow in microtubule panel), whereas the mature branch contains multiple microtubules. From [35]

I.B.1.b.3 Interaction between actin and microtubules

The fundamental mechanisms underlying axon collateral branching rely on interactions between dynamic microtubules and actin filaments. Indeed, timelapse imaging studies have shown that at branch points, the splaying of microtubules is colocalized with focal accumulation of actin filaments. Furthermore, application of drugs that repress either microtubules or actin dynamics also inhibit polymerization of the other cytoskeleton element [55], [56]. Although understanding of the mechanism coordinating actin and microtubules reorganization is still rather limited, there are a few proteins that have attracted attention as candidates for the role of coordinator of both cytoskeletal systems during axon branching.

First Drebrin , a F-actin-binding protein involved in actin filament bundling regulation, has been referred to as a link between the actin and microtubule system [57]. Drebrin binds to EB3,

a microtubule plus end binding protein that associates with the tips of polymerizing microtubules [57]. Debrin can be found in actin patches and in the proximal part of filopodia, an ideal position to guide the entry of microtubule plus ends into the filopodia shaft.

Septins are a family of GTP binding proteins that regulate actin and microtubule organization, their crosstalk, and their binding to other effectors [58]. Several studies have pointed out the combined role of Septin 6 and 7 for the coordination of the cytoskeleton during axon collateral branching [59]–[61]. Septin 6 is present in actin patches and recruits cortactin to trigger the formation of filopodia, while Septin 7 guides the entry of axonal microtubules into filopodia (see **Figure I-18 b**).

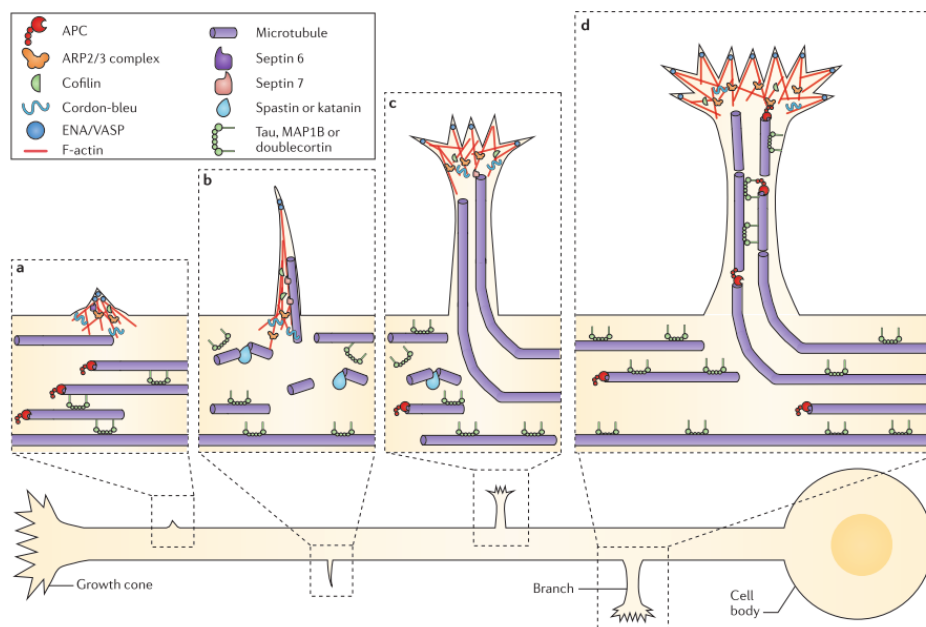


Figure I-18 : Reorganization of the cytoskeleton at different stages of axon branching. a) The first step for the formation of membrane protrusion is the focal accumulation of actin filaments which forms actin patches. Actin filament nucleation is regulated by ARP 2/3 and cordon bleu, actin filament branching by ARP 2/3 and actin filament elongation by ENA/VASP. Cofilin mediates turnover of F-actin, and Septin 6 is also present in the actin patch. In the axon shaft microtubules are stabilized by microtubule associated proteins (MAPs), tau and doublecortin. They are also capable of extension at their plus ends, this polymerization is mediated by microtubules plus end proteins (+TIPs) such as APC. b) The emergence of filopodia from the axon shaft is accompanied by localized splaying and fragmentation of microtubules. These microtubules then enter the filopodium along actin bundles. Microtubules severing is regulated by katanin and spastin, while the entry of microtubules in the filopodium is promoted by Septin 7. c) and d) Stabilization and maturation of the nascent branch. As the branch continues to grow, it is invaded by microtubules which are bundled and stabilized by MAPs. Some of the microtubules in the axon shaft are protected from the severing proteins by MAPs. The branch continues to extend, and is led by its own growth cone. From [33].

I.B.1.c) *Signaling mechanisms underlying axon collateral branching*

Branching is triggered by local extracellular cues in the target regions, which signal through receptors on the axonal membrane. These receptors can activate intracellular signaling pathways that regulate the cytoskeleton dynamics. In the following section we will give several examples of these different signaling pathways.

I.B.1.c.1 **NGF-induced branching and PI3K signaling pathway**

The neurotrophin family consists of molecules that regulate neuronal growth and survival. Among them, NGF (Nerve Growth Factor) is one of the extracellular signals that mediates axon collateral branching [33], [39]. Several studies have demonstrated that NGF promotes the formation of axon collateral branching in sensory axons through activation of the phosphatidylinositol-3 kinase (PI3K) pathway [35], [41]. The PI3K pathway is a major regulator of axonal growth, through the control of gene expression and cytoskeleton elements during neuronal morphogenesis. PI3K is a lipid kinase that transforms PIP2 (phosphatidylinositol [4,5] biphosphate) into PIP3 (phosphatidylinositol [3,4,5] triphosphate). PIP3 can in turn recruit a wide range of proteins to the membrane. On the opposite, phosphatase such as PTEN can turn PIP3 back into PIP2, and genetic deletion of axon branching *in vivo* increases branching [62].

The current model for the NGF-signaling pathway has NGF activate the TrkA membrane receptor, which results in activation of the PI3K signaling pathway, thereby activating the RAC1 GTPase to drive WAVE1 activity which in turns activates the actin nucleating complex Arp 2/3 [42], as can be seen in **Figure I-I-20**.

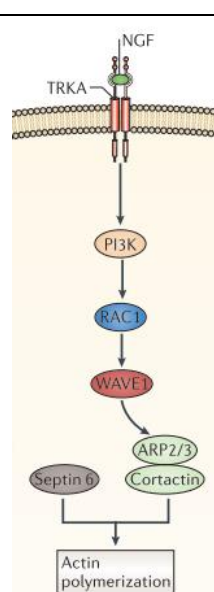


Figure I-I-20 : Nerve growth factor (NGF)-induced signalling promotes axon branching in chick sensory dorsal root ganglion axons. It does this by activating PI3K and, in turn, RAC1, which activates actin-associated proteins to increase actin polymerization and the formation of actin patches. Cortactin, which is recruited by septin 6, promotes the emergence of filopodia from actin patches. From [33].

I.B.1.c.2 GSK3- β

In other models of axon branching, extracellular cues have been shown to influence axon branching through the regulation of microtubule dynamics via GSK3 β signalling. GSK3 (Glycogen synthase kinase-3) is a serine/threonine kinase that has emerged as an important regulator of axon branching by regulating the reorganization of microtubule. This protein is a downstream effector of several extracellular cues, among which Wnts (secreted glycoproteins that activate different intracellular signal transduction pathways) and NGF[63]. Inhibition of GSK3 activity was shown to induce axon branching in embryonic sensory neurons [64]. GSK3- β mediates the activity of several microtubule associated proteins, including MAP1b [65] and doublecortin (DCX) [66].

I.B.1.c.3 Calcium

Intracellular calcium level is a major regulator for several cellular mechanisms. Indeed calcium can activate a multitude of intracellular signaling pathways, though the signaling effectors downstream of calcium are not yet fully understood. Netrin-1 can promote axon branch formation by increasing the frequency of calcium transients along cortical axons, which

leads to the formation of branches [67]. Conversely, the initiation of axonal branches induced by the local application of NGF to sensory axons was found to require neither intracellular nor extracellular sources of calcium [35]. To conclude with, the role of calcium seems to be dependent on the neuron type and on the signal inducing the response (eg. NGF vs Netrin-1).

I.B.1.c.4 Rho-GTPases

Rho-family GTPases (Rho, Rac and Cdc42) are a class of proteins that control cytoskeletal dynamics downstream of nearly all guidance signaling receptors. Rho-GTPases play a major role in axon extension, guidance, as well as branching. Their activity is controlled by GEFs (guanine nucleotide exchange factors) and GAPs (GTPase activating proteins) which can turn the GTPases on and off respectively.

Several studies have shown that Rac1 promotes axon collateral branching [68], [69]. In sensory neurons, Rac1 is activated by the NGF-PI3K and its activity stimulates the formation of actin patches [69].

In neurons, RhoA, through its downstream effector RhoA- Kinase (ROCK), is generally considered to promote actomyosin driven contractility and repress the protrusion of actin filament based structures [39]. RhoA-ROCK has been observed to inhibit the elaboration of actin patches as well as the emergence of filopodia from actin patches by activation of Myosin II [70]. Conversely, RhoA has been shown in another study to promote activity-dependent axon branching, through its positive regulation of actin polymerization. Thus, the role of RhoA might be influenced by neuronal activity.

I.B.2. Branching through growth cone splitting

The second mode of branching happens through growth cone splitting. Indeed, growth cone bifurcation at the tip of the extending axon can give rise to two axon branches. Axon branching through growth cone bifurcation is not considered to be a major mechanism for axon branching, and has been frequently linked to axon guidance [71]. It is an essential mechanism to the development of the nervous system during embryogenesis. Nevertheless, in vertebrates, dorsal root sensory neurons have been reported to branch through growth cone bifurcation after entering into the spinal cord [72], [34], [73]. The sensory axon growth cone splits into branches that project rostrally and caudally to their target fields. Growth cone bifurcation has also been studied in the context of axon guidance in *C. elegans*. [74].

In vitro studies have described in details the different steps of branching through growth cone bifurcation. First, a suppression of protrusion at the leading edge of the axon is observed, in

the direction corresponding to the axis of axon outgrowth. Meanwhile, the sides of the growth cone maintain their protrusive activity (see **Figure I-21**). This asymmetry results in the separation of the growth cone into distinct zones that eventually extend into mature branches.

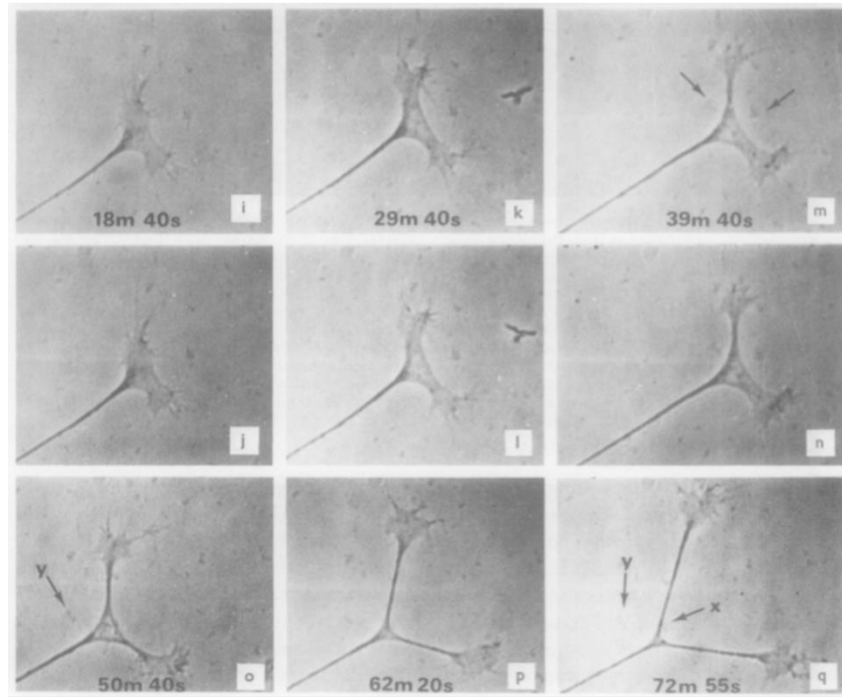


Figure I-21 : Branching of cultured parasympathetic neurons: Pairs of frames are adjacent movie frames or frames separated by only one other frame; thus, they are either 4 or 8 secondset apart. From [75]

In vitro, growth cone splitting has often been observed in presence of a repulsive cue. For example, sensory axons bifurcate after contact with inhibitory sclerotome cells [76]. When faced with a repulsive environment, branching through growth cone bifurcation enables the growth cone to explore two additional routes. Therefore, this mode of branching could underlie the axon ability to reach its target despite various physical and chemical constraints *in vivo*. A very limited number of studies have investigated this mode of branching. Branching through growth cone bifurcation has been frequently linked to guidance. Indeed, the cytoskeleton rearrangements involved are similar to those happening during growth cone reorientation [72], [77]. For this reason, in the next section we will investigate growth cone turning.

I.C. Axon turning through growth cone steering

During the development of the nervous system, each neuron extends an axon that must navigate a complex environment to reach its target. The growth cone, which can be found at the tip of axons and dendrites, plays a crucial role in axon guidance. This highly dynamic structure can integrate multiple extracellular cues and respond to them in a way that allows the axon to find its target with accuracy. In particular, according to the environmental directions it receives, the growth cone will continue its progress forward or decide to initiate turning in another direction, for example towards an attractive cue.

The path of the growth cone *in vivo* is composed of adhesive molecules such as molecules from the extracellular matrix (for example fibronectin or laminin) or molecules presented on a neighboring cell (for example transmembrane cell adhesion molecules CAMs). On the other hand, anti-adhesive molecules surface-bound molecules (such as ephrins) can act as barriers to axon outgrowth by inhibiting growth cone advance. Finally, diffusible chemical cues (such as netrins) act as “roadsigns”, attractive or repulsive cues that guide the growth cone advance [20]. In the following section, we will examine the different biological features that allow the growth cone to translate environmental guidance cues into steering. We will present the different steps of localized cytoskeletal remodeling that characterize growth cone turning.

I.C.1. The cytoskeletal dynamics of turning

I.C.1.a) Exploration of the environment by the growth cone

As seen in I.A.3.c), the shape and movement of the growth cone shape and motility are largely driven by the activity of lamellipodia and filopodia at the leading edge.

The dynamic properties of filopodia and lamellipodia are generally thought to be controlled by the balance between three processes: the polymerization of F-actin at the periphery, the transport of actin from the leading edge of the cell towards the center in a process called F-actin retrograde flow, and depolymerization of actin in the growth cone center (at the T zone), as can be seen in **Figure I-22**. The balance between the rate of polymerization and retrograde flow determines if the growth cone extends or withdraws protrusions [78].

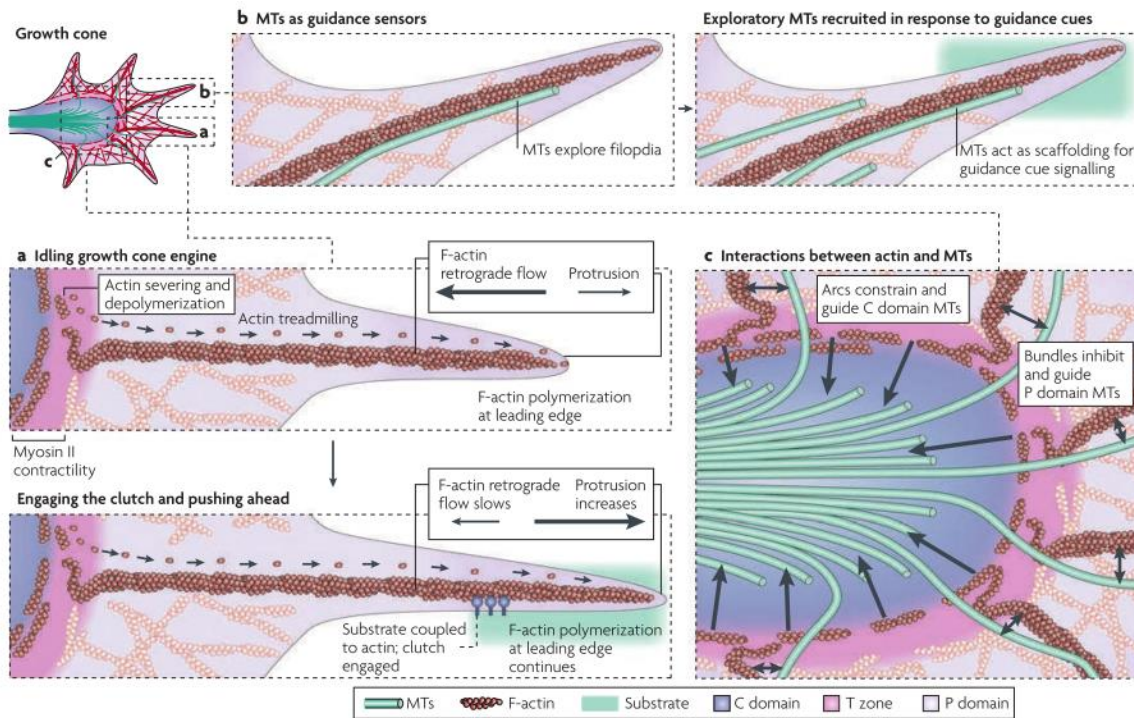


Figure I-22 : The growth cone ‘vehicle’. Boxed regions of the growth cone are shown in subsequent panels. a) Together, (F)-actin treadmilling (in which F-actin is polymerized at the leading edge and severed at the transition (T) zone, with the subunits recycled back to the leading edge) and F-actin retrograde flow (the continuous movement of F-actin from the leading edge towards the center of the growth cone) keep the growth cone engine idling. When retrograde flow and polymerization forces are balanced, no protrusion occurs. When filopodia encounters an adhesive substrate, growth cone receptors bind to the substrate and are coupled to F-actin through ‘clutch’ proteins. This engages the clutch, anchoring F-actin with respect to the substrate and attenuating F-actin retrograde flow. Further F-actin polymerization pushes the membrane forward, which results in growth cone protrusion. b) Peripheral (P) domain microtubules (MTs) explore filopodia along F-actin bundles and might act as guidance sensors. As a filopodium encounters a guidance cue, exploratory MTs might act as scaffolding for further signalling, and additional MTs are recruited to the region. c) Actin has a role in determining MT localization in the growth cone. Actin arcs constrain and guide central (C) domain MTs (single arrows), and F-actin bundles inhibit and guide P domain MTs (double arrows). From [20].

During environmental exploration, filopodia act as guidance sensors at the leading edge of the growth cone [79]. When filopodia encounter an adhesive substrate, growth cone receptors bind to the substrate and are coupled to F-actin through the formation of a complex that acts as a molecular clutch [80], [81]. This anchors the growth cone actin cytoskeleton with respect to the substrate and attenuates F-actin retrograde flow. Further F-actin polymerization pushes the membrane forward which results in growth cone protrusion.

Microtubules also play a crucial role in growth cone exploration. Through dynamic instability, individual peripheral (P) domain microtubules can explore filopodia along F-actin bundles [82]. The introduction of a localized adhesive cue leads to a recruitment of exploratory microtubules that interact with the adhesion site. That is why they have been suggested to act as guidance sensors. These dynamic MTs could either carry signals involved in turning to and from the

membrane or act as a scaffold for the recruitment of signaling molecules such as RhoGTPases [83]. For example, dynamic microtubules are involved in the localized accumulation of active Src family kinase at sites of adhesion, a protein which is required for growth cone turning [84]. It has been shown that dynamic microtubules exploration is regulated by actin. Indeed, while actin retrograde flow normally pushes back most microtubules to the C domain, locally reduced microtubules-actin coupling allows an increased number of dynamic microtubules to explore the growth cone periphery [83]. Of note, the microtubule motor protein dynein allows the uncoupling of dynamic MTs from actin retrograde flow. Interestingly, a recent study demonstrated that the motor proteins kinesin 5 and 12, working antagonistically with dynein, have a key role in controlling MT extension into the P domain during growth cone turning and are specifically phosphorylated on the side opposite the invasion of MTs before turning [77].

I.C.1.b) Protrusion towards the selected site

As we saw before, dynamic remodeling of the actin cytoskeleton underlies growth cone motility. When a guidance cue is detected by the growth cone sensors, the actin cytoskeleton is asymmetrically reorganized to allow turning in the appropriate direction. In the case of an attractive cue, it is widely assumed that the response involves first increased protrusion on the side of the growth cone closest to the chemoattractant [78], as can be seen in Figure I-23. This could be due to a local attenuation of the actin retrograde flow resulting in an accumulation of actin on the attractive cue side. Marsick et al. have reported that application of chemoattractive guidance cues NGF or netrin 1 to dorsal root ganglion neurons induced increased protrusion, F-actin accumulation and increased barbed end density on the side closed to the gradient [85]. On the opposite, in the case of a repulsive growth cone signal, turning results from retraction caused by local disruption of F-actin structures and actomyosin contraction on the side of the repulsive cue. These dynamic regulations of actin are mediated by multiple regulators, such as the actin nucleators, actin-related protein (Arp)2/3 complex and the formins, the F-actin polymerization factors (ENA/VASP), ADF/cofilin which can promote actin depolymerization and motors such as myosin II which has been shown to drive actin retrograde flow along with actin treadmilling [86].

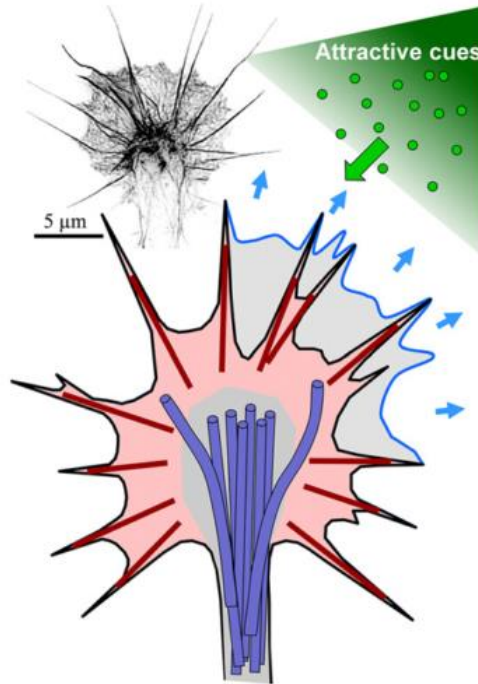


Figure I-23 : Actin cytoskeleton of a growth cone undergoing an attractive guidance response. The growth cone's periphery contains actin-rich lamellipodia (light red shaded) and filopodia (dark red lines). The lamellipodia consists of a network of short, branched actin filaments that serves as the protrusion machinery of the growth cone. Newly formed lamellipodia on the side undergoing a positive turning response is shown in blue. Filopodia are composed of long bundles of actin filaments. They participate in environment sensing and guidance. Microtubules in the growth cone (shown in purple) are largely restricted to the central region gray shaded by the actin cytoskeleton. The inset on the top left shows a fluorescent image of the actual F-actin architecture within the growth cone. This image was obtained using the Nikon N-SIM Super Resolution microscope and inverted in grayscale for display. Scale bar: 5 μ m. [87]

In parallel to the accumulation of actin at the selected site, there is evidence pointing to accumulation of surface receptors at the membrane through asymmetric endocytosis. During myelin-associated glycoprotein (MAG) induced repulsion, there is a rapid spatial remodeling of cell adhesion components, including the surface receptor β 1-integrin, with their distribution shifting toward the side that is opposite to the one stimulated by MAG[88] .

I.C.1.c) Site stabilization: engorgement and consolidation

After the protrusion step, microtubules proceed to invade the selected side in a process called engorgement. This polarized invasion of microtubules into the peripheral domain on one side of the growth cone is essential for it to turn towards the selected direction. This step requires bending and cutting of microtubules which is accomplished by several MAPs such as spastin and katanin [77].

The engorgement step begins after actin finishes clearing from the corridor between the selected site and the central (C) domain, perhaps as F-actin behind the clutch is severed and

removed (see **Figure I-24**). This is followed by the invasion of stable bundled C domain microtubules into the area of new growth, as a new region of the axon shaft is consolidated behind them, thereby fixing axon direction. This site-directed microtubule invasion might be regulated by the actin arcs situated in the T-domain [89].

Finally, during the last stage of turning, microtubules are compacted by myosin II-containing actin arcs into the newly localized C domain. F-actin protrusive activity is suppressed in the new axon shaft region, which further promotes axon shaft consolidation [70].

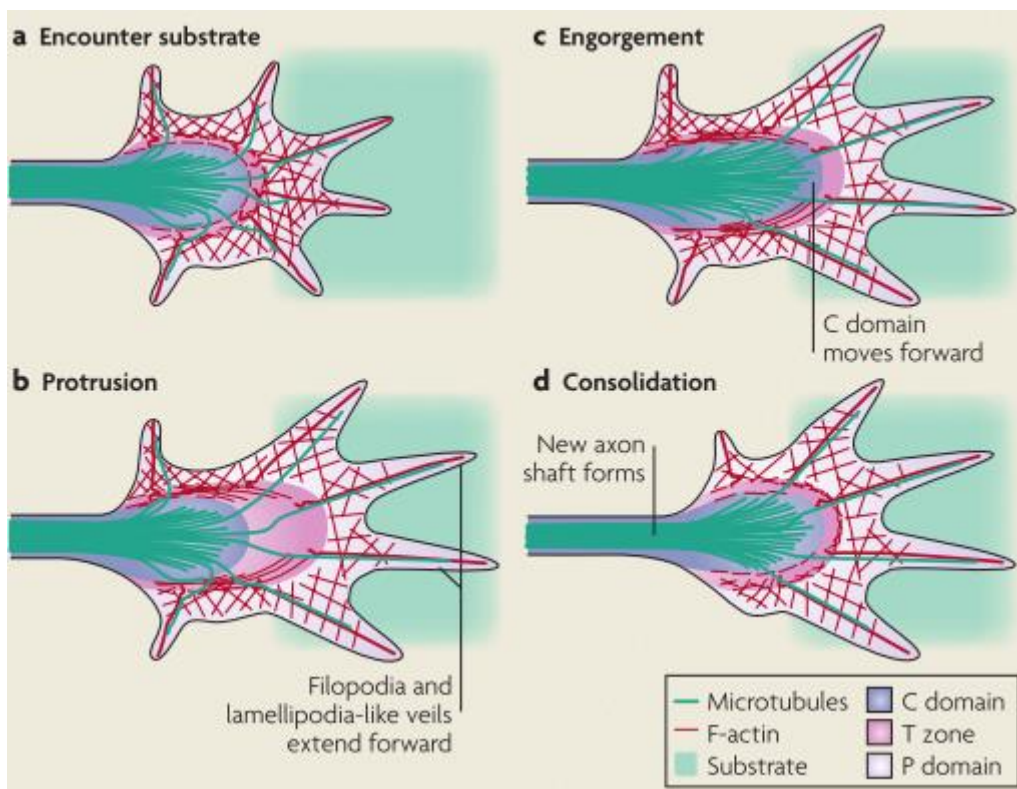


Figure I-24 : Stages of axon outgrowth towards a selected direction. a). The binding of growth cone receptors activates intracellular signalling cascades and begins the formation of a molecular ‘clutch’ that links the substrate to the actin cytoskeleton. During protrusion, this clutch strengthens, resulting in regional attenuation of filamentous (F)-actin retrograde flow. b) This anchors the actin with respect to the substrate so that, as F-actin polymerization continues in front of the clutch site, the lamellipodia-like veils and filopodia of the peripheral (P) domain move forward to extend the leading edge. c) Engorgement occurs after actin clears from the corridor between the adhesion and the central (C) domain, perhaps as F-actin behind the clutch is severed and removed F-actin arcs turn from the C domain towards the site of new growth, followed by the invasion of C domain microtubules (MTs) into this region, which are guided by transition (T) zone actin arcs and C domain actin bundles. Finally, consolidation of the recently advanced C domain occurs as the proximal part of the growth cone compacts at the growth cone neck to form a new segment of axon shaft (see the figure, part d). The myosin II-containing actin arcs compress the MTs into the newly localized C domain (followed by MT-associated protein stabilization). Retraction of the filopodia away from the area of new growth occurs as F-actin protrusive activity is suppressed in these regions, further promoting axon shaft consolidation. From [20].

I.C.2. Signaling mechanisms underlying turning

So far, we have described the elaborate cytoskeletal machinery that underlies growth cone turning. We have yet to answer the question of how the growth cone translates spatiotemporal cues into steering directions. To do that, we will present here the key molecules in the regulation of the growth cone response to environmental directions.

I.C.2.a) *RhoGTPases*

As mentioned before, RhoGTPases are a family of protein acting as signaling nodes that link upstream guidance cues to downstream cytoskeletal remodeling. RhoGTPases can either promote actin polymerization for protrusion or disassembly and recycling of actin for retraction [90]. Upstream regulators of RhoGTPases, which include GEFs and GAPs (respectively activating and inhibiting the RhoGTPases), can be activated in a spatially specific manner. While RhoGTPases have been extensively studied in non neuronal cells, our understanding of their function in the growth cone is more limited[91]. The study of RhoGTPases role in growth cone steering is complicated by the fact that multiple GTPases can be activated with the same guidance cues. A study in neuroblastoma cells proposed that spatial compartmentalization of RhoGTPases regulators allows the same GTPase to be regulated by different GAPs or GEFs in different locations inside the growth cone [92].

Interestingly, the activation of the same GTPase can generate opposite outcomes. For example, while RhoA can promote growth cone retraction (through enhanced myosinII contractility) [93], it can also lead to axon outgrowth (by suppressing the F-actin severing ADF/cofilin activity) [94]. This can be explained by the fact that RhoGTPase function is dependent on its localization inside the growth cone, and more specifically on the nature of the downstream effectors that are impacted. Finally, only of a few RhoGTPase effectors have been studied in the growth cone, among which ROCK[90]. The multiple targets of ROCK include myosin light chain kinase (MLCK) and LIM domain kinase (LIMK). MLCK enhances myosin II activity and promotes its association to F-actin, which results in increased actomyosin contraction and F-actin retrograde flow [90]. LIMK can suppress the activity of ADF/cofilin through phosphorylation [94]. After being activated, RhoGTPases effectors can act on several downstreams targets to coordinate the growth cone cytoskeleton remodeling in a spatially biased manner.

I.C.2.b) Focal adhesion Kinase

Focal adhesion Kinase is a protein that acts as a direct link between adhesions and intracellular signaling pathways [95]. It can regulate Src-family kinases as well as RhoGTPases activity, adhesion components, and actin binding proteins and microtubules associated proteins [96]. In neurons, FAK has been shown to be activated downstream of netrins and integrins, and is required to assemble, stabilize and break down adhesions [97]. In growth cones, localized activation of FAK has been reported to contribute to both attractive and repulsive signaling [98]. Like RhoGTPases, FAK activation can have different effects according to when and where it is activated, and recent studies have begun to elucidate the dynamics of FAK activation within subcellular structures [99], [100].

I.C.3. Conclusion

Directional growth cone motility is controlled by a combination of mechanism, working in concert to enable the growth cone to respond to environmental directions. While much work has been done concerning the ways individual guidance cues are interpreted, the next objective will be to understand how the growth cone reacts to multiple overlapping gradient of cues. Recent work with microfluidic devices has enabled the production of stable, precisely controlled gradients with both diffusible and substrate-bound guidance cues [101]. These types of cues can mimic the conditions of the *in vivo* environment and hold great potential for deepening our understanding of the growth cone steering mechanism.

I.D. Studying neuronal branching *in vitro*: a review of different systems

I.D.1. Studying neuronal cell development *in vitro*

The nervous system is composed of highly complex neural networks in which neurons are connected to each other through axons and dendrites. Most approaches to study biological neuronal networks use *in vivo* or brain slices preparations. The use of dissociated neuronal cell cultures is a complementary approach which enables a higher degree of biochemical and biophysical control over the cells microenvironment, as well as easier imaging of cells. Hippocampal rodent embryos neurons have often been used as a model system in neurosciences. Indeed, the hippocampus is a structure that is relatively easy to dissect and that is composed of a rather homogenous neuronal population consisting in more than 85-90% of pyramidal cells

[102]. Hippocampal neuronal growth *in vitro* has been well characterized and is described in extensive details in [103]. As can be seen in **Figure I-25**, when seeded after dissociation of the hippocampal tissue, hippocampal neurons follow a set of specific growth and polarization steps *in vitro*. Soon after plating, lamellipodia and filopodia start appearing at the periphery of the soma (stage 1). After several hours, these structures become immature neurites (stage 2) whose navigation is guided by a growth cone. Then one neurite begins to elongate faster than others. This neurite will progressively acquire the molecular characteristics of the axon, while other neurites will fully differentiate into dendrites (stage 3). The last stages correspond to the apparition of dendritic spines after two weeks of culture, which characterize a mature network.

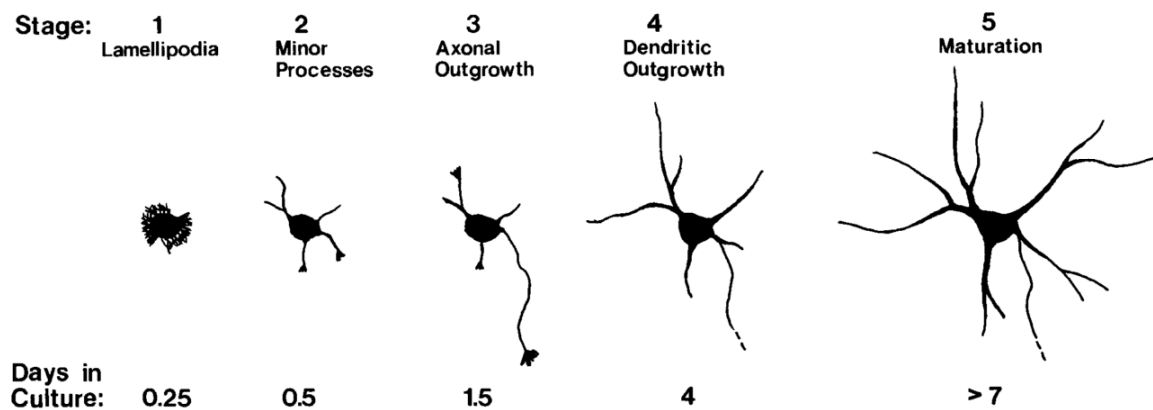


Figure I-25: Stages of development of neuronal cells in culture. The approximate timing of the stages is indicated. From [2]

The properties of neuronal cells developing *in vitro* have been shown to match corresponding neuronal cell types *in vivo* on many levels, for example their ability to form inhibitory and excitatory synapses [104], respond to different stimuli [105], as well as their activity patterns [106].

I.D.2. Microengineering tools to study neuronal growth *in vitro*

Studying neuronal cell culture *in vitro* allows for a greater degree of control of the cells microenvironment. One of the ways to achieve this control is through the use of microengineering tools originally developed for microelectronics. The technology of

micropatterning has been developed two decades ago with the aim of controlling neuronal cells shape, position and connectivity patterns at the individual cell level [107]. On the other hand, microfluidics have emerged as a powerful method to achieve cell compartmentalization through topological confinement, for example in [108].

As we will see below, the combination of these two technologies makes it possible to reconstitute the neuronal cell physiological microenvironment *in vitro* in a highly controllable way. It has therefore been successfully used to further our understanding of the complex biological mechanisms underlying neuronal growth such as polarization, axon guidance and branching.

1.D.2.a) Shaping single cells with micropatterning

Chemical micropatterning is a technology that enables the drawing of microstructures of chosen geometries on a substrate with cell-adhesive molecules on a repellent background. The most commonly used adhesive molecules are molecules from the extracellular matrix such as laminin or fibronectin, and polyamines such as poly-lysine (PLL, PDL) which enable non-specific cell adhesion through electrostatic interactions. Repellent backgrounds can be created through the use of anti-fouling polymers such as hydrophilic polymer polyethylene glycol (PEG) whose brush-like structure prevents cell adhesion [109]. A wide range of geometries can be adopted by cells with micrometric precision. It is also possible to print micropatterns of biomimetic gradients of proteins. Through the use of various types of patterning, a great variety of biological phenomena have been studied such as cellular polarization [110], differentiation [111] or migration [112].

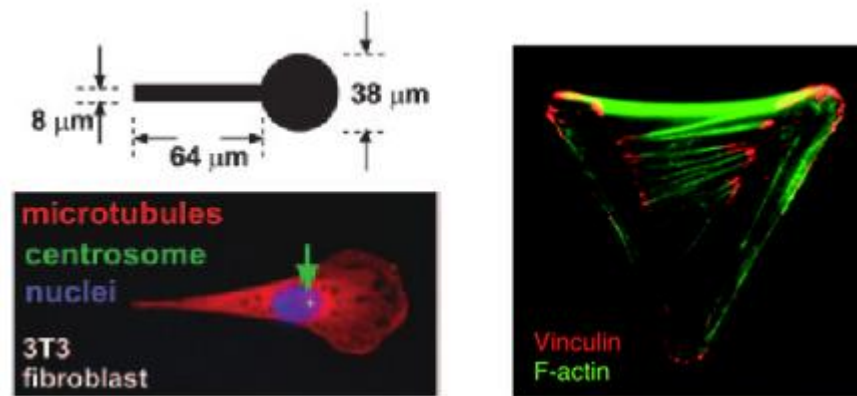


Figure I-26 : Examples of micropatterned cells. Left: Asymmetric patterns polarized immobilized cells. From [112]. **Right:** A “V” shape micropattern promote the assembly of stress fibers. From [113].

In the case of neurons, the micropatterning technology was adapted more than a decade ago to constrain neuronal shape and create organized in vitro neuronal networks. One of the first extensive study of in vitro organized neuronal networks was performed by Wyart et al. [114]. Big square areas were implemented for soma adhesion and 2-4 μm stripes to guide neurite growth. However this pattern design did not allow for the control of axon localization. Further works demonstrated high control of axo-dendritic polarity by using different curvatures and cell body constraints [115], [116], and more recently in changes of stripe width [117]. Guidance of axons can also be achieved through the use of printed gradients as seen in [118]. The most commonly used geometry is the square grid but a wide range of geometries, from triangular grids [119], to two-cells networks have been produced with the methods mentioned above [120].

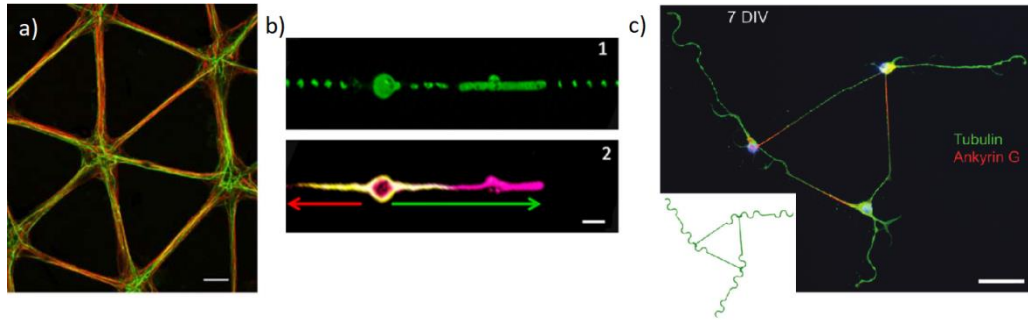


Figure I-27 : Micropatterning neurons. a) Fluorescence image of triangular patterned neuronal networks at DIV 14. MAP-2 immunolabeling of soma and dendrites in red, Neurofilament 160kD immunolabeling of axons in green. Scale bar 20 μ m. From [119] b) Immunolabeling of neurons at DIV3 growing on a PLL-FITC/laminin gradient pattern. The neurons grew along the pattern to become bipolar neurons, and polarized in the direction of the gradient. Scale bar 10 μ m. 1. Fluorescence image of PLL-FITC/laminin pattern 2. Immunolabeling of MAP-2 (cell body) and dendrite in yellow, Tau1 (axon) in red. From [118] c) Triangular looped circuit made of three connected neurons at DIV7. Microtubules (anti-tyrosinated tubulin, green) and axon initial segment (anti-ankyrinG, red) labellings are superimposed on nuclei staining (Hoechst, blue). Inset: the pol-lysine adhesion pattern (in green). Scale bar 50 μ m. From [116].

The behavior of patterned neuronal networks was studied in details, and it has been found that activities characteristic to *in vivo* and random *in vitro* networks are also produced by patterned neuronal cultures [105], [121], [122].

The different techniques available to engineer neuronal networks have been reviewed in [123]. One of the first chemical patterning methods developed uses photolithography to print the desired geometry of adhesive molecules on the substrate [124]. Other methods rely on laser ablation of self-assembled monolayers. One such method is based on sequential UV etching through a quartz photomask to create an adhesive pattern on a repellent background. This technique requires no clean room facilities but is limited in resolution to 3 μ m by the diffraction of light [125]. Finally, microcontact printing or μ cP, is the most commonly used method and uses a micropatterned elastomer stamp fabricated with photolithography to transfer adhesive molecules to the substrate [126], [127] as can be seen in **Figure I-28**.

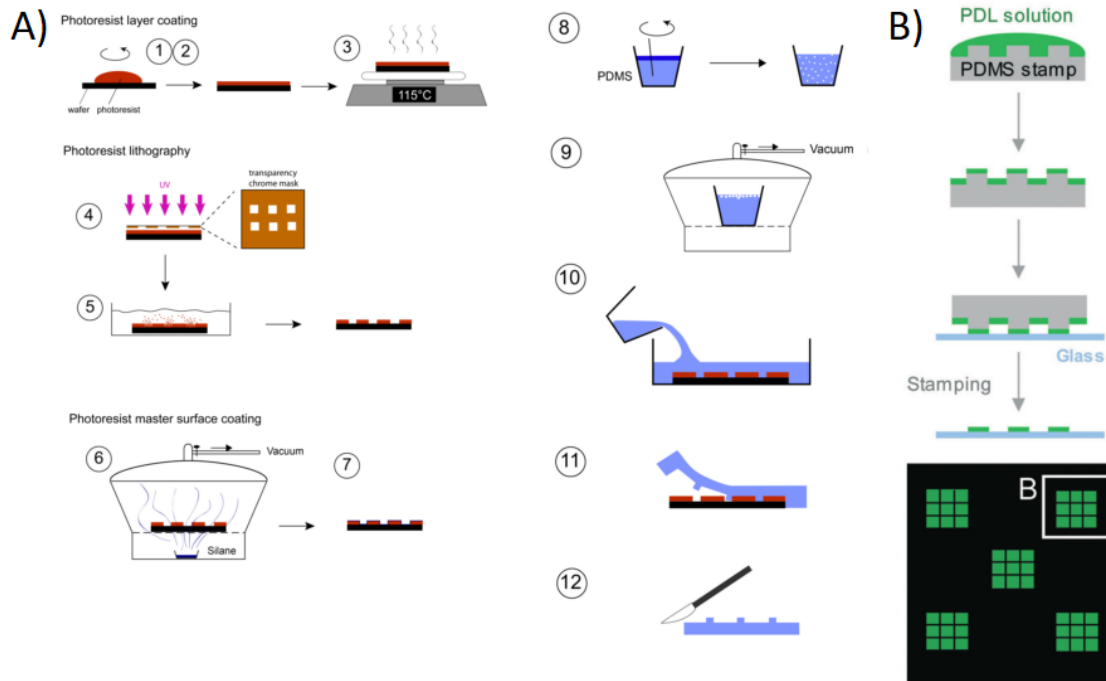


Figure I-28 : Microcontact printing (A) scheme illustrating the different steps to produce microstamps (1) to (7) using photolithography to construct the stamp mold (8) to (12) fabrication of microstamps with PDMS. From [127]. (B) A procedure for micro-contact printing. PDL solution was overlaid on a PDMS stamp and transferred onto a glass coverslip by stamping. From [108].

I.D.2.b) Guiding neurites with microfluidics

Microfluidics is the use of microfabricated devices that include microchannels and chambers to control flows at the micrometric scale. Most of these devices are made in Polydimethylsiloxane (PDMS), a biocompatible and transparent silicon-based organic polymer. Microfluidics is well known for the miniaturization of processes in the diagnostics field with lab-on chips devices, as well as organ-on-chips devices which provide a controlled microenvironment for cells.

In the case of neurons, microfluidics has been used to achieve axo-somatic compartmentalization [128] and to control the connections between neuronal populations. Neurons have been seeded in chambers and connected by microchannels that act as a guide for the growth of axons. By playing with the geometries of these microchannels, the directionality of connections can be controlled. Peyrin et al. have implemented unidirectional connectivity through the design of axon diodes, tapered microchannels that promote axonal growth in the

direction of the smaller channel opening [129]. More recently, our group has used a mesh of straight and curved microchannels “arches” to achieve the same unidirectional connectivity [130].

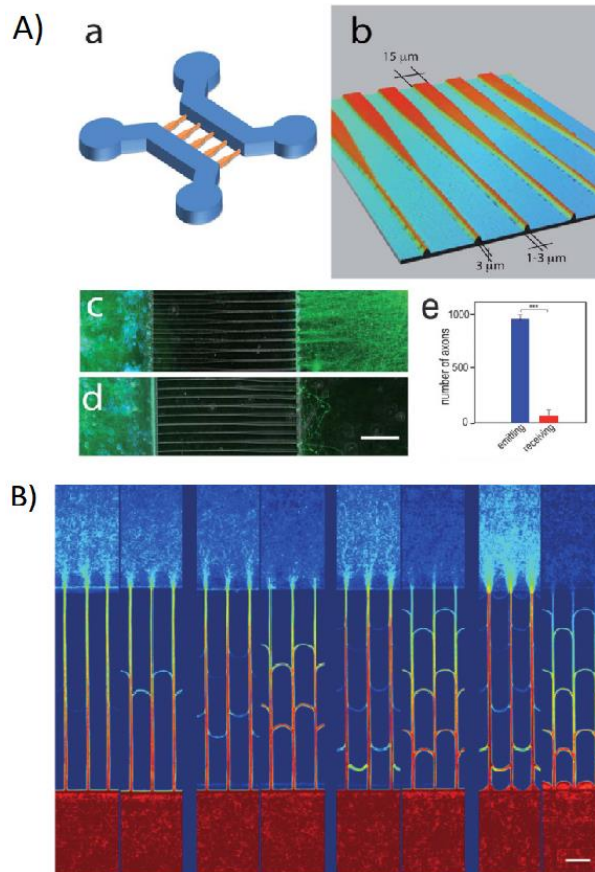


Figure I-29 : (A) In vitro reconstruction of a neuronal network using “axonal diodes” in microfluidic culture devices. (a) Global 3D view of the microfluidic device comprising asymmetrical microchannels (b) 3D view of the funnel-shaped micro-channels as observed by white-light optical profiling (WLOP) with an interference microscope. Immunofluorescent images of microfluidic cultures (green: a-tubulin, blue: Hoechst) in which cortical neurons were seeded either on the wide (c, 15 mm) or the narrow (d, 3 mm) side, Note the lack of labeling in the wide chamber when cortical neurons are seeded in the narrow side (d). (e) Quantification showing that the axonal diodes efficiently polarize axonal growth (***) p-value < 0.001). Scale bar 50 μm. From [129]. (B) Direction selectivity of arches, both sides seeded. This image shows the average intensity maps of axons in the different designs (log scale). This design with arches promotes unidirectional connectivity by specifically making the axons growing in the undesired direction turn away. The top chambers are seeded with non-fluorescent neurons. Experiment realized after 8 DIV. Scale bar: 100 μm. From [130]

Microfluidics can also be used for chemical micropatterning on substrates, for example through the creation of gradients of laminin [131]. Furthermore, a new microfluidic device developed by Dermutz et al. has now made possible the patterning of neurons *in situ* ie. after their seeding. These authors have built a device based on AFM cantilevers integrated in a

microfluidics set up that enables the user to write PLL lines onto a PLL-g-PEG background, thus enabling the connection of two clusters of neurons [132]. This study paves the way for the spatiotemporal control of neurite outgrowth.

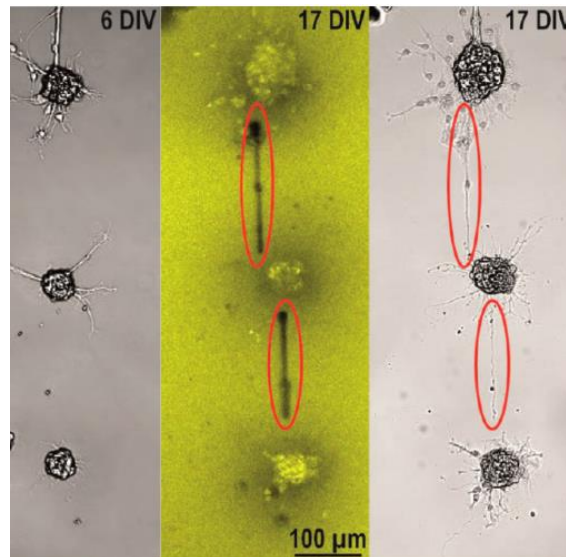


Figure I-30 : Bright field image of neuron clusters before (left) and 11 days after the PLL line writing (right). The *in situ* deposited PLL lines are highlighted in the confocal image using Atto settings (middle). It can be clearly seen that the neurites reacted to the deposited PLL lines. From [132]

I.D.3. Application of microengineering tools to the study of neuronal branching *in vitro*

As we saw above, microtechnology has facilitated the development of *in vitro* assays for investigating axons under various extracellular signals that are crucial to axonal growth. Some examples of systems that have been specifically designed to study axon branching will be presented below.

I.D.3.a) *Effects of substrate geometry on branching through the use of chemically homogeneous micropatterns*

Vogt et al. have been among the first groups to use micropatterning to study the effects of substrate geometry on neuronal connectivity, including axon branching in 2005 [133]. In their study they reported on the growth and branching behavior of E18 embryonic rat cortical cells on PLL rectangular grid patterns on polystyrene petri dishes with 4 μ m-wide lines and nodes 12- μ m in diameter at the intersections. The patterning was performed through the use of the microcontact printing method presented in **Figure I-28**. Cells were seeded on the patterned substrate then microinjected with patch solution to perform triple patch-clamp measurements to measure the connectivity of the patterned neuronal networks.

To investigate branching behavior of neurons on surface, the fluorescence image of 19 neurons were evaluated. First, neuritic behavior at node intersections was examined. All the examined cells had initially two neurites, growing along the pattern lines in both directions. At the intersection they encountered three available paths, one in the original direction, and one at 90° on each side (see **Figure I-31 A**). The results are summarized in **Figure I-31 B**). In summary, branching occurred for only half the available branching points. Among the neurites that did not branch at intersections, more than half crossed the node without taking a 90° turn, which indicates a slight preference to proceed in the initial direction. On more than half of the intersections, at least one neuritic branch crossed the node without taking a 90° turn, which indicates a slight preference to proceed in the initial direction.

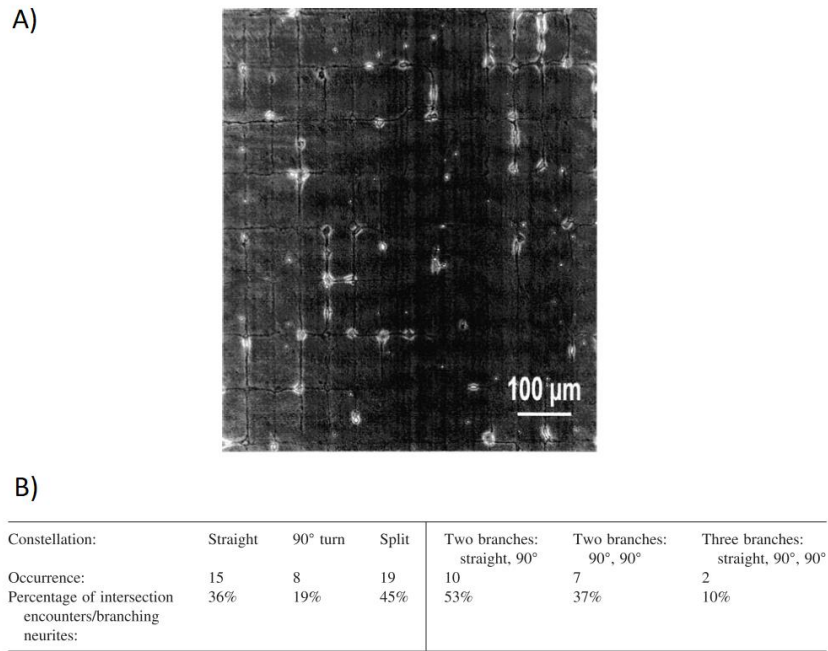


Figure I-31: Branching behavior of neurons growing on a PLL grid pattern. (A) Patterned rat cortical neuronal culture at DIV 11. (B) Table presenting neurite behavior on grid intersections. Neurites of 19 microinjected neurons were evaluated and each neurite–intersection encounter was counted as one event. Neurites were first classified as crossing the node without a change of direction, as turning at 90°, or as splitting into more than one branch. Next, splitting neurites were classified as splitting into two or three branches and the directions taken. From [133].

Withers et al. have also reported on the effects of substrate geometry on growth cone behavior and branching in more details in 2006 [124]. In their study, they cultured hippocampal neurons cells at a low density (1000 cells/cm²) on a polylysine grid of narrow (2 or 5 μm wide) intersecting lines on glass coverslips. The shapes of the intersections varied from circular nodes 15 μm in diameter PLL lines patterns to simple crossed lines (nodeless intersections). Patterns were fabricated with photolithography. The group studied the neuronal behavior through timelapse recording of a duration of 16-40 hours.

First, the behavior of the neurites at the intersection was evaluated. More specifically, node and nodeless intersections were compared. At node intersections, growth cones split as they migrated along the edge of the node, leaving behind separate fragments or buds. When crossing a node intersection, the growth cone paused for hours, and microtubules appeared to defasciculate. After the crossing of the node, filopodial and lamellipodial protrusions persisted

at that site, sometimes eventually forming a branch. On average, growth cones required 7.07 ± 4.6 (mean \pm SD) h to extend past a node, and only 0.97 ± 1.2 h to extend past a nodeless intersection. When the growth cone encountered a nodeless intersection, it split into several regions, some of which later extended into branches. Moreover, as summarized in **Figure I-32 A**), on nodeless intersections, branching occurred more often and with minimal pausing. Neurites that encountered nodeless intersections branched at the intersection more than 75% of the time, more than twice as often as at node intersections. Overall these results suggest that changes in substrate geometry can induce branch formation by increasing the probability of growth cone splitting.

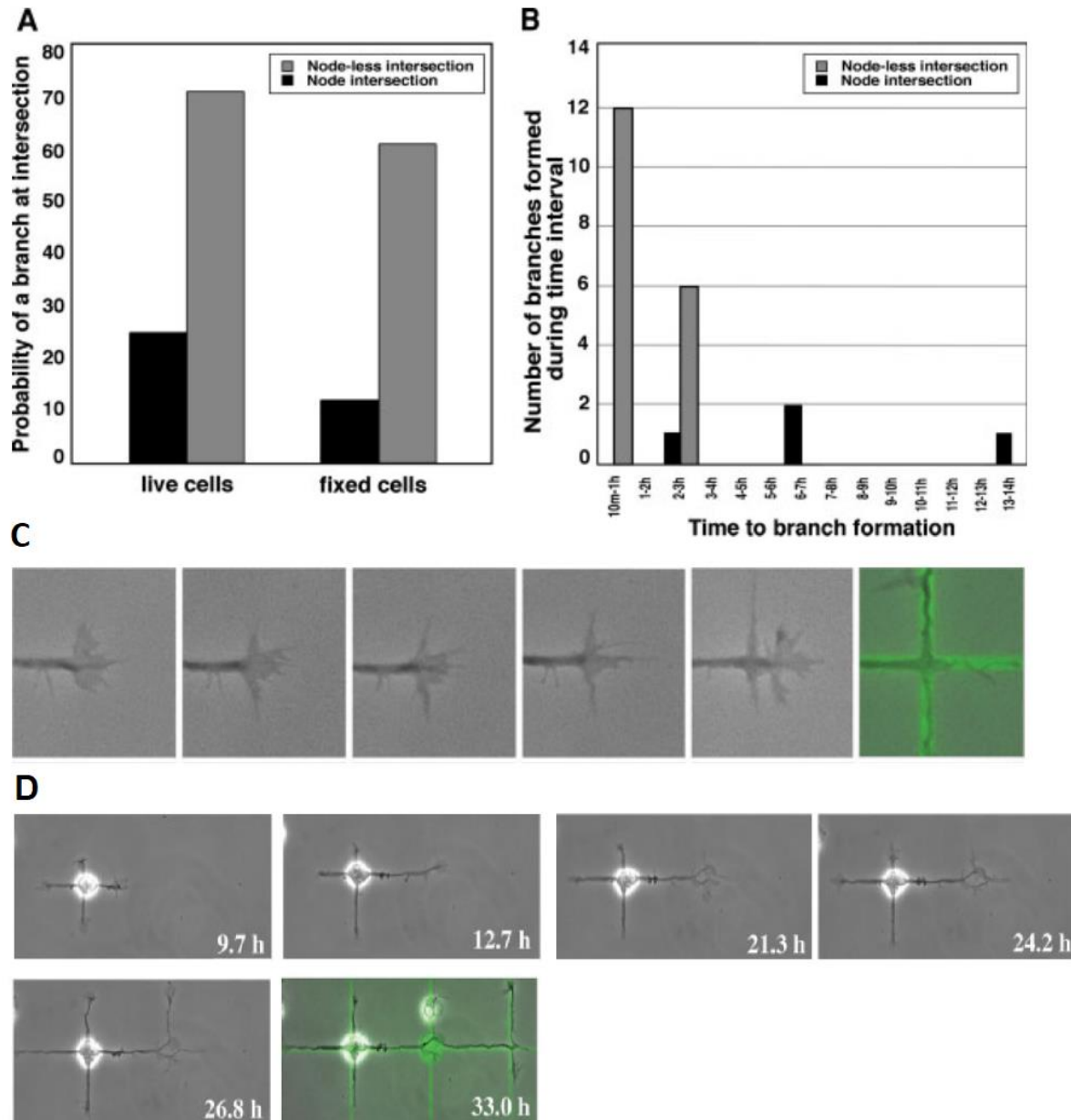


Figure I-32 : Analysis of axonal branching at node and nodeless intersections. (A) Within the first 24 h in culture, the probability of a branch occurring is much greater at nodeless intersections than at nodes. For data gathered during time-lapse recordings (live cells), a branch could arise at any point during the recording to be included in the data set. For fixed cells, any growth cone positioned on an intersection was scored as unbranched. (B) Length of time to branch formation after encountering nodeless or node intersections during time-lapse recording. Not only did fewer branches form at the node intersections, but they took markedly longer to emerge. (C) Changes in growth cone shape at a nodeless intersection. As a growth cone progresses past a nodeless four-way intersection it divides into three regions, each of which extends to form a branch. (D) Changes in growth cone shape at a node intersection: At a node intersection, a growth cones also splits as it migrates along the edge of the node, leaving behind separate fragments or buds. Adapted from [124].

Withers et al. also examined the preferred angled for branching. On unpatterned PLL substrate they observed that most neurons branch at angles between 40 and 90°, with an average of 71 ± 21

(mean \pm SD, measured as the angle between the two branches). They observed the behavior of neurites at intersections where the growth cone has 8 available paths at 0°, 45° 90° and 135° from the initial neurite direction (see **Figure I-33**).

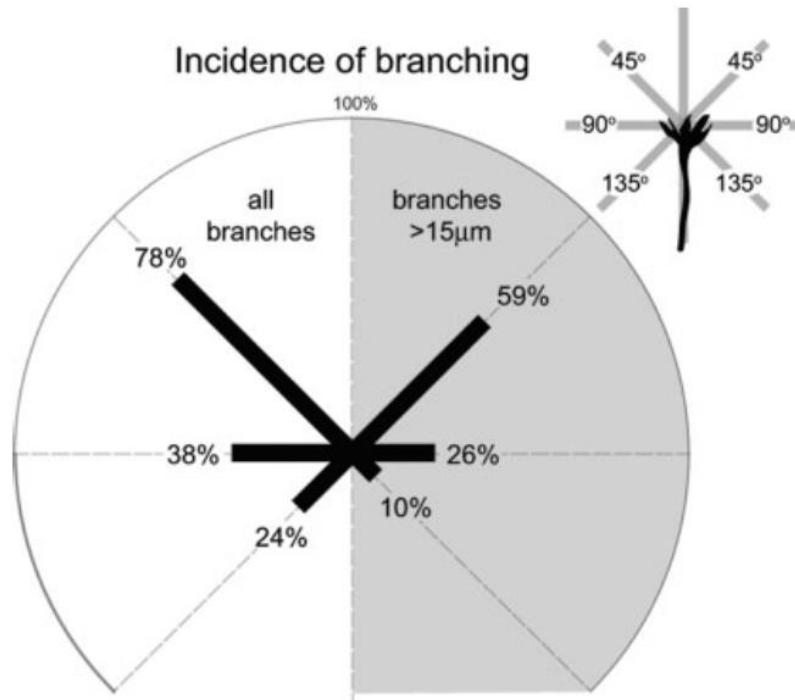


Figure I-33 : Analysis of branches arising at six- and eight-way intersections shows that there is a strong preference for branches to form at angles less than 90°. While branches can appear at angles of 135°, the likelihood that they will occur is low. For these data, cells were fixed and the incidence of branching at each angle was recorded to determine the probability of a branch forming at 45, 90, and 135° angles. The maximum possible incidence at each angle is 100%. From [124].

The results showed an intrinsic preference for branching angles inferior to 90°. The group attributed these results to the endogenous stiffness of microtubules, which might reduce the probability of microtubules growth at angles greater than 90°.

Kim et al. have reported on the behavior of cultured embryonic E18.5 mice hippocampal neurons on a PLL microdots array pattern [108]. Arrays of 3, 5 and 10µm spaced PLL spots of 5µm diameter were printed with microcontact printing on glass coverslips. The group observed that neuronal branches number and neuritic length were globally unaffected by the patterns. 10µm spaced patterns had no quantifiable effects on the neurons. Nevertheless, for the 3 and 5µm pattern, most axonal branches initiated from a dot and terminated at the closest

dot, resulting in a rectangular branch formation (see **Figure I-34** A) and B)). The authors suggest that stronger adhesion of cellular membrane on the dots might stabilize the intracellular actin network and therefore trigger the formation of branch. Timelapse imaging and immunostaining of fixed cells showed the pausing of axons when encountering microdots as well as the disorganization of actin and tubulin which might allow the association of proteins required for branch formation such as the actin nucleation factor Arp 2-3.

Consequently, while on unpatterned substrates the average branching angle measured was about 60-70°, on the dot array, a large number of branches grew with an angle of approximately 90° at DIV3 (**Figure I-34** C))

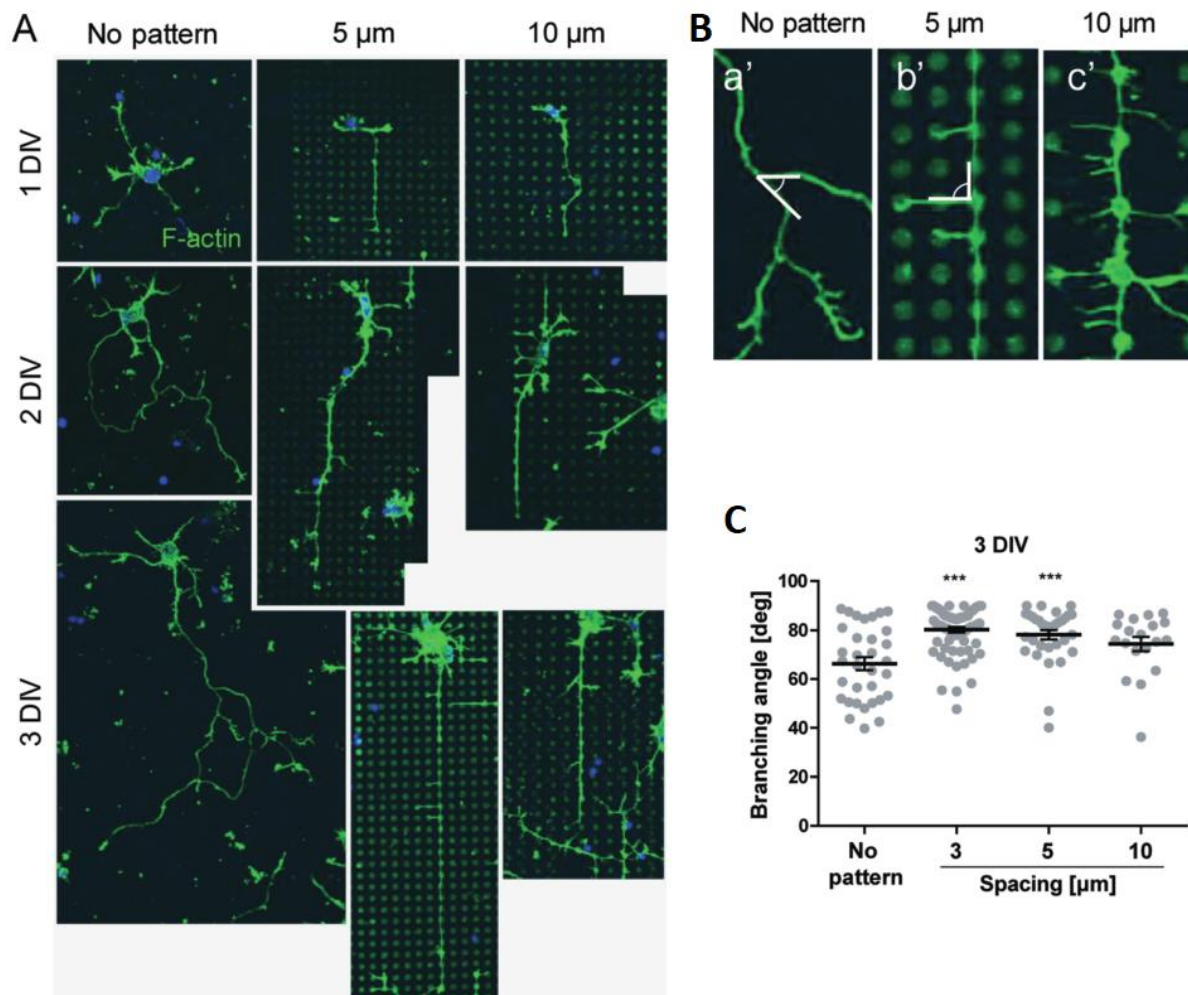


Figure I-34 : (A) Representative images of cultured hippocampal neurons on dot arrays. (B) Representative image of axonal branches from hippocampal neurons without pattern (a'), or with 5 μm (b') and 10 μm (c') spacing. (C) Angle of primary branches from an axon 3 DIV, mean ± SEM, *p < 0.05, ***p < 0.001, one-way ANOVA. From [108].

In summary, these results suggest that microdots arrays pattern can simplify the shape of the axonal branching tree, which could enable digital quantification of the branch growth property.

Overall, these studies show that changes in the geometry of a chemically homogeneous substrate can influence growth cone behavior and in turn regulate axonal branching.

I.D.3.b) Effects of gradients of extracellular molecules on branching

Liu et al. reported in 2013 on the behavior of E18 mice hippocampal neuronal cells on micropatterns of varying laminin density [131]. The group used two types of patterns for their study; first a chemically homogenous pattern with the technology of microcontact printing, then a chemically inhomogenous pattern with the combination of microcontact printing (μCP) and microfluidics printing (μFP). Both patterns had strictly the same geometry in order to study specifically the effects of the change of laminin density. The patterns fabrication and design is described in details in **Figure I-35**. It is composed of a series of $5\mu\text{m}$ wide stripes on which the neurons are seeded, encountering on both side a wider rectangular region called “branch region”. Due to different fabrication methods, in the first case the stripes and the branch have the same laminin density while in the second case the “branch region” displays a lower laminin density.

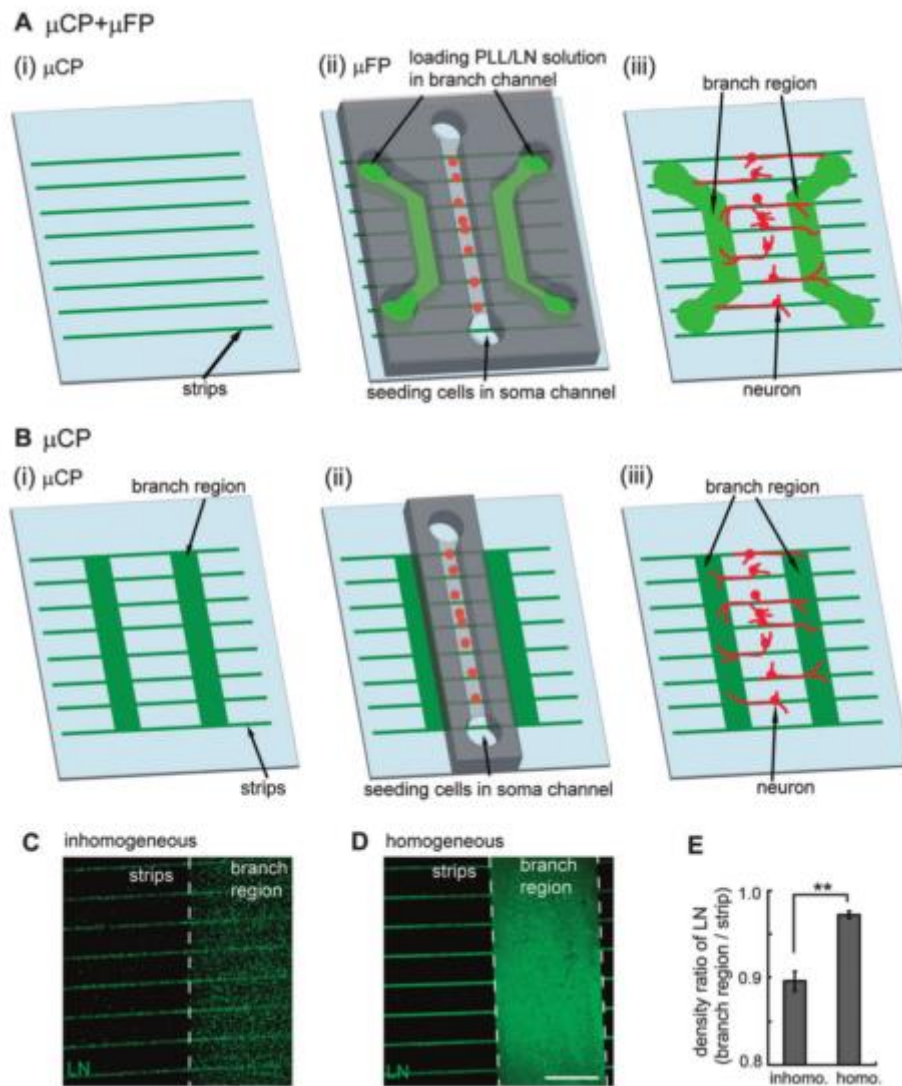


Figure I-35 : Fabrication of inhomogeneous and homogeneous substrate. (A) Schematic diagram of the micropattern system for generating inhomogeneous substrate. (i) The strips are printed by mCP and the branch regions are patterned by mFP (ii). FITC-BSA was added to the mixed solution of PLL and LN, so the micropattern shows green fluorescence. The red spots represent neurons. (iii) Neurons develop processes on the inhomogeneous substrate after peeling off the PDMS channel. (B) Scheme of the micropattern system for generating homogeneous substrate. (i) Both the strips and branch region are printed by mCP. (ii) Soma channel is between the two printed branch regions. (iii) Neurons develop processes on the homogeneous substrate after peeling off the PDMS channel. By immunostaining laminin, inhomogeneous substrate (C) and homogeneous substrate (D) show significant differences of change of laminin density on the intersection (E). The dotted white lines are the boundaries of the strips and branch region. “inhomo.” and “homo.” represent inhomogeneous substrate and homogeneous substrate respectively. Scale bar is 100 μm . $n = 6$ for each group in (E). Data are mean \pm s.e.m. t-test, ** $P < 0.01$. From [131].

First, Liu et al. classify the axons contacting the branch region in different types: type I axons, which branched at the beginning of the strip-branch channel intersection region ($<10 \mu\text{m}$ from the beginning of the branch region). Type II axons branched at a distance superior to $10 \mu\text{m}$ to the intersection and Type III axons did not branch at all. Using timelapse, they studied

the behavior of type I axons, ie axons who branched at the intersection. When the growth cone of type I axons contacts the strip–branch channel intersection, they paused and remained motile without forward advancement for 9.9 hours on average. When the growth cone advanced again, an axonal filopodia protrusion initiated in the intersection region. On the other hand type II axons which did not branch at the intersection grow across the beginning of the branch region within only 0.4 hours on average. These results suggest that the intersection of the strips and branch channel can stimulate axon branching through the growth cone pausing mode.

The group then investigated the influence of sharp changes of geometry on axon branching. The pattern geometry is modified so that the stripes take varying width, while keeping the density of laminin equal in all the adhesive zones. As the width of strips increased from 5 μm to 50 μm , the proportion of type I axon branching decreased from 30% to 13%, type II axon branching remains at 25%. These data suggests that when an axon grows through a geometrically restricted region with homogeneous substrate molecules the sharp broadening of the substrate significantly contributes to axon branching.

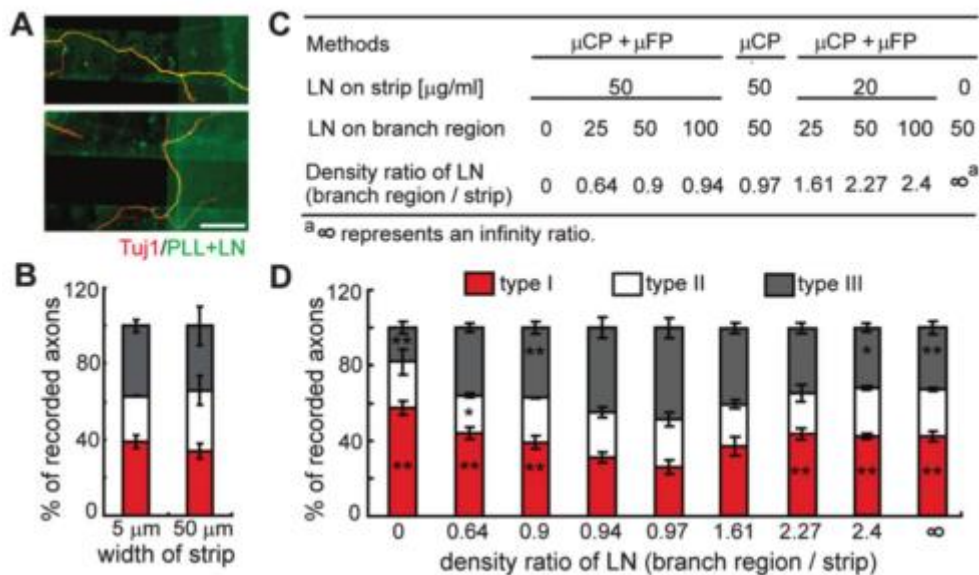


Figure I-36 : Sharp change of laminin density stimulates axon branching. (A and B) Strip width has no effect on axon branching on the inhomogeneous substrate (density ratio of laminin is 0.9). Scale bar is 50 μm . n = 617. (C) The different density ratio of laminin (branch region/strip) obtained by changing the printing methods and laminin concentration on strip and branch region. (D) When the ratio is lower than 1.0, type I axon branching decreases with the increase of the ratio. When the ratio is larger than 1.0, type I axon branching increases with the increase of ratio. n = 2848. Data are mean \pm s.e.m. w2 test, * P<0.05, ** P<0.01. Data of ratio = 0.97 were used for comparison in the t-test. From [131].

Following this study of the geometrical influence of substrate geometry on axon branching, the

group examined the influence of laminin density. While keeping the laminin density on the strip regions fixed the laminin density in the branch region was changed to a wide range of values. The results are summarized in **Figure I-36**, and indicate that a greater change of laminin density, no matter whether an increase or a decrease promote more axon branching.

Finally, the group examined the behavior of the growth cone at the stripe–branch region intersection to understand the origin of this increased branching. Immunostaining of growth cones for integrin $\beta 1$ showed that laminin stimulates the focal adhesion formation on the growth cone locally and tends to promote the extension of filopodia in the direction of the laminin density gradient. This results in a change in the growth cone morphology that could be a precursor to axon branching. (see **Figure I-37**).

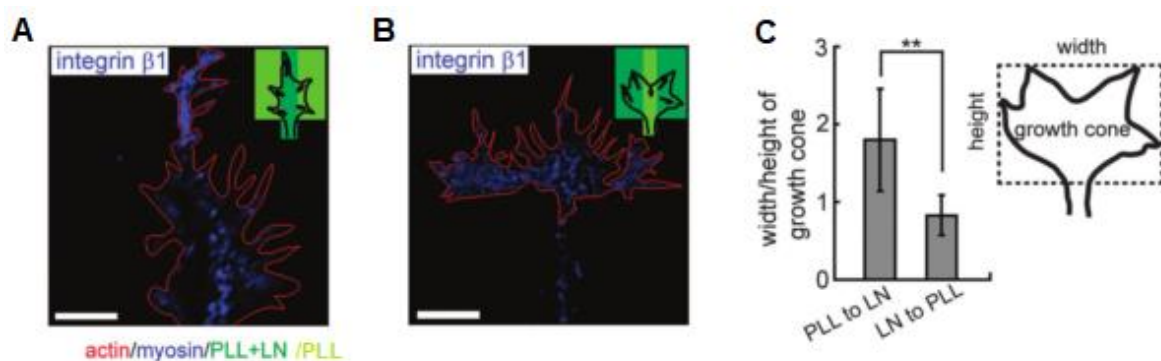


Figure I-37 : Changes in laminin density impacts growth cone morphology and results in asymmetric filopodia extension (A) Immunostaining of integrin $\beta 1$ in growth cones grown from laminin strip to PLL modified branching region. The figure in the top right corner illustrates the intersection, dark green represents PLL+laminin, light green PLL. Scale bar is 10 μm (B) Immunostaining of integrin $\beta 1$ in growth cones grown from the PLL strip to the laminin-modified branching region. The figure in the top right corner illustrates the intersection, dark green represents PLL+laminin, light green PLL. Scale bar is 10 μm (C) Ratio between width and height of growth cone's bounding box in these two conditions. t-test, ** $P < 0.01$. Adapted from [131].

Overall, this study partially explains the mechanism of laminin-regulated axon branching and also provides a method to control axon branching *in vitro*

I.D.3.c) Conclusion

In summary, these studies show that a sharp change in the axon microenvironment, whether in terms of substrate geometry or chemical composition, can locally induce branching. Each of the groups investigated the growth cone behavior to explain this phenomenon. Both Withers et al. and Liu et al. have reported extended growth cone pausing when encountering a

sharp change in geometry, such as for example the transition from a restrictive line to a more spacious area. This pausing is accompanied by a disruption of the cytoskeleton organization: bundles of actin and microtubules are disorganized while the axon stretches and flattens over the larger adhesive area. Several studies have shown that an extended pause in growth is a hallmark of later collateral branch emergence [134], [38], [135]. The observation in these studies are consistent with the idea that a pause in outgrowth can lead to increased protrusion activity later resulting in the emergence of a collateral branch.

Finally, both Withers et al. and Kim et al. have evaluated the average branching angle on fully adhesive substrates for hippocampal rodent neurons at a value of around 70° .

Chapter II. Materials and Methods

Contents

Chapter II. Materials and Methods	58
II.A. Introduction	60
II.B. Primary cell cultures.....	60
II.B.1. Neuronal cell cultures	60
II.B.2. Fixation.....	62
II.B.3. Immunofluorescence	63
II.C. Patterned substrates	66
II.C.1. Static patterns	66
II.C.2. Dynamic patterns.....	71
II.D. Microscopy observations.....	81
II.D.1. Time-lapse experiments	81
II.D.2. Fixed cells	81
II.E. Analysis methods	81
II.E.1. Growth cone analysis.....	81
II.E.2. Branching probability and measure of branch length.....	84
II.E.3. Time-lapse analysis	84
II.E.4. Statistical tests	87

List of abbreviations and nomenclatures:

- EDTA**..... Ethylenediaminetetraacetic acid
- PBS**..... Phosphate-buffered saline
- DIV** Days In Vitro
- HS**.....Horse Serum
- BSA**.....Bovine Serum Albumine
- PLO**PolyOrnithine
- GFP**.....Green Fluorescent Protein
- PLL**.....Poly-L-Lysine
- PEG**Poly (Ethylene Glycol)
- APP**Azido- Polylysine grafted on Poly (ethylene glycol)
- PLL-g-PEG**PolyLysine grafted on Poly (Ethylene Glycol)
- PLL-g-PMOXA** PolyLysine grafted on Poly(2-methyl-2-oxazoline)
- BCN**.Bicycle [6.1.0]nonyne
- NHS**..... N-Hydroxysuccinimide
- NMR**.....Nuclear Magnetic Resonance

II.A. Introduction

The expertise in neuronal shape control of Catherine Villard's team started in Grenoble, in Institut Néel where there is a high degree of knowledge in micro and nanotechnologies. Throughout 3 PhDs projects [136]–[138], the application of micropatterning to neurons was developed and optimized. The protocols were adapted to the environment of the Pierre Gilles de Gennes Institute during Céline Braïni's PhD [139]. In this chapter, these protocols will be presented in detail.

II.B. Primary cell cultures

The experiments reported in this manuscript have employed embryos from the C57 Black6 inbred strain of laboratory mice and, occasionally, rat embryos.

II.B.1. Neuronal cell cultures

Neuronal cell cultures have been conducted using hippocampus of mouse embryos at sixteen to eighteen days of gestation. This corresponds to the phase just before birth, since the gestation period is about 19 – 21 days. This choice was motivated by three reasons (i) hippocampus development has been well-characterized *in vitro*, (ii) young cells are more adaptable in constrained *in vitro* environments and (iii) dissociated hippocampal tissues provide a relatively homogeneous cell population, mainly composed of pyramidal neurons and a very low concentration of glial cells (less than 1% [140]). The last point is fundamental for the study of isolated neurons on micropatterns. Indeed, glial cells can secrete proteins enabling them to colonize the initially repulsive space between patterns, therefore providing a substrate for non-controlled neuronal adhesion. The culture protocol employed is based on the method developed by Banker [141], [142] and the medium compositions have been kindly provided by the group of A. Triller (IBENS, Paris, France).

II.B.1.a) *Dissection of hippocampi*

One of the essential points to guarantee the cell survival *in vivo* is the quality of the dissection of embryo. The maximum duration recommended between the animal euthanasia and the cell seeding is between 1 and 2h. Dissections were made using a stereomicroscope,

narrow pincers and scissors (Fine Science Tools). **Figure II-1** illustrates the main steps of dissection of hippocampus and cortex from mouse embryonic brains. The typical length of a mouse embryonic hippocampus (at 18 days of gestation) is about 2 mm when straightened. Tissues are extracted in the dissection medium at $\sim 4^{\circ}\text{C}$. Hippocampi are then incubated during 10 min at 37°C in 3 ml of the same medium supplemented with 10% of Trypsin without EDTA (2.5%, Life Technologies), rinsed three times with the dissection medium (see Table 1) at room temperature and dissociated with a 1 ml pipette in 1 ml (20 passages max. through the tip) in the plating medium (**Table 1**) at 37°C . A few μL of this solution is then used to calculate the cell concentration.

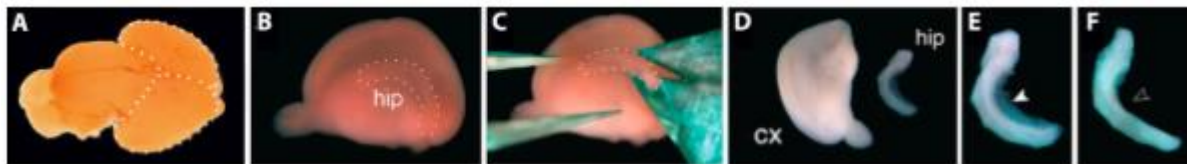


Figure II-1 : Dissection of hippocampus and cortex from mouse embryonic brains. A) Fetal mouse brain. Left and right hemispheres of the cerebral cortex are delimited by the dashed white line (external view). B) Right hemisphere (inner view) and the olfactory bulb. Hippocampus ("hip") is delimited by the dashed white line. Meninges surrounding each hemisphere are removed. C) The hippocampus is removed with a microscissor. D) Cortex("cx") and hippocampus("hip") are separated. E, F) The fimbriae (arrowhead) on the concave side of the hippocampus are removed (open arrowhead). Adapted from [143].

II.B.1.b) Cell seeding and culture conditions

One hippocampus usually provides about 0.3 – 0.7 million neurons and one cortical hemisphere about 2 – 3 millions of cells. Substrates are prepared before the dissection and kept in PBS at room temperature until the seeding step. PBS is aspirated by taking care of not drying the substrates. Cells are then plated at a given concentration in a plating medium, MEMc medium. Usually, in the case of micropatterned substrates, to obtain cells that are still isolated after 1 to 3 days in vitro (DIV), we plate 30 000 cells per 24x24mm glass coverslips. In the case of timelapse experiments, a seeding density of 40 000 cells per glass coverslips is preferred to improve neuron survival. Samples are then placed in an incubator at 37°C and controlled atmosphere of 5% of CO_2 . After 3 – 4 h, MEMc medium is quickly replaced by a maintenance medium, NBc medium, containing Neurobasal. Interestingly, NBc is characterized by a lower osmolarity than MEMc. The compositions of all media employed are detailed in **Table 1**. Of note, all the media preparation and seedings steps are done inside a sterile environment provided by a laminar flow hood.

Dissection medium: HH [50ml]	Plating Medium: MEMc [50mL]	Maintenance Medium: NBc [50mL]
Hank's Hank Balanced Salt Solution (HBSS) 10x : 10% [4mL] Hepes 1M : 2% [1mL] Deionized sterile water: [44mL]	Horse Serum (HS): 10% [5mL] Glutamax 200mM: 1% [500µL] Sodium Pyruvate 100mM: 1% [500 µL] Gentamicin 0.2% [100 µL] Minimal Essential Medium (MEM): [43,9mL]	B27 50x: 2% [1mL] Glutamax 200mM: 1% [500 µL] Gentamicin 0.2% [100 µL] Horse serum (HS): 1% [500µL] Neurobasal (NB): 47. 9mL

Table 1 : Dissection, plating and maintenance media, HH, MEMs and NBs respectively. The “c” stands for “complete”, in the sense that several elements have been added to Minimum Essential Medium (MEM) and Neurobasal medium (NB), respectively. Before use, all the components are mixed and filtered at 220nm. All components except for DI water are purchased from Thermo Fisher Scientific.

A low concentration of antibiotics is added to avoid contamination. Compared to the original protocol developed by Banker [142], Penicillin-Streptavidin was replaced by Gentamicin, more stable in cell media. Experimentally, we observed less contamination with the use of gentamicin.

Let us also note that a low concentration of serum (HS, 1%) has been added to the maintenance medium in order to improve neuronal survival

II.B.2. Fixation

There are several methods of cell fixation. Each protocol is adapted to the type of antibody used and the microscopy technique employed for observations. For the experiments reported in this manuscript, we have use paraformaldehyde, with the following protocol: after a washing with warm PBS (37°C), neurons are fixed in 4% paraformaldehyde (PBS dilution) during 15 min. Paraformaldehyde can be also directly diluted in the culture medium. While

PBS can be stressful for cells, it is also an efficient way to remove dead cells and debris from the substrates. Of note, paraformaldehyde has to be at room temperature or lukewarm, so as not to depolymerize microtubules during fixation. Cells are then washed three times with PBS at room temperature and used for immunofluorescence or stored at 4°C in PBS.

II.B.3. Immunofluorescence

Immunofluorescence labeling consists in targeting proteins of interest, the antigens, based on specific antibodies. First cells are incubated with an antibody that binds the target molecule or antigen, the primary antibody. This first antibody is produced in a specific animal. Cells are then incubated with a secondary antibody, labeled with a fluorophore that recognizes the host species of the primary antibody. There are also some antibodies that are fluorescently labeled and can specifically target a protein of interest. Primary antibodies are incubated together, as well as the secondary antibody. It is important to make sure not to use primary antibodies made with the same animal species, otherwise the secondary antibody will label all the molecules bound to the primary ones.

Experimentally, the samples (glass coverslides with neurons) are first quickly rinsed with PBS at 37°C. Then there is a preliminary step of permeabilization and blocking of non-specific binding of antibodies. Triton X100 is used to permeabilize the cells and allow antibodies access to the cytoplasm. To get high antibody specificity, the blocking is performed using Bovine Serum Albumine (BSA). The permeabilization and blocking solution is prepared by mixing BSA at 2% and Triton at 0.25% in PBS. Coverslids are incubated in this mix for 15-30min, followed by a rinsing step in PBS. Immunolabeling is then achieved using the following protocol:

- Primary antibodies incubation, diluted in PBS-X (PBS with 0.1% Triton X100), during 1h at room temperature (can also be done overnight)
- Three washings in PBS-X
- Second antibodies incubation, diluted in PBS-X, during 45-60min, protected from light
- Three washings in PBS-X
- Hoechst incubation for nuclei staining, diluted in PBS-X, during 5 min
- Short washings in PBS-X, then in PBS, then finally in deionized water.

Finally, coverslips are mounted with a drop of mounting medium on a microscope slide. Drying is performed at 4°C, under a cover to protect the samples from light. Primary and secondary antibodies employed for the results exposed in this manuscript are summarized in **Table 2**.

Antibody I				
Target molecule	Target localization	Host animal	Dilution	Reference
β III-tubulin	Neuronal microtubules	Mouse	1:300	Millipore MAB1637
$\alpha\beta$ -tubulin	Microtubules	Sheep	1:500	Cytoskeleton ATN02
Monoclonal Tau-1	Tau dephosphorylated serines sites – Axon specific MAP	Mouse	1:1000	Millipore AB5622

Antibody II				
Target animal	Fluorophore	Host animal	Dilution	Reference
Mouse	Alexa Fluor 488	Goat	1:500	Lifetech A11017
Mouse	Alexa Fluor 647	Goat	1:500	Lifetech A21237
Sheep	Alexa Fluor 550	Donkey	1:300	Agrisera AS121983

AB – Direct immunofluorescence				
Target molecule	Target localization	Fluorophore	Dilution	Reference
Phalloidin	F-actin	Atto 488	1:300	Sigma 49403
Phalloidin	F-actin	Alexa Fluor 647	1:300	Invitrogen A2228
DNA (Hoechst)	Nuclei	Blue	1:1000	Sigma 861405

Table 2 : Primary antibodies, secondary antibodies and antibodies used for direct immunofluorescence

II.C. Patterned substrates

II.C.1. Static patterns

In this section, we will describe the different steps involved in the fabrication of static chemically micropatterned substrates. The expertise of neuronal shape control in the group of Catherine Villard started in Grenoble in Institut Néel, where micro and nanotechnologies are highly employed. Throughout 4 PhD projects [136]–[139], protocols to adapt micropatterning to neurons were optimized. The protocol that was used in this work consists in (1) a silanization step followed by (2) photolithography and lastly (3) surface functionalization with adhesive molecules. These steps will be described below.

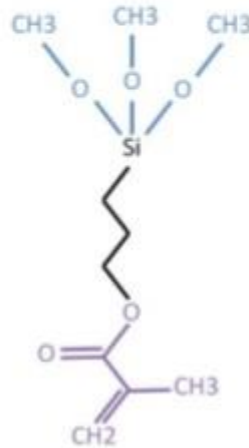
II.C.1.a) Silanization

Silanization is performed to alter the glass coverslip surface hydrophobicity, in such a way that it will be high enough to prevent cell adhesion but still low enough for the subsequent step of photoresist spreading.

First, the surface is oxidized with an O₂ plasma for 3min which not only cleans the surface but also triggers the formation of free O⁻ and OH⁻ radicals, thus increasing the surface affinity with the silane solution. Incubation in the silane solution occurs immediately after the plasma.

A Silane formula: $R-(CH_2)_n-Si(X)_3$

Bind Silane:
 $(C_4H_5O_2)-(CH_2)_3-Si(OCH_3)_3$



B

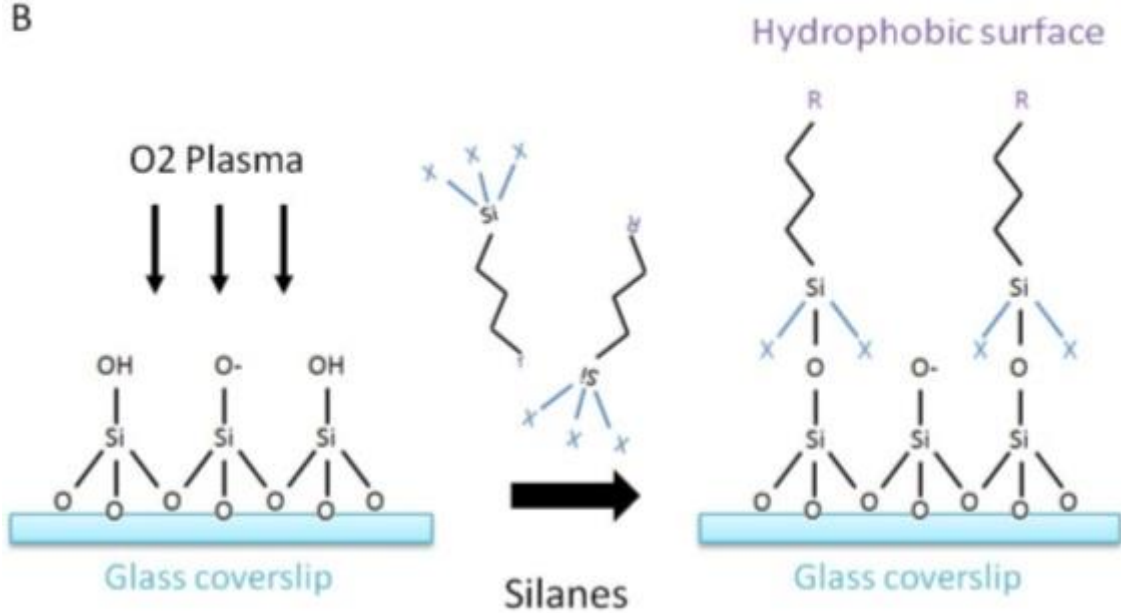


Figure II-2 : Silane formula and steps of silanization process (A)Bind silane formula. The number of CH₂ groups defines the hydrophobicity of the silane (n=3, green). (B) **Steps of silanization.** O₂ plasma oxidation, leading to free O⁻ and OH⁻ radicals, is followed by silane deposition. A final phase of hydrolysis binds the silane molecules to the glass coverslip with a covalent link. Adapted from [139].

The solution used in this work is called Bind-Silane. It was used on glass coverslides with the following protocol:

- Preparation of a solution of Bind Silane, 3-methacryloxypropyl-trimethoxysilane: $(C_4H_5 O_2)-(CH_2)_3-Si(OCH_3)_3$, Fischer Scientific. Solution for 15mL ethanol (absolute, $\geq 99.8\%$, Sigma-Aldrich): acetic acid (484 μ L) and Bind Silane (56 μ L).
- A drop of 200 μ L of Bind Silane solution is applied on the surface during 2min
- Glass coverslides are then dried with a cleanroom wiper (dust-free, microfiber)

Silanization consists in the binding of monolayer of silanes, amphiphilic molecules whose generic formula is $R-(CH_2)_n-Si(X)_3$ (where R is a hydrophobic group and n defines the length of the silane carbon chain tuning the hydrophobicity of the silane.) to the glass coverslip substrate. Of note, silane binds to the coverslip with a covalent link. After being silanized, glass coverslides can be stored up to 1 month at room temperature if protect from air.

II.C.1.b) Photolithography

The principle of the photolithography step relies on the fabrication of a photoresist stencil over the coverslip surface. The function of this stencil is to protect the areas that should remain hydrophobic and to select the complementary zones intended to be covered with cell adhesive molecules in later steps of the process.

The first part of this process is the design of a mask optimized for neuronal cultures. Then, once the mask has been fabricated, it is employed to create a photoresist stencil over glass coverslides inside a clean room, an environment protected from dust and UV light. These steps will be described below.

II.C.1.b.1 Designing the masks

In vitro hippocampal neurons developing on uniformly adhesive surfaces typically have neurites of 1-2 μ m width [102]. 2 μ m wide lines are typically chosen as substrates of adhesion for neurons in the aim of mimicking these spontaneous morphological characteristics. Furthermore, the distance between parallel stripes is often set to 100 μ m, as this value maximizes the number of cells adhering on a coverslip while minimizing the number of neurites crossing over the non-adhesive gaps separating the lines.

We used the software Clewin to design chromium masks for the fabrication of the micropatterned substrates.

A key point of the mask design also resides in the creation of a zone for unpatterned neurons, surrounding the patterned areas (**Figure II-3**). This zone is intended to allow for the growth of a population of unconstrained neurons on the coverslips, which have been observed to boost

the survival rate of patterned neurons [139]. Moreover, this unpatterned zone also facilitates the recognition of sub-zones of differing patterns on the coverslip. An example of mask design is presented **Figure II-3**. The mask design is adjusted to fit the dimensions of commercial standard coverslips. Square 24mm coverslips were used.

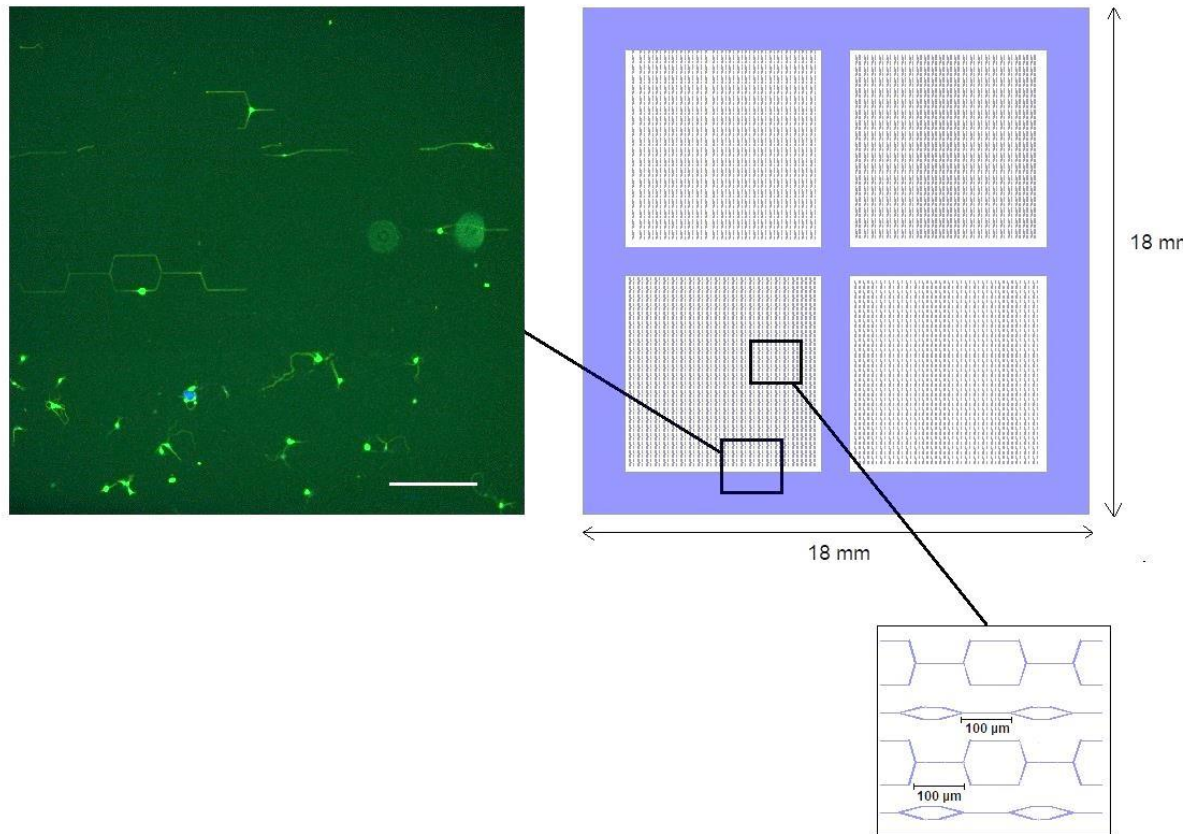


Figure II-3 : Example of typical mask design with four subzones surrounded by non-patterned zones. Purple parts represent adhesive area. Inset: Left. Fluorescence image at the frontier between non-patterned neurons and patterned neurons. Green: β_3 -tubulin. Blue: Hoechst (nucleus). Scale bar: 200 μ m. Right : example of pattern design. Lines are 2 μ m wide.

II.C.1.b.2 Fabrication of photoresist stencil

The fabrication of a photoresist stencil was performed inside the IPGG clean room using the following protocol:

- Positive photosensitive resist (S1805 from Shipley) is spincoated on the silanized coverslips with an acceleration of 4000 rpm/s and a speed of 4000rpm during 30s, producing a resist layer of 0.5 μ m.
- The photoresist is then annealed over a heating plate at 115°C during 1min

- The coverslip is exposed under UV light at a wavelength of 435nm (G-line) with a MJB4 aligner (Suss Microtech), through the chosen chrome mask, for an exposure time determined by the formula below.
- The exposed area of the photoresist are then dissolved through immersion in a developer solution (Megaposit MF-26A, Shipley) for 1min, during which the coverslip is gently agitated with a pair of tweezers.
- The sample is then rinsed in deionized water and dried with an air gun.

The UV dose energy E needed for S1805 is about $50\text{-}60 \text{ mJ}\cdot\text{cm}^{-2}$. The exposure time t is calculated after measuring the lamp power P through the equation:

$$t = \frac{E}{P}$$

With the MJB4 aligner of the IPGG cleaning room, the typical exposure time is 4s.

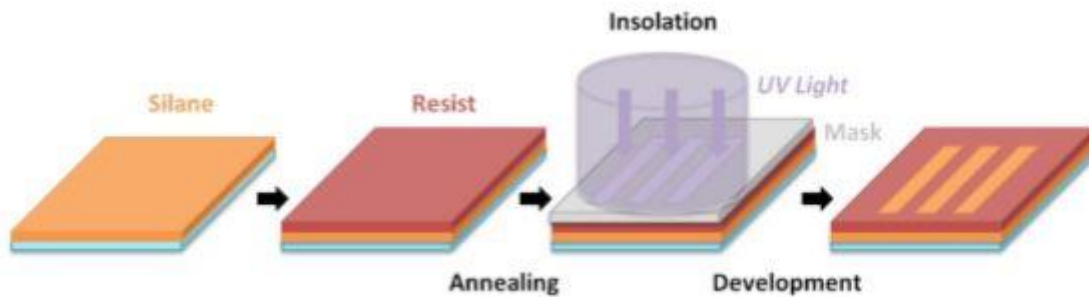


Figure II-4 : Steps of the photolithography process. From left to right: spinning of the photoresist layer and annealing, exposition to ultraviolet (UV) light through a chrome mask, photoresist development to dissolve the exposed regions of the photoresist layer (positive photoresist) followed by a washing step in deionized (DI) water. Light blue: glass coverslip. Orange: silane. Red: photoresist. Grey: chromed regions of the mask. From [139].

II.C.1.c) Surface functionalization

In order to allow cell adhesion on the UV-light exposed parts of the substrate, the coverslip is first activated with a O_2 plasma for 3min, then incubated in an aqueous solution of polycations, in our case Poly-Ornithine (PLO) at a concentration of $80 \mu\text{g}/\text{mL}$. After rinsing the coverslips in PBS to remove the excess PLO, the resist is removed by immersion in an absolute ethanol bath and exposition to ultrasounds for 1min30s (lift-off step). The coverslips

are subsequently rinsed twice with PBS and then inserted inside 6-well plates filled with PBS. All the steps previously described are summarized in **Figure II-5**.

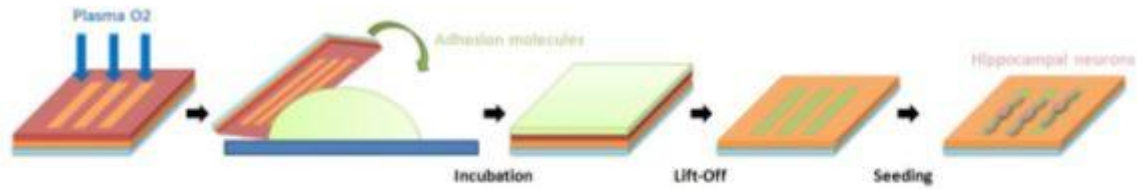


Figure II-5 : Surface functionalization with adhesive molecules. From left to right: Surface activation by O₂ plasma. Incubation of the coverslip on a drop of PLO overnight at room temperature. Lift-off in an absolute ethanol ultrasonic bath in order to remove the photoresist. Seeding of cells which will adhere only on adhesive molecules, adopting the pattern shape. From [139].

II.C.2. Dynamic patterns

II.C.2.a) *Reactives for dynamic patterning*

In this section, we will introduce the components used for dynamic patterning and give the chosen references or synthesis methods, as well as the concentration values.

II.C.2.a.1 Cell repelling polymers

The first repellent background that we tried is made with PLL-g-PEG. PEG is a hydrophilic polymer that is one of the most used molecules to prevent protein adsorption and subsequently cell attachment [144], [145]. The antifouling behaviour of PEG is not fully understood and is still an area of active research, although it is suggested that the dense solvated brush-like PEG structure that is often fabricated for anti-fouling purposes shields surface charges and disallows interaction of proteins with the underlying surface [146]. PLL-g-PEG is a polymer consisting in a PLL backbone grafted with PEG strands. The PLL-g-PEG solution that we employed has been manufactured by Surface Solutions, Switzerland. We observed some variations in the non-fouling behavior of PLL-PEG towards cell adhesion between the different stocks that were purchased. The second polymer that we employed is PLL-g-PMOXA. Structurally, PMOXA could be described as a poly(ethylene imine) backbone with an acetyl group bound to the nitrogen atom in each repeating unit. It has been reported that PLL-g-PMOXA is more stable than PLL-g-PEG under cell culture conditions [147]. Using PMOXA, we managed to achieve better results

of adhesion contrast with hippocampal neurons. Unfortunately, this polymer is still in development, and consequently the repellent effect was inconsistent amongst different stocks. The references and concentrations of the polymers listed above can be found in Table 3.

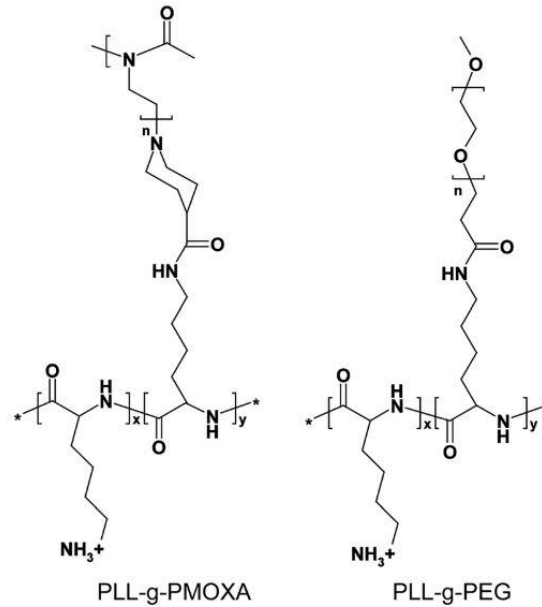


Figure II-6 : Chemical structures of PLL-g-PMOXA and PLL-g-PEG.

II.C.2.a.2 Adhesive molecules

We explored adhesive patterning with molecules from the extracellular matrix such as laminin on which adhesion is mediated by integrins [88]. Cationic molecules such as Poly-L-Lysine (PLL) were also employed. The later type of molecules enables non specific adhesion of neurons. References and concentrations of the adhesive molecules listed above can be found in Table 3.

II.C.2.a.3 APP, a click adhesive polymer

Dynamic patterning requires the implementation of switchable surfaces whose adhesion can be tuned after the seeding of cells on the substrate. There are several click-adhesive molecules that can be employed to create such remotely controlled surfaces. For example, pH-responsive (eg. PLL-*block*-PLGA [148]) and thermally-responsive (eg. PNIPAAm [149]) polymers have been designed.

In this work, we chose to use azido PLL-g-PEG or APP, a PEGylated derivatives of PLL that display azide (“clickable”) functions at the end of PEG strands, enabling non toxic surface attachment of alkyne-coupled peptides (by simple bath application of reactive peptides in the cell culture), which triggers on demand cell spreading.

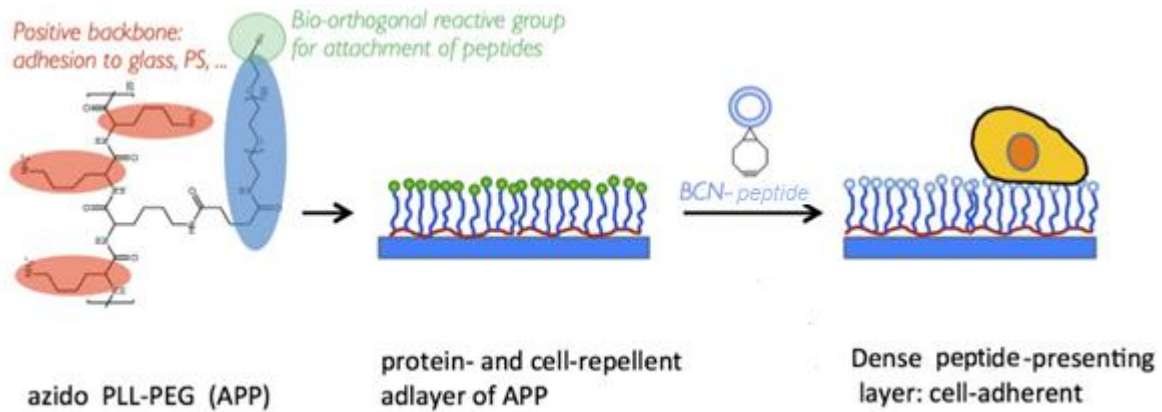


Figure II-7 : Cell-repellent APP coating switched *in vitro* into an adhesive peptide-presenting surface. Red: PLL backbone, blue: PEG chains, and green for the “clickable” azide function turning into light blue after binding with the adhesive peptide.

APP was synthesized by the Chemical Biophysics group of ENS using the following protocol: PLL•HBr with an average molecular weight of 20 kDa is dissolved in a sodium tetraborate buffer (STBB, 50 mM in D₂O, 1 mg PLL•HBr per 50 μ L STBB). After dissolution, the pH of the solution is set to 8.5. Subsequently, the solution is added to the desired amount of NHS-activated PEG (based on the desired grafting density - assuming a quantitative reaction), and the suspension is shaken vigorously to promote dissolution of the NHS-activated PEG. The reaction progress is monitored by ¹H-NMR. Upon achieving the desired grafting ratio (which generally takes only several minutes), the solution is transferred to a dialysis tube and dialysed against MilliQ for 16 hours, with at least three changes of the dialysis bath. The solution is lyophilised producing the desired APP as a white fluffy powder (near quantitative yield). The APP obtained has a grafting density of 1 PEG chain per 3 lysine residues, and will be referred to as APP 100% from now on.

In this work, we have used different dilutions of APP in order to tune its cell-adhesive abilities. To obtain diluted solutions of APP, a solution of APP 100% at 0.1mg/mL was mixed with a solution of PLL-g-PEG at 0.1mg/mL with the corresponding dilution ratio.

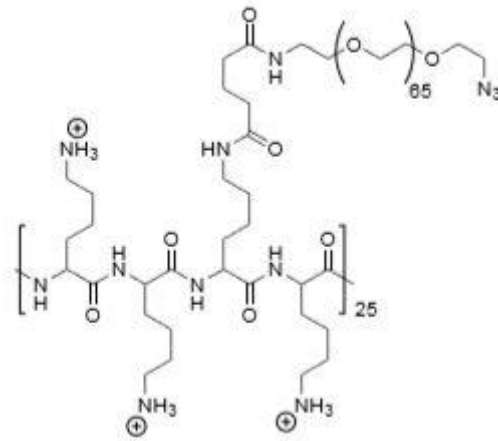


Figure II-8 : Chemical structure of APP.

II.C.2.a.4 Peptide

Different peptides were employed for the functionalization of APP-coated surfaces. To be able to click with the azide function these peptides, a bicyclo[6.1.0]nonyne (BCN) function must be first added to the peptide. The peptide that was first used to develop APP-based dynamic patterning of cells is RGD, a derivative of the extracellular molecule fibronectin. For the hippocampi neurons that we have used in our work, this peptide does not provide good adhesion, as fibronectin is a poor substrate for hippocampal neurons adhesion. Therefore we have decided to use peptides derived from YIGSR, a portion of the chain B1 of laminin. It has been reported that neurons can adhere on surfaces functionalized with YIGSR [150]

Three derivatives of YIGSR were tested: BCN-LamPEG, BCN-LamA and BCN-Compound3-3 (see Table 3 for chemical structures). Neurons have been found to adhere for APP rails functionalized with each of these peptides.

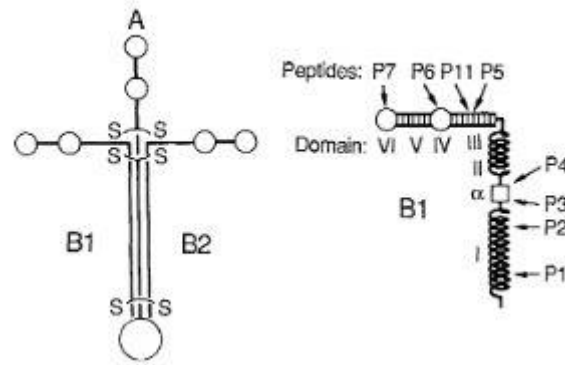


Figure II-9 : Schematic model for the structure of laminin. Seven structural domains in the B1 chain of laminin have been described and these are designated I-VI and α . The circles designate the globular regions of the laminin and the square designates an unusual cysteine-rich homologous repeat. P11 (residue 925-933), CDPGYIGSR. From [151]

II.C.2.a.5 Summary

Anti-fouling polymers				
Name	Chemical structure	Specifications	References	Concentration
Poly(ethylene glycol)	PLL-g-PEG	PLL:20kDa PEG :2kDa	Surface Solutions, Switzerland	0.1mg/mL and 1mg/mL in deionized water
Poly(2-methyl-2-oxazoline)	PLL-g-PMOXA	PLL:20kDa PMOXA :4kDa grafting density 19%	Synthesized by AlveoleLab	1mg/mL in deionized water

Adhesive molecules			
Name	Chemical structure	References	Concentration
Laminin	glycoprotein	Sigma-Aldrich 114956-81-9	0.01 to 0.04 mg/mL in PBS
Laminin-rhodamine	glycoprotein	Tebu-bio (Cytoskeleton) LMN01-A	0.01mg/mL in PBS
Poly-L-lysine-Fluorescein isothiocyanate	PLL-FITC	Sigma Aldrich P3069	0.1mg/mL in PBS

Click adhesive molecules				
Name	Chemical structure	Specifications	Synthesis	Concentration
APP Azido- Polyethylene glycol	PLL-g-PEG – NH ₃	PLL: 20kDa PEG : 2kDa Grafting density of 33% ¹	See section Cell repelling polymers II.C.2.a.1	0.1mg/mL in deionized water

Peptides			
Name	Chemical structure	Synthesis	Concentration
BCN-LamPEG	{PEG6}YIGSR	By Biophysics group of ENS	100µM in deionized water
BCN-LamA	GGGYIGSR	By Biophysics group of ENS	100µM in deionized water
BCN- Coumound3-3	CGGGYIGSR	By Biophysics group of ENS	100µM in deionized water

Table 3 : List of different reactivities employed for dynamic patterning protocols.

II.C.2.b) *Patterning methods*

II.C.2.b.1 **Deep UV etching method**

Clean glass coverslips were exposed to an O₂ plasma for 3min. Cleaned wafers were then laid on top of a 200 µL drop of 0.1 mg/mL PLL-g-PEG at room temperature for 1 hour or PLL overnight (this volume has to be adapted to the coverlip size to allow complete coverage of the wafer by the solution with the minimal amount of water). The wafers were rinsed once with PBS, twice with deionized water and then dried with an air gun.

For photopatterning, a chromium synthetic quartz photomask (Selba, Switzerland) was cleaned with ethanol and then exposed to deep UV light for four minutes. Then, a PLLg-PEH-coated quartz wafer was placed on the mask with 2 µL of water (this volume has to be adapted

¹ Grafting density of 33% : one azidoPEG chain per three lysine residue

to the glass coverslip size to allow complete coverage of the wafer by water using the minimal amount necessary). The masked substrate was subsequently exposed to deep UV light for 15 min, after which the wafer was dried with an air gun. The irradiated areas were coated with APP or laminin after patterning.

In case of double patterning, the substrate was then incubated in a solution containing the second molecule, after which the photopatterning step was repeated, with attention given to the alignment of the two patterns.

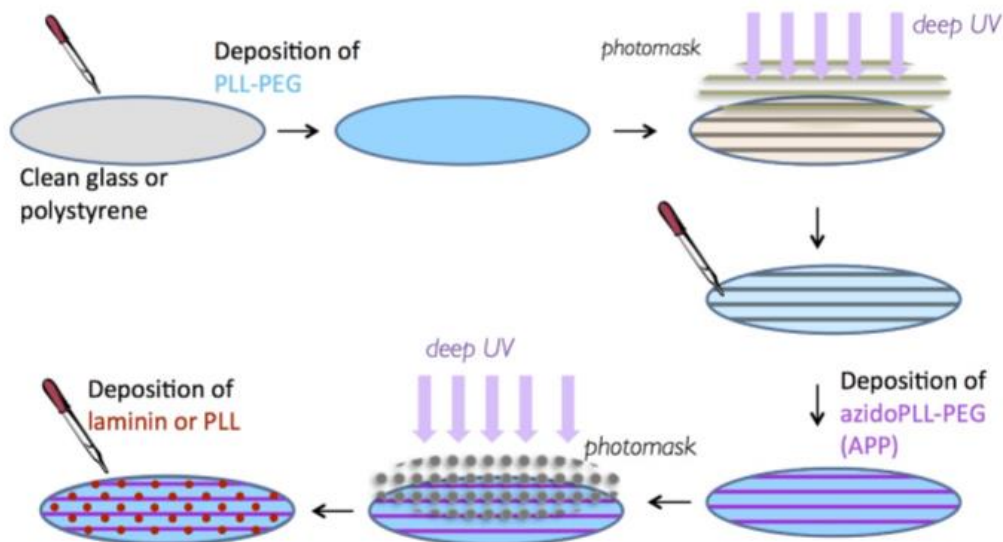


Figure II-10: Illustration of double patterning of APP (purple), and a set of permanently adhesive wells (red) on a PLL-g-PEG (blue) background with deep sequential UV etching.

II.C.2.b.2 Patterning with Primo

Primo is a device that enables direct printing of proteins on cell culture substrates. It is manufactured by the AleveoleLab company. Directly mounted on an inverted microscope, it consists of an optical illumination module coupled with the use of PLPP, a photo-activator molecule. The image to be printed is projected by a UV laser (375nm) through the microscope in the presence of PLPP, which catalyses the UV effect. The protein is then added and will bind to the illuminated areas [152].

Primo is piloted by the Leonardo Software (AleveoleLab).

Figure II-11 illustrates an example of double patterning realized with Primo with the following protocol:

- First, the coverslip is incubated in a solution of PLL-g-PEG (or PLL-g-PMOXA) for 1h at concentrations indicated in **Table 3**, then rinsed with PBS
- Then the coverslide is mounted on the Primo set up, and PLPP is added
- The coverslip is exposed to UV light. Exposure time calculation is described below.
- The polymer (or protein) is then added, and incubated for the required time (30min for APP, 15min for proteins)
- The coverslip is rinsed with PBS

For additional patterning, the previous steps are repeated (see **Figure II-11**).

The UV dose energy E needed for patterning PLL-g-PEG coated glass coverslides is about $750 \text{ mJ}\cdot\text{mm}^{-2}$. The exposure time t for a surface S is calculated by the Leonardo software after measuring the laser power P through the equation:

$$t = \frac{E}{P} \times S$$

The laser used in this work has a typical power of 3mW. For a surface corresponding to a x20 objective field (about 0.15 mm^{-2}), we have a typical type of 20s for a PLL-g-PEG coated coverslip. (respectively 40s for a PLL-g-PMOXA coated coverslip).

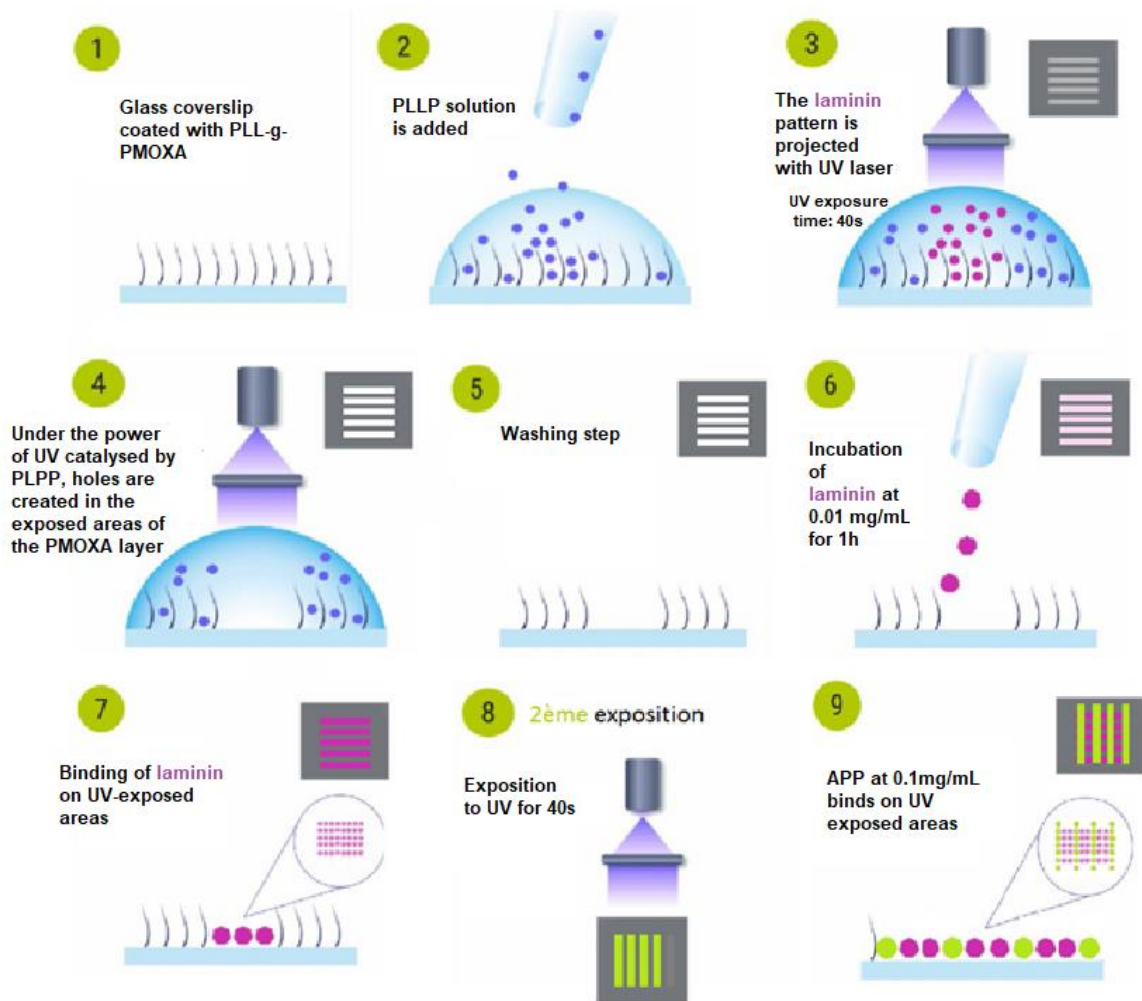


Figure II-11 : Illustration of double patterning with Primo. Patterning of APP stripes (green), and permanently adhesive stripes (purple) on a cell-repellent poly(2-methyl-2-oxazoline) (PMOXA) (blue) background with the Primo module. Adapted from [152]

II.C.2.b.3 Patterning adhesive stipes with positive photoresist

The following method was used to create adhesive stripes on a repulsive background. It is a variant of the photolithography technique described in II.C.1.b) .

First, the glass coverslip is silanized with the protocol described in II.C.1.a). Then, a photoresist stencil is fabricated inside the IPGG clean room using the following protocol:

- Positive photosensitive resist (S1805 from Shipley) is spincoated on the silanized coverslips with an acceleration of 4000 rpm/s and a speed of 4000rpm during 30s, producing a resist layer of 0.5 μ m.
- The photoresist is then annealed over a heating plate at 115°C during 1min
- The coverslip is exposed under UV light at a wavelength of 435nm (G-line) with a MJB4 aligner (Suss Microtech), through the chosen chrome mask, for an exposure time determined by the formula below.
- The exposed area of the photoresist are then dissolved through immersion in a developer solution (Megaposit MF-26A, Shipley) for 1min, during which the coverslip is gently agitated with a pair of tweezers.
- The sample is then rinsed in deionized water and dried with an air gun.

The UV dose energy E needed for S1805 is about 50-60 $\text{mJ}\cdot\text{cm}^{-2}$. The exposure time t is calculated after measuring the lamp power P through the equation:

$$t = \frac{E}{P}$$

With the MJB4 aligner of the IPGG cleaning room, the typical exposure time is 4s.

Then, in order to allow cell adhesion on the UV-light exposed parts of the substrate, the coverslip is incubated in an aqueous solution of PolyLysine (PLL) at a concentration of 100 $\mu\text{g}/\text{mL}$. After rinsing the coverslip in PBS to remove the excess PLL, the resist is removed by immersion in an absolute ethanol bath and exposition to ultrasounds for 1min30s (lift-off step). The coverslip is subsequently rinsed twice with PBS.

Finally, the coverslip is incubated in a solution of PLL-PEG at a concentration of 0.1 mg/mL for 1hour. It is then rinsed 3 times with PBS and inserted inside a 6-well plate filled with PBS.

II.C.2.c) APP surfaces functionalization

To test whether APP-peptide stipes were neuron-adhesive, we also incubated some APP patterned coverslips in solutions of peptide, following the protocol below.

The glass coverslips were incubated in a BCN-peptide solution at 100 μM and left to react at room temperature for 1 hour. Afterwards, the surfaces were washed with PBS, and repetitively rinsed (3 x) with deionized water. The conjugated surfaces were subsequently dried with an air stream, and rinsed with PBS prior to use.

II.D. Microscopy observations

II.D.1. Time-lapse experiments

Images of living neurons were acquired using Leica DMI8 videomicroscopes equipped with a heated workplate or incubator, a humidifier, a CO₂ delivery system and a motorized stage allowing multi-position and multi-condition acquisitions. Microscopes were piloted by the Metamorph softwares. Time-lapse observations require some compromises. Indeed, the interval between two acquisitions has to be (i) sufficiently short to follow the event dynamics (e.g. actin waves along the neurites) and (ii) sufficiently long in order to reduce the stress induced by phototoxicity. The typical progression type of actin waves along neurites has been observed to be $\sim 3 \mu\text{m}/\text{min}$. For this reason, we have chosen intervals of 2-3min between images and durations of 24 – 48 h.

II.D.2. Fixed cells

Isolated immunostained fixed neurons were analyzed by phase contrast or fluorescence imaging with Leica DMI8 videomicroscopes piloted by the Methamorph software.

II.E. Analysis methods

II.E.1. Growth cone analysis

To take into account the complexity and diversity of growth cone shapes, we used two parameters to characterize growth cone: β and β_x . They respectively correspond to the growth cone angular extent (following the main shape of the growth cone) and the growth cone total angular extent. β_x takes into account any filopodia that might jut out from the growth cone main body.

We adopted the following protocol to measure β and β_x (see **Figure II-12**):

- First, we traced a line (A) following the axis of the neurite shaft (black dashed vertical line in **Figure II-12**)
- Then we trace a second line (B), following the main shape of the growth cone right hand side (blue dashed line)
- β_2 , the angle between lines (A) and (B), is measured

- A third line (C) is traced, whose origin is the intersection of (A) and (B) and direction follows the growth cone shape, including filopodia that deviates from the growth cone main body (red dashed line). Of note, if there are no filopodia jutting out from the growth cone main body, we have $\beta_2 = \beta_{x2}$
- β_{x2} , the angle between lines (A) and (C), is measured
- The same process is repeated on the left hand side of the growth cone (with respect to the axis of the neurite shaft, oriented with the growth cone to the top) and yields the value of β_1 and β_{x1} . Of note, if there are no filopodia jutting out from the growth cone main body, we have $\beta_1 = \beta_{x1}$
- Finally we obtain the value of β and β_x with the formula: $\beta = \beta_1 + \beta_2$ and $\beta_x = \beta_{x1} + \beta_{x2}$

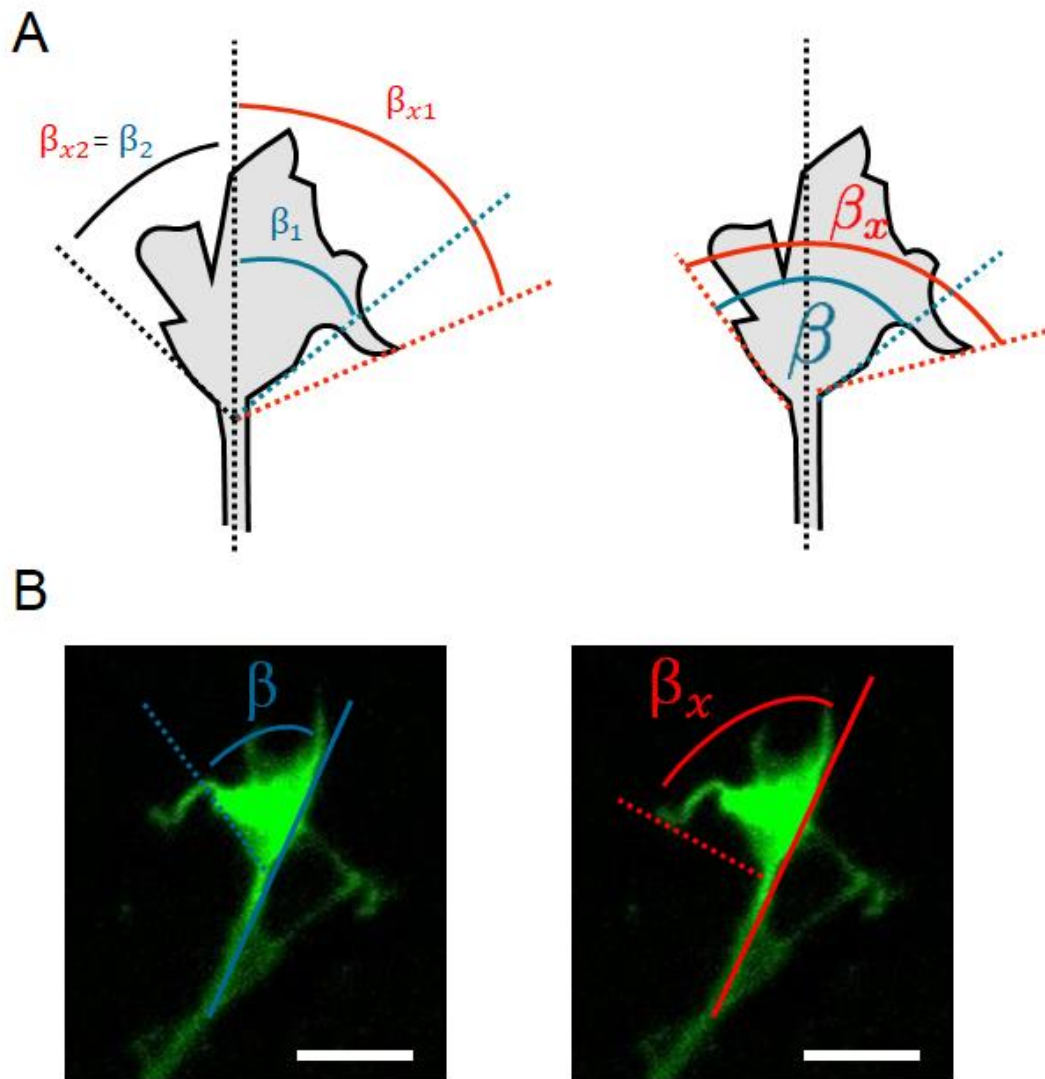


Figure II-12 : Characterizing growth cone morphology with parameters β and β_x : A) Cartoon representing the definition of β , β_x , β_1 and β_2 , β_{x1} and β_{x2} . B) Fluorescence images of a growth cone from a fixed E16 mice hippocampi neuron fixed at DIV1. Green: F-actin. Scale bar: 10 μ m

Of note, collapsed and branching growth cones were excluded from the scope of this analysis.

Line tracing and angle measurement was performed on fluorescence images of the growth cone F-actin using ImageJ software.

II.E.2. Branching probability and measure of branch length

In this work, we have investigated the influence of substrate geometry on branching probability. For each isolated neuron, at each potential branching point (ie. an intersection of two patterned adhesive lines), we observed whether the incident neurite branched or turned. A branching event is defined as a separation of the neurite into two daughter branches who each have a length superior to 30 μ m. In the opposite case, the situation was considered a turning event.

The branching probability $p_{branching}$ was defined as:

$$p_{branching} = \frac{n_{branching}}{n_{branching} + n_{turning}}$$

where $n_{branching}$ represents the number of branching events and $n_{turning}$ the number of turning events.

Length measurement of branches was performed with ImageJ software.

II.E.3. Time-lapse analysis

For the analysis of time-lapses recordings, we used a program custom designed by Marianne Renner from Institut du Fer à Moulin, SpeedPlot . We focused on the measure of growth cone pausing time.

First, the trajectory of growth cones of interest was tracked using ImageJ software, recorded as text files and analyzed with the following procedure:

Each file corresponds to one initial neurite. The file is separated into the trajectories of the neurite branches growth cones, for example the mother branch and the daughter branches. Of note, the time point chosen for the beginning of the daughters trajectories (and the end of the mother trajectory) corresponds to a separation of the growth cone in two distinct areas. The resulting file takes the form represented in **Figure II-13**:

Number of trajectory	Frame	X coordinate (pixels)	Y coordinate (pixels)	Origin (branching order)
1	1	573	95	0
1	2	571	125	0
...

Figure II-13 : Example of trajectory file for a neurite. Each branch trajectory is designated by a number (generally 1 for the mother branch, 2 and 3 for the daughter branches. A parameter also indicate the branching order: 0 for a mother branch, 1 for a daughter neurite.

For each trajectory, the file is then entered as an input variable in the program SpeedPlot. Speedplot first calculates the growth cone speed at each time point over a sliding window, and plots it with a color code corresponding to the speed value.

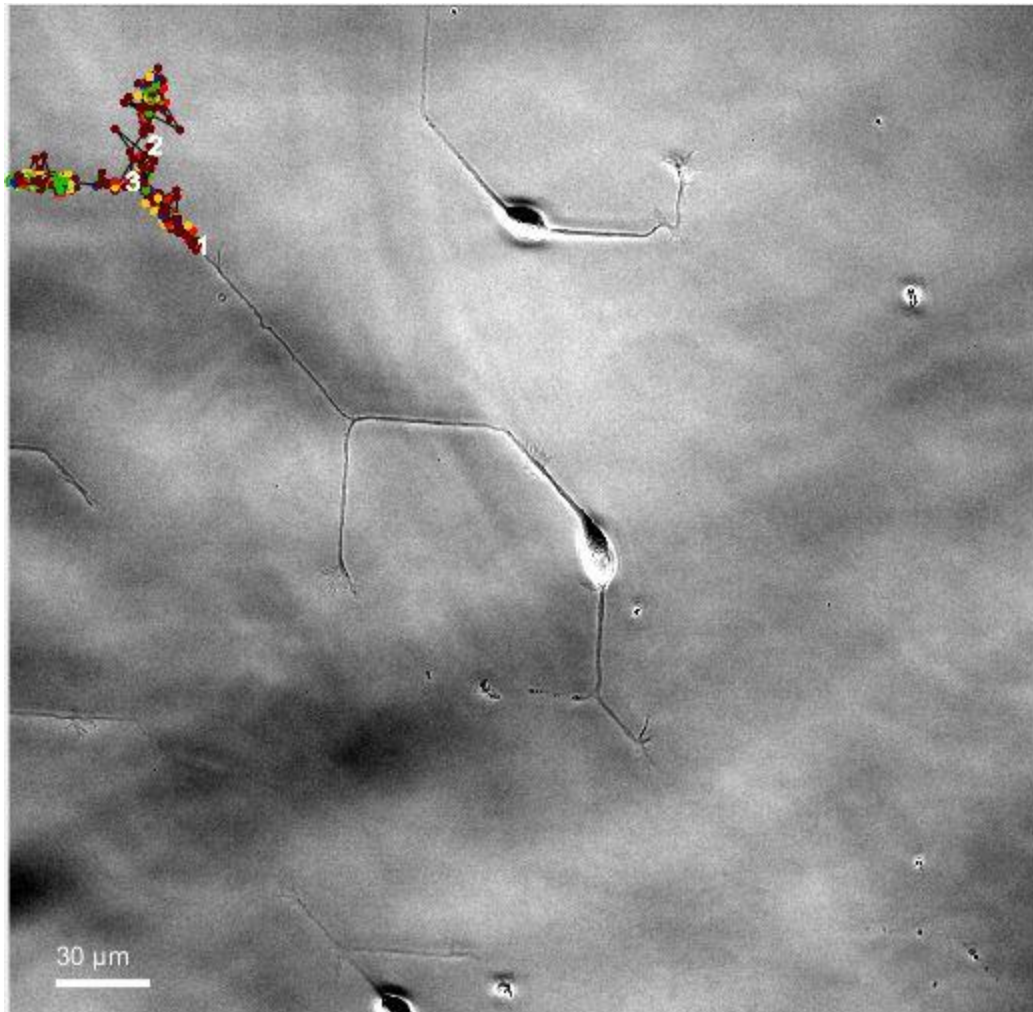


Figure II-14 : Screenshot of the representation of growth cone speed values given by the program for a branching neurite. Phase image of E16 mouse hippocampi neurons at DIV1. 1: mother branch, 2 and 3: daughter branches

A circular area is then drawn over the region of interest (ROI) ie in case of branching or turning, the intersection between 2 adhesive lines. In case it is the growth cone pausing time over a straight line that is desired, a circle is drawn around the adhesive line.

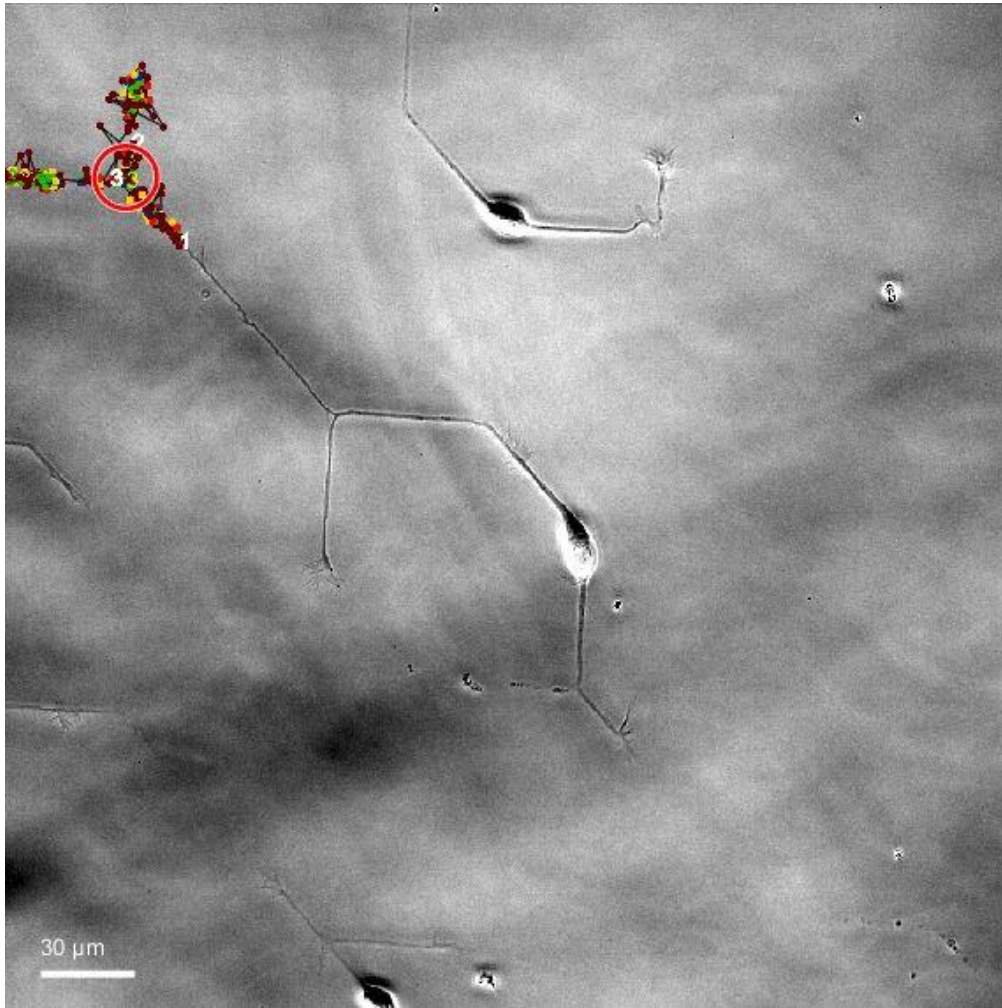


Figure II-15 : Drawing of a region of interest around a branching point. Phase image of E16 mouse hippocampi neurons at DIV1. 1: mother branch, 2 and 3: daughter branches

For each branch, the program computes the residency time inside the ROI. The branching pausing time is obtained with the following formula:

$$t_{pausing} = t_{mother} + \max(t_{daughter1}, t_{daughter2})$$

In case of turning or on a straight line, the trajectory file consist of only one branch trajectory so the growth cone pausing time corresponds to this branch residency time into the chosen ROI.

II.E.4. Statistical tests

The statistical analyses of our experimental data have been performed with the GraphPad Prism software that provides a large panel of statistical tests. In our studies, we often deal with

large populations, i.e. samples greater than 100 cells. As most of biological data, measured data follow bell-shaped distributions. When samples are huge, they can be often approximated to Gaussian distributions and parametric tests are quite robust. However, in order to also process data obtained on smaller samples, we have mainly adopted non parametric tests. These tests make few assumptions about the distribution of the data and result adapted both for Gaussian distributions and for smaller samples. We will describe in this section the main tests we used depending on the type of available data.

➤ Mann–Whitney test

The unpaired nonparametric Mann–Whitney test was employed to compare, for example, two series of cells belonging to the same culture batch but experiencing different growth conditions (for example two kinds of patterns). Samples are independent and may have different sizes.

➤ Fisher’s and Chi-square tests

These tests were used to compare frequency values. Contingency tables are created, where the categories defining the rows and columns must be mutually exclusive. These tests can for example be dedicated to the comparison between the polarization rates between two populations of cells grown on two different types of patterns or to a random condition (i.e. to a probability of 50%). For series of small sizes, the Fisher’s test is considered more accurate than the Chi-square test.

➤ Linear regression: slope comparison

Linear trends are fitted by linear curves with methods based on the least squares approach. Slopes are compared between two similar interpolation fits or with a null slope in order to identify a significant linear trend.

Data sets collected from equivalent experimental conditions and configurations in different samples and cell cultures were pooled together only after having checked that they were not significantly different.

In all cases, the null hypothesis when comparing two populations is that they are the same. In this manuscript, we have reported the experimental results giving the two-tailed p value associated to the adapted statistical test. p values provide an indication of the probability that the null hypothesis is true, with a significance level depending on the confidence interval.

Commonly, a 95% of confidence threshold is chosen and it indicates how precisely the p value is determined. We have adopted the common asterisk code to describe values levels of statistical significance according to the table below.

p value	Code	Interpretation
<0.001	***	Extremely significant
0.001 to 0.01	**	Very significant
0.01 to 0.05	*	Significant
>0.05	ns	Not significant

Table 4 : Asterisk code employed to describe values levels of statistical significance.

Chapter III. Results

Contents

Chapter III. Results	92
III.A. Static micropatterning to study neuronal branching	94
III.A.1. Introduction	94
III.A.2. Methodology	95
III.A.3. Analysis of growth cone morphology	101
III.A.4. Static analysis of branching	110
III.A.5. Dynamic analysis of neuronal branching on static patterns.....	131
III.A.6. Conclusion	135
III.B. Dynamic patterning to study neuronal branching.....	136
III.B.1. Context and objective of the project	136
III.B.2. Methodology and results	138
III.B.3. Conclusion	147

List of abbreviations and nomenclatures:

DIV Days In Vitro

PLO PolyOrnithine

GFP..... Green Fluorescent Protein

PLL..... Poly-L-Lysine

PEG Poly (Ethylene Glycol)

APP Azido- Polylysine grafted on Poly (ethylene glycol)

PLL-g-PEG PolyLysine grafted on Poly (Ethylene Glycol)

PLL-g-PMOXA PolyLysine grafted on Poly(2-methyl-2-oxazoline)

BCN: bicycle [6.1.0]nonyne

It has been reported that substrate geometry can influence branching [124]. In the present work, we have investigated this issue by imposing morphological constraints to neurons through the use of different chemical micropatterning techniques.

First, we have investigated neuronal branching on substrates patterned with narrow adhesive lines intersecting at varying angles. The distributions of branching probability and branches length were measured as a function of branching angle. Timelapse recordings of neurons on micropatterned substrates also shed light on the dynamics of the branching and turning growth cones. Results concerning this part of our work will be presented in section **III.A**.

In parallel to this study on static patterns, we have also worked on the development of a dynamic patterning technique based on spontaneous adsorption of comb-like derivatives of poly-L-lysine (PLL) to form switchable patterns on highly cell-repellent surfaces. The different strategies employed as well as the results that were obtained will be detailed in section **III.B**.

III.A. Static micropatterning to study neuronal branching

III.A.1. Introduction

Using photolithography-based micropatterning technology, we have designed regularly spaced polygonal shapes linked by straight lines. The vertices of these polygonal shapes define the meeting points of three lines intersecting at varying angles (according to the specific geometry of the polygonal shape). We then studied the behavior of neurons developing on these micropatterned substrates. At each intersection, neurites growing on a straight line were presented with two distinct paths and could choose either to branch or to turn (see **Figure III-1**).

First, as a preliminary step of our investigation, neuronal growth cone morphology on micropatterned substrates was analyzed. Indeed, as seen in Part I, the growth cone plays a fundamental role in branching. Next, we played with the different angular parameters characterizing the patterns to quantify how the decision to branch was influenced by an asymmetric or symmetric geometry. Subsequently, we decided to refine our analysis by comparing branching behavior between axons and undifferentiated neurons.

Next, we measured the lengths of neuritic branches in all angular configurations so as to further our understanding of the influence of substrate geometry on neurite branching and growth.

While these two first steps provided essential insights, they were performed on fixed samples and needed to be completed by a dynamic analysis of branching. For this reason, in the final step of our investigation, time-lapse recording of neurons developing on micropatterned substrates were realized. These experiments enabled us to start a characterization of the kinetics of branching in our set-up. We decided to focus in particular on one of the key parameters of branching kinetics: the growth cone pausing time at branching points.

III.A.2.Methodology

In this work, we have mainly studied neuronal branching on hippocampal mice neurons until the stage 3 of development *in vitro* (see **Figure I-25**). Typically that corresponds to 0-3 Days In Vitro (DIV).

III.A.2.a) Definition of branching parameters

We have defined three parameters to characterize branching and turning behavior at an intersection. As can be seen in **Figure III-1**, the first one, α , corresponds to the angle between the two daughter branches.

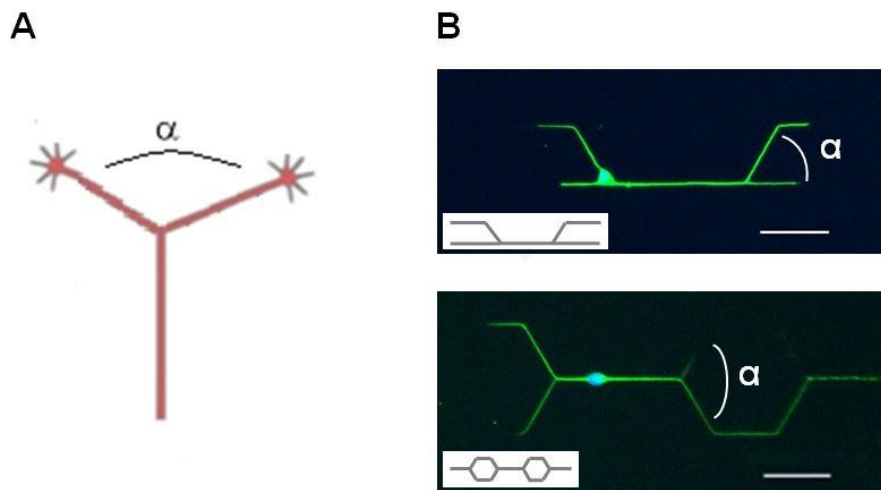


Figure III-1 : Definition of parameter α . A) Cartoon representing the definition of α as the angle between the two daughter branches. B) Examples of the values of α on branching neurons on micropatterns. Fluorescence image of fixed E16 mice hippocampal neurons at DIV2: Green: β_3 -tubulin. Blue: Hoechst (nucleus) Top: $\alpha=60^\circ$, Bottom : $\alpha=120^\circ$. Inset: adhesive patterns. Scale bar: 50 μ m.

The second ones, (α_1, α_2) , represent the angles between the direction of the incident neurite and the direction of each daughter branch. The convention $\alpha_1 \leq \alpha_2$ was chosen.

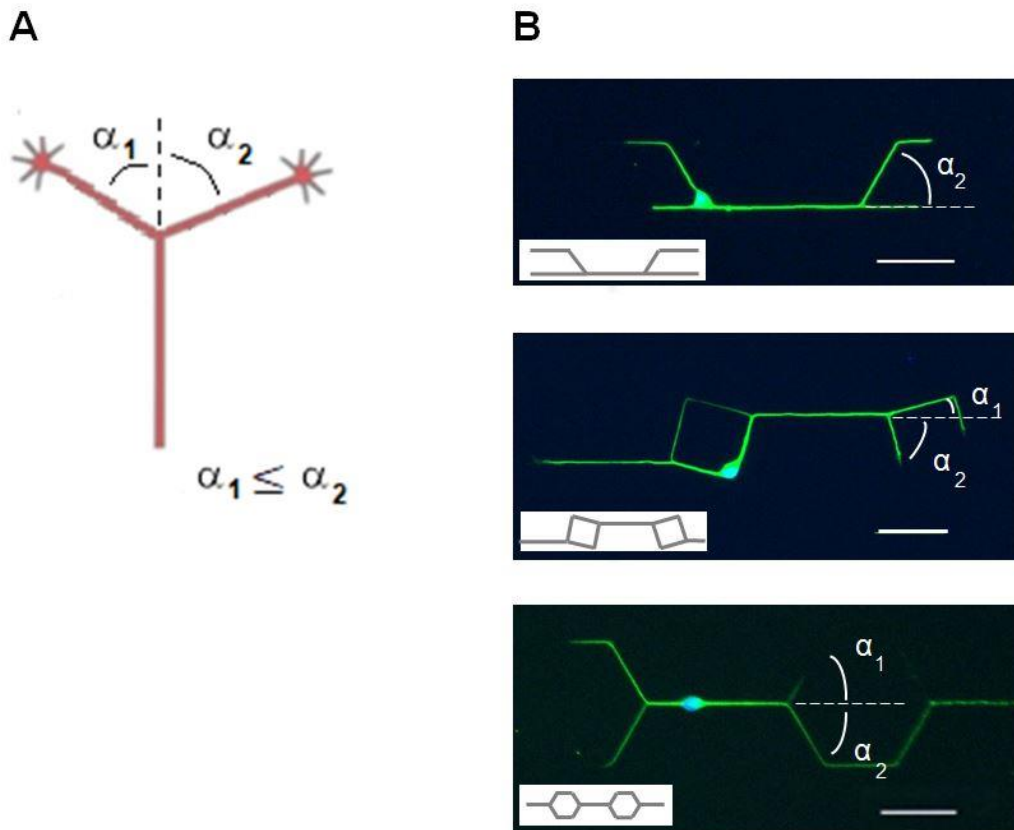


Figure III-2 : Definition of parameter (α_1, α_2) A) Cartoon representing the definition of (α_1, α_2) , as the angles between the direction of the incident neurite and the direction of each daughter branch, $\alpha_1 \leq \alpha_2$. B) Examples of (α_1, α_2) values on neurons. Fluorescence image of fixed E16 mice hippocampal neurons at DIV2: Green: β_3 -tubulin. Blue: Hoechst (nucleus) Inset: adhesive patterns. Top: $\alpha_1=0^\circ$ and $\alpha_2 = 60^\circ$, Middle: $\alpha_1=15^\circ$ and $\alpha_2 = 75^\circ$, Bottom : $\alpha_1=60^\circ$ and $\alpha_2 = 60^\circ$, Scale bar: $50\mu\text{m}$. Inset: adhesive patterns.

These parameters enabled us to distinguish between 2 categories of branching: “symmetric” and “asymmetric” branching, defined by $\alpha_1 = \alpha_2$ and $\alpha_1 \neq \alpha_2$ respectively.

III.A.2.b) *Micropatterns designed to study neuronal branching*

The control of the geometry of adhesion has enabled us to perform an angular analysis of branching in varying configurations. Several types of patterns were designed. As *in vitro* hippocampal neurons developing on uniformly adhesive surfaces typically have neurites of 1-2 μm width [102], 2 μm wide lines were chosen to draw our patterns in order to mimic these spontaneous morphological characteristics.

The first mask (see **Figure III-3**) was designed by a former post-doc of our team, Laura Daroles (SwitchNeuroTrail project, in collaboration with C. Specht, IBENS). It was separated in 4 zones, each characterized by a different angle between the intersecting lines. This pattern allowed us to explore branching behaviors in a wide range of geometries. Both bifurcations and trifurcations could be observed.

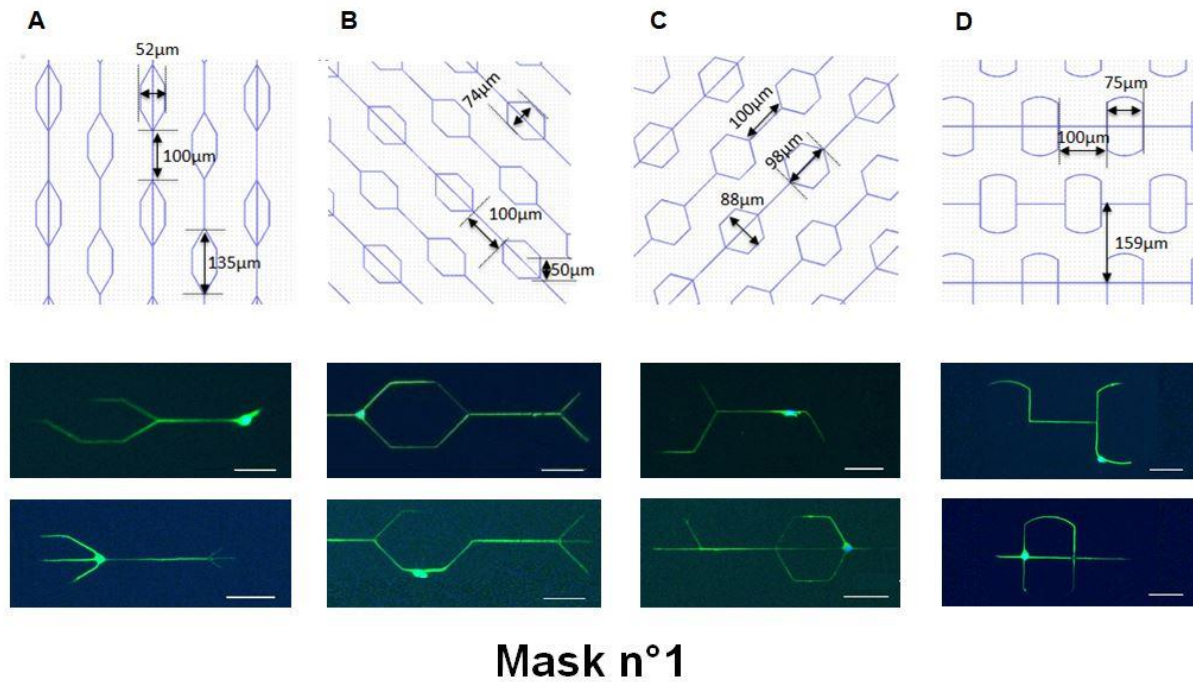


Figure III-3 : Design of the first mask used for our study of the influence of geometry on neurite branching. The first mask (mask n°1) is separated into four zones, each of them characterized by different angles between the intersecting lines: 30° and 60° (A), 45° and 90° (B), 60° and 120° (C), and 90 and 180° (D). Top: Pattern design. Lines are 2µm wide. Bottom: Fluorescence image of mouse hippocampal neurons at DIV2. Green: β_3 -tubulin, Blue: Hoechst (nucleus). Scale bar: 50µm. Both bifurcations and trifurcations could be observed on the substrates patterned with this mask.

For the second mask (i.e. Mask 2), we decided to simplify our study by focusing on bifurcation and removing any possibilities of trifurcations. We also aimed at refining our understanding of the angular dependency of branching by adding new angle values (see **Figure III-4**).

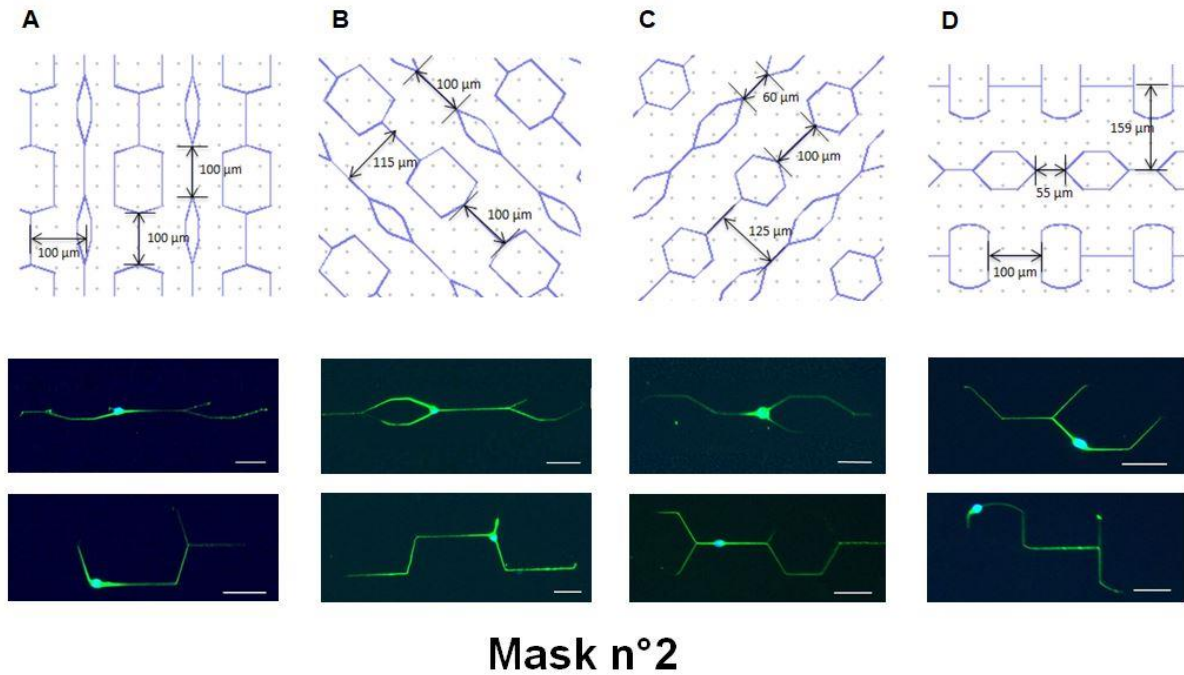
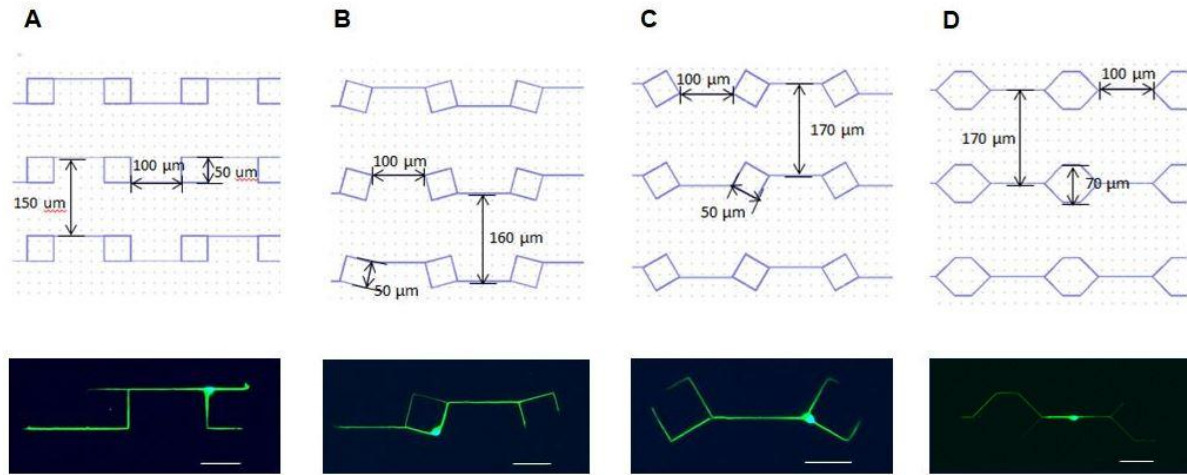


Figure III-4 : Design of the second mask. The second mask (mask n°2) is separated into four zones, each of them characterized by two different angles between the intersecting lines: 15° and 67.5° (A), 22.5° and 75° (B), 30° and 60° (C), and 45° and 90° (D). Top: Pattern design. Lines are $2\mu\text{m}$ wide. Bottom: Fluorescence image of mouse hippocampal neurons at DIV2. Green: β_3 -tubulin, Blue: Hoechst (nucleus). Scale bar: $50\mu\text{m}$.

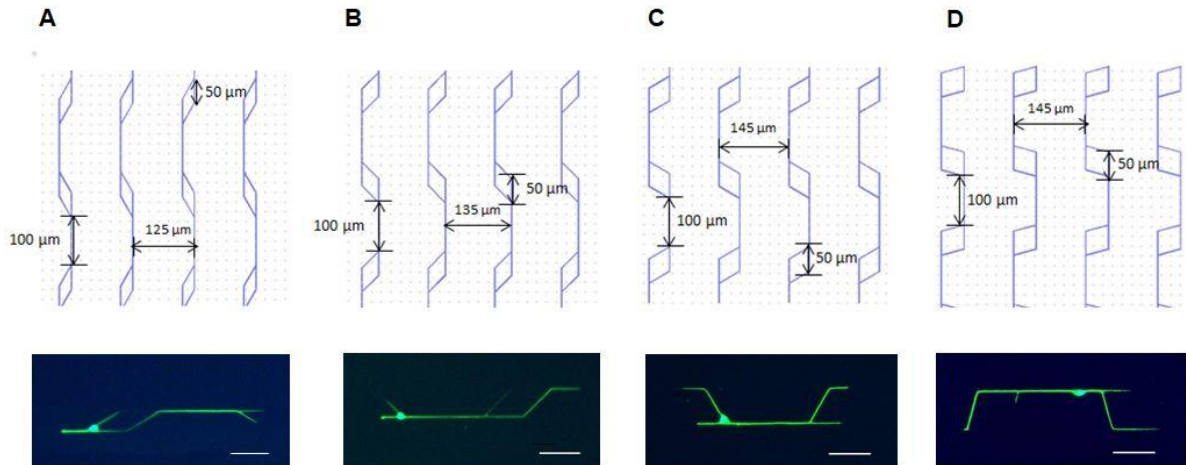
Finally, we decided to explore the influence of asymmetric geometries on the branching behavior. The first question that we asked was how, keeping the angle between the daughter branches α constant equal to 90° , does the asymmetry of the pattern influence the probability of branching and the length of the branches? To answer that, we designed patterns consisting in lines intersecting at an angle of 90° with varying orientations (Mask 3, zone 1).



Mask n°3, zone 1

Figure III-5 : Design of the third mask. Zone 1 of mask n°3 is separated into four areas, each of them with lines intersecting at an angle of 90° with different orientations with respect to the bisector of this angle : ($0^\circ, 90^\circ$) A), ($15^\circ, 75^\circ$) B), ($45^\circ, 45^\circ$) (C), and ($30^\circ, 60^\circ$) D). Top: Pattern design. Lines are $2\mu\text{m}$ wide. Bottom: Fluorescence image of mouse hippocampal neurons at DIV2. Green: β_3 -tubulin, Blue: Hoechst (nucleus). Scale bar: $50\mu\text{m}$.

The second question we asked was how, keeping $\alpha_1 = 0$, do increasingly asymmetric configurations affect branching behavior? A last type of patterns was designed in that aim. (Mask 3, zone 2, see **Figure III-6**)



Mask n°3, zone 2

Figure III-6 : Design of the third mask : Zone 2 of mask n°3 is separated into four areas, each of them consisting in straight lines bifurcating in two lines separated by an angle of varying different value : 30° (A), 45° (B), 60° (C), and 75° (D). Top: Pattern design. Lines are 2 μ m wide. Bottom: Fluorescence image of mouse hippocampal neurons at DIV2. Green: β_3 -tubulin, Blue: Hoechst (nucleus). Scale bar: 50 μ m.

Finally, let us note that each type of pattern gives the possibility to observe several branching angles. For example, for pattern D of mask n°3, zone1, branching events of angle 90° and 135° could be observed, as can be seen in **Figure III-7**. A table detailing, for each branching angle, the corresponding branching configurations on the micropatterns can be found in **Appendix**.

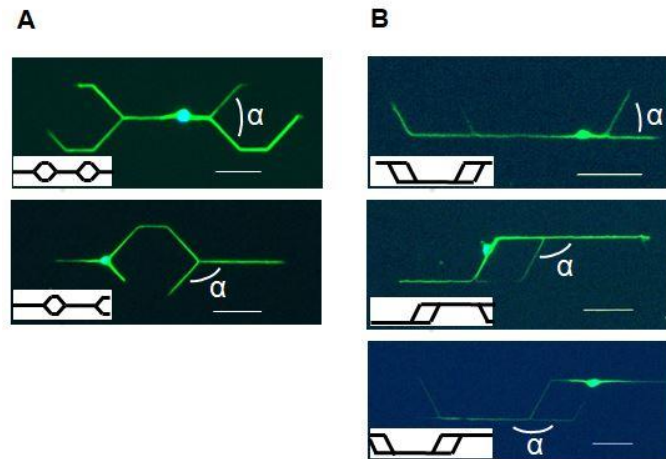


Figure III-7 : Examples of neurons on micropatterned substrates. Depending on the positioning of the soma, different branching angles can be observed on the same pattern. **A.** Fluorescence images of neurons at DIV2 on substrates patterned with mask 3, zone1, pattern D. Top: $\alpha=90^\circ$. Bottom: $\alpha=135^\circ$. Green: β_3 -tubulin, Blue: Hoechst (nucleus). Scale bar: $50\mu\text{m}$. **B.** Fluorescence images of neurons at DIV2 on substrates patterned with mask 3, zone2, pattern C. Top: $\alpha=60^\circ$. Middle: $\alpha=120^\circ$. Bottom: $\alpha=180^\circ$. Green: β_3 -tubulin, Blue: Hoechst (nucleus). Scale bar: $50\mu\text{m}$.

III.A.3. Analysis of growth cone morphology

We have started our work with a preliminary study of growth cone morphology on micropatterned substrates. Indeed, the growth cone plays a fundamental role in the formation of branches. For this reason, knowledge of the growth cone morphology is an essential tool to interpret results concerning branching behavior on micropatterned substrates.

III.A.3.a) Methodology

To study growth cone morphology, we cultivated hippocampal neurons from E16 mice embryo on uniformly adhesive substrates and on micropatterned substrates.

We first characterized growth cone morphology by measuring a parameter which we will call β and which corresponds to the growth cone angular extent, or in other words the angular distribution of growth cone filopodia. To do that, we drew, on both sides of the growth cone, (1) a line between the direction of the neurite shaft and (2) a line beginning at the base of the growth cone and ending at a point situated on the lateral edge of the growth cone. In that way, we obtained 2 angles: β_1 and β_2 . β , the angular extent of the growth cone, was then calculated by adding these 2 angles together: using the formula $\beta = \beta_1 + \beta_2$. (see **Figure III-8**).

Of note, branching growth cones were excluded from the scope of this analysis.

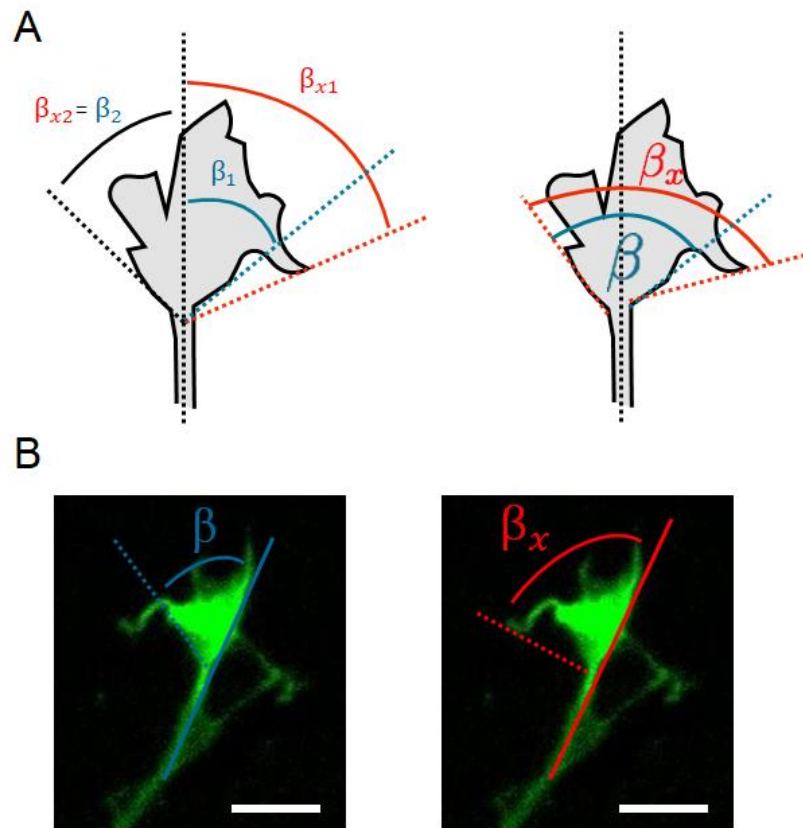


Figure III-8 : Characterizing growth cone morphology with parameters β and β_x : A) Cartoon representing the definition of β , β_x , β_1 and β_2 , β_{x1} and β_{x2} . B) Fluorescence images of a growth cone from a fixed E16 mice hippocampi neuron fixed at DIV1. Green: F-actin. Scale bar: 10 μ m.

Because of the complexity and diversity of growth cones morphologies, we decided to add an additional parameter β_x . While parameter β characterized the shape of the growth cone main body, parameter β_x takes into account any structure that might jut out from the growth cone main body, as can be seen in **Figure III-8**. (For more details on the measure of β and β_x , see **Chapter II**).

III.A.3.b) Growth cone morphology on uniformly adhesive substrates

First, we examined growth cone morphology on fully adhesive substrates, as a point of reference. Samples of hippocampi neurons developing on fully adhesive substrates were fixed at DIV1 and stained for F-actin.

Based on our observations, we have classified the growth cones of neurons on fully adhesive substrates in 2 categories according to their morphology: spread and collapsed (see **Figure III-9**). The “spread” morphology corresponds to a fan like-shape inside which filopodia are continuously distributed. On the other hand, the collapsed morphology refers to a narrow shape and corresponds to situations where the growth cone is indistinguishable from the rest of the neurite shaft.

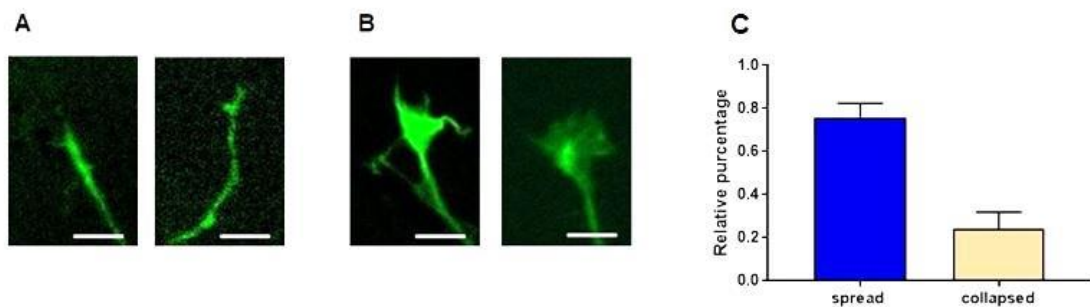


Figure III-9 : Morphological classification of growth cones. A. Collapsed growth cones, B. Spread growth cones. Fluorescence images of a growth cone from a fixed E16 mice hippocampi neuron fixed at DIV1. Green: F-actin. Scale bar: 10 μ m. C. Proportion of spread, intermediary and collapsed growth cones uniformly adhesive substrates at DIV1. Branching growth cones were excluded from the analysis. Mean values, error bars denote the 95% confidence interval.: 2 coverslips, n= 37 neurons, n'=174 growth cones.

As can be seen in **Figure III-9**, the majority (76%) of the growth cones of neurons growing on uniformly adhesive substrates assume a “spread” morphology, and the remaining 24% were collapsed.

The distributions of spread growth cone angular extent β and β_x can be found in **Figure III-10**.

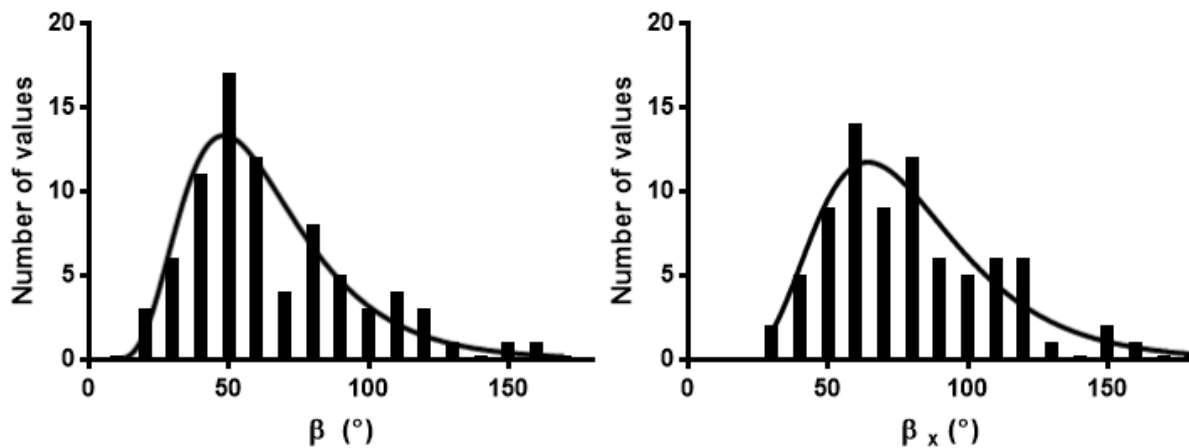


Figure III-10 : Distribution of spread growth cone angular range on uniform adhesive substrates as defined by β and β_x . Black line: lognormal fit (2 coverslips, $n=37$ neurons, $n'=80$ growth cones)

The angular distributions of β and β_x seem to follow log-normal laws centered on $48^\circ \pm 13^\circ$ (β) and $64^\circ \pm 12^\circ$ (β_x). As expected, the distribution was shifted toward higher values for the β_x criterion which takes into account more exploratory structures. Let us also remark that a majority of growth cones (85% for β , 74% for β_x) had an angular extent smaller than 90° .

Then we investigated the degree of asymmetry of growth cones shape with respect to the neurite shaft direction. As can be seen in **Figure III-11**, for 85% of growth cones we measured a value of $|\beta_2 - \beta_1|$ smaller than 20° (respectively 67% for $|\beta_{x2} - \beta_{x1}|$). This tends to indicate that growth cone morphology is mostly symmetric with respect to the neurite shaft direction.

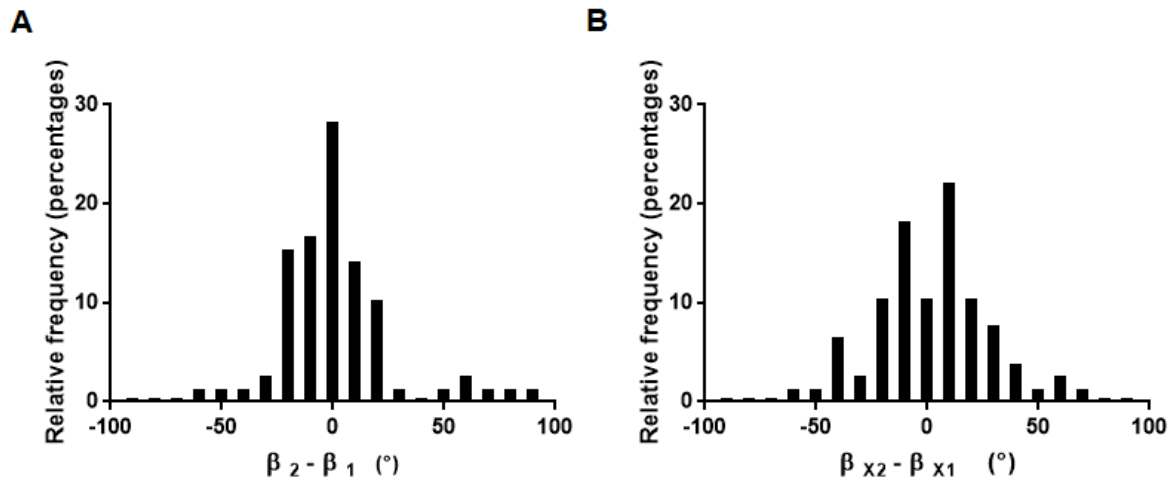


Figure III-11 : Distribution of spread growth cone asymmetry as defined by A. ($\beta_2 - \beta_1$) and B. ($\beta_{x2} - \beta_{x1}$) (2 coverslips, $n=37$ neurons, $n'=80$ growth cones)

III.A.3.c) Growth cone morphology on micropatterned substrates

We then proceeded to characterize the growth cone morphologies of neurons developing on micropatterned substrates. For this study, we chose patterns consisting in intersecting $2\mu\text{m}$ wide lines, which are described in detail in **Figure III-5**. To follow precisely the morphology of growth cones, we used hippocampal neurons from GFP-LifeAct mice embryo, which are genetically modified to express actin associated with GFP. Time-lapse recordings of LifeAct hippocampal neurons plated on micropatterned substrates were realized at DIV1.

The first striking features we observed was that, contrarily to what observed on non-patterned substrates, the majority of the growth cones of neurons growing on $2\mu\text{m}$ wide lines were collapsed, as can be seen in **Figure III-12**).

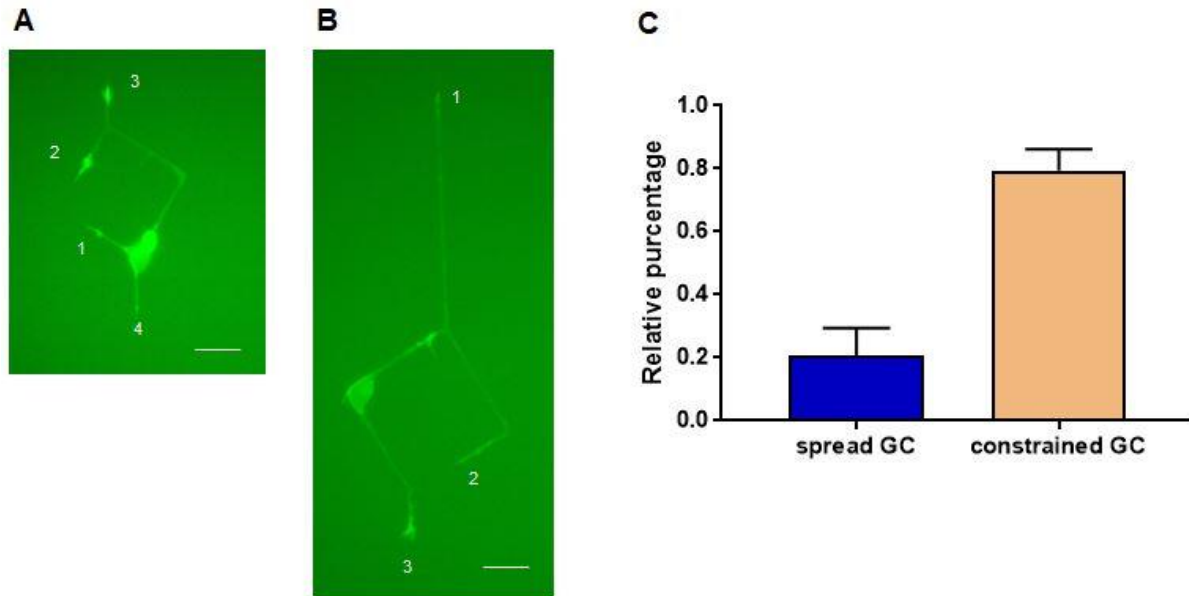


Figure III-12 : Influence of micropatterned substrates on growth cone morphology. **A and B:** Fluorescence images of hippocampal LifeAct neurons growing on $2\mu\text{m}$ -wide line patterned substrates. **A.** Growth cones n°2 and 3 assume a typical fan like shape and are spread beyond the limits of the adhesive patterns, while growth cone n°1 is narrower. **B.** Growth cones 1 and 2 are collapsed while growth cone n°3 has spread beyond the adhesive pattern. Green: F-actin. Scale bar $25\mu\text{m}$. **C.** Proportion of spread and collapsed growth cones on micropatterned substrates at DIV1. Growth cones in the proximity of intersections were excluded from the analysis. Mean values, error bars denote the 95% confidence interval.: 2 coverslips, $n=44$ neurons, $n'=139$ growth cones.

We then proceeded to quantify the proportions of spread growth cones in several samples. As can be seen in **Figure III-12**, only 20% of the growth cones that could be observed on $2\mu\text{m}$ -wide stripes were spread beyond the limits of the adhesive pattern. As the micropatterns that were used for the experiment are characterized by an expected number of 3 neurites (and growth cones) for each neuron, this proportion corresponds to less than 1 spread growth cone per neuron.

Next, we characterized the morphology of the spread growth cones of neurites growing on $2\mu\text{m}$ -wide stripes. Timelapse recordings enabled us to determine the angular extent of several growth cones over different time points. An example of the evolution of a growth cone angular extent over time can be found in **Figure III-13**. Growth cones typically transitioned between spread and collapsed states over time.

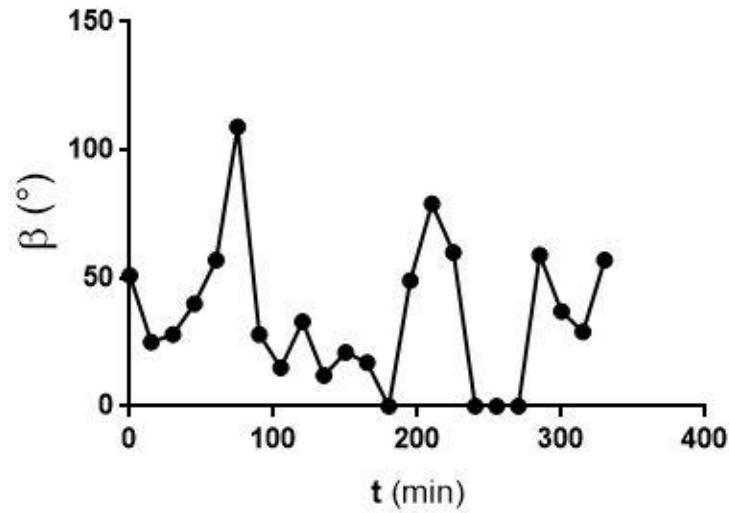


Figure III-13 : Evolution of a growth cone angular extent on 2- μ m wide lines micropatterned substrates. Measurements were realized on 6h long timelapse recordings of an hippocampal E16 LifeAct neuron growth cone at DIV1. Though the growth cone initially assumed a spread shape, its angular range oscillated between 0° and 109° over the course of the recording, oscillating between a spread state and a collapsed state.

In the case of spread morphologies, the distributions of growth cone angular extent can be found in **Figure I-14**.

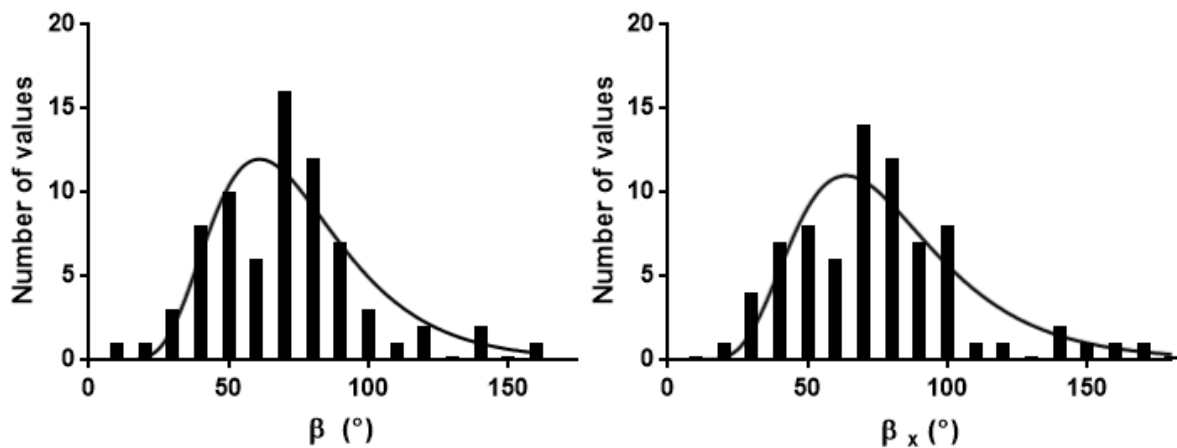


Figure III-14 : Distribution of spread growth cone angular extent on 2- μ m wide lines micropatterned substrates as defined by β and β_x . From timelapse recordings of Lifeact E16 hippocampi neurons at DIV1 (n=16 neurons, n'=19 growth cones, 5 time points). Only the data concerning growth cones in a spread state are represented here. Growth cones in the proximity of intersections were also excluded from the analysis. Black line: lognormal fit

Let us first remark that the angular distributions of β and β_x seem to follow log-normal laws centered on $70^\circ \pm 4^\circ$ (β) and $74^\circ \pm 4^\circ$ (β_x). The distribution was shifted toward higher values for the β_x criterion which takes into account more exploratory structures. Once again, we observed that most of the growth cones (91% for β , 86% for β_x) had an angular extent smaller than 90°

We also examined the asymmetry of the spread growth cones of neurites growing on $2\mu\text{m}$ -wide stripes (see **Figure III-15**). For about 75% of spread growth cones, we measured a value of $(\beta_2 - \beta_1)$ smaller than 20° . This indicated that most growth cones growing on micropatterned substrates assume a shape that is symmetric with respect to the direction of the neurite shaft.

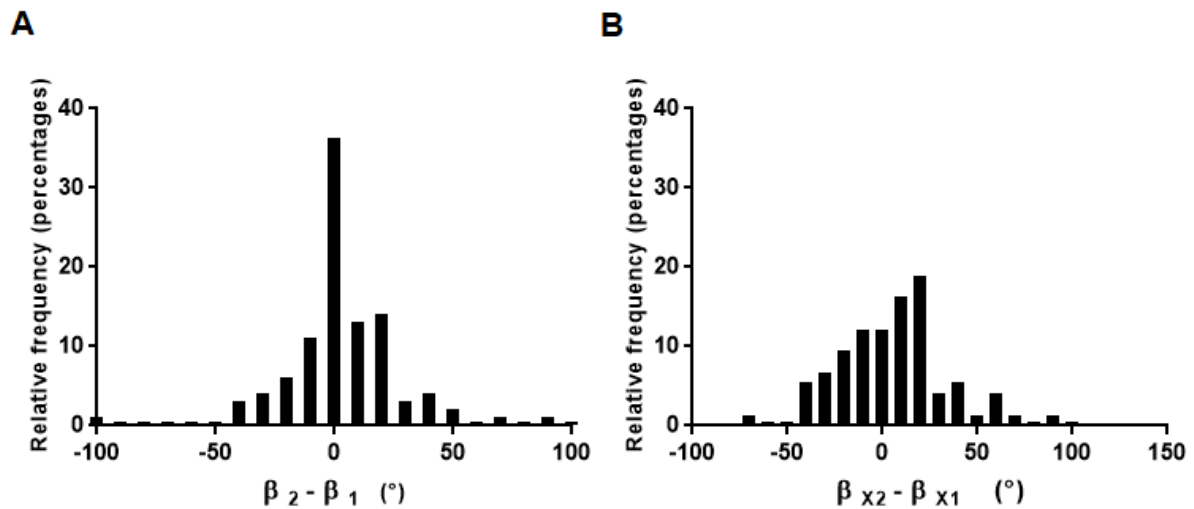


Figure III-15 : Distribution of spread growth cone asymmetry as defined by A. $(\beta_2 - \beta_1)$ and B. $(\beta_{x2} - \beta_{x1})$
 From timelapse recordings of Lifeact E16 hippocampi neurons at DIV1 (n=16 neurons, n'=19 growth cones, 5 time points)
 Only growth cones that assumed a spread shape were considered. Growth cones in the proximity of intersections were excluded from the analysis

III.A.3.d) Comparison of growth cone morphology on uniformly adhesive substrates and micropatterned substrates

Finally, we proceeded to compare measurements of growth cone morphological characteristics on uniform substrates and on micropatterned substrates using averaged values of the corresponding distributions.

		Uniform adhesive pattern	2 μ m wide stripes	Test
Angular extent ($^{\circ}$)	β	48 \pm 13	70 \pm 4	ns
	β_x	64 \pm 12	74 \pm 4	ns
Asymmetry factor ($^{\circ}$)	$ \beta_2 - \beta_1 $	17 \pm 18	20 \pm 19	ns
	$ \beta_{x2} - \beta_{x1} $	19 \pm 15	22 \pm 18	ns

Table 5 : Comparison of angular extent and asymmetry factor of growth cones of neurites growing on micropatterned substrates and on uniform adhesive substrates. (mean \pm SD).For growth cones on micropatterned substrates, the mean angular extent and asymmetric factors were evaluated using only values concerning spread growth cones. Refer to **Figure III-10** to **Figure III-15** for data information. Test values represent the results of the Mann-Whitney test.

Overall, the influence of the 2 μ m-wide lines micropatterns consists in a dramatic reduction of the growth cone angular extent. On the 2 μ m lines, 80% of growth cones were collapsed and had narrow, rectangular shapes matching the shape imposed by the pattern. Nevertheless, among the growth cones whose shape was not restricted by the pattern, the typical angular extent was quite similar to the one observed on uniform substrate (around 70 $^{\circ}$ in average). Statistical tests performed to compare the distributions of angular extent on uniform and micropatterned substrate did not suggest a significant difference. The measurements also suggested similar levels of asymmetry between the growth cones observed on uniform substrates and the spread growth cones observed on micropatterned substrates.

In conclusion, growth cones on micropatterned substrates either assume a narrow morphology matching the pattern shape, or a spread fan-like shape that is similar to the one observed on uniform adhesive substrates. Furthermore, most of the growth cones observed possessed an angular extent between 0 $^{\circ}$ and 90 $^{\circ}$. The average value of spread growth cone angular extent is 70 $^{\circ}$ on fully adhesive substrates as well as on 2- μ m wide lines. Interestingly, this value match the average branching angle measured for hippocampal mice neurons *in vitro* [124],[108] .

III.A.4.Static analysis of branching

To study the branching behavior of neurons, we have analyzed fixed samples of hippocampal neurons developing on micropatterned substrates. Samples were fixed at DIV 2 or DIV 3.

III.A.4.a) *Analysis of branching probability in different geometric configurations*

First, we investigated the influence of substrate geometry on branching probability. For each isolated neuron, at each potential branching point, we observed whether the incident neurite branched or turned. A branching event is defined as a separation of the neurite into two daughter branches who both have a length superior to 30 μ m. In the opposite case, the situation was considered a turning event. Cases where both branches have a length smaller than 30 μ m were excluded from the analysis, as there was no sufficient evidence to qualify them as either branching or turning events.

The branching probability $p_{branching}$ was defined as:

$$p_{branching} = \frac{n_{branching}}{n_{branching} + n_{turning}}$$

where $n_{branching}$ represents the number of branching events and $n_{turning}$ the number of turning events.

The distribution of branching probability $p_{branching}$ as a function of the angle between the daughter branches α was represented in **Figure III-16**.

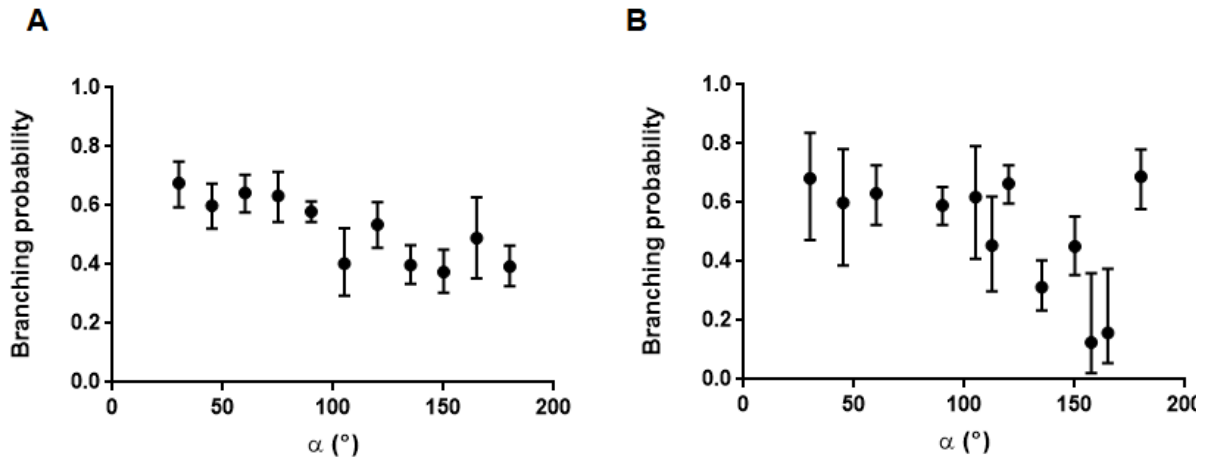


Figure III-16 : Branching probability versus α . **A. Branching probability at DIV2 versus α .** Error bars denote the 95% confidence intervals. The measures were performed on mouse hippocampal neurons growing on samples patterned with mask n°1 and n°3 (zone 1 and 2). 2cultures, 27 coverslides, 2209 branching points. **B. Branching probability at DIV3 versus α .** Error bars denote the 95% confidence intervals. The measures were performed on mouse hippocampal neurons growing on samples patterned with mask n°1 and n°2. 2cultures, 9 coverslides, 916 branching points. See [Appendix](#) for the list of branching configurations corresponding to each value of α represented here.

Furthermore, to simplify the analysis, only bifurcations (branching events giving rise to 2 daughter branches) were considered, and trifurcations were excluded.

The first striking feature that we observed was that, with an average probability of 0.52 ± 0.11 at DIV2 (mean \pm SD, the mean value being computed over all branching angles), and 0.50 ± 0.20 at DIV3, branching and turning seem equally probable taking into account the whole angular range of analysis (see **Figure III-16**). We then noted that branching probability decreases as α increases. As can be seen in **Figure III-17**, at DIV2, a linear regression test on branching probability vs α yields a slope value statistically different to 0, with $p=0.0011$ (**).

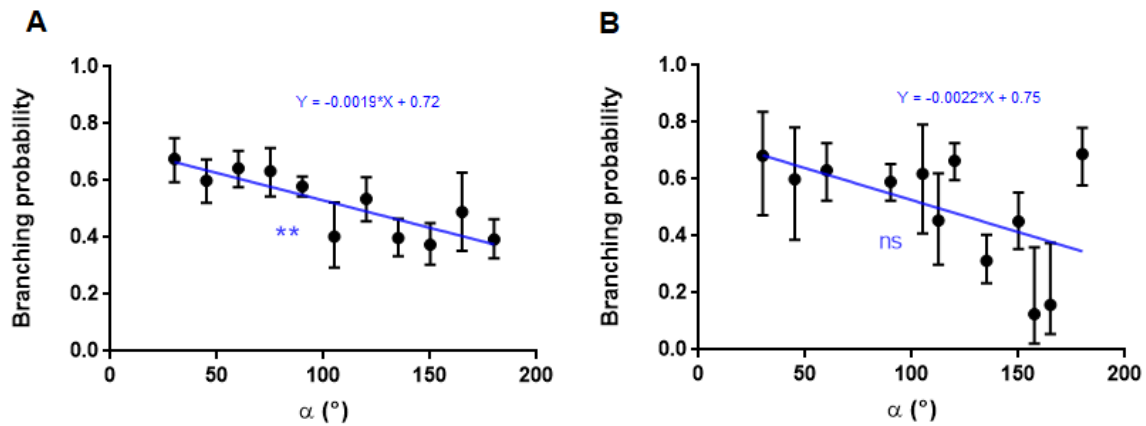


Figure III-17 : Linear fit of branching probability versus α . **A. Branching probability at DIV2 versus α .** Error bars denote the 95% confidence intervals. The measures were performed on mouse hippocampal neurons growing on samples patterned with mask n°1 and n°3 (zone 1 and 2). $y = -0.0019x + 0.72$, $r^2 = 0.71$, $p = 0.0011$ (**, Linear regression test, slope compared to zero). 2cultures, 27 coverslips, 2209 branching points. **B. Branching probability at DIV3 versus α .** Error bars denote the 95% confidence intervals. The measures were performed on mouse hippocampal neurons growing on samples patterned with mask n°1 and n°2. $y = -0.0022x + 0.75$, NS (Linear regression test, slope comparison to zero). 2cultures, 9 coverslips, 916 branching points. See **Appendix** for the list of branching configurations corresponding to each value of α represented here.

Next, we asked ourselves whether the branching probability decrease was continuous or if it was caused by the presence of two separated plateaus, one for $\alpha < 90^{\circ}$ and one for $\alpha > 90^{\circ}$. This second hypothesis would be consistent with our observations of growth cone morphology in III.A.3.b). Indeed we previously noted that most growth cones have angular extent lower than 90° . As can be seen in **Figure III-18**, a linear regression test for branching probability for angles in the $[0^{\circ}, 90^{\circ}]$ range and in the $[90^{\circ}, 180^{\circ}]$ range yield slope values that are not statistically different from 0 and significantly different from each other. This supports the existence of 2 plateaus. Assuming this 2 plateaus hypothesis, for values of α below 90° , with an average of branching probability measured at 0.62 ± 0.04 (0.63 ± 0.04 at DIV3), branching phenomena seems favored compared to turning (see **Figure III-18**). Above 90° , the average branching probability is 0.43 ± 0.06 (mean \pm SD) (0.43 ± 0.22 at DIV3). We then performed a Mann-Whitney test to compare branching probability for angles lower and higher than 90° . We obtained a p value of 0.0043 (***) which support the 2 plateau hypothesis for the branching probability.

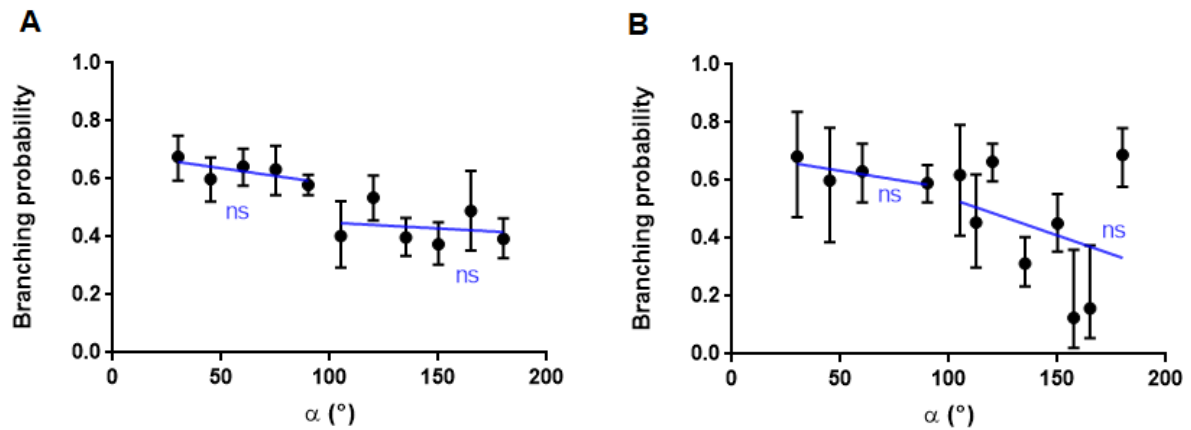


Figure III-18 : 2 plateaus model for branching probability versus α . **A. Branching probability at DIV2 versus α .** Error bars denote the 95% confidence intervals. The measures were performed on mouse hippocampal neurons growing on samples patterned with mask n°1 and n°3 (zone 1 and 2). From left to right: $y=-0.0011x+0.69$, NS (Linear regression test, slope compared to zero); $y=-0.00041x+0.49$, NS (Linear regression test, slope compared to zero). 2cultures, 27 coverslides, 2209 branching points. **B. Branching probability at DIV3 versus α .** Error bars denote the 95% confidence intervals. The measures were performed on hippocampal neurons growing on samples patterned with mask n°1 and n°2. From left to right: $y=-0.0012x+0.69$, NS (Linear regression test, slope comparison to zero); $y=-0.0026x+0.80$, NS (Linear regression test, slope comparison to zero). 2cultures, 9 coverslides, 916 branching points. See **Appendix** for the list of branching configurations corresponding to each value of α represented here.

To further explore the influence of substrate geometry on branching probability, we decided to separate branching configurations in 2 categories: symmetric configurations and asymmetric configurations.

III.A.4.a.1 Comparison between symmetric branching and asymmetric branching

In this work, we defined two categories of geometries for neurites at intersections: symmetric and asymmetric configurations, respectively defined by $\alpha_1 = \alpha_2$ and $\alpha_1 \neq \alpha_2$ (see **Figure III-19**). Furthermore, we defined $(\alpha_2 - \alpha_1)$ as the asymmetry factor. Indeed, the higher $(\alpha_2 - \alpha_1)$ is, the higher the differences of angular choices proposed to the neurite.

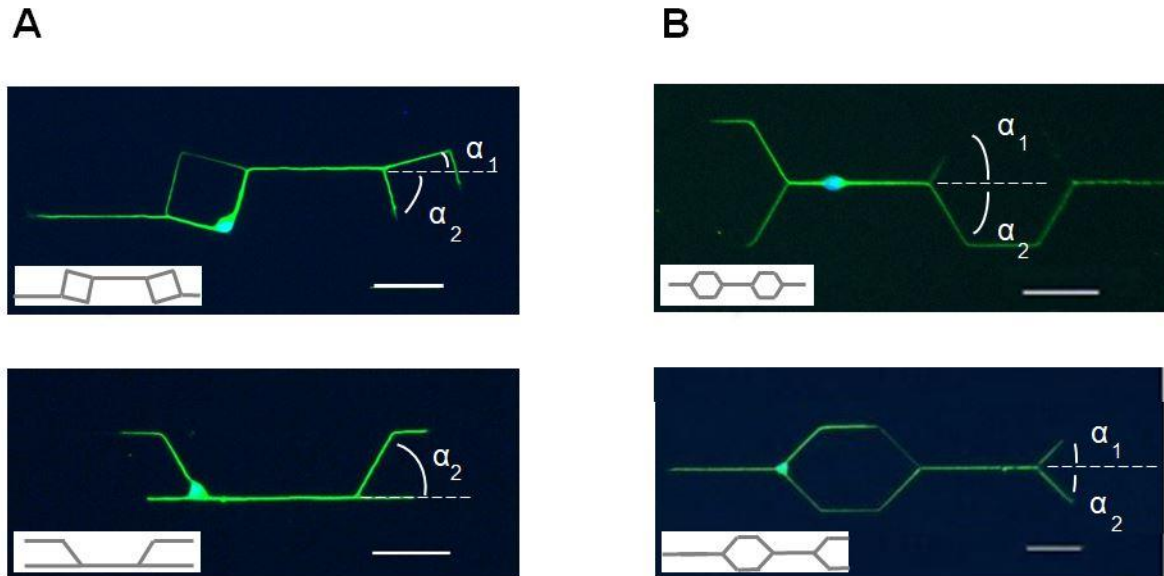


Figure III-19: Asymmetric branching configurations versus symmetric branching configurations. Fluorescence images of mouse E16 hippocampal neurons at DIV3. Green : β -tubulin. The branching point is indicated with a white circular arc. Inset: adhesive patterns. A. Asymmetric branching configurations. Top: $\alpha=90^\circ$, $\alpha_1 = 15^\circ$, $\alpha_2 = 75^\circ$, $\alpha_2 - \alpha_1 = 60^\circ$. Bottom: $\alpha=60^\circ$, $\alpha_1 = 0^\circ$, $\alpha_2=60^\circ$, $\alpha_2 - \alpha_1 = 60^\circ$. B. Symmetric branching configurations: Top: $\alpha=120^\circ$, $\alpha_1 = 60^\circ$, $\alpha_2 = 60^\circ$, $\alpha_2 - \alpha_1=0^\circ$. Bottom: $\alpha=90^\circ$, $\alpha_1 = 45^\circ$, $\alpha_2 = 45^\circ$, $\alpha_2 - \alpha_1=0^\circ$.

I.A.1.a)1.i Symmetric branching

First we decided to explore symmetric branching. The distributions of branching probability in symmetric configurations at DIV2 and DIV3 versus α can be found in **Figure III-20**.

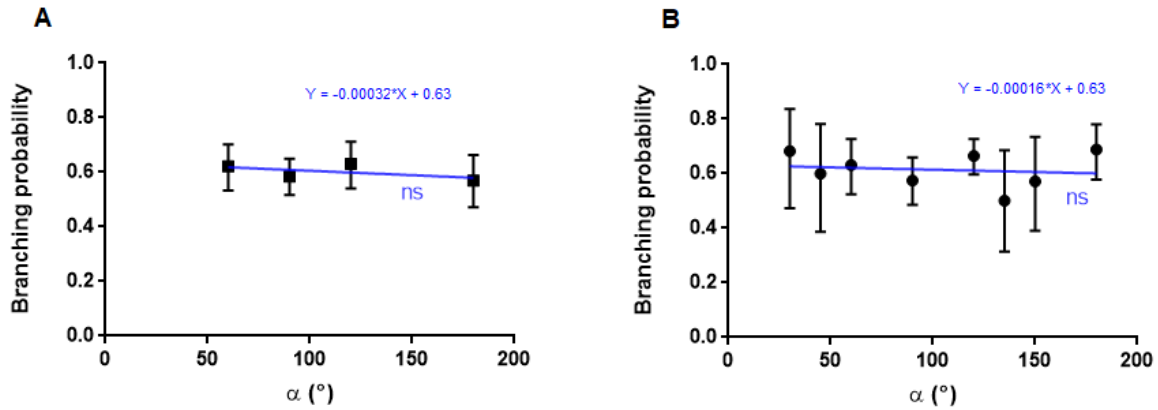


Figure III-20 : Branching probability in symmetric configurations versus α . **A. Branching probability in symmetric configurations at DIV2.** Error bars denote the 95% confidence intervals. The measures were performed on mouse hippocampal neurons growing on samples patterned with mask n°1 and n°3. NS, $r^2=0.32$ (Linear regression test, slope comparison to zero). This suggests that the branching probability is independent of α in symmetric configurations. 2 cultures, 27 coverslides, 552 branching points. **B. Branching probability in symmetric configurations at DIV3.** Error bars denote the 95% confidence intervals. The measures were performed on mouse hippocampal neurons growing on samples patterned with mask n°1 and n°2. NS, $r^2=0.02$ (Linear regression test, slope comparison to zero). This suggests that the branching probability is independent of α in symmetric configurations. 2 cultures, 9 coverslides, 572 branching points. See **Appendix** for the list of branching configurations corresponding to each value of α represented here.

In symmetric configurations of branching, we saw that the probability of branching appeared independent of α . In other words, the branching probability seems independent of the branching angle in cases where the 2 branches form the same angle with the mother branch. Furthermore, as can be seen in **Figure III-20**, with an average branching probability of 0.60 ± 0.03 (mean over all branching angles \pm SD), and 0.61 ± 0.06 at DIV3, symmetric branching is favored compared to turning.

I.A.1.a)1.ii Asymmetric branching :

We then proceeded to examine the influence of asymmetry on branching probability.

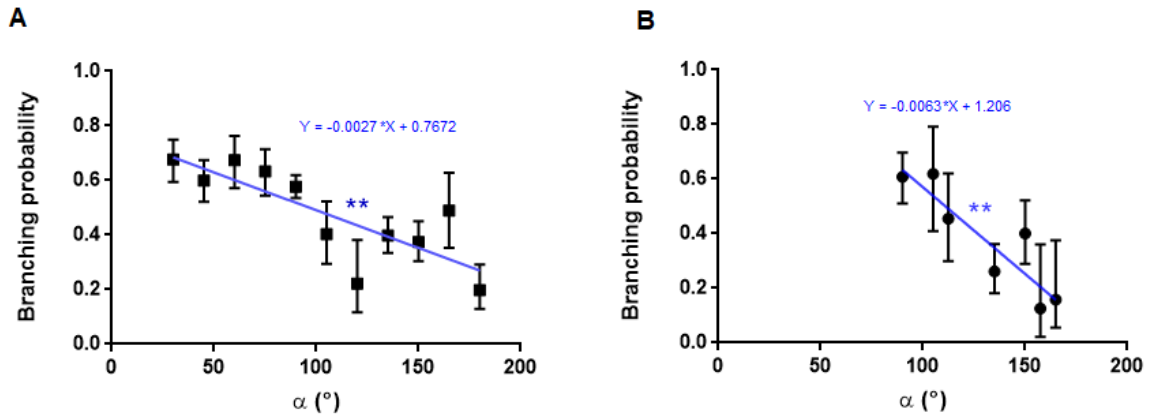


Figure III-21 : Branching probability in asymmetric configurations versus α . **A. Branching probability in asymmetric configurations at DIV2.** Error bars denote the 95% confidence intervals. The measures were performed on mouse hippocampal neurons growing on samples patterned with mask n°1 and n°3. $p=0.0029$, $r^2=0.64$ (**, linear regression test, slope comparison to zero). 2 cultures, 27 coverslips, 1657 branching points. **B. Branching probability in asymmetric configurations at DIV3.** Error bars denote the 95% confidence intervals. The measures were performed on mouse hippocampal neurons growing on samples patterned with mask n°1 and n°2. $p=0.0051$, $r^2=0.82$ (**, linear regression test, slope comparison to zero). 2 cultures, 9 coverslips, 344 branching points. See **Appendix** for the list of branching configurations corresponding to each value of α represented here.

The first striking feature that we observed was that, overall, asymmetric branching seems less favored than symmetric branching. This phenomenon is especially marked for values of α superior to 90° where at DIV2 asymmetric branching probability average at 0.35 ± 0.11 (mean over all branching angles \pm SD) whereas symmetric branching probability is 0.60 ± 0.04 (mean over all branching angles \pm SD). (respectively 0.34 ± 0.19 vs. 0.60 ± 0.08 at DIV3).

As can be seen in **Figure III-21**, the probability of asymmetric branching seems to decrease with the increase of the branching angle. Once again, we asked ourselves whether this is a continuous decrease or if there are 2 plateaus, one before and one after $\alpha = 90^\circ$.

For values of α inferior to 90° , the branching probability value average at DIV2 is 0.63 ± 0.04 (mean \pm SD), which means that branching phenomena are privileged compared to turning. On the contrary, for values of α superior to 90° , the average branching probability at DIV2 is 0.35 ± 0.11 (mean over all branching angles \pm SD). So for α superior to 90° , asymmetric turning is clearly preferred to asymmetric branching.

Next, we compared the branching probability angular distribution between DIV2 and DIV3 for angles $\geq 90^\circ$ (see **Figure III-22**). Linear regressions tests yielded a higher slope at DIV3 compared to DIV2 (-0.015 at DIV2 vs. -0.0063 at DIV3). This indicates that at DIV3,

there is a sharper decrease of branching probability as a function of branching angle α . Considering the expected increase in the number of polarized neurons at DIV3 compared to DIV2, the source of the difference in the angular dependence of the branching probability between the two conditions might be the presence of a higher proportion of axons in the population of neurites studied at DIV3.

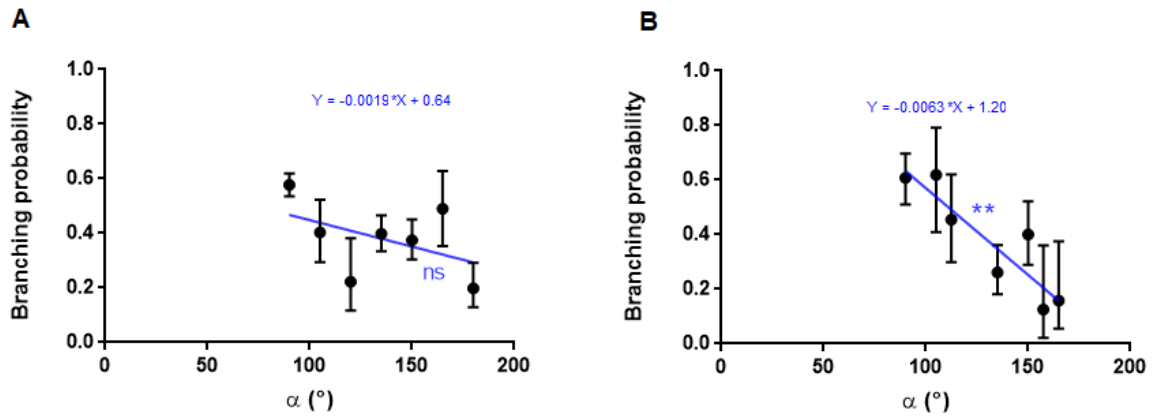


Figure III-22 : Comparison of branching probability in asymmetric configurations versus α at DIV2 and DIV3. A. Branching probability in asymmetric configurations at DIV2 for $\alpha \geq 90^\circ$. Error bars denote the 95% confidence intervals. The measures were performed on mouse hippocampal neurons growing on samples patterned with mask n°1 and n°3. $p = 0.0029$, $r^2 = 0.64$ (**, linear regression test, slope comparison to zero). 2 cultures, 27 coverslides, 1657 branching points. **B. Branching probability in asymmetric configurations at DIV3.** Error bars denote the 95% confidence intervals. The measures were performed on mouse hippocampal neurons growing on samples patterned with mask n°1 and n°2. $p = 0.0051$, $r^2 = 0.82$ (**, linear regression test, slope comparison to zero). 2 cultures, 9 coverslides, 344 branching points. See **Appendix** for the list of branching configurations corresponding to each value of α represented here.

In light of these results, i.e. a clear difference of branching properties in symmetrical compared to asymmetrical configurations, we asked ourselves a new question: does the degree of asymmetry of a geometric configuration negatively impact the branching probability? To test that hypothesis, we selected specific sets of geometric configurations and evaluated the branching probability inside these sets.

First, keeping the angle between daughter branches α constant equal to 90° , we looked at how the branching probability varied as a function of the asymmetry of the configuration, measured by $(\alpha_2 - \alpha_1)$. Zone n°1 of mask n°3 was designed with that aim.

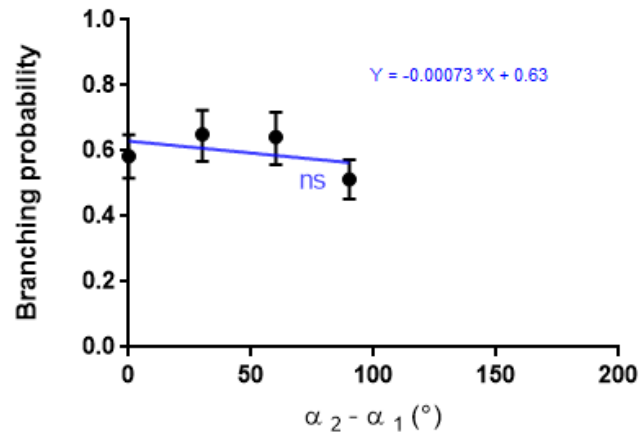


Figure III-23 : Branching probability in asymmetric configurations with $\alpha=90^\circ$ versus $(\alpha_2-\alpha_1)$. Error bars denote the 95% confidence intervals. The measures were performed on mouse hippocampal neurons growing on samples patterned with mask n°3, zone 1. Samples were fixed at DIV2. NS, $r^2=0.22$ (Linear regression test, slope comparison to zero). 2 cultures, 27 coverslides, 746 branching points. See **Appendix** for the list of branching configurations corresponding to each value of α represented here.

In this first case, we did not observe any conclusive evidence of the influence of asymmetry (represented by parameter $(\alpha_2-\alpha_1)$) on the branching probability as can be seen in **Figure III-23**. This may not be surprising when considering that the branching probability for $\alpha=90^\circ$ in symmetric configurations, evaluated at 0.58, is not significantly different from the branching probability for $\alpha=90^\circ$ in asymmetric configurations, also measured at 0.58. Tests with the same type of geometries and higher or lower values of α might yield more significant results

Then, for branching geometries where one of the daughter branch continues in the same direction as the mother branch (ie. $\alpha_1 = 0$) we examined how the branching probability evolved as function of asymmetry factor $(\alpha_2-\alpha_1)$. Of note, in this case $\alpha = (\alpha_2-\alpha_1)$. Zone n°2 of mask n°3 was designed in that aim.

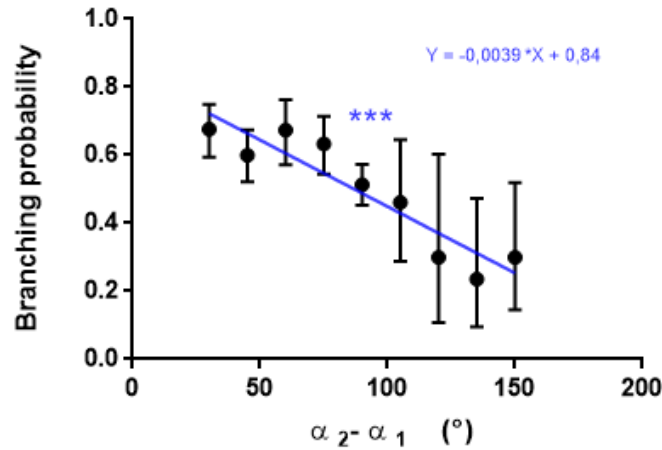


Figure III-24 : Branching probability in asymmetric configurations with $\alpha_1 = 0$ versus $\alpha = (\alpha_2 - \alpha_1)$. Error bars denote the 95% confidence intervals. The measures were performed on mouse hippocampal neurons growing on samples patterned with mask n°3, zone 1 and zone 2. Samples were fixed at DIV2.. $p=0.0003$ $r^2=0.86$ (***, Linear regression test, slope comparison to zero). 2 cultures, 27 coverslides, 836 branching points. See **Appendix V.B.** for the list of branching configurations corresponding to each value of α represented here.

In this case, we could remark a strong decrease of branching probability as $(\alpha_2 - \alpha_1)$ increases which tends to indicate that when a choice between forming a new branch at a non-zero angle and going straight without branching is proposed, the last solution is preferred.. We could also observe an important decrease of branching probability for values of α superior to 90° .

I.A.1.a)1.iii Conclusion

In conclusion, when no angular choice is proposed at an intersection (symmetric cases), the branching probability seems angle independent in the range $[30^\circ, 180^\circ]$. On the contrary, when an angular choice is proposed (asymmetric configurations), we could see a clear decrease of branching probability for values of α superior to 90° . Also, we observed that the higher the difference between the 2 angles proposed, the less likely it is that branching will occur.

III.A.4.a.2 Comparison between axon branching and undifferentiated neurite branching

In order to refine our analysis of neuronal branching and to better understand the differences observed between DIV2 and DIV3, we chose to separate populations of neurites between axons and undifferentiated neurites. Samples were fixed at DIV2 and stained with a Tau-1 antibody. The Tau protein, and more specifically the gradient of Tau phosphorylation, is often used as an early axonal marker. The monoclonal Tau-1 antibody, which recognizes dephosphorylated serine sites [16], is commonly used to identify the axon.

A Tau-1 gradient-positive neurite was considered an axon (see **Figure III-25**). A Tau-1 gradient-negative neurite was considered a future dendrite if it belonged to a neuron possessing a Tau-1 gradient-positive neurite, or an undifferentiated neurite if it belonged to a neuron having no Tau-1 gradient-positive neurite.

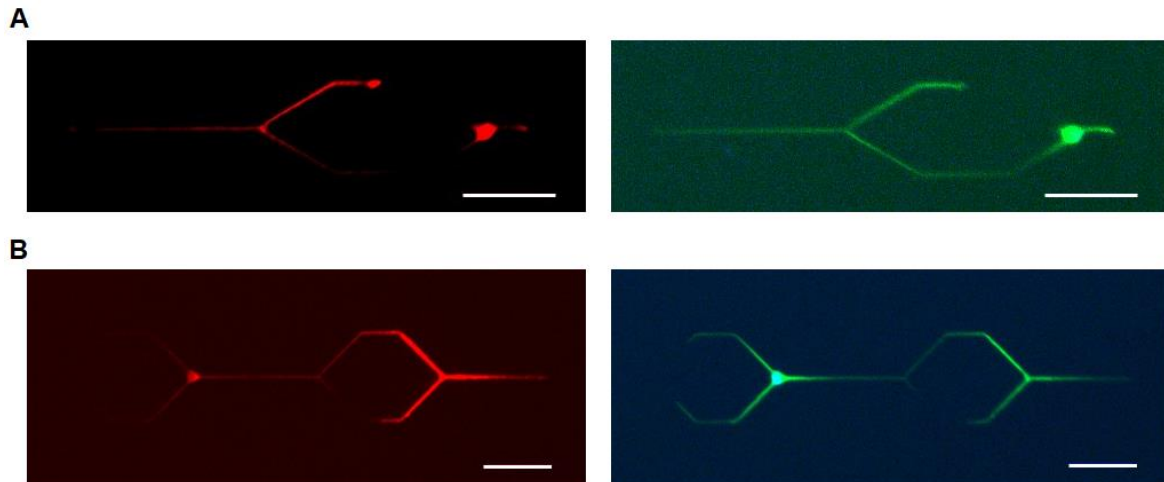


Figure III-25 : Tau-1 gradient in branching axons. Fluorescence image of mice E16 hippocampal neurons growing on micropatterned substrates. Samples were fixed at DIV2 and stained with β -tubulin antibody (green), Tau-1 antibody (red) and Hoechst (blue). The neurite presenting a gradient of Tau-1 can be identified as the axon. Let us note that in A. only one of the axonal branches displays a gradient of Tau-1, whereas in B., both axonal branches present continued gradient of Tau-1. Scale bar: 50 μ m.

While assessing the fluorescence images of samples stained with Tau-1 antibody we observed that after an axon branched, two situations were possible. Either the gradient of Tau-1 was continued in both daughter branches (as in **Figure III-25 B.**) or only one of the daughter branches retained a gradient of Tau-1 (as seen in **Figure III-25 A.**). We have asked ourselves whether this observation indicates that an axon branch can have the molecular characteristics of a dendrite. Further investigation would be needed to quantify this phenomenon and answer this question.

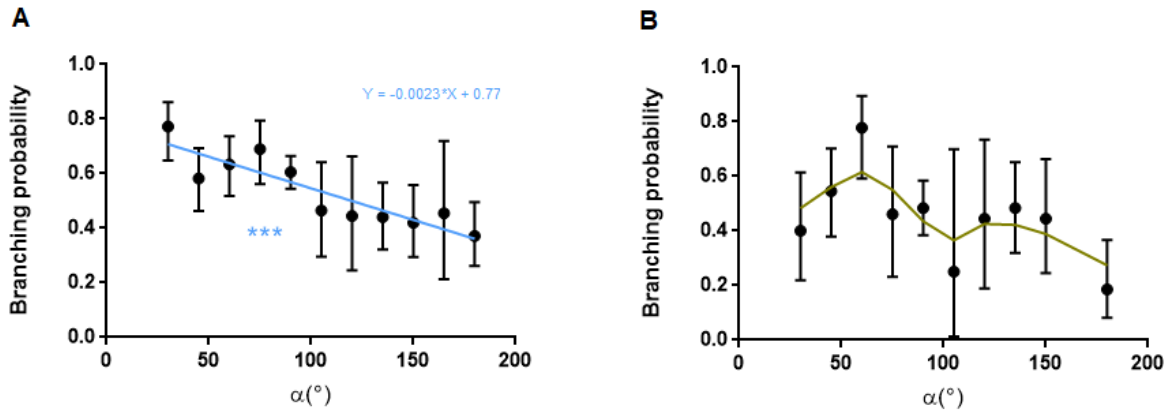


Figure III-26 : Branching probability for axons and undifferentiated neurites versus α . **A. Branching probability for axons versus α .** Error bars denote the 95% confidence intervals. The measures were performed on mouse hippocampal neurons growing on samples patterned with mask n°1 and n°3. Samples were fixed at DIV2. Tau-1 gradient-positive neurites were considered as axons. $p=0.0002$, $r^2=0.8$ (Linear regression test, slope comparison to zero). 1 culture, 12 coverslides, 732 branching points **B. Branching probability for undifferentiated neurites versus α .** Error bars denote the 95% confidence intervals. The measures were performed on mouse hippocampi neurons growing on samples patterned with mask n°1 and n°3. Samples were fixed at DIV2. Green line: guide for the eyes. 1 culture, 12 coverslides, 278 branching points. See **Appendix** for the list of branching configurations corresponding to each value of α represented here.

We then obtained the angular distributions of branching probability for both axons and undifferentiated neurites (see **Figure III-26**). For axons, we observed once again a strong decrease of the branching probability as the angle α increases. With a branching probability of 0.66 ± 0.08 (mean \pm SD), axonal branching seems favored for values of α inferior to 90° , whereas turning seems to be more probable for values of α superior to 90° . A linear regression was performed on the axonal branching probability measurements and yielded a value of $r^2 = 0.8$ which shows a strong linear tendency.

It is harder to draw conclusions from the branching probability data for undifferentiated neurites. While undifferentiated neurite branching probability follows the same decreasing trend for values of $\alpha > 90^\circ$, it seems to increase for values of $\alpha < 60^\circ$. Furthermore, the undifferentiated neurite branching probability appears to possess a maximum at around 70° . Further measurements would be needed to validate this observation.

I.A.1.a)1.i Symmetric branching

First, an analysis of the branching behavior of axons and undifferentiated neurites in symmetric configurations was performed.

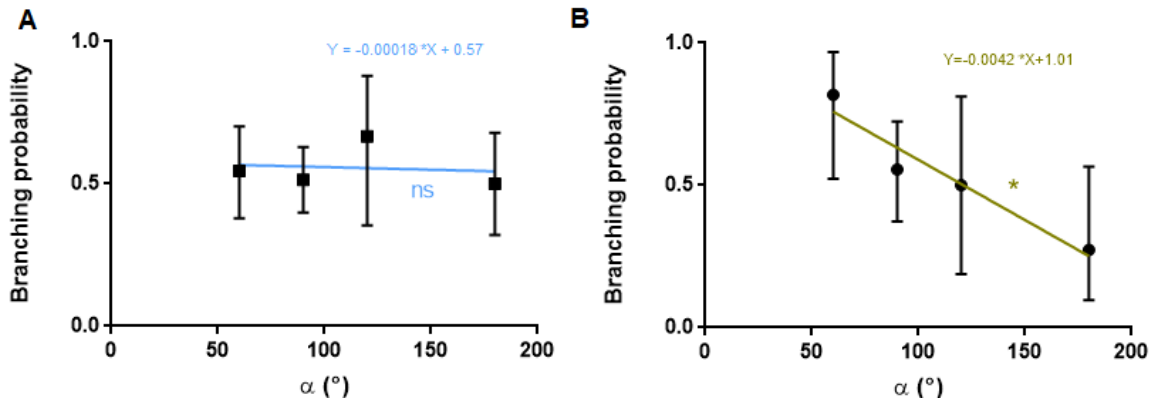


Figure III-27 : Branching probability in symmetric configurations versus α . **A. Branching probability for axons in symmetric configurations.** Error bars denote the 95% confidence intervals. The measures were performed on mouse hippocampal neurons growing on samples patterned with mask n°1 and n°3. Tau-1 gradient-positive neurites were considered as axons. Samples were fixed at DIV2. NS, $r^2=0.02$ (Linear regression test, slope comparison to zero). 1 culture, 12 coverslides, 136 branching points. **B. Branching probability for undifferentiated neurites in symmetric configurations.** Error bars denote the 95% confidence intervals. The measures were performed on mouse hippocampal neurons growing on samples patterned with mask n°1 and n°3. Samples were fixed at DIV2. $p=0.032$, $r^2=0.93$ (*, Linear regression test, slope comparison to zero). 1 culture, 12 coverslides, 55 branching points. See **Appendix** for the list of branching configurations corresponding to each value of α represented here.

In the case of axons, let us remark that the probability of symmetric branching appeared independent of α (angle between the daughter branches). On the contrary, in the case of undifferentiated neurites, there seems to be a decrease of the probability of growth cone symmetric scission as α increases. However this phenomenon was only measured on samples belonging to one culture and should be confirmed with additional measurements. It would be interesting to measure values of symmetric branching for undifferentiated neurites with values of $\alpha < 60^\circ$ to see if we obtain the same kind of curve as the asymmetric angular distribution of branching probability in **Figure III-26 B**. As it is, it might suggest that, contrary to axons, in symmetric configurations, undifferentiated neurites would prefer turning rather than branching when increasing the branching angle.

I.A.1.a)1.ii Asymmetric branching

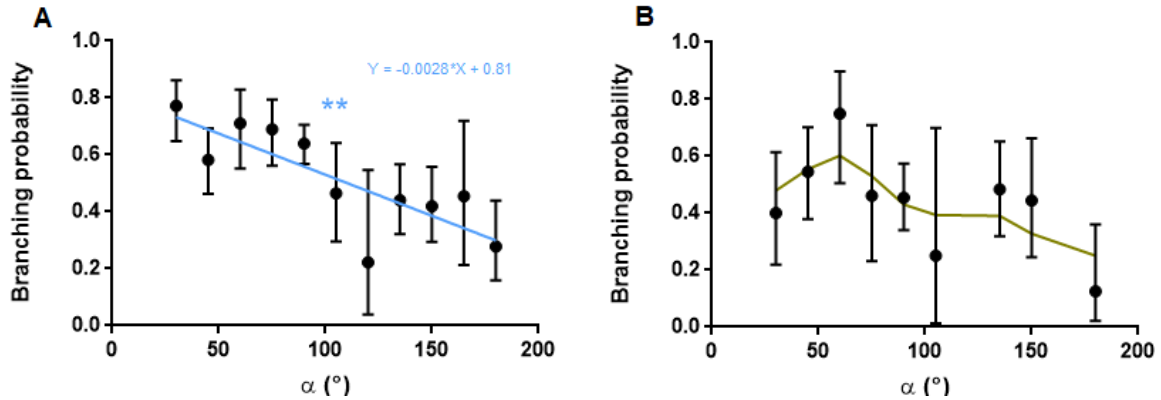


Figure III-28 : Branching probability in asymmetric configurations versus α . **A. Branching probability for axons in asymmetric configurations.** Error bars denote the 95% confidence intervals. The measures were performed on mouse hippocampal neurons growing on samples patterned with mask n°1 and n°3. Tau-1 gradient-positive neurites were considered as axons. Samples were fixed at DIV2. $y = -0.0028x + 0.4495$, $p = 0.0027$, $r^2 = 0.65$ (**, Linear regression test, slope comparison to zero). 1 culture, 12 coverslides, 596 branching points. **B. Branching probability for undifferentiated neurites in asymmetric configurations.** Error bars denote the 95% confidence intervals. The measures were performed on mouse hippocampi neurons growing on samples patterned with mask n°1 and n°3. Samples were fixed at DIV2. Green line: guide for the eyes. 1 culture, 12 coverslides, 223 branching points. See **Appendix** for the list of branching configurations corresponding to each value of α represented here.

The branching probability of axonal growth cone asymmetric scission seems to decrease when the scission angle α increases. For $\alpha < 90^\circ$, axonal asymmetric branching is favored and for $\alpha > 90^\circ$, it is turning that is the privileged solution chosen by axons. As seen previously, the behavior of undifferentiated neurites branching appears very different with a branching probability peaking at values of α around 70° .

Then, for branching geometries where one of the daughter branch continues in the same direction as the mother branch (ie. $\alpha_1 = 0$) we examined how the branching probability of axons and undifferentiated neurites evolved as function of asymmetry factor ($\alpha_2 - \alpha_1$). Of note, in this case $\alpha = (\alpha_2 - \alpha_1)$.

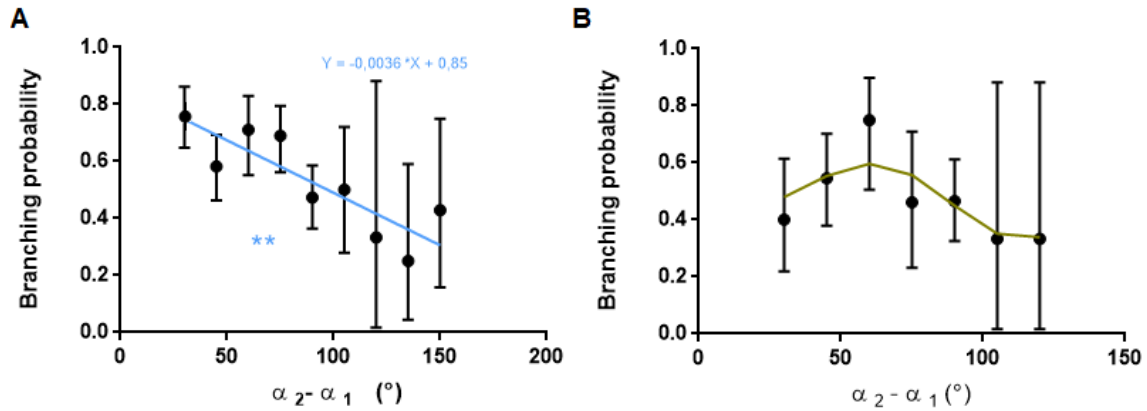


Figure III-29: Branching probability in asymmetric configurations with $\alpha_1 = 0$ versus $(\alpha_2 - \alpha_1)$. **A. Branching probability for axons in asymmetric configurations with $\alpha_1 = 0$.** Error bars denote the 95% confidence intervals. The measures were performed on mouse hippocampi neurons growing on samples patterned with mask n°3, zone 1 and zone 2. Samples were fixed at DIV2. Tau-1 gradient-positive neurites were considered as axons. $p=0.0034$, $r^2=0.73$ (**, Linear regression test, slope comparison to zero). 1 culture, 12 coverslides, 328 branching points. **B. Branching probability for undifferentiated neurites in asymmetric configurations with $\alpha_1 = 0$.** Error bars denote the 95% confidence intervals. The measures were performed on mouse hippocampi neurons growing on samples patterned with mask n°3, zone 1 and zone 2. Samples were fixed at DIV2. Green line: guide for the eyes. 1 culture, 12 coverslides, 183 branching points. See **Appendix** for the list of branching configurations corresponding to each value of α represented here.

Let us remark that there is a decrease of axonal branching probability as $(\alpha_2 - \alpha_1)$ increases. In other words, when there is an angular choice proposed, the greater the difference between the two proposed angles, the most likely it is that an axon will favor turning over branching. For undifferentiated neurites the angular branching probability follows the same trend as in **Figure III-28 B**, ie. an increase for values of $\alpha = (\alpha_2 - \alpha_1) < 70^\circ$ and a decrease for greater values.

III.A.4.a.3 Conclusion

We have shown that when no angular choice is proposed (symmetric configurations), axonal branching is equally probable for values of branching angle in the range $[30^\circ, 180]$. On the contrary, when an angular choice is proposed (asymmetric configurations), axonal branching becomes less likely as the value of the branching angle increases. Whether this decrease is a continuous phenomenon or caused by the existence of two distinct plateaus for angle values in $[0^\circ, 90^\circ]$ and in $[90^\circ, 180^\circ]$ remains to be seen. For values of branching angles $< 90^\circ$, asymmetric axonal branching seems favored over turning. On the contrary, for values of angles $> 90^\circ$, in cases where an angular choice is proposed, an axon is more likely to turn than to branch. This is consistent with the angular distribution of growth cone filopodia observed in **III.A.3**. Indeed, we saw that growth cone filopodia are mostly present in a 90° wide area centered around the axis of the neurite shaft. Outside of this area, there is less exploration by filopodia (which can act as precursors to branching) and thus a lesser probability of branch

formation.

We have also seen that for undifferentiated neurites, the branching probability first increases until a branching angle of 70° and decreases for superior values of α . In other words, it seems that the branching angular probability of undifferentiated neurites is peaked at around 70° , a value which interestingly corresponds to the most probable angular extent of growth cone on $2\mu\text{m}$ wide stripes (see **III.A.3**). This results also indicates that, for angles $< 60^\circ$, turning will be favored for non-axonal branches when axons facing the same situation will prefer to branch. This might indicate that axons are less prone to turn compared to undifferentiated neurites.

Table 6 recapitulates the different results concerning branching probability.

		α	Axons	Undifferentiated neurites
Average branching probability (%)	All configurations	$\leq 90^\circ$	0.66 ± 0.08	0.53 ± 0.14
		$> 90^\circ$	0.43 ± 0.03	0.36 ± 0.13
	Symmetric configurations	$\leq 90^\circ$	0.53 ± 0.02	0.69 ± 0.19
		$> 90^\circ$	0.58 ± 0.12	0.39 ± 0.16
	Asymmetric configurations	$\leq 90^\circ$	0.68 ± 0.07	0.52 ± 0.14
		$> 90^\circ$	0.38 ± 0.10	0.38 ± 0.19

Table 6 : Comparison of average branching probability at DIV2 in symmetric configurations and asymmetric configurations. (mean over all branching angles \pm SD). Refer to **Figure III-16** to **Figure III-29** for data information.

III.A.4.b) Analysis of branches length

In the first part of our analysis, we raised the following questions: is branching a phenomenon that evolves continuously as a function of the branching angle? Or are there instead two branching regimes, one for values of branching angles below 90° and one for values of branching angles above 90° ? Another important question might be, in case there is an angular choice, which direction is favored by the neurite?

To answer these questions, we have decided to perform an analysis of the lengths of neuritic branches. The direction closest to the neurite initial direction was characterized by angle α_1 and length L_1 , and the furthest respectively by α_2 and length L_2 (see **Figure III-30**).

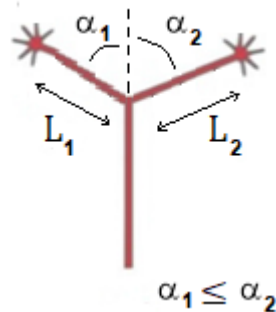


Figure III-30 : Definition of the daughter branches length L_1 and L_2 . The direction closest to the mother branch is characterized by angle α_1 , and a daughter branch of length L_1 and the furthest respectively by α_2 and a daughter branch of length L_2 .

First, in cases of turning, in situations where angular choice is proposed (such as in asymmetric configurations), we looked at the direction chosen by the neurite. Results can be found in **Figure III-31 B**. We observed that for both axons and undifferentiated neurites, in more than 80% of cases, the direction closest to the neurite initial direction (characterized by angle α_1) was chosen.

Then, in cases of branching, we measured the lengths of daughter branches L_1 and L_2 . For both axons and undifferentiated neurites, we found that L_1 was the longest branch in more than 60% of cases (see **Figure III-31 A**). In other words, we found once again a marked preference for the direction closest to the initial neurite direction, though less strong than the one observed for turning cases.

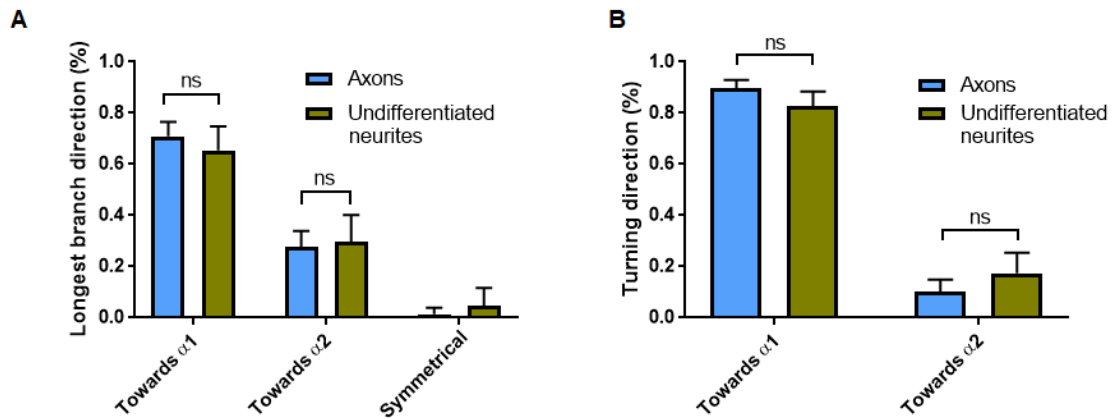


Figure III-31 : Favored directions of neuritic growth in case of asymmetric branching. A. Direction of the longest daughter branch at branching points. Samples were fixed at DIV2. The measures were performed on mouse hippocampal neurons growing on samples patterned with mask n°1 and n°3. Mean values, error bars denote the 95% confidence intervals. In blue, direction of the longest daughter branch at axonal branching points. (1 culture, n= 224 branching points, 12 coverslides). In green, direction of the longest daughter branch at branching points of undifferentiated neurites. NS (χ^2 test). NS (χ^2 test). (1 culture, n= 84 branching points, 12 coverslides). **B. Turning direction at intersections.** Samples were fixed at DIV2. The measures were performed on mouse hippocampal neurons growing on samples patterned with mask n°1 and n°3. Mean values error bars denote the 95% confidence intervals. In blue, turning direction of axons at intersections. (1 culture, n=234 branching points, 12 coverslides). In green, turning directions of undifferentiated neurites at intersections. NS (Fisher's test). NS (Fisher's test). (1 culture, n= 115 branching points, 12 coverslides). For the data represented in this figure, the branching/turning ratio was 49%/51% for axons and 42%/58% for undifferentiated neurites. See **Appendix** for the list of branching configurations corresponding to each value of α represented here.

Overall these results indicate a preference for the direction closest to the mother branch direction.

Next, we looked at the distribution of the ratio $\frac{L_2}{L_1}$ versus branching angle α , in asymmetric configurations. We separated datas coming from axons and undifferentiated neurites in order to account for the difference in neurite growth between polarized and unpolarized neurons.

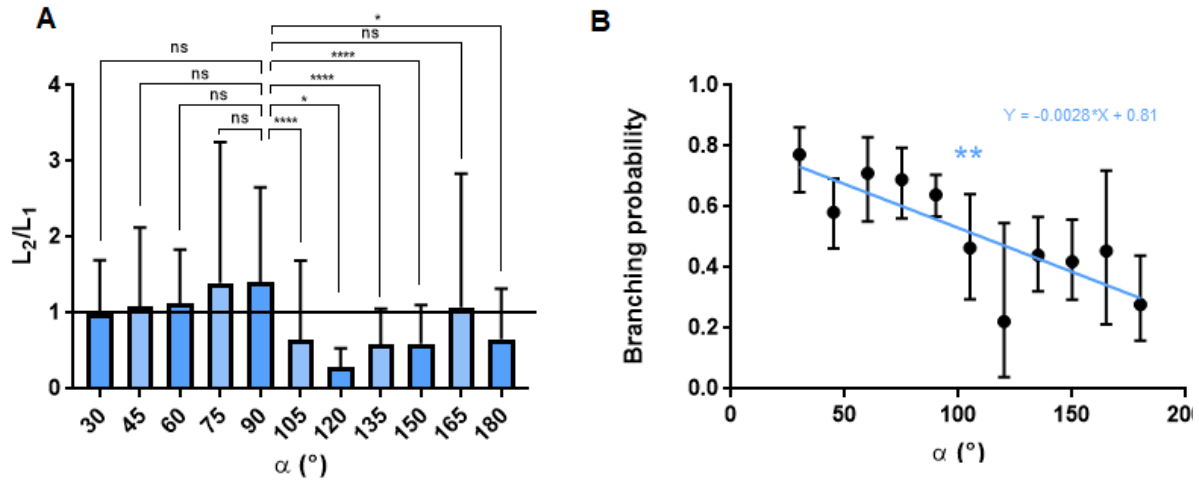


Figure III-32 : Influence of α on axonal branching behavior in asymmetric configurations. A. Ratio between the lengths of the daughter branches for axons versus α in asymmetric configurations. Samples were fixed at DIV2. The measures were performed on mouse hippocampal neurons growing on samples patterned with mask n°1 and n°3. Mean \pm SD. Black line: $\frac{L_2}{L_1} = 1$. (1 culture, n=256 branching points, 12 coverslides). The probability values represented correspond to results of Mann-Whitney tests. **B. Branching probability versus α in asymmetric configurations.** Samples were fixed at DIV2. The measures were performed on mouse hippocampal neurons growing on samples patterned with mask n°1 and n°3. Error bars denote the 95% confidence intervals. Blue line: $y = -0.0015x + 0.74$, NS (Linear regression test, slope comparison to zero); $y = -0.0004881x + 0.4495$, $p = 0.0027$, $r^2 = 0.65$ (**, Linear regression test, slope comparison to zero). 1 culture, 12 coverslides, 596 branching points. See **Appendix** for the list of branching configurations corresponding to each value of α represented here.

We found that, for axons in asymmetric configurations, the angular distribution of $\frac{L_2}{L_1}$ appears to follow 2 different regimes for values of branching angles α below and above 90° (see **Figure III-32**). This observation is consistent with the branching probability measured in these conditions. For values of α below 90° , $\frac{L_2}{L_1}$ averages at values around 1 which means that for in these conditions both daughter branches tend to have the same length. For $\alpha > 90^\circ$, we have $\frac{L_2}{L_1} = 0.63 \pm 0.7$ (mean \pm SD) instead which indicates a much longer daughter branch along the direction defined by the smallest angle relative to the direction of the parent branch.

Next, for branching geometries where one of the daughter branch continues in the same direction as the mother branch (ie. $\alpha_1 = 0$), we examined how the ratio of axonal daughter branches length $\frac{L_2}{L_1}$ evolved as function of branching angle α . In this situation, the decrease of $\frac{L_2}{L_1}$ for values of branching angle α above 90° is also very marked.

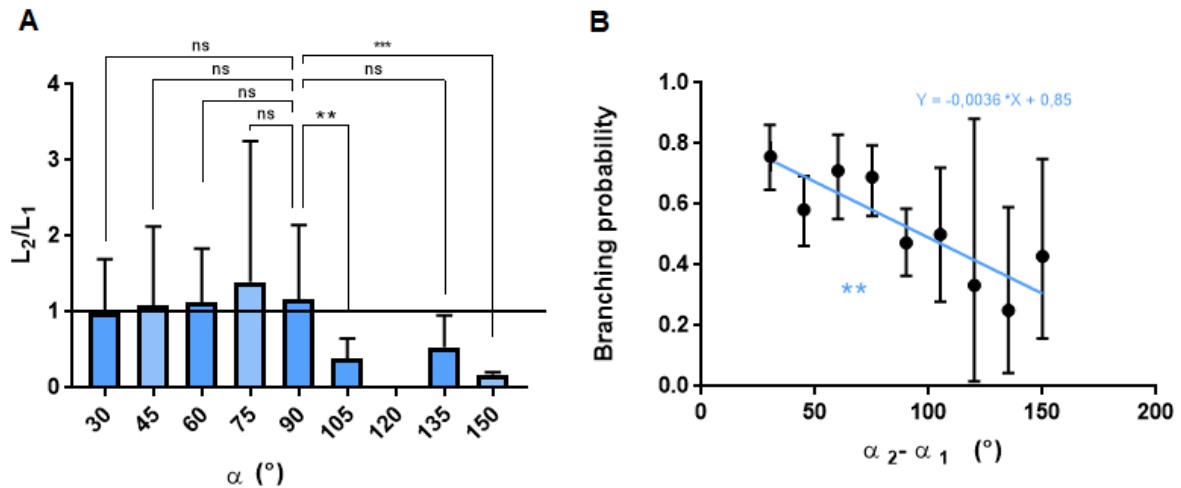


Figure III-33 : Influence of asymmetry on neuronal branching behavior in configurations with $\alpha_1 = 0$. **A. Ratio between the lengths of the daughter branches for axons versus $(\alpha_2 - \alpha_1)$ in asymmetric configurations with $\alpha_1 = 0$.** Samples were fixed at DIV2. Mean \pm SD. The measures were performed on mouse hippocampal neurons growing on samples patterned with mask n°3, zone 1 and zone2. Black line: $\frac{L_2}{L_1} = 1$. (1 culture, n=132 branching points, 12 coverslides). The probability values represented correspond to results of Mann-Whitney tests. **B. Branching probability versus $(\alpha_2 - \alpha_1)$ in asymmetric configurations with $\alpha_1 = 0$.** Samples were fixed at DIV2. The measures were performed on mouse hippocampal neurons growing on samples patterned with mask n°3, zone 1 and zone 2. Error bars denote the 95% confidence intervals. (1 culture, n=328 branching points, 12 coverslides). See **Appendix V.B** for the list of branching configurations corresponding to each value of α represented here.

Finally, we looked at the influence of asymmetry on the ratio of axonal daughter branches length $\frac{L_2}{L_1}$. We observed that for values of $(\alpha_2 - \alpha_1)$ superior to 90° , the longest branch is systematically L_1 , ie. the daughter branch with the angle closest to the mother branch direction (see **Figure III-34**).

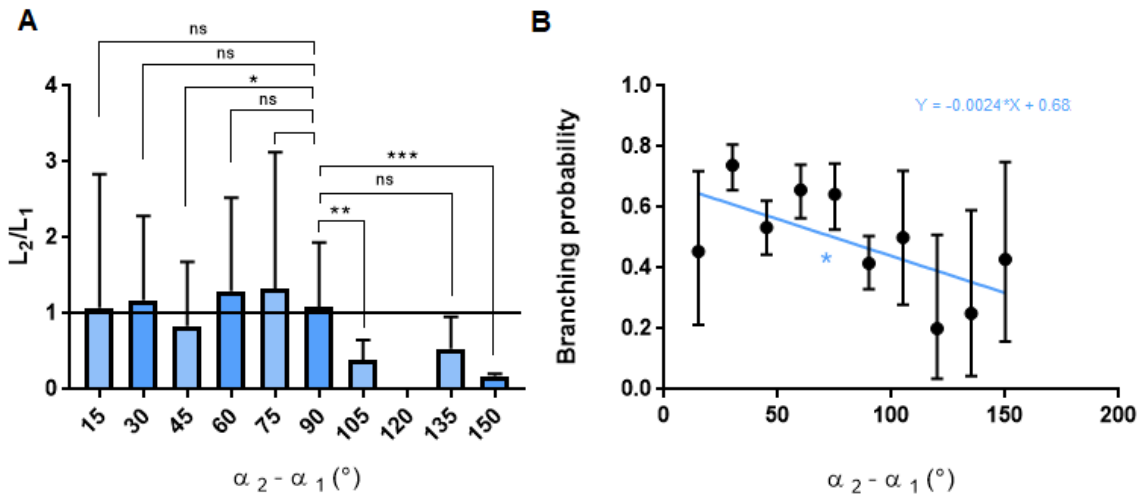


Figure III-34 : Influence of asymmetry on neuronal branching behavior. A. Ratio between the lengths of the daughter branches for axons versus ($\alpha_2 - \alpha_1$) in asymmetric configurations. Samples were fixed at DIV2. The measures were performed on mouse hippocampal neurons growing on samples patterned with mask n°1 and n°3. Mean \pm SD. Black line: $\frac{L_2}{L_1} = 1$. The probability values represented correspond to results of Mann-Whitney tests. (1 culture, n=256 branching points, 12 coverslides). **B. Branching probability versus ($\alpha_2 - \alpha_1$) in asymmetric configurations** Samples were fixed at DIV2. The measures were performed on mouse hippocampal neurons growing on samples patterned with mask n°1 and n°3. Error bars denote the 95% confidence intervals. (1 culture, n=596 branching points, 12 coverslides). See **Appendix** for the list of branching configurations corresponding to each value of α represented here.

III.A.4.c) Conclusion

In conclusion, measurements of axonal daughter branches length support the hypothesis of two different behaviors for branching angle values below and above 90° . We saw that in asymmetric configurations, for values of α below 90° , daughter branches are of similar length, whereas for $\alpha > 90^\circ$ the growth of the branch closest to the direction of the mother neurite appears to be favored. This is consistent with measurements of axonal branching probability, for which we observed an intrinsic preference for neurons to form branches at an angle less than 90° in asymmetric configurations. Our findings concerning axonal branches length are also consistent with the angular distribution of growth cone filopodia on micropatterns seen in **III.A.3.b**). Indeed, we saw that growth cone filopodia are mostly present in a 90° wide area centered around the axis of the neurite shaft. Outside of this area, there is less exploration by filopodia, the main precursors to branching, and thus a lesser probability of branch formation. We have also observed that undifferentiated neurites appear most likely to branch for values of branching angle around 70° . Interestingly, it has been reported that the average branching angle on fully adhesive substrate for hippocampi neurons cultured *in vitro* is around 70° , which might

explain our data as this value was measured on populations consisting mostly of undifferentiated neurites and dendrites. [108], [124], [153].

III.A.5. Dynamic analysis of neuronal branching on static patterns

The first steps of our investigation of neuronal branching on micropatterned have been realized mostly on data coming from measurements of fixed samples. These data did not allow for a characterization of the kinetics of branching in our set-up. For this reason, we decided to complete this static analysis of branching behavior by a dynamic analysis. Time-lapse recording of neurons developing on micropatterned substrates were realized. We have chosen to focus in particular on one of the key parameters of branching kinetics: the growth cone pausing time at branching points.

III.A.5.a) *Neurite behavior at intersections*

Time-lapse recordings of hippocampal neurons developing on micropatterned substrates were realized with a video microscope. At the beginning of the experiments, we selected cells with neurites approaching an intersection of patterned adhesive lines. In this way we were able to record several branching and turning events in various geometrical configurations.

We observed that as the growth cone approaches an intersection, it gradually broadens while filopodial protrusion at the front decreases. For angles up to 180° , we observed filopodia gradually reorient themselves away from the neurite shaft axis to explore a wider angular range (as can be seen in **Figure III-36** and in **Figure III-37**). We then saw a progressive scission of the growth cone into two areas. In cases of branching, the two growth cone areas eventually developed into independent branches with their own growth cones (see **Figure III-35** and **Figure III-37**). In cases of turning, part of the growth cone area gradually saw a decrease in activity while the other part continued developing (see **Figure III-38**). These observations led us to conclude that the branching events observed on our micropatterned substrates derive from the growth cone bifurcation mode of branching (see Part I).

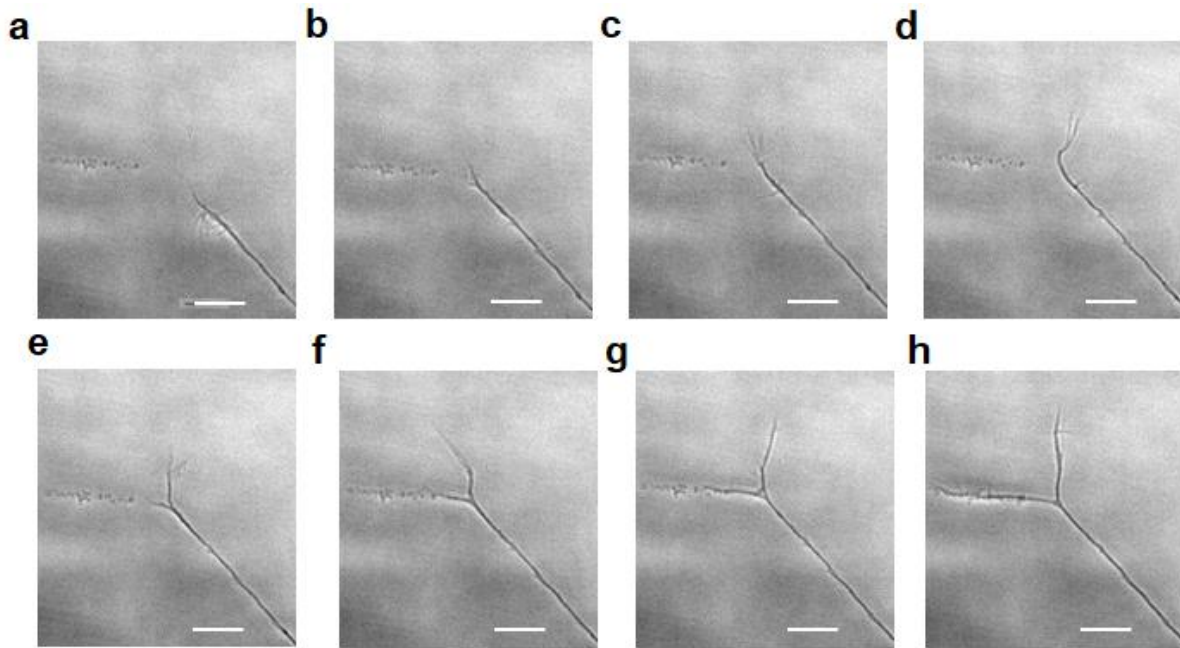


Figure III-35 : Branching in a symmetric configuration with a 90° angle. Phase images of mouse E16 hippocampi neuron at DIV1 on micropatterned substrate. Patterning has been realized with mask n°1. Here $\alpha=90^\circ$, $\alpha_1 = \alpha_2 = 45^\circ$. a. t=0min b. t=40min c. t=56min d. t=76min e. t=80min f. t=104min g. t=110min h. t=180min. Scale bar : 10 μm

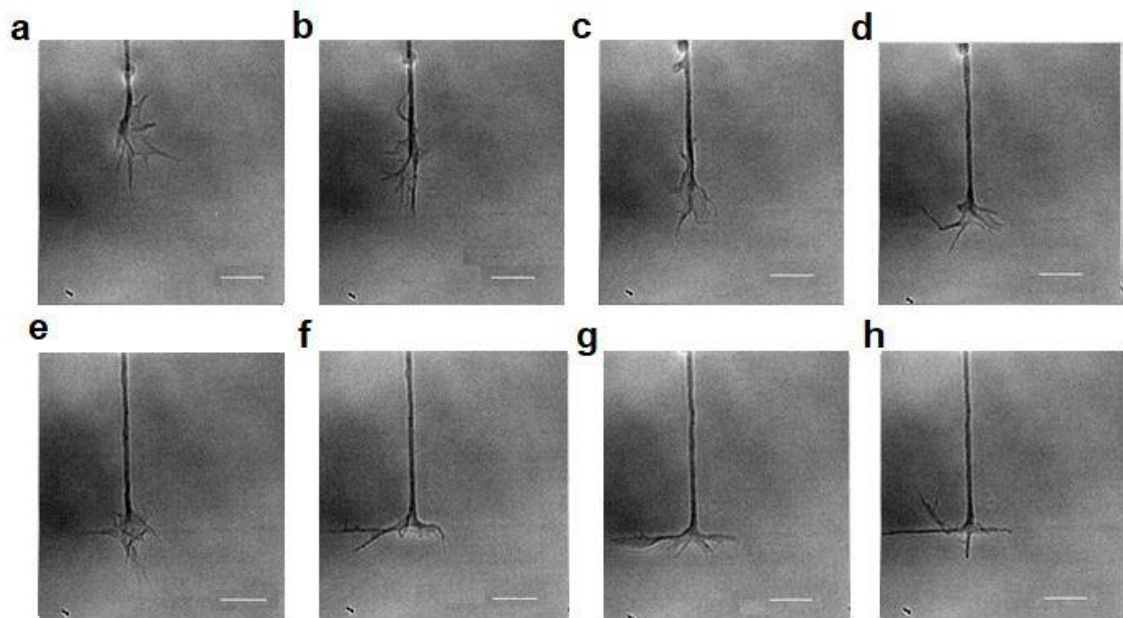


Figure III-36 : Branching in a symmetric configuration with a 180° angle. Phase images of mouse E16 hippocampi neuron at DIV1 on micropatterned substrate. Patterning has been realized with mask n°1. Here $\alpha=180^\circ$, $\alpha_1 = \alpha_2 = 90^\circ$. a. t=0min b. t=20min c. t=40min d. t=46min e. t=52min f. t=58min g. t=64min h. t=70min. Scale bar : 10 μm

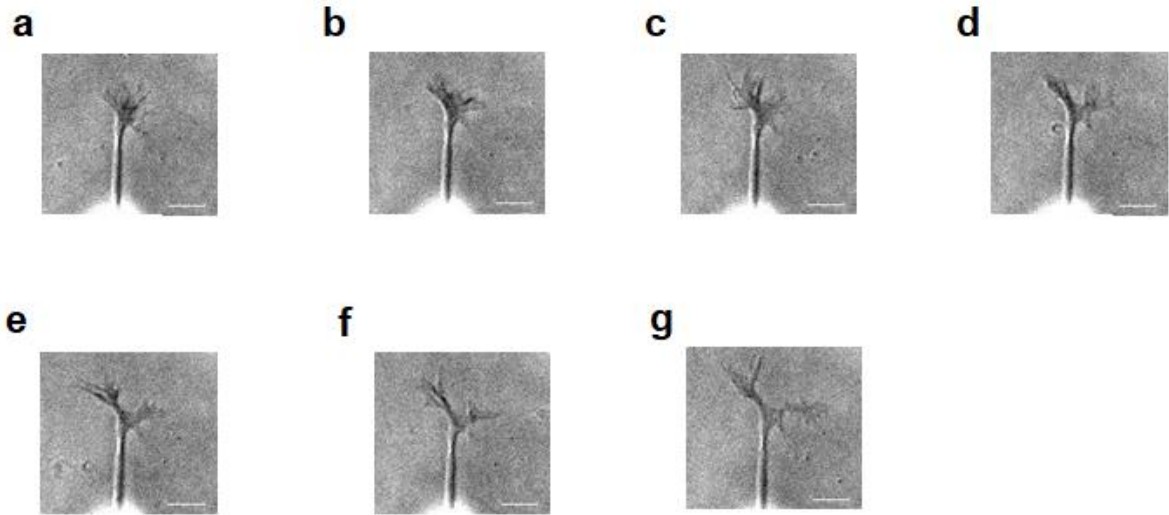


Figure III-37 : Branching in an asymmetric configuration. Phase images of mouse E16 hippocampi neuron at DIV1 on micropatterned substrate. Patterning has been realized with mask n°1. Here $\alpha=135^\circ$, $\alpha_1 = 45^\circ$; $\alpha_2 = 90^\circ$. a. $t=0\text{min}$ b. $t=16\text{min}$ c. $t=24\text{min}$ d. $t=34\text{min}$ e. $t=44\text{min}$ f. $t=70\text{min}$ g. $t=166\text{min}$. Scale bar : $10\mu\text{m}$

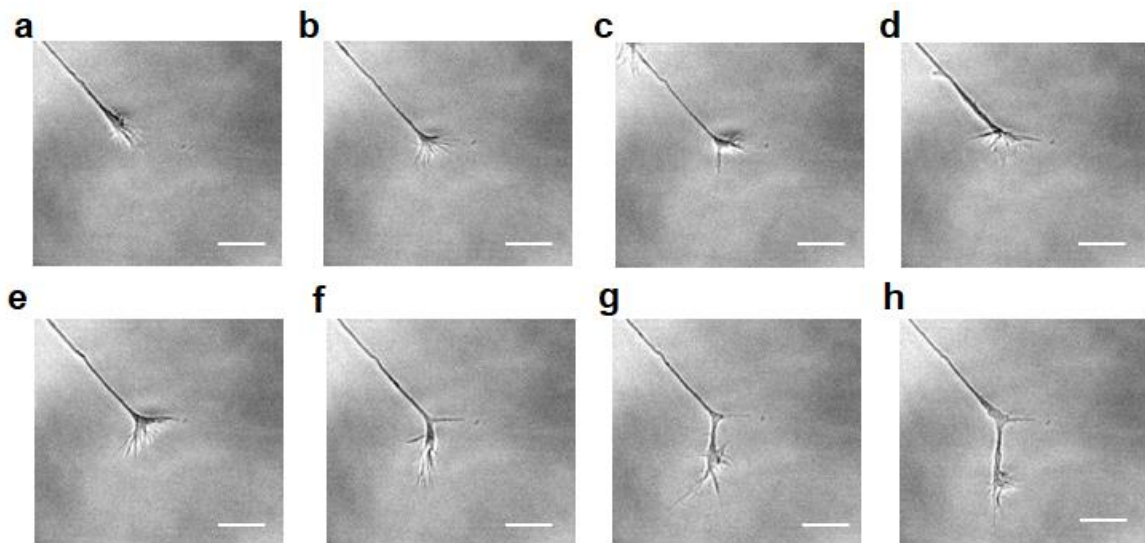


Figure III-38 : Turning in a symmetric configuration. Phase images of mouse E16 hippocampi neuron at DIV1 on micropatterned substrate. Patterning has been realized with mask n°1. Here $\alpha=90^\circ$, $\alpha_1 = \alpha_2 = 45^\circ$. a. $t=0\text{min}$ b. $t=20\text{min}$ c. $t=30\text{min}$ d. $t=38\text{min}$ e. $t=44\text{min}$ f. $t=48\text{min}$ g. $t=60\text{min}$ h. $t=104\text{min}$. Scale bar : $10\mu\text{m}$

III.A.5.b) Analysis of growth cone pausing times at branching and turning points

For each video of a neurite approaching an intersection, we drew a circular area centered on the potential branching point. Then with a program designed by Marianne Renner from Institut du Fer à Moulin, we were able to calculate the time that the recorded neurites' growth cones spent inside that circular area. With these data we could infer the growth cone residency time at intersections (ie. the time the growth cone spends in close proximity of an intersection, see Part II Methods for more details). As a point of reference, we also calculated for each neuron, the time spent by a growth cone on a straight line in a circular area of the same diameter.

The results for areas of 5 μm around the branching and turning points can be found in **Figure III-39**. Although more data would be needed to perform a statistical analysis, the first results tend to show that the growth cone spends a longer time around branching and turning points than on a straight line. This supports the hypothesis that branching and turning events are accompanied by a pausing of the growth cone advance.

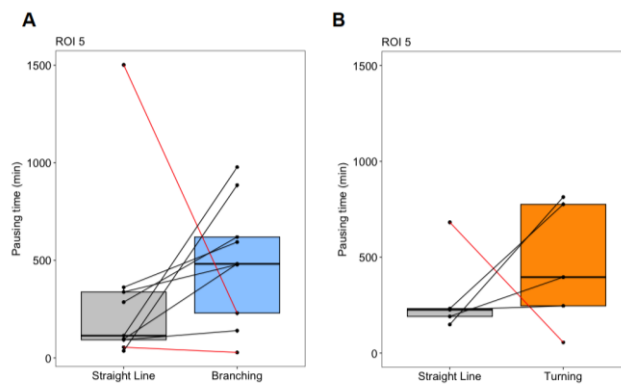


Figure III-39 : Comparison of growth cone residency times at branching points, turning points and on straight lines in an area of 5 μm diameter centered on the intersection. A. Comparison of growth cone residency times at branching points and on straight lines in an area of 5 μm diameter. From time-lapse recordings of hippocampi neurons growing on micropatterned substrates at DIV1. (3 cultures, n= 9 neurons. Lines connect values of pausing time measurements realized on the same growth cone in different conditions (left: on a straight line, right: at a branching point). Color code for lines: black if the branching growth cone pausing time is higher than the pausing time on a straight line; red if the branching growth cone pausing time is lower than the pausing time on a straight line **B. Comparison of growth cone residency times at turning points and on straight lines in an area of 5 μm diameter.** From time-lapse recordings of hippocampi neurons growing on micropatterned substrates at DIV1. Lines connect values of pausing time measurements realized on the same growth cone in different conditions (left: on a straight line, right: at a turning point). Color code for lines: black if the turning growth cone pausing time is higher than the pausing time on a straight line; red if the turning growth cone pausing time is lower than the pausing time on a straight line (3 cultures, n= 5 neurons)

III.A.6.Conclusion

Our study of neurons developing on static micropatterns has revealed several mechanisms concerning branching.

- We have shown that on fully adhesive substrates as well as 2 μ m wide patterned stripes, the angular distribution of filopodia is symmetric and comprised in a 90° wide angular area centered on the neurite shaft axis.
- The average value of growth cone angular extent (excluding collapsed growth cones) is 70° on fully adhesive substrates as well as on our micropatterned substrates.
- When approaching an intersection, the growth cone gradually broadens and finally separates into 2 independent areas. Then either one of these areas retracts while the other continues developing (turning) or both areas mature into two independent daughter branches (branching).
- The growth cone appears to pause at branching points and turning points, which might be caused by a local disruption of the cytoskeleton organization.
- In symmetric configurations, neurons prefer branching to turning. Furthermore they show no angular preference and are as likely to branch at a 90° angle than at a 180° angle.
- When an angular choice is presented to axons, branching is preferred to turning for smaller branching angles. On the other hand, turning is favored for branching angles bigger than 90°.
- Undifferentiated neurites branching probability is peaked at 70°: it increases for angles < 70° and decreases for larger angles.
- We also observed preferential branch growth in the direction closest to the mother branch direction.

III.B. Dynamic patterning to study neuronal branching

The first part of our study was realized using static micropatterns, ie. patterns whose design cannot be modified once the cells are seeded onto the substrate. While we have shown that static micropatterning can provide useful insight on branching behavior, this technique has some limitations. For example, it cannot be used to for spatio-temporal control of branching events. That is why, in parallel to our study with static micropatterns, we have also worked on the development of dynamic patterning for neurons with the aim of creating a new tool to understanding the branching phenomenon. This part of our project was led in collaboration with the Chemical Biophysics group of ENS.

III.B.1.Context and objective of the project

Dynamic patterning is a type of chemical patterning that enables the creation of remotely switchable adhesive surfaces onto the substrate. In the case of neuronal branching, these switchable surfaces could be used to manipulate outgrowth and retraction of neuronal branches. The strategy that we attempted to implement is based on a comb-like derivated of poly-L-lysine (PLL) that displays clickable azide functions at the end of comb-like PEG (Poly Ethylene Glycol^o) strands: azidoPLL-g-PEG (APP). APP-patterned surfaces can be easily functionalized by simple bath application of reactive peptides in the culture medium [154] (see **Figure II-7**). This dynamic patterning strategy has already been successfully implemented with HELA cells by the group of Matthieu Piel in collaboration with the Chemical Biophysics group of ENS [155].

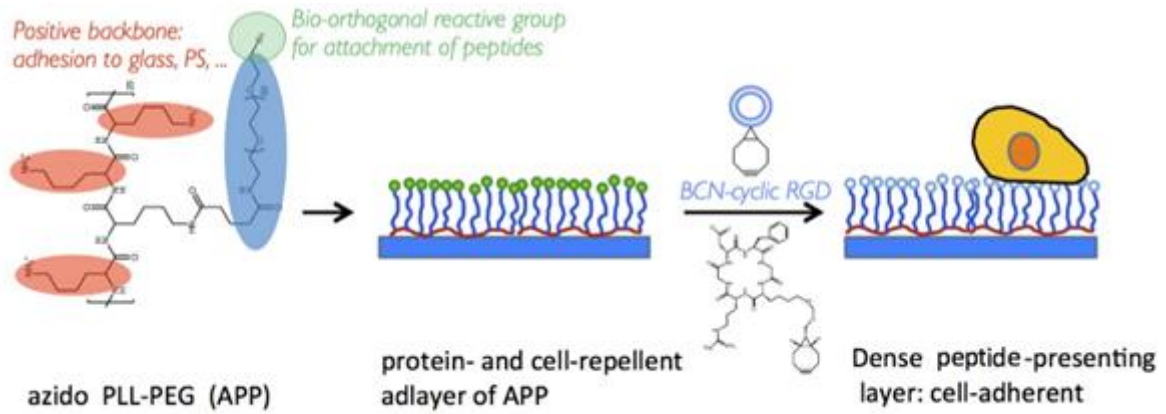


Figure III-40 : Cell-repellent APP coating switched *in vitro* into an adhesive peptide-presenting surface. Red: PLL backbone, blue: PEG chains, and green for the “clickable” azide function turning into light blue after binding with the adhesive peptide.

The objective of our project was to manage to pattern, on the same surface: adhesive paths (with molecules such as poly-L-lysine or laminin), click-adhesive paths (with APP) on a cell-repulsive background (constructed with PLL-g-PEG for example in **Figure III-41**).

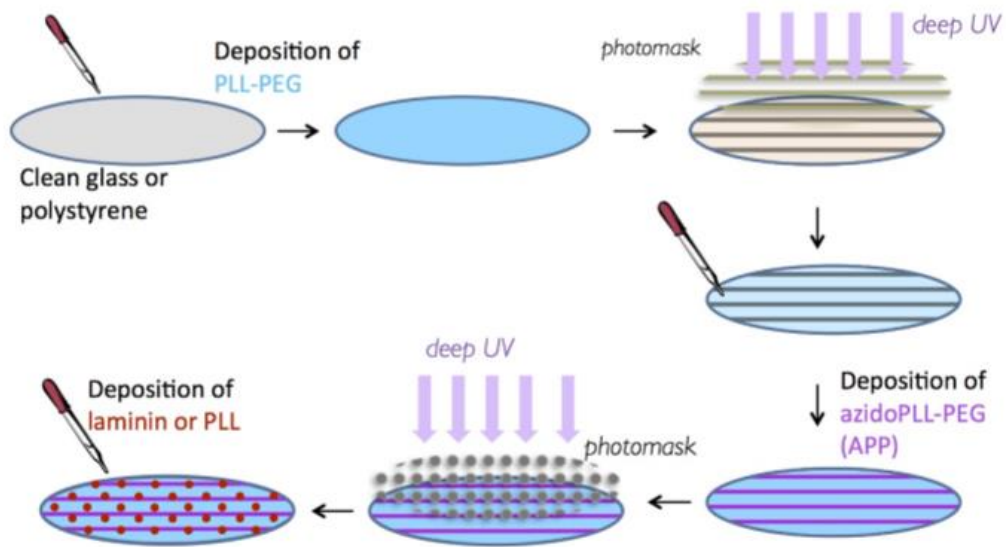


Figure III-41 : Illustration of double patterning of APP (purple), and a set of permanently adhesive wells (red) on a PLL-g-PEG (blue) background with deep sequential UV etching.

III.B.2.Methodology and results

III.B.2.a) *Choosing the micropatterning technique*

The strategy that we chose to implement dynamic patterning requires three steps: (1) the treatment of the substrate surface with a cell-repulsive molecule such as PLL-PEG to create a repellent background, (2) the patterning of permanently adhesive surfaces with molecules like laminin or PLL and (3) the patterning of switchable adhesive surfaces with APP. Therefore, we had to select a technique enabling us to pattern two different molecules as well as align the different patterns design chosen for each molecule. The photolithography-based technique that we used to create static patterns in the previous part of our work did not fit these criteria. For this reason, we have decided to work with three different techniques: sequential UV etching (illustrated in **Figure III-41**), a technique based on the Primo module developed by Alveole (see **Figure III-42**) and an adapted photolithography-based technique that will be described in **III.B.2.c**). All the protocols used with these techniques are described in details in Part II Methods.

Sequential deep UV etching is the technique that was used by the group who designed the strategy of APP and adhesive molecules patterning that we have adopted [155]. It has the major inconvenient of requiring a physical quartz mask, which is not cost-effective and also makes alignment difficult. This technique is limited in resolution due to the diffusion of light in the water droplet that holds the coverslip against the mask to values down to 3 μm . On the other hand, the Primo-based technique has the advantage of not requiring a physical mask which makes alignment easier. It is also more precise than sequential UV etching, with a resolution of 2 μm . Lastly, it does not require any drying of the sample which could damage molecules like laminin. Unfortunately, for surfaces in the order of magnitude of a glass coverslip, it is much slower than sequential deep UV etching. It takes 2 hours to fill a 24x24mm coverslip using the Primo module against 15min for sequential deep UV etching.

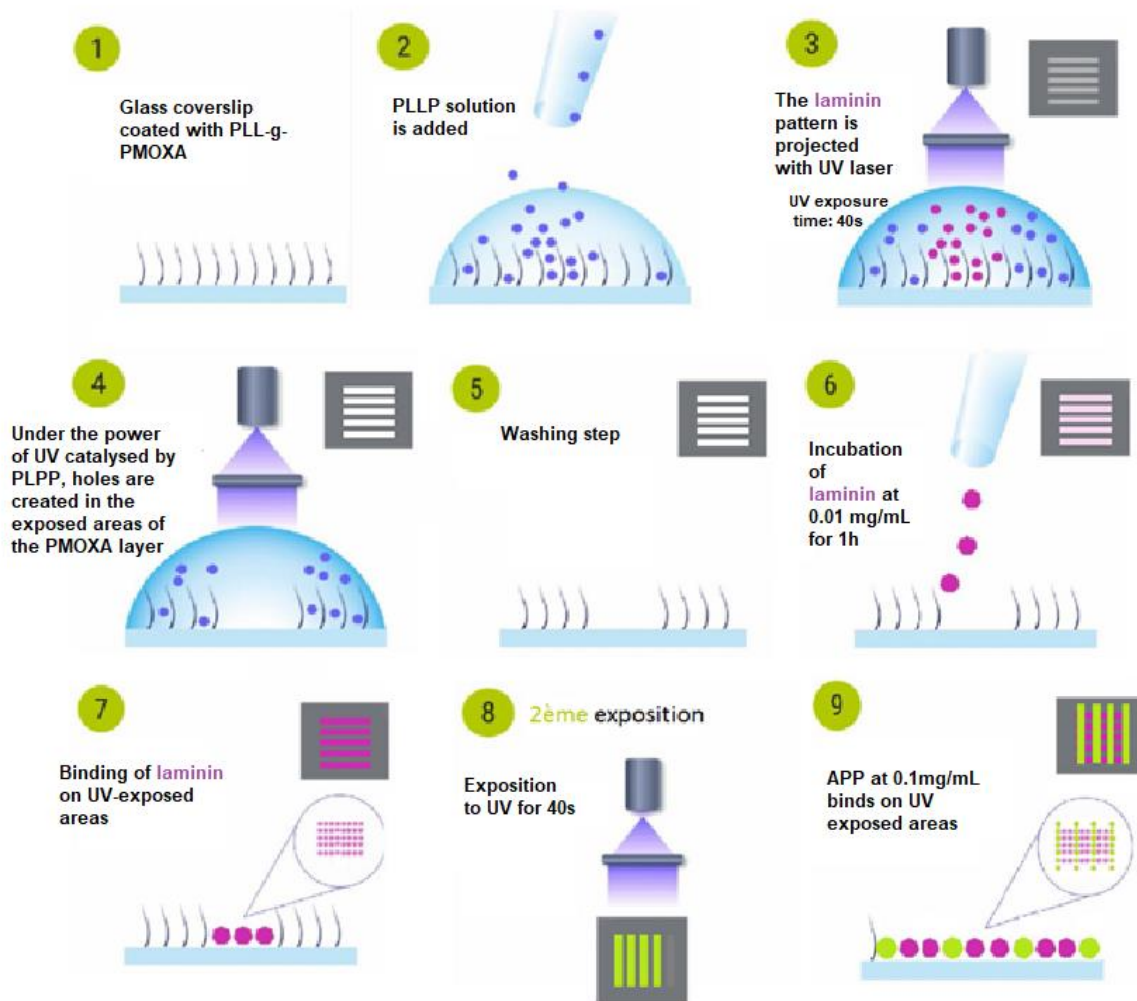


Figure III-42 : Illustration of double patterning of APP stripes (purple), and permanently adhesive stripes (green) on a cell-repellent poly(2-methyl-2-oxazoline) (PMOXA) (blue) background with the Primo module. Adapted from [152].

III.B.2.b) Repulsive background

First, we set out to find a repulsive background for neuronal cells that was compatible with our chosen strategy for dynamic patterning of neurons. Several different backgrounds were tested. The first repellent background that we tried was functionalized with PLL-g-PEG. PEG is a hydrophilic polymer that is one of the most used molecules to prevent protein adsorption and subsequently cell attachment [144],[145]. The antifouling behaviour of PEG is not fully understood and is still an area of active research, although it is suggested that the dense solvated brush-like PEG structure shields surface charges and disallows interaction of proteins with the underlying surface [146]. PLL-g-PEG is a polymer consisting in a PLL

backbone grafted with PEG strands. We used a PLL-g-PEG with a molecular weight of 20 kDa for PLL and 2kDa for PEG, a grafting ratio of 35% and at a concentration of 1mg/mL and 0.1mg/mL. We did not obtain a good contrast of adhesion with hippocampal neurons for either of the concentrations used (see **Figure III-43**) and decided to try out other repellent molecules.

We then tried using the polymer PLL-g- PMOXA. Structurally, PMOXA (poly(2-methyl-2-oxazoline)) could be described as a poly(ethylene imine) backbone with an acetyl group bound to the nitrogen atom in each repeating unit. It has been reported that PLL-g-PMOXA is more stable than PLL-g-PEG under cell culture conditions [147]. Using PMOXA, we managed to achieve better results of adhesion contrast with hippocampal neurons. Unfortunately, this polymer was still in in development at the time of these experiments, and consequently the repellent effect was inconsistent amongst different stocks.

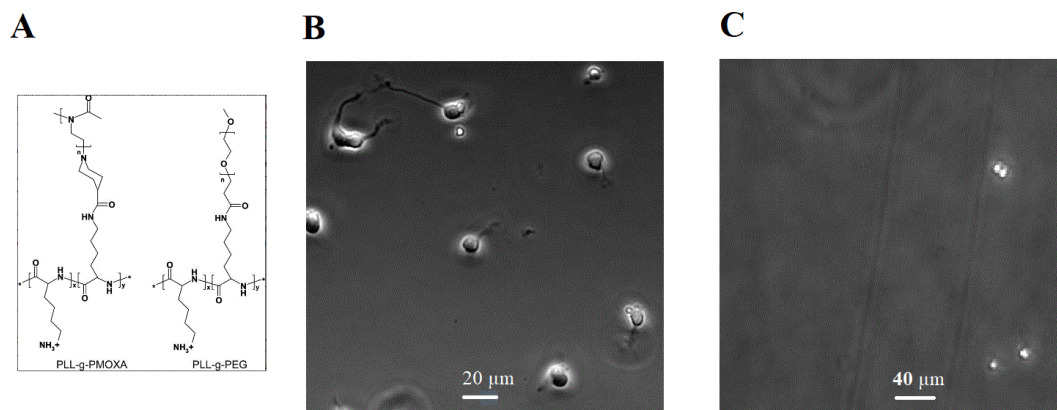


Figure III-43 : Repellent backgrounds to prevent neuronal adhesion. A. Chemical structure of PLL-g-PEG and PLL-g-PMOXA B. Phase image of a glass coverslide coated with PLL-g-PEG at 1mg/mL (with a molecular weight of 20 kDa for PLL and 2kDa for PEG, a grafting ratio of 35% and at a concentration of 1mg/mL) C. Phase image of a glass coverslide coated with PLL-g-PMOXA. Compared to PLL-g-PEG, the adhesion of neurons on PLL-g-PMOXA is strongly decreased.

III.B.2.c) Adhesive rails

We then set out to pattern adhesive rails for neurons on repellent backgrounds such as PLL-g-PEG. We explored adhesive patterning with ECM molecules such as laminin on which adhesion is mediated by integrins [88] and also with cationic molecules such as Poly-L-Lysine (PLL) which fosters a non-integrin mediated adhesion of neurons.

Four different techniques were explored to create adhesive lines on a PLL-g-PEG repellent background.

First, using the deep UV sequential etching technique, we patterned laminin rails. The mask used was composed of 2 μm -wide lines. Unfortunately, due to low adsorption of laminin on the glass surface the observed survival of neurons was low. Furthermore, the laminin rails width value was measured at a value of 3.5 μm due to the limits in resolution of the deep UV sequential etching technique.

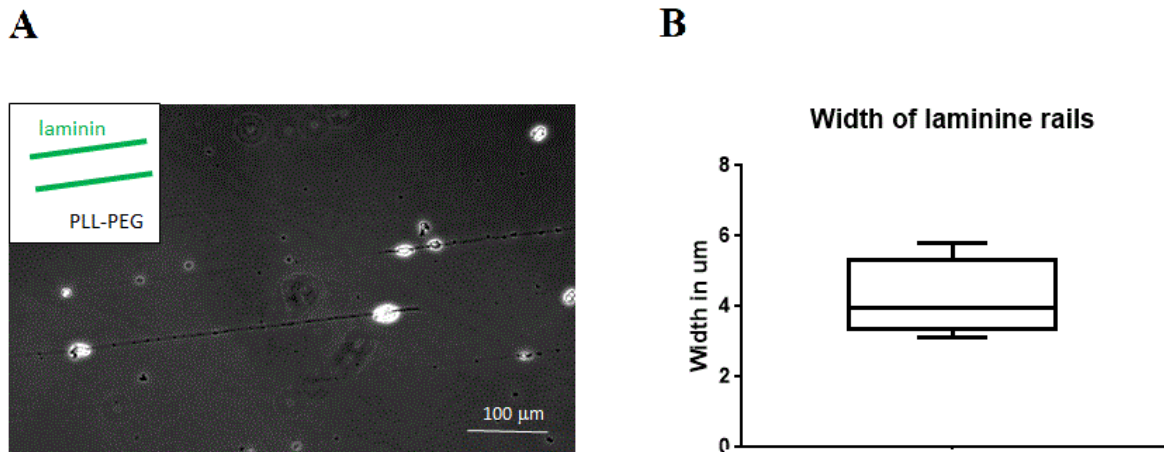


Figure III-44 : Laminin rails on PLL-g-PEG background with deep UV sequential etching. A. Phase image of hippocampal neurons taken at DIV 5, density 34 cells/ mm^2 , laminin at 0,1mg/mL in a 2 μm wide, 100 μm distant 2 μm wide line pattern. PLL-PEG at 0.1mg/mL B. Measurement of laminin rails width. n=18 rails, 2 coverslides. Box and whiskers: quartiles and median, end of whiskers represent minimum and maximum values. Inset: pattern

Next, also using deep UV sequential etching technique, we tried patterning PLL rails with an inverted 2 μm -wide lines mask. PLL cannot be directly patterned on a PLL-PEG background because when added to a PLL-g-PEG coated substrate, it goes in-between PEG chains, making the PLL-g-PEG adhesive. Once again, we observed a very low survival of neurons. Indeed, when measuring the width of the PLL lines we found values averaging at 1.5 μm , due to the diffusion of UV light by the water layer in-between the coverslip and the mask.

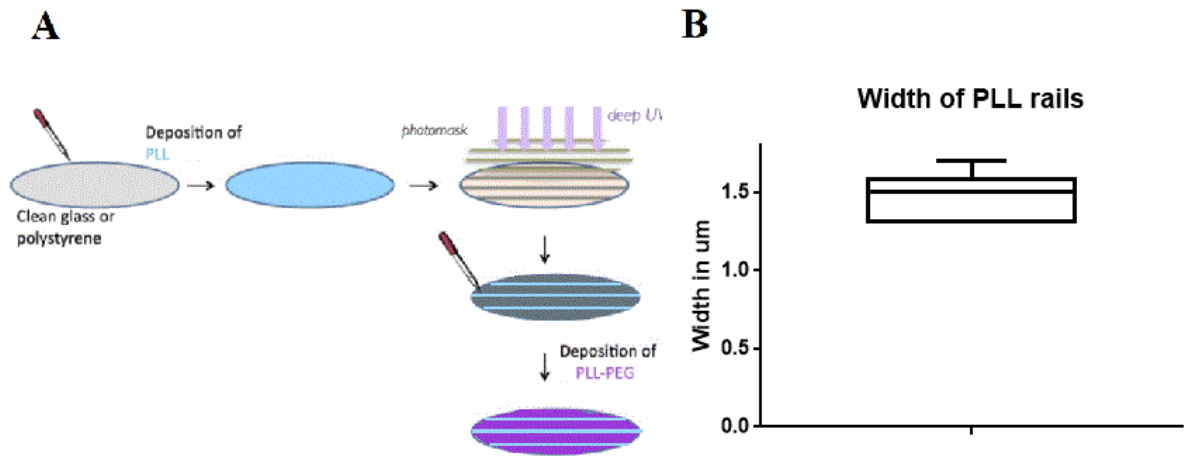


Figure III-45 : PLL rails patterning with an inverted mask on PLL-g-PEG background with deep UV sequential etching. **A.** Cartoon representing the patterning steps. **B.** Measurement of PLL rails width. PLL at 0.1mg/mL, PLL-PEG at 0.1mg/mL. n=18 rails, 2 coverslips. Box and whiskers: quartiles and median, end of whiskers represent minimum and maximum values.

Then we decided to use the photolithography based technique developed by our group to create PLL lines on a PLL-g-PEG background. We first spincoated photoresist S1805 on our substrates, then exposed it to UV through a 2 μm -wide lines chromium mask. After that, we incubated our substrate in a PLL solution. The resist was dissolved with the use of ultrasounds and a bath of absolute ethanol. Finally we finished with a step of incubation in a PLL-g-PEG solution. The PLL rails obtained displayed excellent neuronal survival as well as a well controlled width (measured at an average of 2 μm).

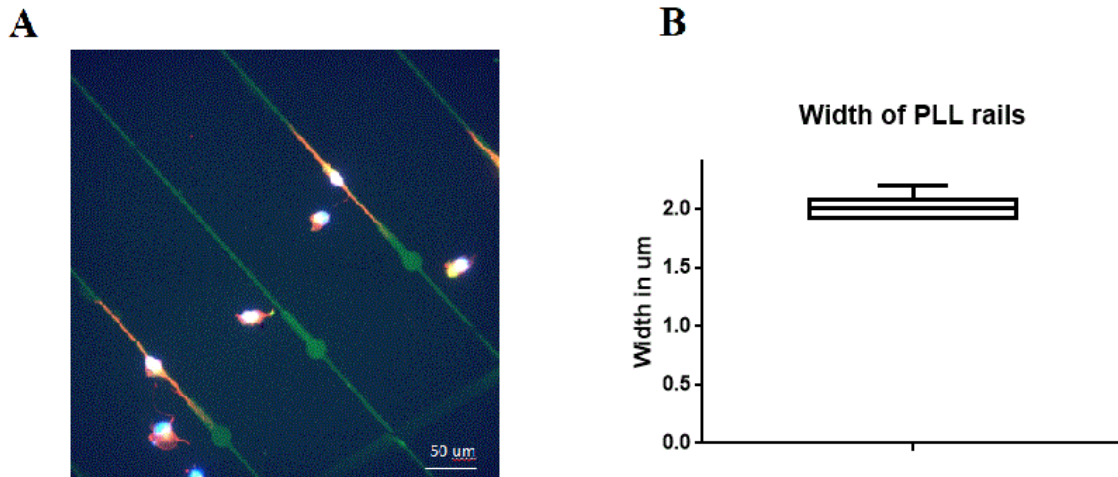


Figure III-46 : PLL lines patterned with photolithography on a PLL-PEG background. A. Fluorescence image of hippocampal E19 neurons on PLL-FITC lines. red: β -tubulin, blue: nucleus, green: PLL. PLL-FITC at 1mg/mL., PLL-PEG at 0.1mg/mL. B. Measurement of PLL rails width. n=18 rails, 2 coverslides. Box and whiskers: quartiles and median, end of whiskers represent minimum and maximum values.

Finally, we tried using the Primo module to create adhesive rails on a PLL-g-PEG background. We patterned the substrate through the following steps (1) exposure of a PLL-g-PEG coated coverslip to UV, (2) Incubation in a netravadin solution and (3) incubation in a biotin-PEG-PLL solution. As biotin has a strong affinity with to netravadin, this protocol enabled us to create lines that were adhesive for neurons.

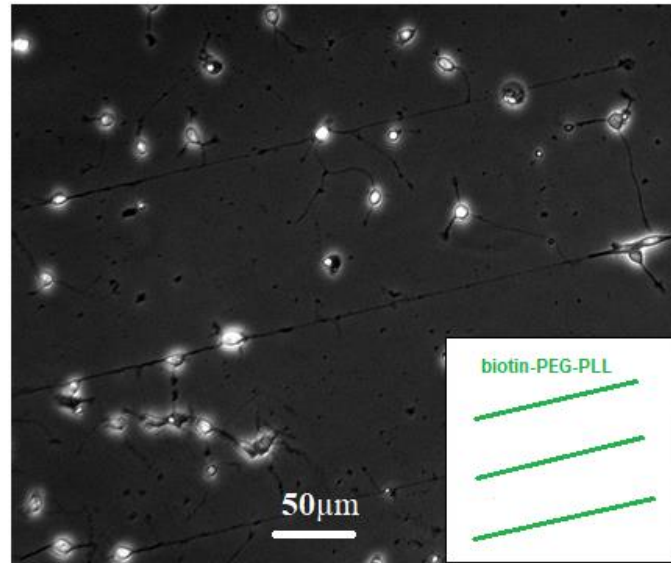


Figure III-47 : Adhesive rails realized with netravdin and biotin-PEG-PLL, using the Primo module on a PLL-PEG background.

III.B.2.d) APP rails

The next part of our project was the implementation of switchable adhesive rails on a repellent surface, using the click-adhesive molecule APP. The objective was to pattern APP stripes that were initially repulsive to neurons and could become adhesive by addition of a reactive peptide in the cell culture medium. We tested different conditions to achieve this result.

First, we started out with the conditions of APP patterning that have been demonstrated to work for HeLa cells patterning in ref, ie APP synthesized with 20kDa PLL and 3kDa azido-PEG with a grafting density of 33% (one azidoPEG chain per three lysine residue), at a concentration of 0.1mg/mL. Surprisingly, we observed that in these conditions, APP rails are adhesive to neurons before even adding a reactive peptide.

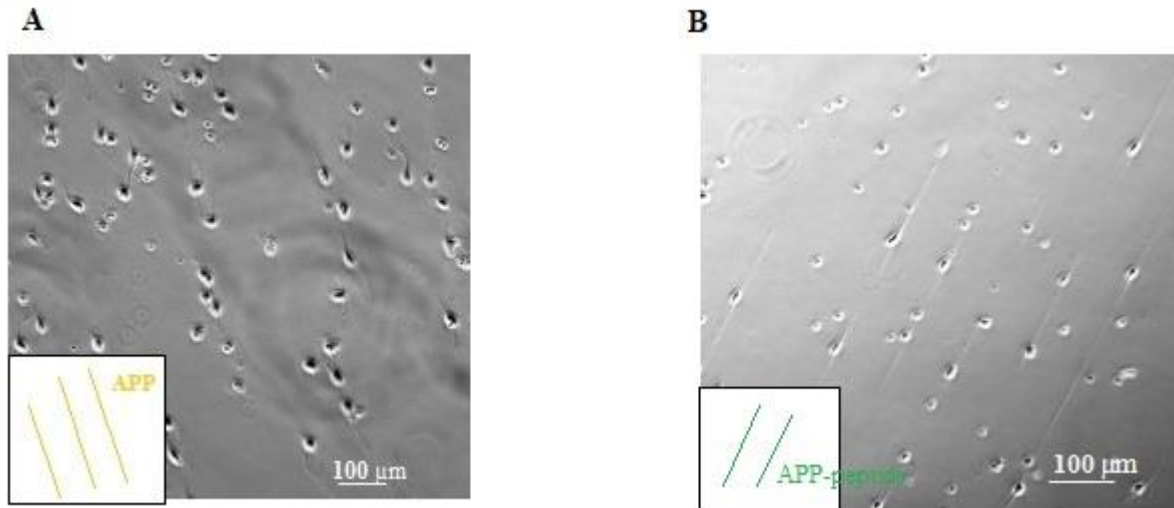


Figure III-48 : Phase contrast images of mouse hippocampal neurons on APP rails on a PLL-PEG background. **A.** Neuronal adhesion on APP rails. **B.** Neuronal adhesion on APP-peptide rails. APP at 0.1mg/mL, PLL-PEG at 0.1mg/mL. Peptide: BCN-(CGGYIGSR) at 100 μ M. Substrates were prepared with deep UV sequential etching. Pictures were taken at DIV3. Inset: patterns

Next, we employed diluted APP to diminish its adhesive character for neurons. A linear relationship between an APP dilution rate and its number of azide functions per unit has been reported in [155]. We experimented with dilutions of APP in PLL-g-PEG solutions of 30% up to 75% at 0.1mg/mL. Unfortunately, we could not find reproducible conditions where APP rails were repulsive for neurons in the absence of peptide and adhesive after being functionalized by a reactive peptide.

III.B.2.e) Peptide

Different peptides were employed to functionalize APP. To be able to click with the azide function, a bicyclo [6.1.0]nonyne (BCN) function must be added to the peptide. The peptide that was first used to develop APP-based dynamic patterning of cells is RGD, a derivative of the extracellular molecule fibronectin. This peptide does not provide good adhesion for hippocampal neurons. Therefore we have used peptides derived from YIGSR, a portion of the chain α of laminin. Three derivatives of YIGSR were tested: BCN-LamPEG (= {PEG6}YIGSR), BCN-LamA (=GGGYIGSR) and BCN-C3-3 (=CGGGYIGSR). Neurons have been found to adhere for APP 100% rails functionalized with each of these peptides.

We could not observe a conclusive influence of the addition of these peptides over the adhesiveness of APP rails for neurons, for any dilution of APP. It is possible that peptide concentration might play a role, as it has been shown that cell spreading over the APP surfaces increases with the concentration of added peptide [154]. However, the preparation of peptide concentration over 100 μ M was made by difficult by the time-consuming step of peptide purification. Another reason for the lack of apparent effect could be peptide aggregation in the cell medium.

III.B.2.f) Grid pattern

We used the techniques previously described to implement grid patterning of APP-lines and adhesive lines on substrates coated with a repulsive background. Neurons were intended to adhere first on the adhesive lines and then, following addition of peptide into the cell medium, develop branches on APP lines.

To simplify the problem, we decide to start by comparing behaviors of neurons on APP/laminin grid patterns and on APP-peptide/ laminin grid patterns. For the latter, the coverslip is incubated in the reactive peptide solution at 100 μ M before the seeding, to maximize peptide attachment to APP. The expected result on APP/laminin grids was a neuronal adhesion restricted to laminin rails. On the other hand, on APP-peptide/laminin grids neurons were expected to develop on both rails. Examples of the behavior of neurons on such grid patterns can be found in **Figure III-49**.

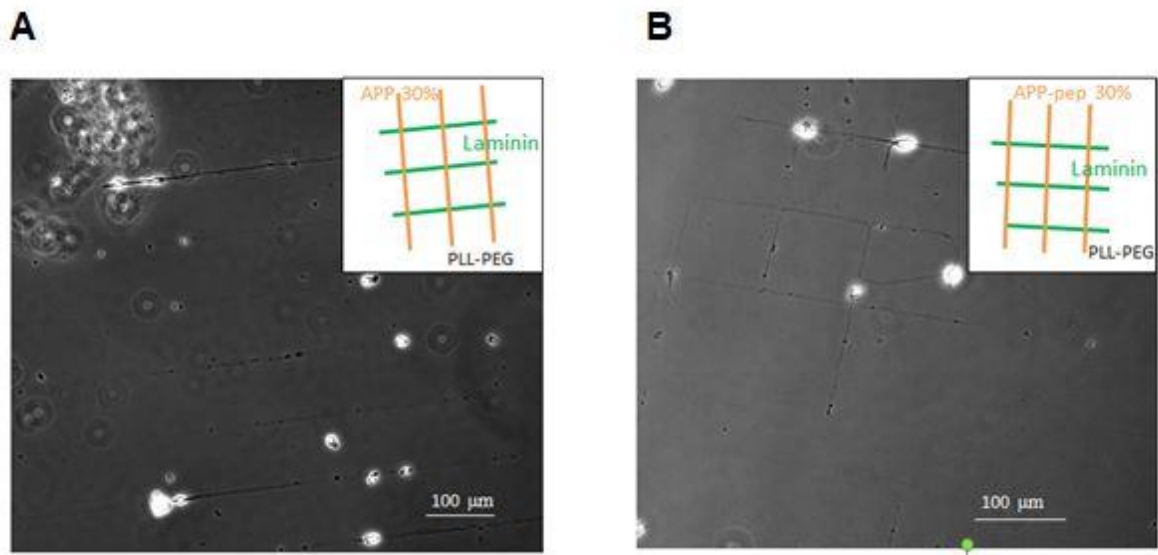


Figure III-49 : Behavior of hippocampal neurons on grid pattern of APP lines and adhesive lines. Cell density 34 cells/mm². A. Grid pattern of APP 30% (0.1mg/mL) and laminin (0.04mg/mL) obtained with deep UV sequential etching. B. Grid pattern of APP-BCN-C33 (0.1mg/mL for APP, 100μM for peptide) and laminin (0.04mg/mL) obtained with deep UV sequential etching. The coverslip was incubated in a solution of BCN-C33 at 100 μM prior to the seeding. In this case the behavior of neurons is as expected: adhesion restricted to the laminin rails in the absence of peptide, and to both rails in the presence of peptide. Insets: patterns

Importantly, with every patterning technique, we observed that it is crucial for the laminin patterning to be done as the first step. Indeed, in cases where we tried to pattern APP first (and laminin in a second step), we saw attachment of laminin both to rails intended for APP and rails intended for laminin. Patterning laminin first makes it possible to avoid that issue, though it can have the inconvenient of giving laminin rails of lesser quality since there is more manipulation of the sample post-laminin incubation.

III.B.3.Conclusion

We were not able to find reproducible conditions for dynamic patterning of neurons with APP. Nevertheless, dynamic patterning remains a promising tool to deepen our understanding of neuronal branching. Other approaches of dynamic patterning, combining the use of innovating tools such as Primo and biotinated adhesive molecules are currently being developed in our group and could eventually pave the way to spatio-temporal control of neuronal branching *in situ*.

Chapter IV. Discussion

Contents

Chapter IV. Discussion	150
IV.A. Actin based exploration of the GC microenvironment.....	152
IV.B. Selection of direction by microtubules	153
IV.C. Axons prefer going straight	154
IV.D. Conclusion	155
Bibliography	158

In this work, we have studied neuronal branching on micropatterns composed of $2\mu\text{m}$ -wide intersecting lines. At each intersection, the growth cone was presented with two available adhesive paths (see **Figure IV-1**). Faced with this microenvironment, the growth cone had two options: branching or turning. In cases where the pattern geometry enabled neurites to grow a branch in the same direction as the mother branch, the growth cone had the additional possibility of going straight.

In all cases we observed that the micropatterns evoked a scission of the growth cone at intersections. Furthermore, in symmetric configurations, we found that neurons preferred branching to turning and were as likely to branch at low angles than at higher ones. On the other hand, when presented with a choice between two different directions, the angle between these two directions determined the behavior of the growth cone. When this angle was lower than 90° , growth cones exhibited a clear preference for branching, whereas for higher angles turning was preferred. Finally, in the case of axons we also saw evidence of preferential branch growth in the direction closest to the mother branch direction. In this chapter, we will discuss how the properties of the neuronal growth cone and its cytoskeleton elements could explain our findings.

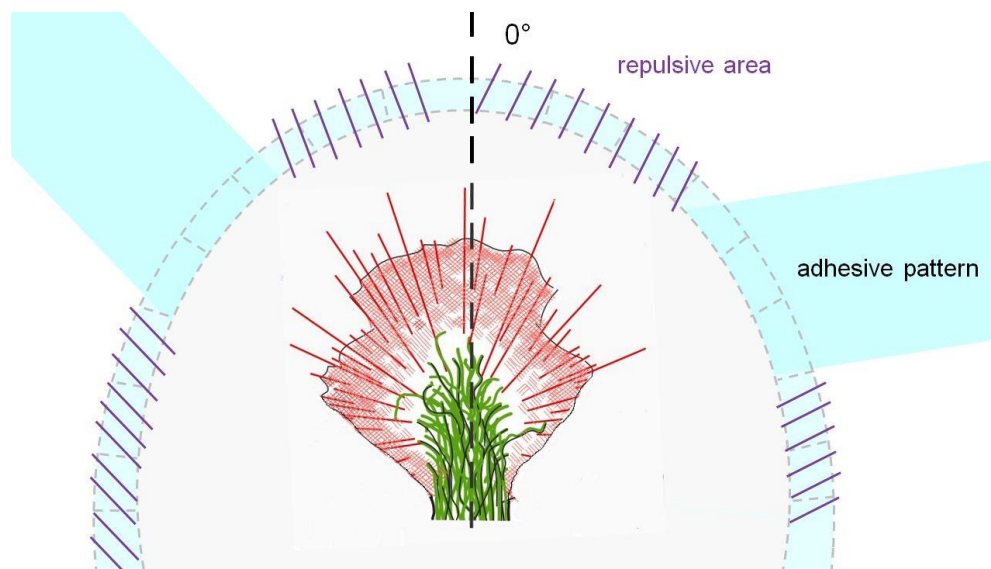


Figure IV-1 : Schematics of our experimental set up. The growth cone is presented with two adhesive paths surrounded by repulsive areas. Filopodia (straight red line) extend from the growth cone in different directions and probe the growth cone microenvironment. A parallel can be drawn between our experimental set-up and situations where the growth cone is presented with two diffusible chemoattractants. Adapted from [156] and [157].

IV.A. Actin based exploration of the GC microenvironment

During brain development, neurons have to migrate through multiple structures, e.g. cortical neurons need to cross several cortical layers to reach their final target. To manage this feat, neuronal cells must be able to explore and invade complex matrices. The main instrument through which neurons achieve this invasive behavior is the growth cone [158]. As was seen in **I.A.3.c** , the growth cone possesses a complex actin structure composed of extending protrusions, the filopodia, which emerge from a larger body, the lamellipodia. Filopodia are finger-like actin bundles which are considered to be the growth cone main sensors and can also act as precursors to branches [159].

In our work, we saw that filopodia distribution in mouse hippocampal neurons is symmetric, mostly comprised in a 90° degree range centered on the neurite shaft axis. At first glance, this angular repartition supports the hypothesis that up to a branching angle of 90° neurons prefer branching to turning and that for higher angles turning is the favored option. Indeed this corresponds to the behavior found in asymmetric configurations. However, this does not match our observation that symmetric branching is as likely at an angle at 90° than it is at 180°.

To account for this discrepancy, we need to consider the growth cone ability to dynamically adapt itself to its surroundings. In timelapse recordings we saw that when approaching a 180° intersection, the growth cone filopodia reorient themselves away from the neurite shaft axis to explore a wider angular range (see **Figure IV-2**). It is possible that in this situation the external filopodia could act as precursors to two daughter branches at a 180° angle. This may explain why growth cone can bifurcate at a 180° angle despite the costly cytoskeleton reorganization needed to do so. Furthermore, the growth cone preference for branching (even at higher angles) in symmetric configurations might make more sense when considering its role as the main structure supporting the exploration of the neuronal microenvironment. Indeed, in our set-up, turning results in leaving one path unexplored while branching by scission enables the growth cone to colonize of the entirety of the available paths, even if it might take more time (as seen in **III.A.5**). Moreover, symmetric growth cone bifurcation has also been observed at high branching angles *in vivo*. It has been reported that sensory neurons branch symmetrically with a 180° angle at the dorsal root entry zone through the growth cone scission mode [34].

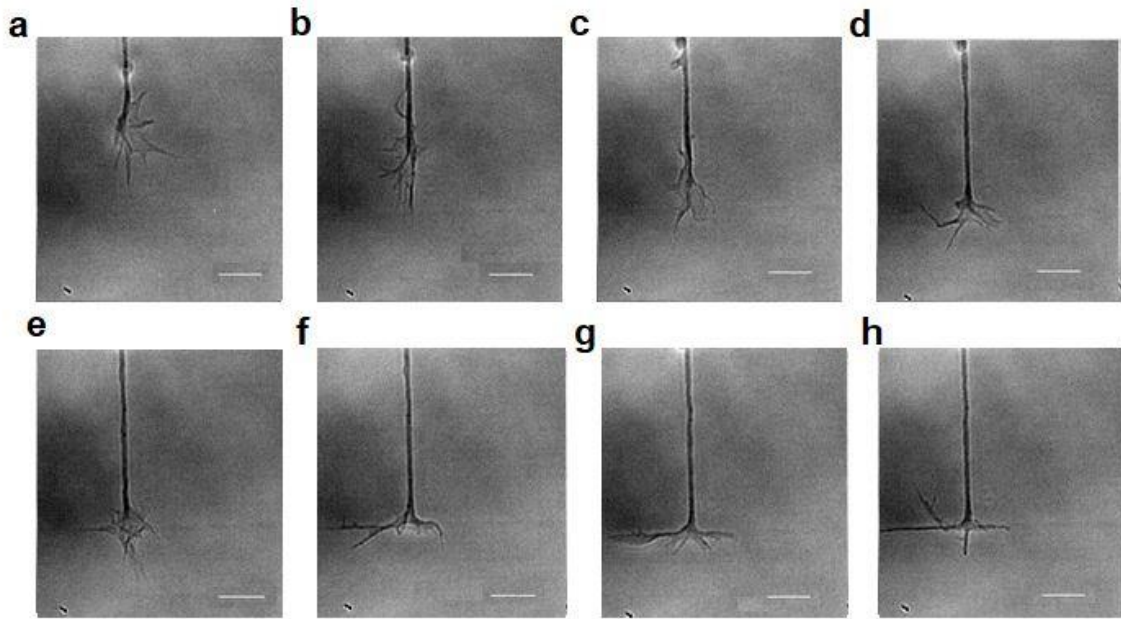


Figure IV-2 : Branching in a symmetric configuration with a 180° angle. Phase images of mouse E16 hippocampi neuron at DIV1 on micropatterned substrate. Patterning has been realized with mask n°1. Here $\alpha=180^\circ$, $\alpha_1 = \alpha_2 = 90^\circ$. a. t=0min b. t=20min c. t=40min d. t=46min e. t=52min f. t=58min g. t=64min h. t=70min. Scale bar : 10 μm . Let us note that when approaching a 180° intersection, the growth cone filopodia reorient themselves away from the neurite shaft axis to explore a wider angular range.

IV.B. Selection of direction by microtubules

Most of the growth cone microtubules can be found at the center of the growth cone, where they form a stable bundle. There are also a few dynamic microtubules that continually explore the growth cone periphery. As we saw in **I.C**, in cases of turning, microtubules selectively invade the area of the growth cone closest to the attractive signal. This rearrangement of microtubules is performed through bending and cutting, thanks to a wide range of microtubules associated proteins (such as spastin and katanin for cutting) and molecular motors (kinesin and dyneins) [77], [160]. In a very similar way, in cases of branching by growth cone scission, microtubules must be bent and cut, but this time to invade not one but two selected sites at the growth cone periphery (see **Figure IV-3**). In both cases, it

is the stabilization of microtubules that determines the fate of the forward motion of the growth cone. Indeed, it has been shown that treating growth cones of dorsal root ganglia (DRG) chick neurons with taxol (a microtubule destabilizing agent) inhibits branching through growth cone bifurcation.[161]

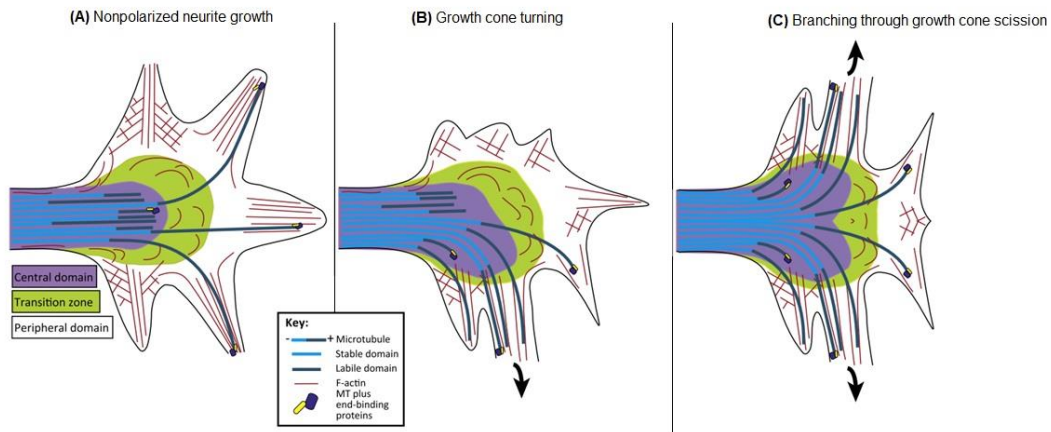


Figure IV-3 : Reorganization of the growth cone during turning and branching by scission. A. Growth cone cytoskeleton during nonpolarized neurite growth. The central domain of the growth cone is the microtubule (MT)-rich region contiguous with the axon shaft. The peripheral domain is the outer-most part of the growth cone. The peripheral domain comprises a broad flat lamellar region in which actin filaments are arranged as a meshwork, as well as elongated thin filopodia in which actin filaments are arranged as aligned bundles. The transition zone is the region between these two domains. Retrograde flow of the actin cytoskeleton in the peripheral domain pushes back most microtubules, compacting them in the central domain. Individual microtubules from the central domain are able to penetrate the transition zone to enter the peripheral domain during growth cone advance. **(B) Growth cone cytoskeleton reorganization during turning.** During growth cone turning, microtubules extend from the central domain through the transition zone preferentially into one side of the peripheral domain. **(C) Growth cone cytoskeleton reorganization during branching by growth cone scission.** During growth cone bifurcation, microtubules extend from the central domain through the transition zone preferentially into two sides of the peripheral domain. This reorganization is similar to the rearrangements observed during turning events. Adapted from [77].

Microtubules can be approximated as rigid rods whose bending has a non negligible energetic cost [162]. For this reason, if a growth cone is faced with a choice between two directions among which a non easy one (ie. forming a large, $>90^\circ$ angle with the mother branch), it might prefer to turn towards the easier direction and abandon the exploration of the difficult path. In this case, the easier path is the one that requires the least bending of microtubules, ie. that forms the smallest angle with the mother branch direction.

IV.C. Axons prefer going straight

Finally, we should also mention that axons have been reported to have a preference for going straight [130]. *In vitro* mouse cortical axons were presented with a choice between turning towards an adhesive signal (following the edges of microchannels coated with adhesive

molecules) or going straight (see **Figure IV-4**). It was found that in this situation cortical axons choose to turn towards the attractive adhesive signal up to angles of 84° . In other words, for larger angles, axons preferred going straight over turning towards the attractive signal. This axonal preference for going straight rather than turn has also been quantified on embryonic frog and chick axons [163]. This phenomenon might explain our results on patterns enabling neurites to continue straight after intersections, on which we saw a marked preference for axons to go straight .

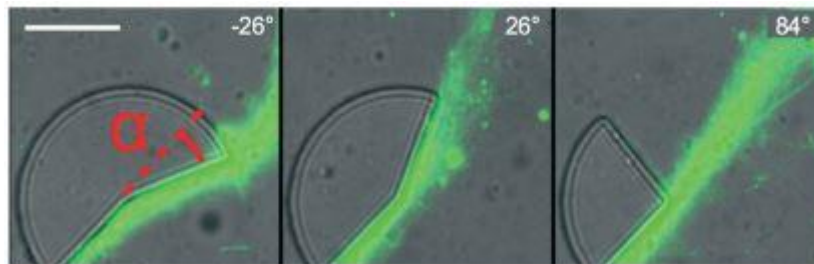


Figure IV-4 : Evolution of the trajectory of cortical axons along an adhesive wall, depending on the intensity of the angle change. Superposition of DIC and fluorescence images (green: microtubules) at DIV 10. For angle changes of -26° and 26° axons follow the wall, but for 84° they prefer going straight. From [130]. Scale bar $25\mu\text{m}$.

IV.D. Conclusion

In conclusion, the behavior of mouse hippocampal neurons on our micropatterned substrates could be explained by a competition between three phenomena affecting the growth cone:

- The urge for the growth cone to explore the entire range of available paths. In the context of our experimental set-up, this favors branching by scission
- The axonal preference for going straight, which explain the behavior of axons on micropatterns where this option is available

- The energetic cost of microtubules bending, which may lead the growth cone to abandon exploration of one available path in favor of an easier one. In the context of our experimental set-up, this leads the growth cone to favor turning in the direction forming the smallest angle with the initial direction.

Bibliography

- [1] A. Ghysen, “The origin and evolution of the nervous system,” *Int. J. Dev. Biol.*, vol. 47, no. 7–8, pp. 555–562, 2003.
- [2] J. T. Kandel ER, Schwartz JH, “Principles of Neural Science,” McGraw-Hil., 2000.
- [3] M. Davies, “The Neuron: size comparison,” *Neuroscience: A journey through the brain*, 2002. .
- [4] E. H. Chudler, “Brain facts and figures: Neuron,” *Neurosciences for Kids*, 2009. [Online]. Available: <http://faculty.washington.edu/chudler/facts.html#neuron>.
- [5] J. W. Hammond, D. Cai, and K. J. Verhey, “Tubulin modifications and their cellular functions.,” *Curr. Opin. Cell Biol.*, vol. 20, no. 1, pp. 71–6, Feb. 2008.
- [6] A. Laser-Azogui, M. Kornreich, E. Malka-Gibor, and R. Beck, “Neurofilament assembly and function during neuronal development,” *Curr. Opin. Cell Biol.*, vol. 32, pp. 92–101, Feb. 2015.
- [7] C. Janke, “The tubulin code: molecular components, readout mechanisms, and functions.,” *J. Cell Biol.*, vol. 206, no. 4, pp. 461–72, Aug. 2014.
- [8] A. Akhmanova and M. O. Steinmetz, “Tracking the ends: a dynamic protein network controls the fate of microtubule tips,” *Nat. Rev. Mol. Cell Biol.*, vol. 9, no. 4, pp. 309–322, Apr. 2008.
- [9] C. H. Coles and F. Bradke, “Coordinating Neuronal Actin–Microtubule Dynamics,” *Curr. Biol.*, vol. 25, no. 15, pp. R677–R691, Aug. 2015.
- [10] J. M. Kollman, A. Merdes, L. Mourey, and D. A. Agard, “Microtubule nucleation by γ -tubulin complexes,” *Nat. Rev. Mol. Cell Biol.*, vol. 12, no. 11, pp. 709–721, Nov. 2011.

- [11] J. Howard and A. A. Hyman, “Growth, fluctuation and switching at microtubule plus ends,” *Nat. Rev. Mol. Cell Biol.*, vol. 10, no. 8, pp. 569–574, Aug. 2009.
- [12] K. C. Flynn, “The cytoskeleton and neurite initiation,” *Bioarchitecture*, vol. 3, no. 4, pp. 86–109, Jul. 2013.
- [13] J. Jaworski *et al.*, “Dynamic Microtubules Regulate Dendritic Spine Morphology and Synaptic Plasticity,” *Neuron*, vol. 61, no. 1, pp. 85–100, Jan. 2009.
- [14] L. C. Kapitein and C. C. Hoogenraad, “Building the Neuronal Microtubule Cytoskeleton,” *Neuron*, vol. 87, no. 3, pp. 492–506, Aug. 2015.
- [15] P. W. Baas, J. S. Deitch, M. M. Black, and G. A. Banker, “Polarity orientation of microtubules in hippocampal neurons: uniformity in the axon and nonuniformity in the dendrite.,” *Proc. Natl. Acad. Sci. U. S. A.*, vol. 85, no. 21, pp. 8335–9, Nov. 1988.
- [16] G. I. Szendrei, V. M.-Y. Lee, and L. Otvos, “Recognition of the minimal epitope of monoclonal antibody Tau-1 depends upon the presence of a phosphate group but not its location,” *J. Neurosci. Res.*, vol. 34, no. 2, pp. 243–249, Feb. 1993.
- [17] M. Stuessi and F. Bradke, “Neuronal polarization: The cytoskeleton leads the way,” *Dev. Neurobiol.*, vol. 71, no. 6, pp. 430–444, Jun. 2011.
- [18] K. G. Campellone and M. D. Welch, “A nucleator arms race: cellular control of actin assembly,” *Nat. Rev. Mol. Cell Biol.*, vol. 11, no. 4, pp. 237–251, Apr. 2010.
- [19] T. D. Pollard, J. A. Cooper, and X. Zhuang, “Actin, a central player in cell shape and movement.,” *Science*, vol. 326, no. 5957, pp. 1208–12, Nov. 2009.
- [20] L. A. Lowery and D. Van Vactor, “The trip of the tip: understanding the growth cone machinery,” *Nat. Rev. Mol. Cell Biol.*, vol. 10, no. 5, pp. 332–343, May 2009.
- [21] A. W. Schaefer, N. Kabir, and P. Forscher, “Filopodia and actin arcs guide the assembly and transport of two populations of microtubules with unique dynamic parameters in neuronal growth cones,” *J. Cell Biol.*, vol. 158, no. 1, pp. 139–152, Jul. 2002.

- [22] G. Ruthel and G. Banker, “Actin-dependent anterograde movement of growth-cone-like structures along growing hippocampal axons: A novel form of axonal transport?,” *Cell Motil. Cytoskeleton*, vol. 40, no. 2, pp. 160–173, Jan. 1998.
- [23] H. Katsuno *et al.*, “Actin Migration Driven by Directional Assembly and Disassembly of Membrane-Anchored Actin Filaments,” *Cell Rep.*, vol. 12, no. 4, pp. 648–660, Jul. 2015.
- [24] C. Tomba *et al.*, “Geometrical Determinants of Neuronal Actin Waves,” *Front. Cell. Neurosci.*, vol. 11, p. 86, 2017.
- [25] K. C. Flynn, C. W. Pak, A. E. Shaw, F. Bradke, and J. R. Bamberg, “Growth cone-like waves transport actin and promote axonogenesis and neurite branching,” *Dev. Neurobiol.*, vol. 69, no. 12, pp. 761–779, 2009.
- [26] S. Mortal *et al.*, “Actin Waves Do Not Boost Neurite Outgrowth in the Early Stages of Neuron Maturation,” *Front. Cell. Neurosci.*, vol. 11, p. 402, Dec. 2017.
- [27] S. M. Lu and R. C. S. Lin, “Thalamic afferents of the rat barrel cortex: A light-and electron-microscopic study using phaseolus vulgaris leucoagglutinin as an anterograde tracer,” *Somatosens. Mot. Res.*, vol. 10, no. 1, pp. 1–16, 1993.
- [28] J. Snider, A. Pillai, and C. F. Stevens, “A universal property of axonal and dendritic arbors,” *Neuron*, vol. 66, no. 1, pp. 45–56, Apr. 2010.
- [29] J. B. Carmel and J. H. Martin, “Motor cortex electrical stimulation augments sprouting of the corticospinal tract and promotes recovery of motor function,” *Front. Integr. Neurosci.*, vol. 8, p. 51, Jun. 2014.
- [30] G. Gallo, “The cytoskeletal and signaling mechanisms of axon collateral branching,” *Dev. Neurobiol.*, vol. 71, no. 3, pp. 201–220, Mar. 2011.
- [31] R. Z. Kuang and K. Kalil, “Development of specificity in corticospinal connections by axon collaterals branching selectively into appropriate spinal targets,” *J. Comp. Neurol.*, vol. 344, no. 2, pp. 270–282, 1994.

- [32] M. Bastmeyer and D. D. O’Leary, “Dynamics of target recognition by interstitial axon branching along developing cortical axons,” *J. Neurosci.*, vol. 16, no. 4, pp. 1450–1459, 1996.
- [33] K. Kalil and E. W. Dent, “Branch management: mechanisms of axon branching in the developing vertebrate CNS,” *Nat. Rev. Neurosci.*, vol. 15, no. 1, pp. 7–18, Jan. 2014.
- [34] L. Ma and M. Tessier-Lavigne, “Dual Branch-Promoting and Branch-Repelling Actions of Slit/Robo Signaling on Peripheral and Central Branches of Developing Sensory Axons,” *J. Neurosci.*, vol. 27, no. 25, pp. 6843–6851, Nov. 2007.
- [35] G. Gallo and P. C. Letourneau, “Localized sources of neurotrophins initiate axon collateral sprouting,” *J. Neurosci.*, vol. 18, no. 14, pp. 5403–14, Jul. 1998.
- [36] M. C. Halloran and K. Kalil, “Dynamic behaviors of growth cones extending in the corpus callosum of living cortical brain slices observed with video microscopy,” *J. Neurosci.*, vol. 14, no. 4, pp. 2161–77, Apr. 1994.
- [37] W. Yu, F. J. Ahmad, and P. W. Baas, “Microtubule fragmentation and partitioning in the axon during collateral branch formation,” *J. Neurosci.*, vol. 14, no. 10, pp. 5872–84, Oct. 1994.
- [38] K. Kalil, G. Szebenyi, and E. W. Dent, “Common mechanisms underlying growth cone guidance and axon branching,” *J. Neurobiol.*, vol. 44, no. 2, pp. 145–158, Aug. 2000.
- [39] G. Gallo, “The cytoskeletal and signaling mechanisms of axon collateral branching,” *Dev. Neurobiol.*, vol. 71, no. 3, pp. 201–220, 2011.
- [40] R. A. Hand, S. Khalid, E. Tam, and A. L. Kolodkin, “Axon Dynamics during Neocortical Laminar Innervation,” *Cell Rep.*, vol. 12, no. 2, pp. 172–182, Jul. 2015.
- [41] A. Ketschek and G. Gallo, “Nerve growth factor induces axonal filopodia through localized microdomains of phosphoinositide 3-kinase activity that drive the formation of cytoskeletal precursors to filopodia,” *J. Neurosci.*, vol. 30, no. 36, pp. 12185–97, Sep. 2010.

- [42] M. Spillane *et al.*, “The actin nucleating Arp2/3 complex contributes to the formation of axonal filopodia and branches through the regulation of actin patch precursors to filopodia,” *Dev. Neurobiol.*, vol. 71, no. 9, pp. 747–758, Sep. 2011.
- [43] Y. Kim *et al.*, “Phosphorylation of WAVE1 regulates actin polymerization and dendritic spine morphology,” *Nature*, vol. 442, no. 7104, pp. 814–817, Jul. 2006.
- [44] R. Ahuja *et al.*, “Cordon-Bleu Is an Actin Nucleation Factor and Controls Neuronal Morphology,” *Cell*, vol. 131, no. 2, pp. 337–350, Oct. 2007.
- [45] J. Fass, S. Gehler, P. Sarmiere, P. Letourneau, and J. R. Bamberg, “Regulating filopodial dynamics through actin-depolymerizing factor/cofilin,” *Anat. Sci. Int.*, vol. 79, no. 4, pp. 173–183, Dec. 2004.
- [46] S. Tilve, F. Difato, and E. Chieragatti, “Cofilin 1 activation prevents the defects in axon elongation and guidance induced by extracellular alpha-synuclein,” *Sci. Rep.*, vol. 5, no. 1, p. 16524, Dec. 2015.
- [47] I. Tint, D. Jean, P. W. Baas, and M. M. Black, “Doublecortin Associates with Microtubules Preferentially in Regions of the Axon Displaying Actin-Rich Protrusive Structures,” *J. Neurosci.*, vol. 29, no. 35, pp. 10995–11010, 2009.
- [48] M. Tsukada, A. Prokscha, E. Ungewickell, and G. Eichele, “Doublecortin association with actin filaments is regulated by neurabin II,” *J. Biol. Chem.*, vol. 280, no. 12, pp. 11361–8, Mar. 2005.
- [49] E. W. Dent, J. L. Callaway, G. Szebenyi, P. W. Baas, and K. Kalil, “Reorganization and movement of microtubules in axonal growth cones and developing interstitial branches,” *J. Neurosci.*, vol. 19, no. 20, pp. 8894–908, Oct. 1999.
- [50] W. Yu, L. Qiang, J. M. Solowska, A. Karabay, S. Korulu, and P. W. Baas, “The Microtubule-severing Proteins Spastin and Katanin Participate Differently in the Formation of Axonal Branches,” *Mol. Biol. Cell*, vol. 19, no. 4, pp. 1485–1498, Apr. 2008.

- [51] L. Qiang, W. Yu, A. Andreadis, M. Luo, and P. W. Baas, “Tau protects microtubules in the axon from severing by katanin,” *J. Neurosci.*, vol. 26, no. 12, pp. 3120–9, Mar. 2006.
- [52] Y. Yokota *et al.*, “The Adenomatous Polyposis Coli Protein Is an Essential Regulator of Radial Glial Polarity and Construction of the Cerebral Cortex,” *Neuron*, vol. 61, no. 1, pp. 42–56, Jan. 2009.
- [53] N. Homma *et al.*, “Kinesin Superfamily Protein 2A (KIF2A) Functions in Suppression of Collateral Branch Extension,” *Cell*, vol. 114, no. 2, pp. 229–239, Jul. 2003.
- [54] H. Koizumi, T. Tanaka, and J. G. Gleeson, “doublecortin-like kinase Functions with doublecortin to Mediate Fiber Tract Decussation and Neuronal Migration,” *Neuron*, vol. 49, no. 1, pp. 55–66, Jan. 2006.
- [55] E. W. Dent and K. Kalil, “Axon branching requires interactions between dynamic microtubules and actin filaments,” *J. Neurosci.*, vol. 21, no. 24, pp. 9757–69, Dec. 2001.
- [56] O. C. Rodriguez, A. W. Schaefer, C. A. Mandato, P. Forscher, W. M. Bement, and C. M. Waterman-Storer, “Conserved microtubule–actin interactions in cell movement and morphogenesis,” *Nat. Cell Biol.*, vol. 5, no. 7, pp. 599–609, Jul. 2003.
- [57] D. C. Worth, C. N. Daly, S. Geraldo, F. Oozeer, and P. R. Gordon-Weeks, “Drebrin contains a cryptic F-actin-bundling activity regulated by Cdk5 phosphorylation,” *J. Cell Biol.*, vol. 202, no. 5, pp. 793–806, Sep. 2013.
- [58] P. J. Sheffield, C. J. Oliver, B. E. Kremer, S. Sheng, Z. Shao, and I. G. Macara, “Borg/septin interactions and the assembly of mammalian septin heterodimers, trimers, and filaments,” *J. Biol. Chem.*, vol. 278, no. 5, pp. 3483–8, Jan. 2003.
- [59] T. Tada, A. Simonetta, M. Batterton, M. Kinoshita, D. Edbauer, and M. Sheng, “Role of Septin Cytoskeleton in Spine Morphogenesis and Dendrite Development in Neurons,” *Curr. Biol.*, vol. 17, no. 20, pp. 1752–1758, Oct. 2007.
- [60] S.-J. Cho, H. Lee, S. Dutta, J. Song, R. Walikonis, and I. S. Moon, “Septin 6 regulates the cytoarchitecture of neurons through localization at dendritic branch points and bases

- of protrusions,” *Mol. Cells*, vol. 32, no. 1, pp. 89–98, Jul. 2011.
- [61] N. Ageta-Ishihara *et al.*, “Septins promote dendrite and axon development by negatively regulating microtubule stability via HDAC6-mediated deacetylation,” *Nat. Commun.*, vol. 4, no. 1, p. 2532, Dec. 2013.
- [62] J. Drinjakovic, H. Jung, D. S. Campbell, L. Strohlic, A. Dwivedy, and C. E. Holt, “E3 Ligase Nedd4 Promotes Axon Branching by Downregulating PTEN,” *Neuron*, vol. 65, no. 3, pp. 341–357, 2010.
- [63] Y. T. Kim, E.-M. Hur, W. D. Snider, and F.-Q. Zhou, “Role of GSK3 Signaling in Neuronal Morphogenesis,” *Front. Mol. Neurosci.*, vol. 4, p. 48, Nov. 2011.
- [64] W. Y. Kim *et al.*, “Essential Roles for GSK-3s and GSK-3-Primed Substrates in Neurotrophin-Induced and Hippocampal Axon Growth,” *Neuron*, vol. 52, no. 6, pp. 981–996, 2006.
- [65] M. Barnat *et al.*, “The GSK3-MAP1B pathway controls neurite branching and microtubule dynamics,” *Mol. Cell. Neurosci.*, vol. 72, pp. 9–21, 2016.
- [66] P. M. Bilimoria, L. de la Torre-Ubieta, Y. Ikeuchi, E. B. E. Becker, O. Reiner, and A. Bonni, “A JIP3-regulated GSK3 β /DCX signaling pathway restricts axon branching,” *J. Neurosci.*, vol. 30, no. 50, pp. 16766–76, Dec. 2010.
- [67] F. Tang and K. Kalil, “Netrin-1 induces axon branching in developing cortical neurons by frequency-dependent calcium signaling pathways,” *J. Neurosci.*, vol. 25, no. 28, pp. 6702–15, Jul. 2005.
- [68] T. M. Gomez and M. Moon, “Balanced Vav2 GEF activity regulates neurite outgrowth and branching in vitro and in vivo,” *Mol. Cell. Neurosci.*, vol. 44, no. 2, pp. 118–128, Jun. 2010.
- [69] M. Spillane, A. Ketschek, C. J. Donnelly, A. Pacheco, J. L. Twiss, and G. Gallo, “Nerve growth factor-induced formation of axonal filopodia and collateral branches involves the intra-axonal synthesis of regulators of the actin-nucleating Arp2/3 complex,” *J.*

- Neurosci.*, vol. 32, no. 49, pp. 17671–89, Dec. 2012.
- [70] R. P. Loudon, L. D. Silver, H. F. Yee, and G. Gallo, “RhoA-kinase and myosin II are required for the maintenance of growth cone polarity and guidance by nerve growth factor,” *J. Neurobiol.*, vol. 66, no. 8, pp. 847–867, Jul. 2006.
- [71] W. a Harris, C. E. Holt, and F. Bonhoeffer, “Retinal axons with and without their somata, growing to and arborizing in the tectum of *Xenopus* embryos: a time-lapse video study of single fibres in vivo.,” *Development*, vol. 101, no. 1, pp. 123–133, 1987.
- [72] B. M. Davis, E. Frank, F. A. Johnson, and S. A. Scott, “Development of central projections of lumbosacral sensory neurons in the chick,” *J. Comp. Neurol.*, vol. 279, no. 4, pp. 556–566, Jan. 1989.
- [73] H. Schmidt *et al.*, “The receptor guanylyl cyclase Npr2 is essential for sensory axon bifurcation within the spinal cord.,” *J. Cell Biol.*, vol. 179, no. 2, pp. 331–40, Oct. 2007.
- [74] K. M. Knobel, W. S. Davis, E. M. Jorgensen, and M. J. Bastiani, “UNC-119 suppresses axon branching in *C. elegans*.,” *Development*, vol. 128, pp. 4079–4092, 2001.
- [75] N. K. Wessells and R. P. Nuttall, “Normal branching, induced branching, and steering of cultured parasympathetic motor neurons,” *Exp. Cell Res.*, vol. 115, no. 1, pp. 111–122, Aug. 1978.
- [76] R. A. Oakley¹ and K. W. Tosney^{1,2}, “Contact-mediated Mechanisms of Motor Axon Segmentation,” *J. Neurosci.*, vol. 73, no. g, pp. 3773–3792, 1993.
- [77] O. I. Kahn and P. W. Baas, “Microtubules and Growth Cones: Motors Drive the Turn,” *Trends Neurosci.*, vol. 39, no. 7, pp. 433–440, Jul. 2016.
- [78] E. W. Dent, S. L. Gupton, and F. B. Gertler, “The growth cone cytoskeleton in axon outgrowth and guidance.,” *Cold Spring Harb. Perspect. Biol.*, vol. 3, no. 3, p. a001800, Mar. 2011.
- [79] P. K. Mattila and P. Lappalainen, “Filopodia: molecular architecture and cellular functions,” *Nat. Rev. Mol. Cell Biol.*, vol. 9, no. 6, pp. 446–454, Jun. 2008.

- [80] S. R. Heidemann, P. Lamoureux, and R. E. Buxbaum, "Growth cone behavior and production of traction force.," *J. Cell Biol.*, vol. 111, no. 5 Pt 1, pp. 1949–57, Nov. 1990.
- [81] C. E. Chan and D. J. Odde, "Traction Dynamics of Filopodia on Compliant Substrates," *Science (80-.)*, vol. 322, no. 5908, pp. 1687–1691, Dec. 2008.
- [82] P. C. Letourneau, "Differences in the organization of actin in the growth cones compared with the neurites of cultured neurons from chick embryos.," *J. Cell Biol.*, vol. 97, no. 4, pp. 963–73, Oct. 1983.
- [83] A. C. Lee and D. M. Suter, "Quantitative analysis of microtubule dynamics during adhesion-mediated growth cone guidance," *Dev. Neurobiol.*, vol. 68, no. 12, pp. 1363–1377, Oct. 2008.
- [84] D. M. Suter, A. W. Schaefer, and P. Forscher, "Microtubule Dynamics Are Necessary for Src Family Kinase-Dependent Growth Cone Steering," *Curr. Biol.*, vol. 14, no. 13, pp. 1194–1199, Jul. 2004.
- [85] B. M. Marsick, K. C. Flynn, M. Santiago-Medina, J. R. Bamberg, and P. C. Letourneau, "Activation of ADF/cofilin mediates attractive growth cone turning toward nerve growth factor and netrin-1," *Dev. Neurobiol.*, vol. 70, no. 8, pp. 565–588, Jun. 2010.
- [86] C. H. Lin, E. M. Espreafico, M. S. Mooseker, and P. Forscher, "Myosin drives retrograde F-actin flow in neuronal growth cones.," *Neuron*, vol. 16, no. 4, pp. 769–82, Apr. 1996.
- [87] E. A. Vitriol and J. Q. Zheng, "Growth Cone Travel in Space and Time: the Cellular Ensemble of Cytoskeleton, Adhesion, and Membrane," *Neuron*, vol. 73, no. 6, pp. 1068–1081, Mar. 2012.
- [88] J. H. Hines, M. Abu-Rub, and J. R. Henley, "Asymmetric endocytosis and remodeling of β 1-integrin adhesions during growth cone chemorepulsion by MAG," *Nat. Neurosci.*, vol. 13, no. 7, pp. 829–837, Jul. 2010.
- [89] A. W. Schaefer, V. T. G. Schoonderwoert, L. Ji, N. Mederios, G. Danuser, and P. Forscher, "Coordination of Actin Filament and Microtubule Dynamics during Neurite

- Outgrowth,” *Dev. Cell*, vol. 15, no. 1, pp. 146–162, Jul. 2008.
- [90] E.-E. Govek, S. E. Newey, and L. Van Aelst, “The role of the Rho GTPases in neuronal development,” *Genes Dev.*, vol. 19, no. 1, pp. 1–49, Jan. 2005.
- [91] M. Watabe-Uchida, E.-E. Govek, and L. Van Aelst, “Regulators of Rho GTPases in neuronal development,” *J. Neurosci.*, vol. 26, no. 42, pp. 10633–5, Oct. 2006.
- [92] O. C. Pertz *et al.*, “Spatial mapping of the neurite and soma proteomes reveals a functional Cdc42/Rac regulatory network,” *Proc. Natl. Acad. Sci.*, vol. 105, no. 6, pp. 1931–1936, Feb. 2008.
- [93] G. Gallo, “RhoA-kinase coordinates F-actin organization and myosin II activity during semaphorin-3A-induced axon retraction,” *J. Cell Sci.*, vol. 119, no. 16, pp. 3413–3423, Jul. 2006.
- [94] Z. Wen, L. Han, J. R. Bamberg, S. Shim, G. Ming, and J. Q. Zheng, “BMP gradients steer nerve growth cones by a balancing act of LIM kinase and Slingshot phosphatase on ADF/cofilin,” *J. Cell Biol.*, vol. 178, no. 1, pp. 107–19, Jul. 2007.
- [95] S. K. Mitra, D. A. Hanson, and D. D. Schlaepfer, “Focal adhesion kinase: in command and control of cell motility,” *Nat. Rev. Mol. Cell Biol.*, vol. 6, no. 1, pp. 56–68, Jan. 2005.
- [96] M. R. Chacón and P. Fazzari, “FAK,” *Cell Adh. Migr.*, vol. 5, no. 1, pp. 52–55, Jan. 2011.
- [97] A. Bechara *et al.*, “FAK–MAPK-dependent adhesion disassembly downstream of L1 contributes to semaphorin3A-induced collapse,” *EMBO J.*, vol. 27, no. 11, pp. 1549–1562, Jun. 2008.
- [98] J. P. Myers and T. M. Gomez, “Focal Adhesion Kinase Promotes Integrin Adhesion Dynamics Necessary for Chemotropic Turning of Nerve Growth Cones,” *J. Neurosci.*, vol. 31, no. 38, pp. 13585–13595, Sep. 2011.
- [99] A. V Karginov, F. Ding, P. Kota, N. V Dokholyan, and K. M. Hahn, “Engineered allosteric activation of kinases in living cells,” *Nat. Biotechnol.*, vol. 28, no. 7, pp. 743–

- 747, Jul. 2010.
- [100] J. K. Slack-Davis *et al.*, “Cellular Characterization of a Novel Focal Adhesion Kinase Inhibitor,” *J. Biol. Chem.*, vol. 282, no. 20, pp. 14845–14852, May 2007.
- [101] I. Dupin, M. Dahan, and V. Studer, “Investigating axonal guidance with microdevice-based approaches,” *J. Neurosci.*, vol. 33, no. 45, pp. 17647–55, Nov. 2013.
- [102] D. L. Benson, F. H. Watkins, O. Steward, and G. Banker, “Characterization of GABAergic neurons in hippocampal cell cultures,” *J. Neurocytol.*, vol. 23, no. 5, pp. 279–295, 1994.
- [103] C. G. Dotti, C. A. Sullivan, and G. A. Banker, “The establishment of polarity by hippocampal neurons in culture,” *J. Neurosci.*, vol. 8, no. 4, pp. 1454–68, Apr. 1988.
- [104] E. Marconi *et al.*, “Emergent Functional Properties of Neuronal Networks with Controlled Topology,” *PLoS One*, vol. 7, no. 4, p. e34648, Apr. 2012.
- [105] M. D. Boehler, S. S. Leondopulos, B. C. Wheeler, and G. J. Brewer, “Hippocampal networks on reliable patterned substrates,” *J. Neurosci. Methods*, vol. 203, no. 2, pp. 344–353, Jan. 2012.
- [106] M. Shein-Idelson, E. Ben-Jacob, and Y. Hanein, “Engineered Neuronal Circuits: A New Platform for Studying the Role of Modular Topology,” *Front. Neuroeng.*, vol. 4, p. 10, Sep. 2011.
- [107] C. S. Chen, M. Mrksich, S. Huang, G. M. Whitesides, and D. E. Ingber, “Geometric control of cell life and death,” *Science*, vol. 276, no. 5317, pp. 1425–8, May 1997.
- [108] W. R. Kim, M. J. Jang, S. Joo, W. Sun, and Y. Nam, “Surface-printed microdot array chips for the quantification of axonal collateral branching of a single neuron in vitro,” *Lab Chip*, vol. 14, no. 4, pp. 799–805, 2014.
- [109] P. Roach, T. Parker, N. Gadegaard, and M. R. Alexander, “Surface strategies for control of neuronal cell adhesion : A review,” *Surf. Sci. Rep.*, vol. 65, no. 6, pp. 145–173, 2010.

- [110] M. Théry *et al.*, “Anisotropy of cell adhesive microenvironment governs cell internal organization and orientation of polarity.,” *Proc. Natl. Acad. Sci. U. S. A.*, vol. 103, no. 52, pp. 19771–6, Dec. 2006.
- [111] J. Tang, R. Peng, and J. Ding, “The regulation of stem cell differentiation by cell-cell contact on micropatterned material surfaces,” *Biomaterials*, vol. 31, no. 9, pp. 2470–2476, Mar. 2010.
- [112] X. Jiang, D. A. Bruzewicz, A. P. Wong, M. Piel, and G. M. Whitesides, “Directing cell migration with asymmetric micropatterns.,” *Proc. Natl. Acad. Sci. U. S. A.*, vol. 102, no. 4, pp. 975–8, Jan. 2005.
- [113] M. Théry, “Micropatterning as a tool to decipher cell morphogenesis and functions.,” *J. Cell Sci.*, vol. 123, no. Pt 24, pp. 4201–13, Dec. 2010.
- [114] C. Wyart, C. Ybert, L. Bourdieu, C. Herr, C. Prinz, and D. Chatenay, “Constrained synaptic connectivity in functional mammalian neuronal networks grown on patterned surfaces,” *J. Neurosci. Methods*, vol. 117, no. 2, pp. 123–131, 2002.
- [115] S. Roth *et al.*, “How Morphological Constraints Affect Axonal Polarity in Mouse Neurons,” *PLoS One*, vol. 7, no. 3, p. e33623, Mar. 2012.
- [116] S. Roth, G. Bugnicourt, M. Bisbal, S. Gory-Fauré, J. Brocard, and C. Villard, “Neuronal Architectures with Axo-dendritic Polarity above Silicon Nanowires,” *Small*, vol. 8, no. 5, pp. 671–675, Mar. 2012.
- [117] C. Tomba, C. Braïni, B. Wu, N. S. Gov, and C. Villard, “Tuning the adhesive geometry of neurons: length and polarity control,” *Soft Matter*, vol. 10, no. 14, p. 2381, Mar. 2014.
- [118] R. Fricke *et al.*, “Axon guidance of rat cortical neurons by microcontact printed gradients,” *Biomaterials*, vol. 32, no. 8, pp. 2070–2076, Mar. 2011.
- [119] M. Jungblut, W. Knoll, C. Thielemann, and M. Pottek, “Triangular neuronal networks on microelectrode arrays: an approach to improve the properties of low-density networks for extracellular recording,” *Biomed. Microdevices*, vol. 11, no. 6, pp. 1269–1278, Dec.

- 2009.
- [120] D. Edwards, M. Stancescu, P. Molnar, and J. J. Hickman, “Two Cell Circuits of Oriented Adult Hippocampal Neurons on Self-Assembled Monolayers for Use in the Study of Neuronal Communication in a Defined System,” *ACS Chem. Neurosci.*, vol. 4, no. 8, pp. 1174–1182, Aug. 2013.
- [121] X. Leinekugel, R. Khazipov, R. Cannon, H. Hirase, Y. Ben-Ari, and G. Buzsáki, “Correlated bursts of activity in the neonatal hippocampus in vivo.,” *Science*, vol. 296, no. 5575, pp. 2049–52, Jun. 2002.
- [122] B. C. Wheeler and G. J. Brewer, “Designing Neural Networks in Culture,” *Proc. IEEE*, vol. 98, no. 3, pp. 398–406, Mar. 2010.
- [123] M. J. Aebersold *et al.*, “‘Brains on a chip’: Towards engineered neural networks,” *TrAC - Trends Anal. Chem.*, vol. 78, pp. 60–69, 2016.
- [124] G. S. Withers, C. D. James, C. E. Kingman, H. G. Craighead, and G. A. Banker, “Effects of substrate geometry on growth cone behavior and axon branching,” *J. Neurobiol.*, vol. 66, no. 11, pp. 1183–1194, Sep. 2006.
- [125] A. Azioune, N. Carpi, Q. Tseng, M. Théry, and M. Piel, “Protein Micropatterns: A Direct Printing Protocol Using Deep UVs,” *Methods Cell Biol.*, vol. 97, pp. 133–146, Jan. 2010.
- [126] G. M. Whitesides and A. Kumar, “Formation of microstamped patterns on surfaces and derivative articles,” 04-Oct-1993.
- [127] M. Théry and M. Piel, “Adhesive micropatterns for cells: a microcontact printing protocol.,” *Cold Spring Harb. Protoc.*, vol. 2009, no. 7, p. pdb.prot5255, Jul. 2009.
- [128] A. Yamada *et al.*, “In-mold patterning and actionable axo-somatic compartmentalization for on-chip neuron culture,” *Lab Chip*, vol. 16, no. 11, pp. 2059–2068, May 2016.
- [129] J.-M. Peyrin *et al.*, “Axon diodes for the reconstruction of oriented neuronal networks in microfluidic chambers,” *Lab Chip*, vol. 11, no. 21, p. 3663, Oct. 2011.

- [130] R. Renault, J.-B. Durand, J.-L. Viovy, and C. Villard, “Asymmetric axonal edge guidance: a new paradigm for building oriented neuronal networks,” *Lab Chip*, vol. 16, no. 12, pp. 2188–2191, Jun. 2016.
- [131] W. Liu, S. Xing, B. Yuan, W. Zheng, and X. Jiang, “Change of laminin density stimulates axon branching via growth cone myosin II-mediated adhesion,” *Integr. Biol.*, vol. 5, no. 10, p. 1244, Sep. 2013.
- [132] H. Dermutz, R. R. Grüter, A. M. Truong, L. Demko, J. Vörös, and T. Zambelli, “Local Polymer Replacement for Neuron Patterning and in Situ Neurite Guidance,” *Langmuir*, vol. 30, pp. 7037–7046, 2014.
- [133] A. K. Vogt, G. J. Brewer, and A. Offenhäusser, “Connectivity patterns in neuronal networks of experimentally defined geometry.,” *Tissue Eng.*, vol. 11, no. 11–12, pp. 1757–67, 2005.
- [134] G. Szebenyi, J. L. Callaway, E. W. Dent, and K. Kalil, “Interstitial branches develop from active regions of the axon demarcated by the primary growth cone during pausing behaviors.,” *J. Neurosci.*, vol. 18, no. 19, pp. 7930–40, Oct. 1998.
- [135] C. Mason and L. Erskine, “Growth cone form, behavior, and interactions in vivo: retinal axon pathfinding as a model.,” *J. Neurobiol.*, vol. 44, no. 2, pp. 260–70, Aug. 2000.
- [136] G. Bugnicourt, “Adhésion, croissance et polarisation de neurones sur substrats micro- et nano- structurés,” Université Joseph Fourier - Grenoble 1, 2006.
- [137] S. Roth, “Réseaux de neurones modèles: Contrôle de la différenciation axonale par micropatterns,” Université Joseph Fourier - Grenoble 1, 2009.
- [138] C. Tomba, “Primary brain cells in in vitro controlled microenvironments : single cells behaviors for collective functions,” Université Joseph Fourier - Grenoble 1, 2014.
- [139] C. Braini, “Approche biophysique des formes neuronales,” Communauté Université Grenoble Alpes, 2016.
- [140] Y. Ikegaya, Y. Itsukaichi-Nishida, M. Ishihara, D. Tanaka, and N. Matsuki, “Distance

- of target search of isolated rat hippocampal neuron is about 150 μm ,” *Neuroscience*, vol. 97, no. 2, pp. 215–217, Apr. 2000.
- [141] G. A. Banker and W. M. Cowan, “Rat hippocampal neurons in dispersed cell culture,” *Brain Res.*, vol. 126, no. 3, pp. 397–425, May 1977.
- [142] S. Kaech and G. Banker, “Culturing hippocampal neurons,” 2007.
- [143] T. Fath, Y. D. Ke, P. Gunning, J. Götz, and L. M. Ittner, “Primary support cultures of hippocampal and substantia nigra neurons,” *Nat. Protoc.*, vol. 4, no. 1, pp. 78–85, Jan. 2009.
- [144] *,†,‡,§ Tahir A. Mahmood *et al.*, “Modulation of Chondrocyte Phenotype for Tissue Engineering by Designing the Biologic–Polymer Carrier Interface,” 2006.
- [145] T. A. Mahmood, R. de Jong, J. Riesle, R. Langer, and C. A. van Blitterswijk, “Adhesion-mediated signal transduction in human articular chondrocytes: the influence of biomaterial chemistry and tenascin-C,” *Exp. Cell Res.*, vol. 301, no. 2, pp. 179–188, Dec. 2004.
- [146] † K. Feldman, *,† G. Hähner, † N. D. Spencer, ‡ and P. Harder, and ‡ M. Grunze*, “Probing Resistance to Protein Adsorption of Oligo(ethylene glycol)-Terminated Self-Assembled Monolayers by Scanning Force Microscopy,” 1999.
- [147] Y. Chen *et al.*, “Comparative assessment of the stability of nonfouling poly(2-methyl-2-oxazoline) and poly(ethylene glycol) surface films: An *in vitro* cell culture study,” *Biointerphases*, vol. 9, no. 3, p. 031003, Sep. 2014.
- [148] T. Koga, A. Nagaoka, and N. Higashi, “Fabrication of a switchable nano-surface composed of acidic and basic block-polypeptides,” *Colloids Surfaces A Physicochem. Eng. Asp.*, vol. 284–285, pp. 521–527, Aug. 2006.
- [149] T. Sun *et al.*, “Reversible Switching between Superhydrophilicity and Superhydrophobicity,” *Angew. Chemie Int. Ed.*, vol. 43, no. 3, pp. 357–360, Jan. 2004.
- [150] J. P. Ranieri, R. Bellamkonda, E. J. Bekos, T. G. Vargo, J. A. Gardella, and P. Aebischer,

- “Neuronal cell attachment to fluorinated ethylene propylene films with covalently immobilized laminin oligopeptides YIGSR and IKVAV. II,” *J. Biomed. Mater. Res.*, vol. 29, no. 6, pp. 779–785, 1995.
- [151] Y. Iwamoto, F. A. Robey, J. Graf, M. Sasaki, K. Hynda, and G. R. Martin, “YIGSR , a Synthetic Laminin Pentapeptide , Inhibits Experimental Metastasis Formation Kleinman , Yoshihiko Yamada and George R . Martin Published by: American Association for the Advancement of Science Stable URL : <http://www.jstor.org/stable/1700857> REF,” vol. 238, no. 4830, pp. 1132–1134, 2016.
- [152] “AlveoleLab website.” [Online]. Available: www.alveolelab.com.
- [153] R. Scorcioni, M. T. Lazarewicz, and G. A. Ascoli, “Quantitative morphometry of hippocampal pyramidal cells: Differences between anatomical classes and reconstructing laboratories,” *J. Comp. Neurol.*, vol. 473, no. 2, pp. 177–193, May 2004.
- [154] S. F. M. van Dongen, P. Maiuri, E. Marie, C. Tribet, and M. Piel, “Triggering Cell Adhesion, Migration or Shape Change with a Dynamic Surface Coating,” *Adv. Mater.*, vol. 25, no. 12, pp. 1687–1691, Mar. 2013.
- [155] S. F. M. van Dongen, J. Janvore, S. S. van Berkel, E. Marie, M. Piel, and C. Tribet, “Reactive protein-repellent surfaces for the straightforward attachment of small molecules up to whole cells,” *Chem. Sci.*, vol. 3, no. 10, p. 3000, Aug. 2012.
- [156] T. Fardet, “Growth and activity of neuronal cultures, Emergence of organized behaviors,” 2018.
- [157] P. W. Grabham, “Microtubule and Rac 1-dependent F-actin in growth cones,” *J. Cell Sci.*, vol. 116, no. 18, pp. 3739–3748, 2003.
- [158] A. S. Nezhad and A. Geitmann, “The cellular mechanics of an invasive lifestyle,” *J. Exp. Bot.*, vol. 64, no. 15, pp. 4709–4728, 2013.
- [159] L. Armijo-Weingart and G. Gallo, “It takes a village to raise a branch: Cellular mechanisms of the initiation of axon collateral branches,” *Mol. Cell. Neurosci.*, vol. 84,

pp. 36–47, Oct. 2017.

- [160] E. Tanaka and J. Sabry, “Making the Connection: Cytoskeletal Rearrangements during Growth Cone Guidance,” *Cell*, vol. 83, pp. 171–176, 1995.
- [161] P. C. Letourneau, T. A. Shattuck, and A. H. Ressler, “Branching of Sensory and Sympathetic Neurites in vitro Is Inhibited by Treatment with Taxol,” *J. Neurosci ence*, vol. 6, no. 7, pp. 1912–1917, 1966.
- [162] S. J. Peter and M. R. K. Mofrad, “Computational modeling of axonal microtubule bundles under tension.,” *Biophys. J.*, vol. 102, no. 4, pp. 749–57, Feb. 2012.
- [163] M. J. Katz, “How straight do axons grow?,” *J. Neurosci.*, vol. 5, no. 3, pp. 589–595, 1985.

Chapter V. Appendix

V.A. List of all the branching configurations possible on the micropatterns

As explained in **Chapter III**, each type of pattern gives the possibility to observe several branching angles, according to the position of the soma on the pattern. Here, we detail the list of possible branching configurations for the micropatterns used in this work. We adopted the corresponding color code: red for the mother branch, green for the daughter branches, dark purple for the micropatterns of adhesion.

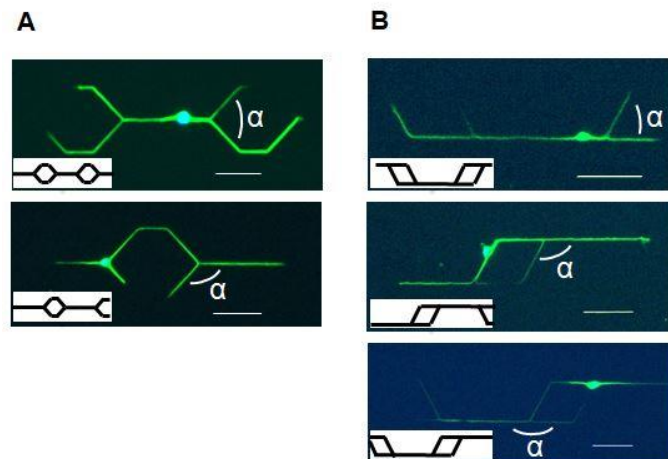
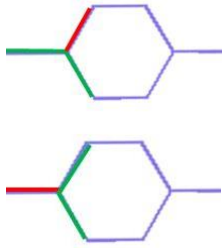
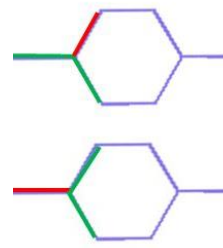
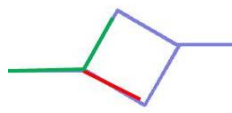
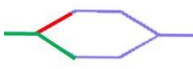
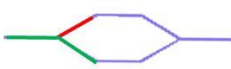
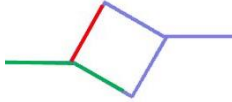
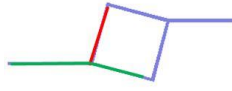
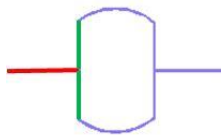
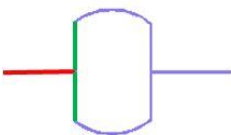
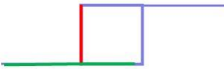
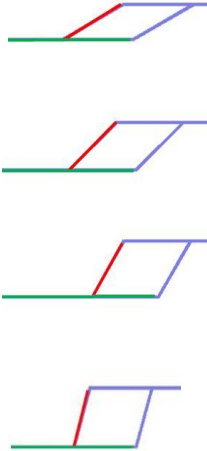


Figure V-1 : Examples of neurons on micropatterned substrates. Depending on the positioning of the soma, different branching angles can be observed on the same pattern. **A.** Fluorescence images of neurons at DIV2 on substrates patterned with mask 3, zone1, pattern D. Top: $\alpha=90^\circ$. Bottom: $\alpha=135^\circ$. Green: β_3 -tubulin, Blue: Hoechst (nucleus). Scale bar: $50\mu\text{m}$. **B.** Fluorescence images of neurons at DIV2 on substrates patterned with mask 3, zone2, pattern C. Top: $\alpha=60^\circ$. Middle: $\alpha=120^\circ$. Bottom: $\alpha=180^\circ$. Green: β_3 -tubulin, Blue: Hoechst (nucleus). Scale bar: $50\mu\text{m}$.

Branching angle α	Mask n°1	Mask n°2	Mask n°3 Zone 1	Mask n°3 Zone 2
30°				
45°				
60°				
75°				
90°	 	 	   	
105°				
112.5°				

Branching angle α	Mask n°1	Mask n°2	Mask n°3 Zone 1	Mask n°3 Zone 2
120°				
135°				
150°				
157.5°				
165°				
180°				

V.B. List of all the branching configurations possible on the micropatterns
with $\alpha_1 = 0$

Branching angle α	Mask n°3 Zone 1	Mask n°3 Zone 2
30°		
45°		
60°		
75°		
90°		
105°		
120°		
135°		
150°		

Résumé

Ce résumé a pour objectif de donner au public non-anglophone un aperçu du travail effectué durant la thèse. Pour chaque chapitre l'introduction est traduite, puis les principaux résultats sont présentés, avec des références aux figures du manuscrit.

Introduction générale

Le fonctionnement du système nerveux repose sur la mise en place de réseaux neuronaux complexes. Pendant le développement embryonnaire, le branchement axonal permet à chaque neurone d'établir des contacts synaptiques avec de multiples cibles. Par exemple, les axons corticaux du thalamus peuvent ramifier dans les cortex moteur, somatosensoriel et sensoriels. Par conséquent, la compréhension des mécanismes du branchement neuronal est essentielle à l'étude du développement des circuits nerveux.

Les cultures de neurones *in vitro* permettent une imagerie des cellules facilitée ainsi qu'un niveau de contrôle plus élevé sur le microenvironnement des cellules. Pour contrôler cet environnement, il est possible d'utiliser des outils de microfabrication à l'origine développée pour la microélectronique. Le micropatterning (de l'anglais *pattern* : motif) a été développé il y a deux décades avec pour objectif de contrôler la forme et la position des cellules nerveuses. Cette technologie rend possible la reconstitution du microenvironnement physiologique *in vitro* de manière contrôlée. Pour cette raison, le micropatterning a souvent été utilisé pour étudier les mécanismes biologiques complexes à l'origine de la polarisation, le guidage de l'axone, et le branchement.

Pendant cette thèse, nous avons mené une étude du branchement en imposant des contraintes morphologiques aux neurones à l'aide de différentes techniques de micropatterning chimique. (i) En utilisant des micropatterns statiques, nous avons exploré le comportement de branchement dans une large gamme de géométries en nous concentrant sur l'influence de l'angle de branchement (ii) En parallèle, nous avons aussi travaillé sur le développement d'une technique de patterning dynamique basée sur l'adsorption spontanée de dérivés de poly-L-lysine afin de former des motifs reconfigurable sur des surfaces répulsives pour les cellules, dans le but de créer une plateforme permettant la génération de branches neuritiques *in situ*, contrôlable spatio-temporellement.

Dans le Chapitre I, nous introduirons le contexte général de cette thèse en présentant la structure des cellules neuronales, les principales étapes du développement neuronal *in vitro*, et le branchement neuronal. Nous concluons ce chapitre avec un état de l'art des principaux exemples dans la littérature d'études du branchement neuronal menés avec des outils de microfabrication. Le Chapitre II portera sur les méthodes employées pendant la thèse. Dans le Chapitre III, nous présenterons nos principaux résultats expérimentaux. Dans un premier temps, nous étudierons le comportement des neurones sur des substrats patternés avec des lignes adhésives étroites s'interceptant à différents angles. Les distributions de probabilité de branchement ainsi que des longueurs des branches en fonction de l'angle de branchement seront analysées. Le Chapitre IV consistera en une discussion des résultats acquis pendant la thèse.

Au sein de ce résumé nous ferons principalement sur une synthèse des résultats et de leur discussion, qui constituent pour moi le cœur de la thèse.

Résultats

Il a été observé dans de nombreuses études que la géométrie du substrat influence le branchement des neurites [124]. Pendant ce doctorat, nous avons étudié cette question en imposant des contraintes morphologiques aux neurones à l'aide de différentes techniques de micropatterning chimiques.

Dans un premier temps, nous avons caractérisé le branchement neuronal sur des substrats patternés avec des lignes s'interceptant à différents angles. Les distributions de probabilité de branchement et de longueurs de branches ont été mesurées en fonction de l'angle de branchement. Des timelapses de neurones sur des substrats micropatternés nous ont aussi permis d'analyser la dynamique du cône de croissance lors d'événements de branchement et de turning.

Micropatterning statique pour étudier le branchement neuronal

Introduction

En utilisant la technologie du micropatterning, basée sur la photolithographie, nous avons mis au point un motif (*pattern*) composé de formes polygonales régulièrement espacées, reliées par des lignes droites. Les sommets de ces formes polygonales définissent le point de rencontre de trois lignes s'intersectant à des angles variés (selon la géométrie de la forme polygonale). A chaque intersection, des neurites poussant sur une ligne droite se retrouvent face à un choix entre deux chemins différents, et peuvent choisir ou bien de brancher, ou bien de tourner (voir **Figure III-1**).

Dans un premier temps, nous avons effectué une étude préliminaire de la morphologie du cône de croissance sur des substrats micropatternés. En effet, comme cela est présenté dans le Chapitre I, le cône de croissance joue un rôle fondamental dans le phénomène du branchement. Ensuite, nous avons joué avec les différents paramètres angulaires caractérisant les patterns afin de quantifier la manière dont la décision de brancher est influencée par une géométrie symétrique ou asymétrique. Après cela, nous avons décidé de poursuivre l'analyse en comparant les comportements de branchements entre axones et neurites undifferentiés. Puis, nous avons mesuré les longueurs des branches neuritiques dans toutes les configurations angulaires possibles afin de mieux comprendre l'influence de la géométrie du substrat sur le branchement neuritique et la croissance neuronale.

Même si ces deux premières étapes nous ont fourni de précieuses informations, elles ont été réalisées sur des échantillons fixés et ont dû être complétées par une analyse dynamique du branchement. C'est pourquoi, dans la dernière partie de notre étude, nous avons examinés des timelapses de neurones se développant sur des substrats micropatternés. Ces expériences nous ont permis de commencer une caractérisation de la cinétique du branchement dans notre set-up expérimental. Nous avons décidé de nous concentrer particulièrement sur l'un des paramètres clés de la cinétique du branchement : le temps de pause du cône de croissance aux points de branchements.

Méthodologie

Au cours de cette étude, nous avons surtout observé le branchement de neurones d'hippocampes de souris jusqu'au stade 3 du développement *in vitro* (voir **Figure I-25**). Cela correspond typiquement à 2-3 jours *in vitro* (DIV : Days In Vitro).

Nous avons défini 3 paramètres pour caractériser le comportement de branchement et de turning aux intersections. Comme on peut le voir dans la **Figure III-1**, le premier paramètre, α , correspond à l'angle entre 2 branches filles.

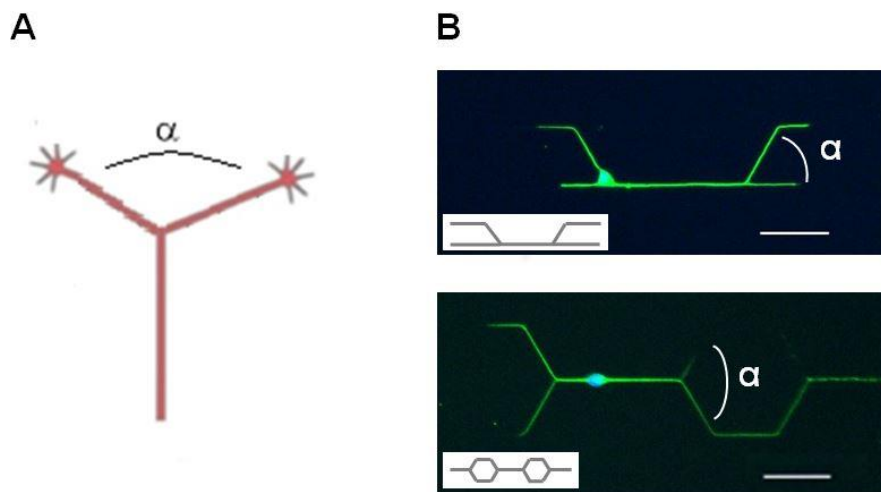


Figure III-1 : Définition du paramètre α . A) Schéma représentant la définition de α comme étant l'angle entre deux branches filles. B) Exemples des valeurs de α pour des neurones branchant sur des micropatterns. Image en fluorescence de neurones d'hippocampes de souris E16 fixés à DIV2 : Vert : β_3 -tubulin. Bleu : Hoechst (noyau). En haut : $\alpha=60^\circ$, en bas : $\alpha=120^\circ$. Encart : Pattern adhésif. Barre d'échelle : $50\mu\text{m}$.

Le deuxième paramètre, (α_1, α_2) , représente les angles entre la direction du neurite incident et la direction de chaque branche fille. Nous avons choisi la convention $\alpha_1 \leq \alpha_2$.

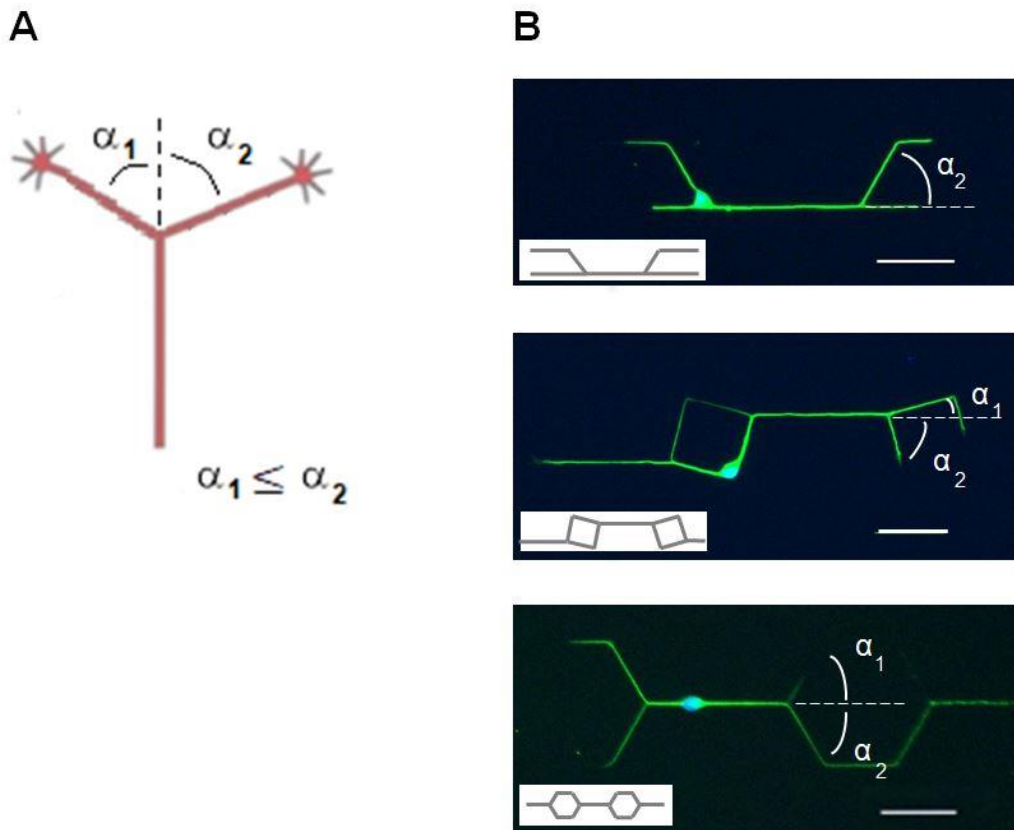


Figure III-2 : Définition du paramètre (α_1, α_2) A) Schéma représentant la définition de (α_1, α_2) , comme étant les angles entre la direction du neurite incident et la direction de chaque branche fille, $\alpha_1 \leq \alpha_2$. B) Exemple de valeurs de (α_1, α_2) . Images en fluorescence de neurones d'hippocampes d'embryons de souris E16 fixés à DIV2. Vert : β_3 -tubulin. Bleu : Hoechst (noyau). En haut : $\alpha_1=0^\circ$ et $\alpha_2 = 60^\circ$, Milieu : $\alpha_1=15^\circ$ and $\alpha_2 = 75^\circ$, en bas : $\alpha_1=60^\circ$ and $\alpha_2 = 60^\circ$. Encart : Pattern adhésif. Barre d'échelle : 50 μ m.

Ces paramètres nous ont permis de distinguer 2 catégories de branchement : le branchement « asymétrique » et le branchement symétrique, défini par $\alpha_1 = \alpha_2$ et $\alpha_1 \neq \alpha_2$ respectivement.

Le contrôle de cette géométrie d'adhésion nous a permis de réaliser une analyse angulaire du branchement dans différentes configurations. Plusieurs types de patterns ont été créés. Comme il a été observé que les neurites des neurones d'hippocampes se développant *in vitro* sur des surfaces uniformément adhésives ont une largeur de 1-2 μ m [162], nous avons choisi des lignes d'épaisseur de 2 μ m pour dessiner nos patterns, afin de se rapprocher de ces caractéristiques

morphologiques spontanées. Le détail des différents masques utilisés figure dans le Chapitre III, voir la figure ci-dessous pour des exemples de neurones sur nos substrats micropatternés.

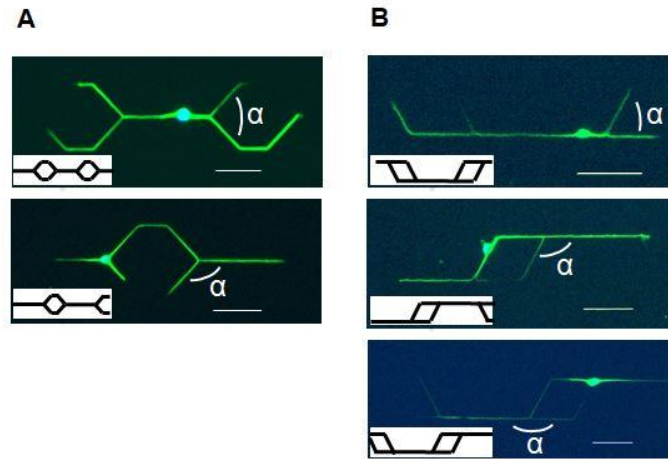


Figure III-7 : Exemples de neurones sur des substrats micropatternés. Selon le positionnement du soma sur le motif d'adhésion, différents angles de branchements peuvent être observé sur le même pattern. A. et B. Images en fluorescence de neurones à DIV2 sur des substrats patternés. Vert : β_3 -tubulin. Bleu : Hoechst (noyau). Encart : Pattern adhésif. Barre d'échelle : 50 μ m.

Analyse de la morphologie du cône de croissance

Nous avons tout d'abord caractérisé la morphologie du cône de croissance en mesurant un paramètre que nous appellerons β et qui correspond à l'écart angulaire des filopodes du cône de croissance. Les cônes de croissance en train de brancher ont été exclu de cette analyse.

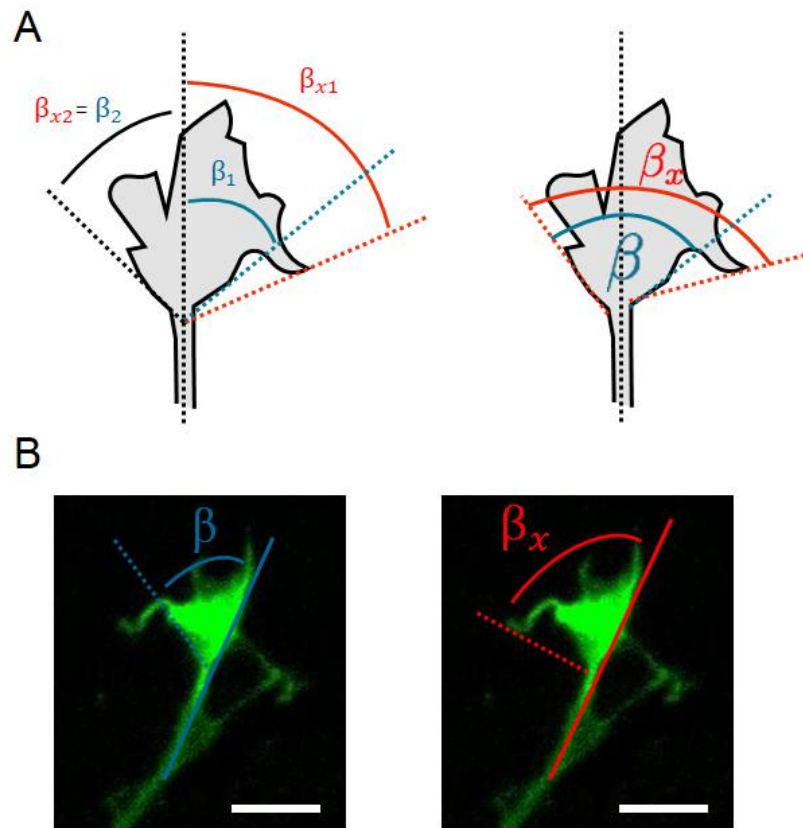


Figure III-8 : Caractérisation de la morphologie du cône de croissance avec les paramètres β and β_x : A : Schéma représentant les définitions des paramètres. B. Images en fluorescence de cône de croissance de neurones d'hippocampes fixés à DIV1. Vert : F-Actine. Barre d'échelle : 10 μ m.

En raison de la complexité et de la diversité des morphologies de cônes de croissance, nous avons décidé d'ajouter un nouveau paramètre β_x . Alors que le paramètre β caractérise la forme du principal corps du cône de croissance, β_x prend en compte toute structure qui pourrait surgir du corps principal du cône de croissance, comme on peut le voir sur la figure III-8.

Nous avons d'abord caractérisé la morphologie des cônes de croissance sur des substrats uniformément adhésifs. Les résultats obtenus sont détaillés dans les figures ci-dessous.

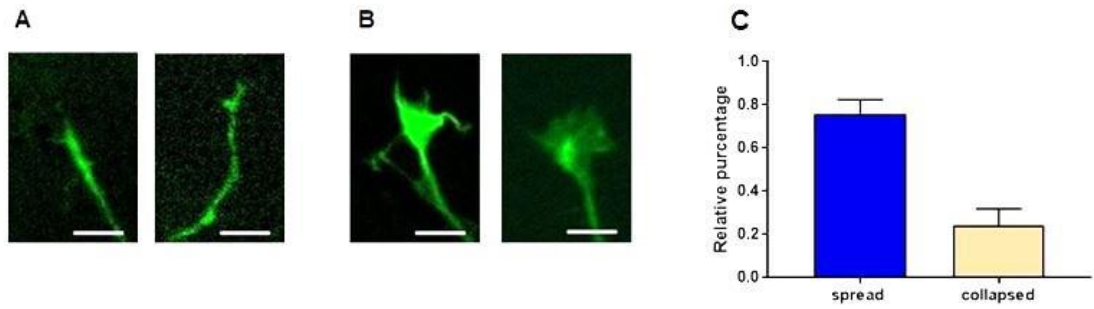


Figure III-9 : Classification morphologique des cônes de croissance sur substrats uniformément adhésifs. A. Cônes de croissance rétractés (collapsed) B. Cônes de croissance étalés (spread) C. Proportions de cône de croissance étalés (spread) et rétractés (collapsed) sur substrats uniformément adhésifs. Valeurs moyennes, les barres d'erreur dénotent les intervalles de confiance à 95%. 2 lamelles, n=97 neurones, n'=174 cônes de croissances

Sur les substrats uniformément adhésifs, la majorité (76%) des cônes de croissance ont une forme étalée (« spread »).

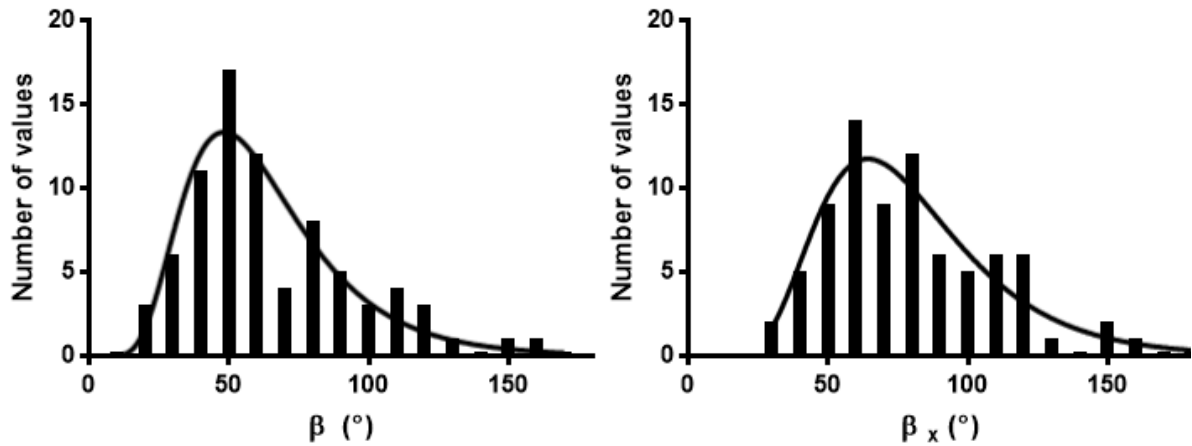


Figure III-10 : Distribution des écarts angulaires de croissances étalés sur des substrats uniformément adhésifs. Ligne noire : fit lognormal (2 lamelles, n=37 neurones, n=80 cônes de croissances).

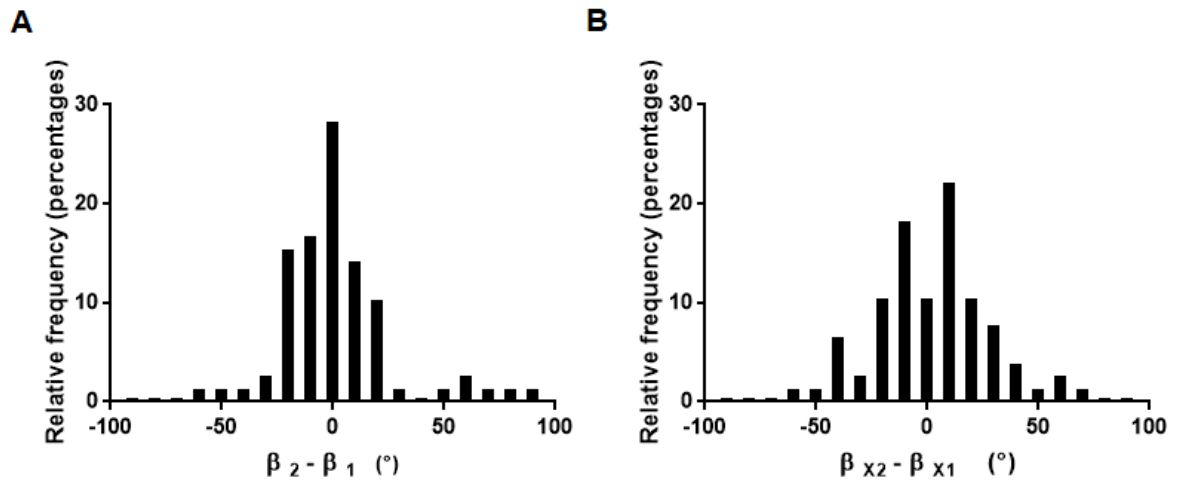


Figure III-11 : Distribution des écarts angulaires de croissances étalés sur des substrats uniformément adhésifs. (2 lamelles, n=37 neurones, n=80 cônes de croissances).

Nous avons ensuite étudié la morphologie des cônes de croissance sur nos substrats micropatternés.

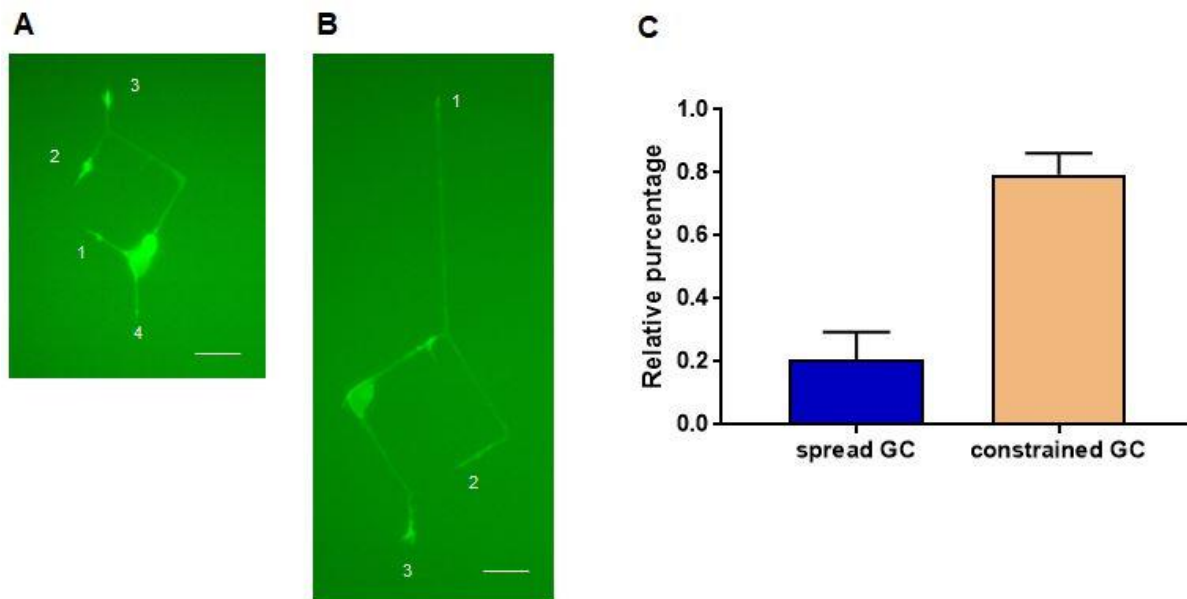


Figure III-12 : Classification morphologique des cônes de croissance sur substrats uniformément adhésifs. A. Cônes de croissance rétractés (collapsed) B. Cônes de croissance étalés (spread) C. Proportions de cône de croissance étalés (spread) et rétractés (collapsed) sur substrats micropatternés. Valeurs moyennes, les barres d'erreur dénotent les intervalles de confiance à 95%. 2 lamelles, n=44 neurones, n'=139 cônes de croissances

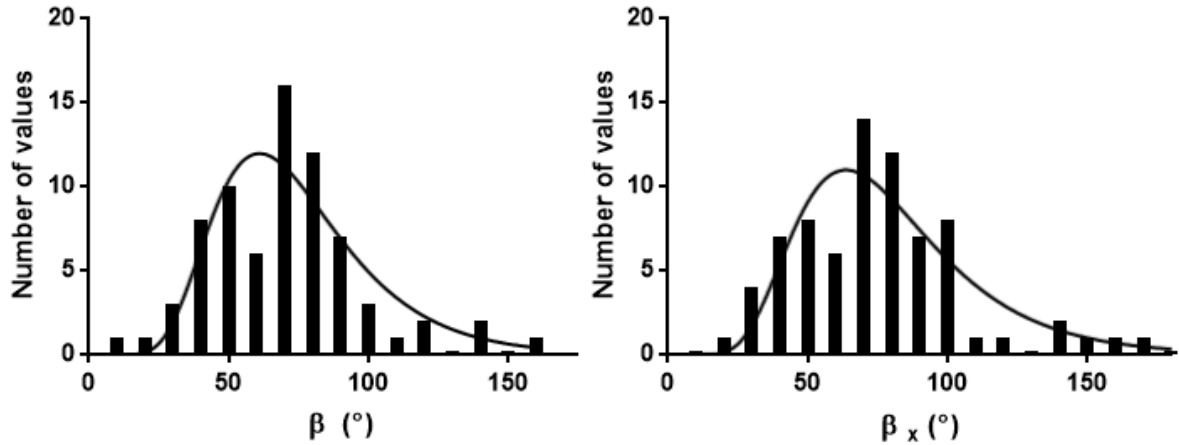


Figure III-14: Distribution des cônes de croissance étalés sur les lignes de 2- μm de nos substrats micropatternés. Mesurés sur images de timelapses de neurones d'hippocampe à DIV1. ($n=16$ neurones, $n'=19$ cônes de croissance, 5 points temporels). Ligne noire : fit lognormal

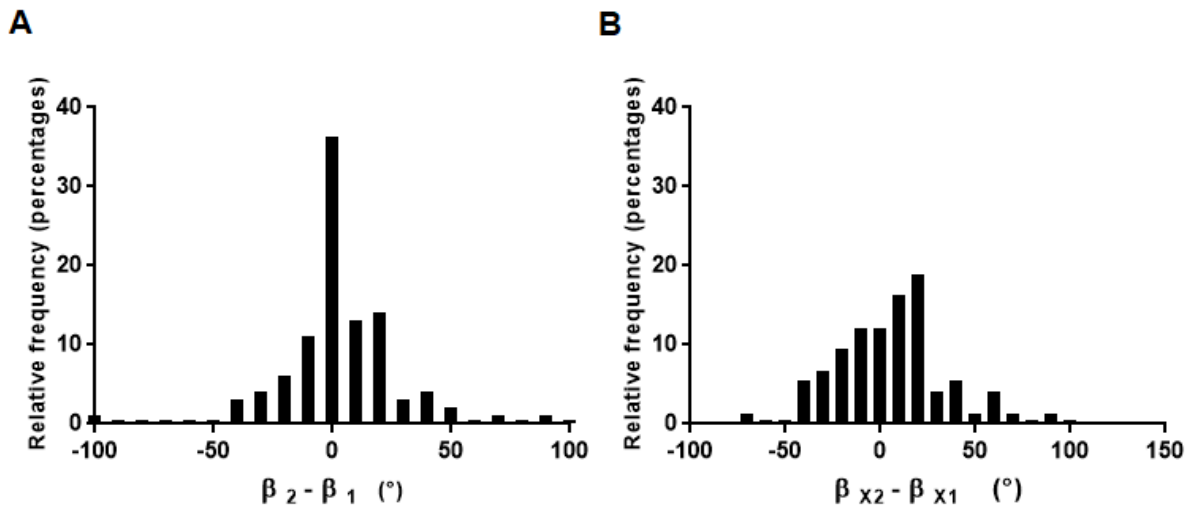


Figure III-15: Distribution des cônes de croissance étalés sur les lignes de 2- μm de nos substrats micropatternés. Mesurés sur images de timelapses de neurones d'hippocampe à DIV1. ($n=16$ neurones, $n'=19$ cônes de croissance, 5 points temporels).

Pour finir, nous avons comparés cônes de croissance sur substrats uniformément adhésifs et sur nos substrats patternés, et obtenus les résultats détaillés dans le tableau ci-dessous.

		Pattern uniformément adhésif	Lignes adhésives de 2µm
Ecart angulaire (°)	β	48±13	70±4
	β_x	64±12	74±4
Facteur d'asymétrie (°)	$ \beta_2 - \beta_1 $	17±18	20±19
	$ \beta_{x2} - \beta_{x1} $	19±15	22±18

Tableau 7 : Comparaison des écarts angulaires de neurites sur substrats uniformément adhésifs et sur nos substrats patternés. (moyenne ±SD)

Etude statique du branchement

Pour étudier le branchement, nous avons commencé par analyser des échantillons fixes de neurones d'hippocampe se développant sur des substrats micropatternés. Les échantillons ont été fixés à DIV 2 et à DIV3.

Nous avons d'abord étudié l'influence de la géométrie du substrat sur la probabilité de branchement. Pour chaque neurone isolé, à chaque point de branchement potentiel, nous avons observé si le neurite branchait ou tournait. Un événement de branchement est défini comme une séparation du neurite en 2 branches filles qui soient toutes les deux d'une longueur supérieure à 30 µm. Dans le cas inverse, l'évènement était compté comme un « turning ». Les cas où les 2 branches avaient une longueur inférieure à 30 µm ont été exclus de l'analyse.

La probabilité de branchement $p_{branching}$ a été définie comme :

$$p_{branching} = \frac{n_{branchement}}{n_{branchement} + n_{turning}}$$

Les figures ci-dessous offrent une présentation concise et exhaustive des résultats obtenus.

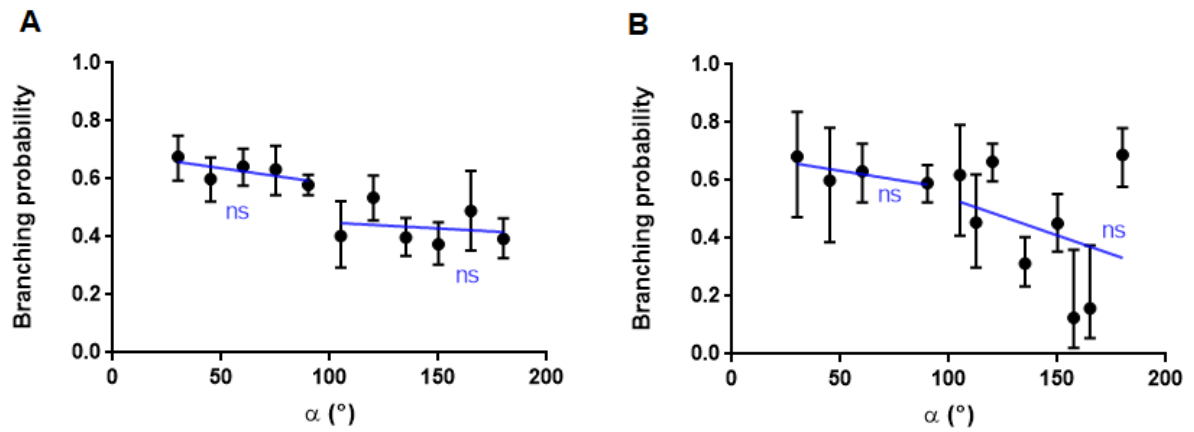


Figure III-18 : A. Probabilité de branchement à DIV2 en fonction de α . Les barres d'erreur dénotent les intervalles de confiance à 95% De gauche à droite : $y=-0.0011x+0.69$, NS (test de régression linéaire, pente comparée à zéro); $y=-0.00041x+0.49$, NS (test de régression linéaire, pente comparée à zéro). 2cultures, 27 lamelles, 2209 points de branchements. **B. Probabilité de branchement à DIV3 en fonction de α .** Les barres d'erreur dénotent les intervalles de confiance à 95% De gauche à droite : $y=-0.0012x+0.69$, NS (test de régression linéaire, pente comparée à zéro); $y=-0.0026x+0.80$, NS (test de régression linéaire, pente comparée à zéro). 2cultures, 27 lamelles, 2209 points de branchements

Nous avons ensuite défini 2 catégories de géométries présentées aux neurites aux intersections : les configurations symétriques et asymétriques, respectivement définies par $\alpha_1 = \alpha_2$ et $\alpha_1 \neq \alpha_2$.

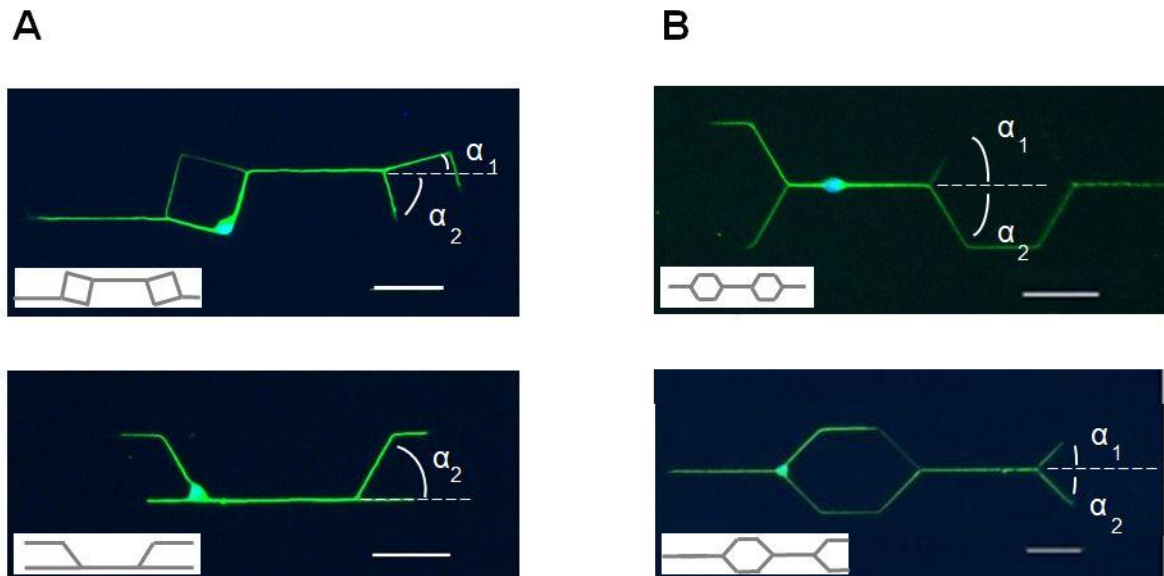


Figure III-19 : A. Configurations de branchements symétriques versus B. Configurations de branchements asymétriques. Images en fluorescence de neurones à DIV2 sur des substrats patternés. Vert : β_3 -tubulin. Bleu : Hoechst (noyau). Encart : Pattern adhésif. Barre d'échelle : 50 μ m.

Pour les configurations symétriques, nous avons obtenu les résultats détaillés dans la figure suivante. La probabilité de branchement symétrique ne semble pas dépendre de l'angle de branchement α .

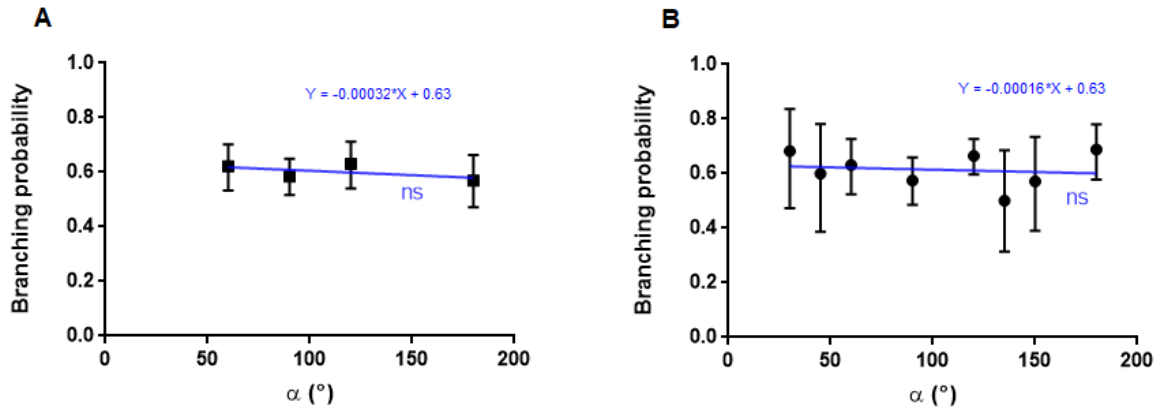


Figure III-20 : Probabilité de branchement symétrique en fonction de α . **A. Probabilité de branchement symétrique à DIV2 en fonction de α .** Les barres d'erreur dénotent les intervalles de confiance à 95%. NS, $r^2=0.32$ NS (test de régression linéaire, pente comparée à zéro); 2 cultures, 27 lamelles, 552 points de branchement. **B. Probabilité de branchement symétrique à DIV3 en fonction de α .** Les barres d'erreur dénotent les intervalles de confiance à 95%. NS, $r^2=0.02$ (test de régression linéaire, pente comparée à zéro); 2 cultures, 9 lamelles, 572 points de branchements.

Pour les configurations asymétriques, nous avons obtenu les résultats détaillés dans la figure suivante. La probabilité de branchement asymétrique semble décroître en fonction de l'angle de branchement α pour des valeurs de $\alpha > 90^\circ$.

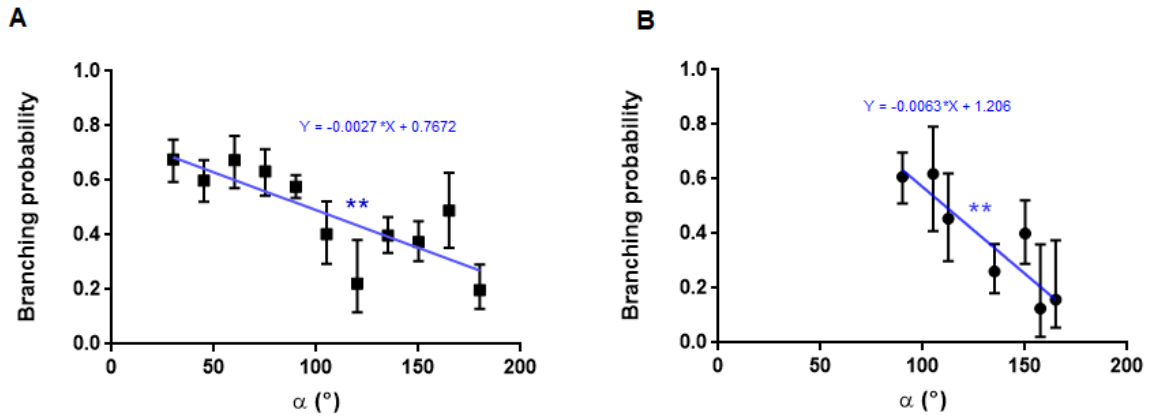


Figure III-21 : Probabilité de branchement asymétrique en fonction de α . A. Probabilité de branchement asymétrique à DIV2 en fonction de α . Les barres d'erreur dénotent les intervalles de confiance à 95%. $p=0.0029$, $r^2=0.64$ (**, test de régression linéaire, pente comparée à zéro); 2 cultures, 27 lamelles, 1657 points de branchement. **B. Probabilité de branchement asymétrique à DIV3 en fonction de α .** Les barres d'erreur dénotent les intervalles de confiance à 95%. $p=0.0051$, $r^2=0.82$ (**, test de régression linéaire, pente comparée à zéro); 2 cultures, 9 lamelles, 344 points de branchements.

Ensuite, nous avons voulu comparer le comportement de branchement des axones à celui des neurites indifférenciés.

Pour distinguer les axones, nous avons utilisé un marquage avec l'anticorps Tau1. La protéine Tau, et plus spécifiquement le gradient de phosphorylation de Tau est souvent utilisé comme marqueur de l'axone. Un neurite présentant un gradient de Tau1 est considéré comme un axone. Un neurite ne présentant pas un gradient de Tau1 a été considéré comme une future dendrite s'il appartenait à un neurone possédant un neurite présentant un gradient de Tau1, comme un neurite indifférencié sinon.

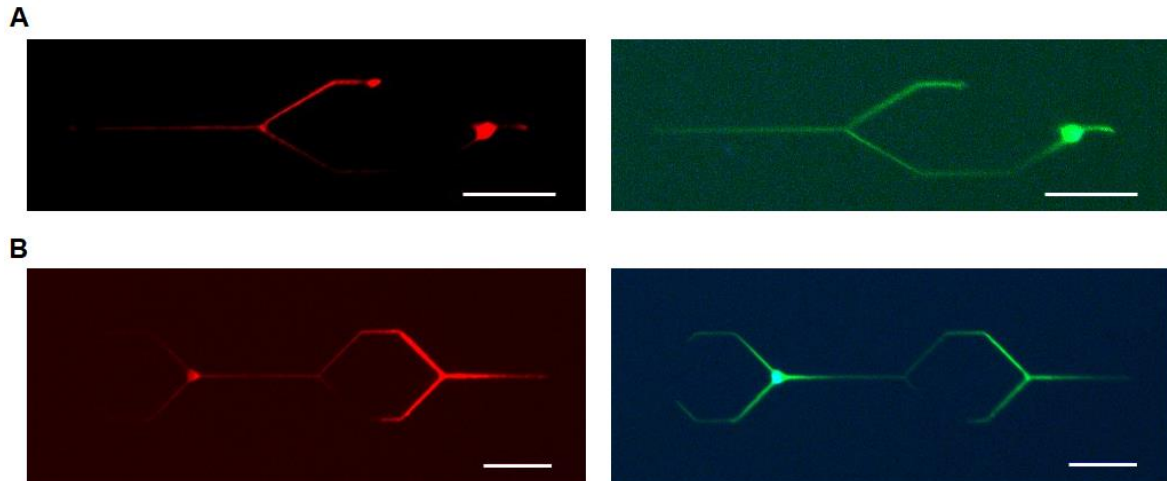


Figure III-25 : Gradient de Tau1 dans un axone branchant. Images en fluorescence de neurones d'hippocampes de souris sur des substrats micropatternés. Les échantillons ont été fixés à DIV2 et marqués avec l'anticorps pour la β -tubuline (vert), pour Tau 1 (rouge) et Hoechst (bleu).

Nous avons ensuite pu comparer les probabilités de branchement entre axones et neurites indifférenciés.

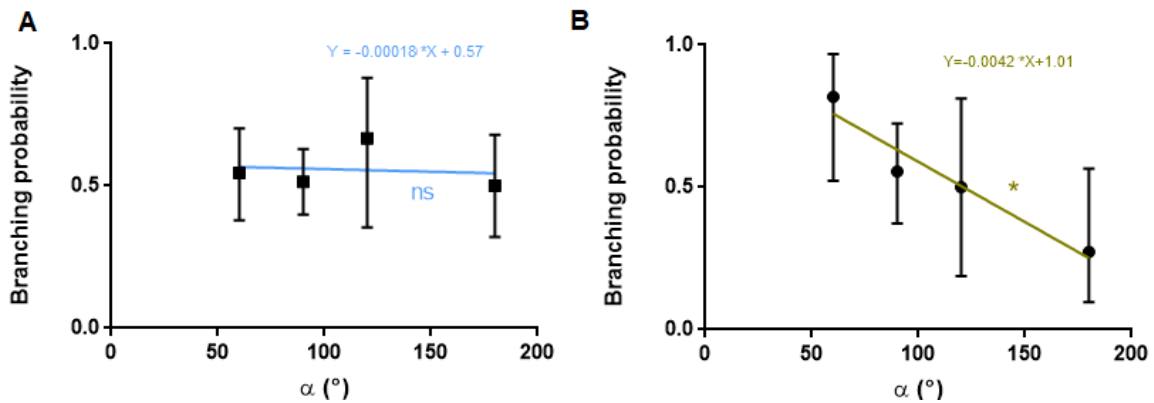


Figure III-27 : Probabilité de branchement dans les configurations symétriques en fonction de α . **A. Probabilité de branchement pour les axones dans les configurations symétriques.** Les barres d'erreur dénotent des intervalles de confiance à 95%. Les mesures ont été réalisées sur des neurones d'hippocampe de souris se développant sur des substrats patternés. Les neurites positifs pour le gradient de Tau-1 ont été comptés comme axones. Les échantillons ont été fixés à DIV2. NS, $r^2=0.02$ (Test de régression linéaire, pente comparée à zéro). 1 culture, 12 lamelles, 136 points de branchements. **B. Probabilité de branchement pour les neurites non différenciés dans les configurations asymétriques.** Les barres d'erreur dénotent des intervalles de confiance à 95%. Les mesures ont été réalisées sur des neurones d'hippocampe de souris se développant sur des substrats patternés. Les échantillons ont été fixés à DIV2. 1 culture, 12 lamelles, 55 points de branchements.

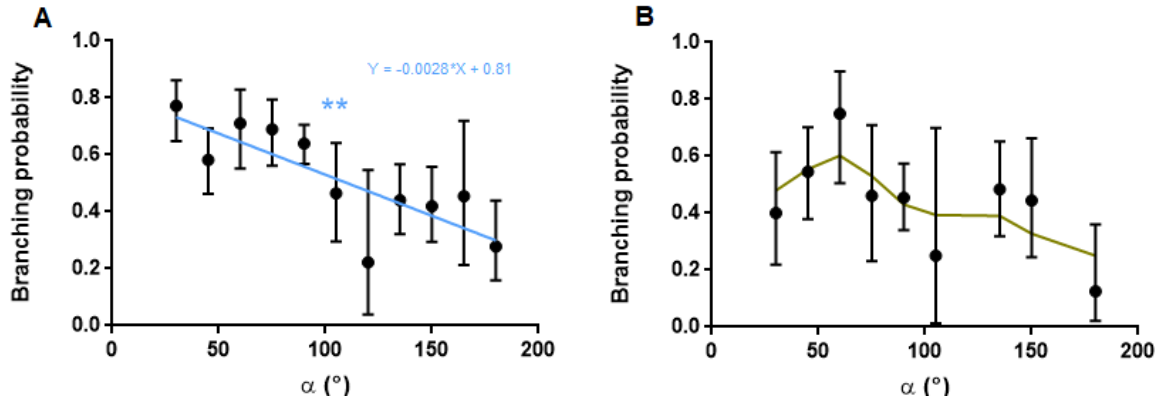


Figure III-28 : Probabilité de branchement dans les configurations asymétriques en fonction de α . A. Probabilité de branchement pour les axones dans les configurations symétriques. Les barres d'erreur dénotent des intervalles de confiance à 95%. Les mesures ont été réalisées sur des neurones d'hippocampe de souris se développant sur des substrats patternés. Les neurites positifs pour le gradient de Tau-1 ont été comptés comme axones. Les échantillons ont été fixés à DIV2. $y=-0.0028x+0.4495$, $p=0.0027$, $r^2=0.65$ (**, Test de régression linéaire, pente comparée à zéro). 1 culture, 12 lamelles, 596 points de branchements. **B. Probabilité de branchement pour les neurites non différenciés dans les configurations asymétriques.** Les barres d'erreur dénotent des intervalles de confiance à 95%. Les mesures ont été réalisées sur des neurones d'hippocampe de souris se développant sur des substrats patternés. Les échantillons ont été fixés à DIV2. 1 culture, 12 lamelles, 223 points de branchements.

Conclusion

Le **Tableau 6** récapitule les différents résultats concernant la probabilité de branchement.

		α	Axones	Neurites non différenciés
Moyenne de la probabilité de branchement (%)	Toutes configurations	$\leq 90^\circ$	0.66 ± 0.08	0.53 ± 0.14
		$> 90^\circ$	0.43 ± 0.03	0.36 ± 0.13
	Configurations symétriques	$\leq 90^\circ$	0.53 ± 0.02	0.69 ± 0.19
		$> 90^\circ$	0.58 ± 0.12	0.39 ± 0.16
	Configurations asymétriques	$\leq 90^\circ$	0.68 ± 0.07	0.52 ± 0.14
		$> 90^\circ$	0.38 ± 0.10	0.38 ± 0.19

Tableau 6 : Comparaison de la moyenne de la probabilité de branchement à DIV2 en configurations symétriques et asymétriques (moyenne sur tous les angles de branchements \pm SD)

Résumé

Le fonctionnement du système nerveux est basé sur l'établissement de circuits neuronaux complexes. Pendant le développement, le branchement axonal permet à chaque neurone de créer des contacts synaptiques avec de multiples cibles. Ce phénomène joue un rôle majeur dans la mise en place des réseaux neuronaux. La compréhension des mécanismes du branchement neuronal est donc essentielle à l'étude du développement des circuits nerveux.

Dans cette thèse, nous avons étudié le branchement neuronal en imposant des contraintes morphologiques aux neurones à l'aide de micropatterns adhésifs. En utilisant des patterns statiques, nous avons pu explorer le comportement des branchements neuronaux dans une large gamme de géométrie. Nous avons en particulier étudié l'influence de l'angle de branchement.

En parallèle, nous avons travaillé sur le développement d'une technique de micropatterning dynamique basée sur l'adsorption spontanée de dérivées PEGylés de poly-L-lysine permettant de créer des patterns reconfigurables, dans le but de pouvoir contrôler spatio-temporellement la génération de branches neuritiques.

Mots Clés

Neurone, branchement, motifs d'adhésion, cône de croissance, patterning dynamique, cytosquelette

Abstract

The function of the nervous system relies on the establishment of complex neuronal circuitry. During development, axon branching allows each neuron to establish synaptic contacts with multiple targets and is essential to the assembly of highly interconnected networks. Therefore, understanding the mechanisms underlying the control of neuronal branching is crucial in the study of neuronal circuit development.

In this thesis, we investigated neuronal branching by imposing morphological constraints to neurons through the use of different chemical micropatterning techniques. Using static micropatterns, we explored branching behavior in a wide range of geometries with a focus on the influence of branching angle. In parallel, we have also worked on the development of a dynamic patterning technique based on spontaneous adsorption of comb-like derivatives of poly-L-lysine to form switchable patterns on highly cell-repellent surfaces, with the aim of creating a platform enabling spatio-temporally controlled generation of neurite branches.

Keywords

Neuron, branching, adhesive patterns, growth cone, dynamic patterning, cytoskeleton